SAPIENZA
UNIVERSITÀ DI ROMA

Dipartimento di Ingegneria Meccanica e Aerospaziale

Dottorato in Tecnologia Aeronautica e Spaziale

Development of modal analysis methodologies for the identification of aerospace structures in operating conditions

by

Chiara Grappasonni

XXV ciclo

cover art: *Vite Aerea* - Leonardo da Vinci (1487/1490)

SAPIENZA
UNIVERSITÀ DI ROMA

Development of modal analysis methodologies for the identification of aerospace structures in operating conditions

by

Chiara Grappasonni

Approved by :

Prof. G. Coppotelli, Advisor

Prof. F. Nitzsche, Advisor

Prof. R. Barboni, Reviewer

Prof. F. Mastroddi, Reviewer

Prof. D.J. Ewins, International Reviewer

Prof. L. Casalino, National Committee Member

Prof. M. Gennaretti, National Committee Member

Prof. E. Martelli, National Committee Member

Date Approved: _____

©*2013 - Chiara Grappasonni*

All rights reserved.

In Principio... Nonna
Fortitudo... Papo
Dulcedo... Mamy
Spes... Giulia

Acknowledgments

First and foremost, I would like to express my deep gratitude to Professor Giuliano Coppotelli and Professor Fred Nitzsche, my research supervisors, for their professional guidance, valuable support, useful and constructive recommendations on my research work. Special thanks should be given to Professor Alessandro Agneni that prematurely passed away last year. He taught me about the theoretical innovations of the good old days. I would also like to express my very great appreciation to Professor Franco Mastroddi for his valuable and constructive suggestions. During the planning and development of this research work I had the possibility to meet many Professors and Researchers worldwide and I would like to thank all of them belonging to the GARTEUR AG-19, Bristol University, Carleton University, Clarkson University and Georgia Institute of Technologies. In particular I want to express my gratitude to Professor Ewins, Professor Marzocca and Professor Ruzzene because they not only allow me to work in their laboratories but also gave me the opportunity to learn how to do it in the good way. My grateful thanks are also extended to Dr Ameri, Dr Chierichetti and Dr Ulker for their help in doing the experimental tests and the data analysis, their willingness to give their time and support so generously has been very much appreciated. Some companies and institutions also supported the research and I would like to thank Smart Rotor System for the activities on the APL, Avio for the activities on the Vega Laucher, the Canadian National Research Center in Ottawa and the German Aerospace Center, DLR, in Braunschweig for the whirl tower tests and the Guidance and Navigation Laboratory of my University for providing the manipulator. I would also like to extend my thanks to the technicians and users of the laboratories I visited worldwide for their help in offering me the resources in running every different test campaign described in this thesis. I want to thank all my friends and colleagues from the Department of Mechanical and Aerospace Engineering. They supported me in my research work with mutual understanding. In particular, since I started to become keen on the structural dynamics, I can say that I always was in good company and I really want to express my gratitude to whom I hold in greatest esteem: That's What It's All About (or "That's for it about"?). Finally, I am most grateful to my family for the needful, open-hearted and prompt support that made everything possible. Since I am truly persuaded that the emotions drive the brain and the research need to be headed by the brain, my work would not be possible without the love and mind of the man who shared with me this experience and something more: I do thank you, Alessandro.

Abstract

Operational modal analysis differs from traditional experimental modal analysis in that it only requires information of the output responses and the modal parameters (in terms of natural frequencies damping ratios and mode shapes) are estimated under the assumption of white noise excitation. It presents several advantages including the availability of modal properties of structure in operation thus representing a closer picture of the structure and its boundary conditions (which are not that easy to realize in laboratory conditions). However, lack of input excitation force information presents several challenges as well as the proper estimation of the frequency response functions and the accurate evaluation of modal parameters in presence of harmonic components in the excitation. Several methodologies have been developed in the last years as described in this thesis and the main purpose of the research is to assess their application in aerospace such as the rotorcraft technology and the environmental testing. Solutions to the main operational modal analysis limitations are suggested and the implementation of the related algorithms allows the application on several test cases after their validation. Taking advantages of this improving in the experimental analysis capabilities, a demanding application within the rotorcraft technology is carried out. Starting from the already developed Active Pitch Link prototype (based on the Smart Spring concept), its use for vibration reduction on rotating blade is numerically and experimentally investigated, thanks to the intensive use of the operational modal analysis for the identification of the real system properties that give the necessary information for the tuning of the numerical model, that in turn suggests the operative test conditions.

Contents

List of Acronym

ACF = Actively Controlled Flap

ACT = Actively Controlled Tip

APL = Active Pitch Link

ARMA = Auto-Regressive Moving-Average

BLADE = Bristol Laboratory for Advanced Dynamics Engineering

BR = Balanced Realization

CMIF = Complex Mode Indicator Function

CMS = Constant Mode Shapes

EMA = Experimental Modal Analysis

ERA = Eigensystem Realization Algorithm

ERAH = Eigensystem Realization Algorithm for Harmonic Excitation

F-SSI = Frequency-Stochastic Subspace Identification

FBG = Fiber Bragg Grating

FDD = Frequency Domain Decomposition

FRF = Frequency Response Function

GARTEUR = Group for Aeronautical Research and Technology in Europe

HHC = Higher Harmonic Control

HTM = Hilbert Transform Method

I/O = Input/Output

IBC = Individual Blade Control

IGE = In-Ground Effect

IRF = Impulse Response Function

ITD = Ibrahim Time-Domain

LSCE = Least Squares Complex Exponential

LSCF = Least-Squares Complex Frequency-domain

LSFD = Least Squares Frequency-Domain

MAC = Modal Assurance Criterion

MCF = Modal Confidence Factor

MDOF = Multi Degree Of Freedom

MIMO = Multiple Input Multiple Output

MLE = Maximum Likelihood Estimator

NF = Non Filtered

NIMA = Natural Input Modal Analysis

OGE = Out of Ground Effect

OMA = Operational Modal Analysis

P-LSCE = Polyreference Least Squares Complex Exponential

PSD = Power Spectral Density

RBN = Receptance Based Normalization

SDOF = Single Degree Of Freedom

SGFRP = Short Glass Fiber Reinforced Plastic

SHARCS = Smart Hybrid Active Rotor Control System

SRR = Sine-to-Random Ratio

SSI = Stochastic Subspace Identification

SVD = Singular Value Decomposition

TSA = Time Synchronous Averaging

UAV = Unmanned Aerial Vehicle

VABS = Variational Asymptotic Beam Section

Introduction

To telle yow al the condicioun,
Of ech of hem, so as it semed me...

[G.Chaucer, The Canterbury Tales]

The experimental investigations on the structural dynamics have relevant interest in updating the numerical model, validating computational predictions and assessing the mission specifications. The high cost associated to the qualification campaign induces severe reductions in the experimental tests. Dealing with aerospace applications, two different types of experimental tests can be carried out, such as ground vibration tests and in-flight tests. The actual market demand is just to reduce cost and duration of both ground vibration and flight tests of aerospace vehicle, while increasing the precision of measurements. To achieve this goal, new measurement techniques and innovative algorithms are necessary to reduce the duration of test preparation (test specimen instrumentation, test area layout, etc.) and increase the accuracy of the results. The experimental modal analysis (EMA) addresses all these tasks by considering that the excitation and the responses of the system are measurable. The new operational modal analysis (OMA) developments made possible to identify the modal characteristics of a structure operating in its actual working conditions, undergone an unknown excitation loading. This leads to a more reliable modal model with respect to the ones that could be estimated through the ground vibration tests and/or other experimental modal analysis tests performed in labs. The key idea, behind all the developed approaches, is represented by the assumption on the input loading, required to be a distributed stochastic load, constant in a broad frequency band. This assumption is generally considered acceptable, since the white noise excitation usually characterizes the operating conditions. On the other hand it is too restrictive in case of

rotorcraft applications, because they cannot prescind from the harmonic aerodynamic loads. Moreover the OMA methodologies are able to estimate the modal parameters, such as the natural frequencies, damping ratios and mode shapes, but cannot reconstruct the frequency response function of the system, because the modes cannot be scaled without further information on the system. These two problems related to the actual OMA state-of-the-art are addressed in this thesis. The overall objective of this thesis is to develop methodologies able to improve the analyses related to the experimental tests by ensuring a good estimate of the dynamical behaviour of the vehicle, able to qualify and validate the corresponding numerical model, also in case of harmonic components embedded in the loading excitation. In this thesis two approaches for the mode scaling are presented as introduced in Ref.[1] and [2]. They are based on the variation of the mass of stiffness properties of the structure in order to induce a known variation on the modal parameters that can be used to reconstruct the loading participation factor, that is unknown in the operating conditions. The application of these techniques is extended, in this thesis, to the environmental testing as it is commonly used for the qualification procedure of the space structures to the launch phase. In fact, the mandatory response analysis preceding the space mission is performed on a vibration benchmark in which the loading is not known, but the acceleration coming from the launch vehicle is reproduced as a base movement during the qualification test campaign. In this contest the OMA can be applied to the system responses when the random excitation is imposed and also the modal parameters can be achieved, providing a full characterization of the structure.

Several OMA techniques, both in frequency and in time domain, have been developed in recent years to deal with the experimental investigation carried out on systems in operating conditions, when the excitation cannot be measured. Belonging to the first group of methodologies, the Frequency Domain Decomposition (FDD, Ref.[3]) and the Hilbert Transform Method (HTM, Ref.[4]) have been spread around and applied in the aerospace field. The first one achieves the natural frequencies and the modes from the singular value decomposition of the response Power Spectral Density (PSD) matrix. HTM is based on the properties of

the Hilbert transform to evaluate the so-called biased frequency response functions from the response PSD. The unknowing about the excitation entails the un-scaling of these functions, which have the same shape of the real ones except for a frequency constant gain. The Stochastic Subspace Identification (SSI, Ref.[5]) techniques associate the state-space model of the system to the observed output responses through the so called orthogonal projection technique. In particular, two approaches has been outlined, that are the Balanced Realization (BR, Ref.[6]) and the frequency-SSI. They differ from each other in the processing of the system responses in time or in frequency domain. The first approach provides the observability matrix of the system starting from the so called Hankel matrix evaluated with the correlation functions among the output time responses, whereas the second method follows the same procedure in the frequency domain computing the Vandermonde matrix with the output spectra. All these methodologies are presented in the thesis, together with several experimental applications. Their intensive use has been possible, thanks to the development of a numerical platform, called NIMA as Natural Input Modal Analysis.

Further methodologies are presented as extensions to the previously described approaches to improve their application in the aerospace technology. In particular a solution to those cases with the lack in the hypothesis concerning the main excitation loading has been assessed with the development of an approach capable to identify the frequencies at which the harmonic excitation is acting and then to remove its effects on the system responses, Ref.[7]. The first task is obtained by means of a statistical characterization of the system responses through the Entropy index, that can be used as a detector of non-Gaussianity signals. In the second instance the bias Frequency Response Functions gained by the Hilbert Transform Method are used as base functions to identify the forced responses. This allows the final evaluation of new FRF, still bias by the white noise broadband excitation, but not more distorted by the operational contributions. This methodologies is presented, validated through numerical simulation and widely used in this thesis in order to prove its effectiveness in dealing with several and different situations in which the stochastic white noise loadings is blended together with high amplitude, with respect to the variance

of the random signal, harmonic excitations. A typical example, in the aerospace field, is the intrinsic periodic nature of the airloads acting on the rotor blade of a rotary wing aircraft. Indeed, rotary wing aircrafts are typically characterized by a severe vibration environment, Fig.1. The aerodynamic phenomena

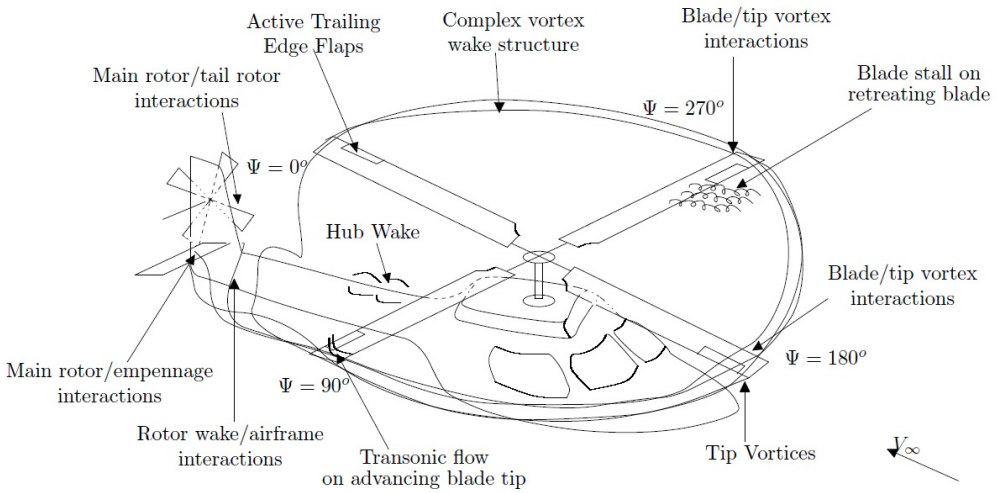

Figure 1: Schematic representation of aerodynamic environment around helicopter in forward-flight, [8].

result in fluctuating aerodynamic loads that, when coupled with the dynamic characteristics and elastic motion of the blade, create a challenging aeroelastic problem, Ref.[9]. The applications in rotorcraft technologies involves several aspects that are addressed in the last part of the thesis from the theorethical numerical and experimetal point of view. In particular the main outcome of the aeroelastic problem is an excessive amount of noise and vibration transmitted to the fuselage through the rotor hub and shaft. This excessive level of vibration degrades helicopter performance, pilot/passanger comfort and contributes to high cost maintenance problems. Moreover, the challenges of the helicopter vibration control problem can be taken into account, leading to the development of control strategies in response to the high demand for helicopter vibration suppression from industry. Recent efforts have concentrated on developing active vibration suppression strategies, Ref.[8]. These include classical Higher Harmonic Control (HHC) [9] and Individual Blade Control (IBC). In general, active vibration control requires three main steps: definition of the system, modeling of the system, and design and implementation of the controller, as demonstrated in

the following Fig.2. Hence, the general goal of this research is to start with a more accurate representation

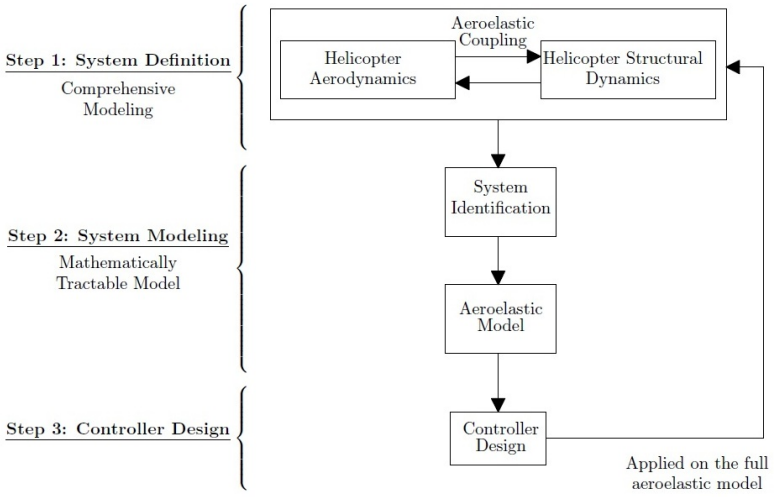

Figure 2: Proposed approach for active vibration control of helicopters [10].

of the helicopter blade aeroelastic system, which can potentially provide means of designing better active control systems still in the preliminary design phase of an active helicopter rotor. Within the thesis activities the design validation and testing of a reduced-scale helicopter blade is performed. The purpose is the validation of the Smart Hybrid Active Rotor Control System (SHARCS), that is an international project lead by the Carleton University Rotorcraft Research Group, Ref.[11]. The hybrid control concept introduced by the SHARCS project uses an Active Pitch Link (APL) to control both the structural and flow properties of the helicopter blade system. In this thesis the identification of the rotating blade is performed and a control law for vibration reduction is experimentally tested in the existing whirl-tower facility at Carleton University that has been modified to simulate forward flight conditions. The problem is addressed from the theoretical, numerical and experimental point of view, taking advantages of the advanced state-of-the-art of the SHARCS project. It is stressed that the mandatory starting point of this complex coupled problem, involving the control of the rotorcraft dynamics, is the identification process of the system, that can be performed during the in-flight conditions taking advantages from the operational modal analysis methodologies. In this case, the identification of the modal parameters from the operational response could be skewed, especially the damping ratios, when a natural frequency of the structure is close

to the one of the harmonic excitation loading coming from the rotor. The improvement of operational modal analysis to accurately identify the modal parameters in such a frequency range, considered critical for the safe life of the structure, is therefore one of the main concern of researchers.

Outline

The thesis can be divided in three parts:

1. The Operational Modal Analysis methodologies are described starting from a theoretical background dissertation on vibration analysis. Here the important methodological contributions given to the modal analysis are introduced and their formulation is explained.

2. The spread validation with aerospace applications is performed in terms of Ground Vibration, Flight, Whirl Tower, Wind Tunnel, Environmental tests, that are described as they have been carried out worldwide with the aim of proving the effectiveness of the methodologies by addressing different problems related to the operating conditions.

3. A detailed dissertation about the rotorcraft applications is included, since the rotorcraft dynamics is recognized as very critical and require a more accurate description of the theoretical aspects for the understanding of the performed numerical and experimental analyses. The developed OMA has been used to drive the identification process of the experimental benchmark and it led to a control strategy able to achieve vibration reduction as numerically predicted using the individual blade control approach.

Part I

Theoretical Basis

Chapter 1

Background on vibration analysis

The understanding of the dynamical behavior of a system cannot leave aside the vibration analysis, on which can be founded and that gives the tools for its understanding. According to D.J.Inman, vibration is the subdiscipline of dynamics that deals with the repetitive motion of objects relative to a stationary frame of reference or nominal position (usually equilibrium), Ref.[12]. Furthermore, the basic vibration properties of the general linear structure form the basis of experimental modal analysis. In this chapter the "theoretical route" for vibration analysis is shown as suggested by D.J.Ewins in [13]. Fig.1.1(a) illustrates the three phases through which a typical vibration analysis progresses. A first description of the structure's physical characteristics is given in terms of its mass, stiffness and damping properties and this is referred to as the *spatial model*. Then the analytical modal analysis of such a model leads to the *modal model*, that is a description of the structure's behavior as a set of vibration modes, in terms of natural frequencies, mode shapes and damping factors. These are called the *normal* or *natural* modes of the structure, since they always describes the various ways in which the structure is capable of vibrating naturally, without any external forcing. The analysis of exactly how the structure will vibrate under given excitation conditions is performed in the third stage in order to obtain a *response model*. Although innumerable solutions could be evaluated depending on the imposed excitation, the Frequency Response Functions (FRFs) are usually

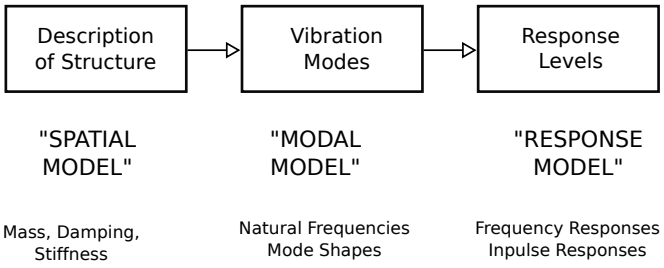

(a) Theoretical Route to Vibration Analysis

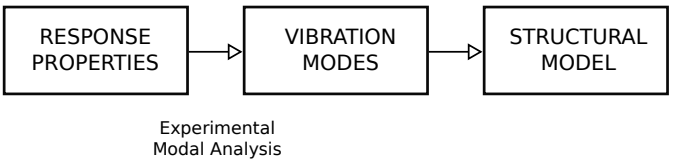

(b) Experimental Route to Vibration Analysis

Figure 1.1: Comparison between theoretical and experimental approaches in vibration analysis, Ref.[13].

considered as the most representative of the system dynamics. They are defined as the responses of the structure when a unit-amplitude sinusoidal force is applied to each point of the structure individually and at every frequency within a specified range. On the other hand, the route to vibration analysis can be undertaken also in the reverse direction, as shown in Fig.1.1(b). Here the experimental investigations lead the process from the measurement of the system's response properties, through the identification of the vibration modes by applying the experimental modal analysis, to the synthesis of a representative structural model.

A detailed study of the analytical dynamics has been developed in the past in order to derive a mathematical formulation of the governing equations describing a mechanical system subjected to vibrations, starting from the conservative principles of the system's mass, momentum and total energy, as well as from the principle of virtual work. Here for the sake of brevity this analytical procedure is not rewritten, and a good description can be found in many books as Refs.[14]-[15]. Nevertheless some basic equations are pointed

out to head the understanding of the devised mathematical formulation.

1.1 Spatial Model

The second order formulation of a linear system with N degrees of freedom can be written in a matrix form:

$$\boldsymbol{M}\ddot{\boldsymbol{x}}(t) + \boldsymbol{C}\dot{\boldsymbol{x}}(t) + \boldsymbol{K}\boldsymbol{x}(t) = \boldsymbol{f}(t) \tag{1.1}$$

where the symmetric matrices $\boldsymbol{M}$,$\boldsymbol{C}$, $\boldsymbol{K}$ represent the mass (or inertia), damping, stiffness matrices, respectively, with dimension $N \times N$, and the vectors $\boldsymbol{x}(t)$ and $\boldsymbol{f}(t)$ are the displacement and the force time-varying vectors, respectively. In Eq.(1.1) the contribution of non-conservative forces due to viscous damping has been taken into account by considering that they are proportional to the velocity as devised by the *Rayleigh's dissipation function*. It is worthwhile to remark that Eq.(1.1) is also known as the Lagrange's equation of motion and can be obtained starting from the Newton's second law (Ref.[15] Sec. 4.3) as well as from the D'Alembert's principle (Ref.[15] Sec. 6.5), under the assumptions that the displacements from the equilibrium position are sufficiently small that the linear force-displacement and force-velocity relations hold. The system's matrices in such Lagrange's equation of motion comes from the definition of the kinetic energy, T, the Reyleigh's dissipation function, D, and the potential energy, V, respectively

$$T = \frac{1}{2}\dot{\boldsymbol{x}}^T\boldsymbol{M}\dot{\boldsymbol{x}} \tag{1.2}$$

$$D = -\dot{\boldsymbol{x}}^T\boldsymbol{C}\dot{\boldsymbol{x}} \tag{1.3}$$

$$V = \frac{1}{2}\boldsymbol{x}^T\boldsymbol{K}\boldsymbol{x} \tag{1.4}$$

that are the matrix expressions of functions generally known as quadratic forms of the displacements (in the latter case) or velocities (in the previous two cases). In particular the kinetic energy is always positive

Throughout the thesis the matrices are represented by upper-case letters in boldface ($\boldsymbol{M}$), while the corresponding element is denoted by generic subscript notation (M_{ij}). Similar notation is used for the vectors with lower-case letters in bold face ($\boldsymbol{v}$) and for the the elements with subscript (v_i).

definite, so that $\boldsymbol{M}$ is positive definite, since it is the matrix whose elements are the coefficients of a positive definite quadratic form. On the other hand the potential energy is positive semi-definite, so that also $\boldsymbol{K}$ is positive semi-definite, by allowing the presence of rigid-body motion in case of the system is unrestrained.

Finally it should be noted that Eq.(1.1) represents a system of linear second-order differential equations (with constant coefficients) with the time as independent variable, therefore two initial conditions has to be considered in order to solve it with a closed form:

$$\begin{aligned} \mathbf{x}(t=0) &= \boldsymbol{x}_0 \\ \dot{\boldsymbol{x}}(t=0) &= \dot{\boldsymbol{x}}_0 \end{aligned} \tag{1.5}$$

1.2 Modal Model

Let's now introduce eigenvalue problem of the system, as the eigenvalue problem associated with matrices $\boldsymbol{M}$ and $\boldsymbol{K}$ in the form:

$$\boldsymbol{K}\boldsymbol{\psi} \;=\; \omega^2 \boldsymbol{M}\boldsymbol{\varphi} \tag{1.6}$$

The determinant of Eq.(1.6), also called the characteristic determinant, should vanish to lead to nontrivial solutions, then

$$|\mathbf{K} - \omega^2 \mathbf{M}| \;=\; 0 \tag{1.7}$$

is an equation of order N in ω^2 and it possesses in general N distinct roots, referred to as characteristic values, or eigenvalues. The square roots of these quantities are the system natural frequencies ω_n $(n = 1, 2, \ldots, N)$ and, associated with every one of them, there is a certain nontrivial vector $\boldsymbol{\psi}^{(n)}$, whose

A function of several variables is said to be positive definite if it is never negative and is equal to zero if and only if all the variables are zero.

A function of several variables is said to be positive semi-definite if it is never negative and can be zero at points other than those for which all the variables are zero.

elements $\psi_i^{(n)}$ are real numbers, that is a solution of the eigenvalue problem, such that

$$\boldsymbol{K}\boldsymbol{\psi}^{(n)} = \omega_n^2 \boldsymbol{M}\boldsymbol{\psi}^{(n)}, \quad n = 1, 2, \ldots, N \tag{1.8}$$

These eigenvectors are also referred to as modal vectors and represent physically the so-called natural modes. It should be noted that the shape of the natural modes is unique, but not the amplitude, since if $\psi_i^{(n)}$ is a solution of the Eq.(1.8), then $\alpha_n \psi_i^{(n)}$ is also a solution, where α_n is an arbitrary constant. This is the reason why in the thesis they are usually referred to as mode shapes. The process of adjusting the elements of the natural modes to render their amplitude unique is called normalization, and the resulting vectors are referred to as normal modes. A very convenient normalization scheme consists of setting α_n, such that if $\boldsymbol{\varphi}^{(n)} = \alpha_n \psi_i^{(n)}$, then

$$\boldsymbol{\varphi}^{(n)T}\boldsymbol{M}\boldsymbol{\varphi}^{(n)} = 1, \quad n = 1, 2, \ldots, N \tag{1.9}$$

which has the advantage that it yields

$$\boldsymbol{\varphi}^{(n)T}\boldsymbol{K}\boldsymbol{\varphi}^{(n)} = \omega_n^2, \quad n = 1, 2, \ldots, N \tag{1.10}$$

Thanks to the properties of the system matrices, highlighted in the previous Sec.1.1, the natural modes posses the property of orthogonality with respect to the mass and stiffness matrices:

$$\boldsymbol{\psi}^{(r)T}\boldsymbol{M}\boldsymbol{\psi}^{(s)} = \delta_{rs} m_r, \quad r, s = 1, 2, \ldots, N \tag{1.11}$$

$$\boldsymbol{\psi}^{(r)T}\boldsymbol{K}\boldsymbol{\psi}^{(s)} = \delta_{rs} k_r, \quad r, s = 1, 2, \ldots, N \tag{1.12}$$

where δ_{rs} is the Kronecker delta [1], m_r and k_r are the modal masses and stiffness such that $\omega_r^2 = k_r/m_r$, for each mode $r = 1, 2, \ldots, N$. If the modes are also normalized according to Eq.(1.9), then they satisfy the relations

$$\boldsymbol{\varphi}^{(r)T}\boldsymbol{M}\boldsymbol{\varphi}^{(s)} = \delta_{rs}, \quad r, s = 1, 2, \ldots, N \tag{1.13}$$

$$\boldsymbol{\varphi}^{(r)T}\boldsymbol{K}\boldsymbol{\varphi}^{(s)} = \delta_{rs}\omega_r^2, \quad r, s = 1, 2, \ldots, N \tag{1.14}$$

[1] The Kronecker delta δ_{ij} is defined as being equal to unity for $i = j$ and equal to zero for $i \neq j$

A standard modal change of coordinates can be performed, if the modal vectors are arranged in a square matrix on order N, known as the modal matrix and having the form

$$\boldsymbol{\psi} = \left[\boldsymbol{\psi}^{(1)}, \boldsymbol{\psi}^{(2)}, \ldots, \boldsymbol{\psi}^{(N)}\right] \tag{1.15}$$

and so the linear transformation is:

$$\boldsymbol{x} \;=\; \boldsymbol{\psi}\boldsymbol{q} \tag{1.16}$$

and the Eq.(1.1), can be written in the form

$$m_r\ddot{q}_r(t) + \sum_{s=1}^{N} d_{rs}\dot{q}_s(t) + m_r\omega_r^2 q_r(t) = g_r(t) \tag{1.17}$$

where $\boldsymbol{q}(t)$ are recognized as the system modal displacements, $\boldsymbol{g}(t)$ are the associated generalized forces, coming from the projection of the vector of the applied forces on the modal base ($g_r(t) = \sum_{s=1}^{N} \psi_s^{(r)} f_s(t)$) and the modal damping matrix is introduced as

$$d_{ij} := \boldsymbol{\psi}^{(i)T}\boldsymbol{C}\boldsymbol{\psi}^{(j)} \tag{1.18}$$

since, in general, it is not diagonal, although it is symmetric and positive, see Ref.[16].

1.2.1 Weakly damped linear structures: Reyleigh-Basile hypothesis

Let's consider the vibration of a weakly damped linear structure, so described by Eq.(1.1) with the assumption that the elements of the matrix $\boldsymbol{C}$ are of an order of magnitude less than those of the matrices $\boldsymbol{M}$ and $\boldsymbol{K}$. The generic eigenvalue problem, extended to all the matrices of this system, can be formulated as

$$(\lambda_n^2\boldsymbol{M} + \lambda_n\boldsymbol{C} + \boldsymbol{K})\boldsymbol{p}^{(n)} = 0 \tag{1.19}$$

being λ_n and $\boldsymbol{p}^{(n)}$ the n-th complex eigenvalue and eigenvector, respectively. According to Ref.[17], if $\Delta\lambda_n$ and $\boldsymbol{\Delta p}^{(n)}$ are the eigenvalues and eigenvectors increments due to the presence of the weak damping, one

has

$$\lambda_n = j\omega_n + \Delta\lambda_n \tag{1.20}$$

$$\boldsymbol{p}^{(n)} = \boldsymbol{\psi}^{(n)} + \boldsymbol{\Delta p}^{(n)} \tag{1.21}$$

Substituting Eqs.(1.21) and (1.20) into the basic damped eigenproblem, Eq.(1.19), yields

$$\left[\left(-\omega_n^2 + 2j\Delta\lambda_n\omega_n + \Delta\lambda_n^2\right)\boldsymbol{M} + \left(j\omega_n + \Delta\lambda_n\right)\boldsymbol{C} + \boldsymbol{K}\right]\left(\boldsymbol{\psi}^{(n)} + \boldsymbol{\Delta p}^{(n)}\right) = 0 \tag{1.22}$$

which, once it is recast avoiding the perturbations grater and equal to the second order, using the Eq.(1.8) gives

$$\left(-\omega_n^2\boldsymbol{M} + \boldsymbol{K}\right)\boldsymbol{\Delta p}^{(n)} + j\omega_n\left(2\boldsymbol{M}\Delta\lambda_n + \boldsymbol{C}\right)\boldsymbol{\psi}^{(n)} = 0 \tag{1.23}$$

Next, if the Eq.(1.23) is pre-multiplied by $\boldsymbol{\psi}^{(n)T}$ and considering the transpose of the Eq.(1.8), one has the scalar relationship

$$\boldsymbol{\psi}^{(n)T}\left(2\boldsymbol{M}\Delta\lambda_n + \boldsymbol{C}\right)\boldsymbol{\psi}^{(n)} = 0 \tag{1.24}$$

or, by recalling Eq.(1.18)

$$\Delta\lambda_n = -\frac{d_{nn}}{2m_n} \tag{1.25}$$

which implies that the first order correction due to the damping on the structural eigenvalues is a real negative number, since $m_n > 0$ and $d_{nn} > 0$ for the positiveness of matrices $\boldsymbol{M}$ and $\boldsymbol{C}$, respectively. Thus the first order damped eigenvalues are given by

$$\lambda_n = \pm j\omega_n - \frac{d_{nn}}{2m_n} \tag{1.26}$$

implying also that the first order correction for the damped eigenvalues involves the diagonal terms only of the modal damping matrix Eq.(1.18). Next, in order to evaluate the eigenvector correction $\boldsymbol{\Delta p}^{(n)}$ due to

this includes also the terms like $\boldsymbol{D}\Delta\lambda_n$ or $\boldsymbol{D}\boldsymbol{\Delta p}^{(n)}$, since the hypothesis of weakly damped structures.

the damping presence, let's consider the following modal base representation for such a vector

$$\boldsymbol{\Delta p}^{(n)} = \sum_{\substack{s=1 \\ s\neq n}}^{N} \gamma_s^n \boldsymbol{\psi}^{(s)} \tag{1.27}$$

where the contribution on the perturbation of the n-th mode on itself has not been obviously considered in the sum because a simple variation of the eigenvector amplitude cannot be considered, for eigenvector definition, as a perturbation for the eigenvector itself. Pre-multiplying Eq.(1.23) by $\boldsymbol{\psi}^{(k)T}$ (with $k \neq n$) and using Eq.(1.27), one has

$$\boldsymbol{\psi}^{(k)T} \left(-\omega_n^2 \boldsymbol{M} + \boldsymbol{K}\right) \sum_{\substack{s=1 \\ s\neq n}}^{N} \gamma_s^n \boldsymbol{\psi}^{(s)} + j\omega_n \boldsymbol{\psi}^{(k)T} \left(2\boldsymbol{M}\Delta\lambda_n + \boldsymbol{C}\right) \boldsymbol{\psi}^{(n)} = 0, \quad \text{with} \quad k \neq n \tag{1.28}$$

or, considering the orthogonality properties,

$$\left(\omega_k^2 - \omega_n^2\right) m_k \gamma_k^n + j\omega_n d_{kn} = 0, \quad \text{with} \quad k \neq n \tag{1.29}$$

The previous relationship allows one to evaluate γ_k^n and then to estimate the complex eigenvector $\boldsymbol{p}^{(n)}$ as

$$\boldsymbol{p}^{(n)} = \boldsymbol{\psi}^{(n)} + \boldsymbol{\Delta p}^{(n)} = \boldsymbol{\psi}^{(n)} + \sum_{\substack{k=1 \\ k\neq n}}^{N} \frac{j\omega_n d_{kn}}{m_k \left(\omega_n^2 - \omega_k^2\right)} \boldsymbol{\psi}^{(k)} \tag{1.30}$$

which is an approximation for the complex eigenvector which is valid if $(\omega_n^2 - \omega_k^2)$ keeps as a finite quantity, *i.e.*, if the modes are separated in the frequency spectrum. It can be noted that the correction for the damped eigenvectors involves the out-of-diagonal terms of the modal damping matrix d_{kn}, therefore the simplified assumption $\boldsymbol{p}^{(n)} \simeq \boldsymbol{\psi}^{(n)}$ is fully consistent with the assumption on the modal damping matrix to be diagonal. This damping model is known as Lord-Rayleigh-Basile damping model and it consistently implies that

$$\boldsymbol{\psi}^{(i)T} \boldsymbol{C} \boldsymbol{\psi}^{(j)} \simeq \delta_{ij} d_{jj} =: c_j \tag{1.31}$$

and therefore Eq.(1.17) is rewritten as

$$\ddot{q}_n(t) + \frac{c_n}{m_n} \dot{q}_n(t) + \omega_n^2 q_n(t) = g_n(t), \quad \text{with} \quad n = 1, \ldots, N \tag{1.32}$$

then a modal damping coefficient ζ_n, associated to the n-th mode, can be defined such that

$$\frac{c_n}{m_n} =: 2\zeta_n\omega_n \tag{1.33}$$

The damping model is often considered proportional and this assumption implies the damping matrix to be a linear combination of the mass and stiffness matrices, namely

$$\boldsymbol{C} \;=\; \alpha\boldsymbol{M} + \beta\boldsymbol{K} \tag{1.34}$$

where α and β are constants, then the matrix (1.15) can be seen as a transformation matrix uncoupling the system differential equation of motion (1.1). Therefore, the linear transformation Eq.(1.16) decouples the Eq.(1.1) in N independent equations, such as Eq.(1.32). This assumption on the damping matrix is usually a reasonable approximation for lightly damped structures, and it is stressed that it entails the same modal model, because the real eigenvectors do not change and the eigenvalues are complex, as λ_n in Eq.(1.20), that using Eqs.(1.25) and (1.33) could be expressed in the form

$$\lambda_n \;=\; -\zeta_n\omega_n \pm j\;\omega_n, \quad n = 1, 2, \ldots, N \tag{1.35}$$

where it has been remarked that the real part is negative to guarantee the system's stability. A complete description of other representations of the damping in the structural problem can be found in Ref.[14].

1.3 Response Model

The governing equation of the system in the frequency domain is derived by taking the Fourier transform of the Eq.(1.1):

$$\left[-\omega^2\boldsymbol{M} + j\omega\boldsymbol{C} + \boldsymbol{K}\right]\boldsymbol{x}(\omega) \;=\; \boldsymbol{f}(\omega) \tag{1.36}$$

The Fourier transform of a integrable time function $g(t)$ is defined as an application from real to complex domains:

$$g(\omega) = \int_{-\infty}^{+\infty} g(t)e^{-j\omega t}dt$$

where $\omega = 2\pi f$ is the angular frequency expressed in [rad/s] and f is the frequency in [Hz], Ref.[18].

where the term in the square bracket on the left-hand side is the dynamic flexibility matrix, commonly recognized as the inverse of the Frequency Response Function (FRF) matrix of the system ($\boldsymbol{H}(\omega)$).

$$\boldsymbol{H}(\omega) \;=\; \left[-\omega^2\boldsymbol{M} + j\omega\boldsymbol{C} + \boldsymbol{K}\right]^{-1} \tag{1.37}$$

Every term of such a matrix $H_{ij}(\omega)$ is a function that relates the i-th degree of freedom of the system response with the j-th degree of freedom of the excitation, as shown in Fig.(1.2). By applying the linear

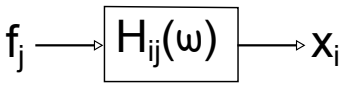

Figure 1.2: Block diagram of the Frequency Response Function.

transformation given by the modal matrix in Eq.(1.15) to the Eq.(1.36), a set of uncoupled equations is achieved as before

$$Diag\left[-\omega^2 m_n + j\omega c_n + k_n\right]\boldsymbol{q}(\omega) \;=\; \boldsymbol{g}(\omega) \tag{1.38}$$

in which the notation $Diag$ is introduced to denote a diagonal matrix made up of the modal masses m_n, damping c_n and stiffness k_n and with $\boldsymbol{g}(\omega)$ the vector of the modal loads in the frequency domain. By introducing the modal parameters in terms of the n-th natural frequency ω_n and damping ratio ζ_n, the Eq.(1.38) can be rewritten as:

$$Diag\left[m_n\left(-\omega^2 + 2j\zeta_n\omega_n\omega + \omega_n^2\right)\right]\boldsymbol{q}(\omega) \;=\; \boldsymbol{g}(\omega) \tag{1.39}$$

where the modal masses are equal to unity if the mode normalization is set as in Eq.(1.13). The analytical expression of the system Frequency Response Function ($\boldsymbol{H}(\omega)$) comes from Eq.(1.39), since the diagonal matrix is easy to be inverted, as follows

$$\boldsymbol{q}(\omega) \;=\; Diag\left[\frac{1}{m_n\left(-\omega^2 + 2j\zeta_n\omega_n\omega + \omega_n^2\right)}\right]\boldsymbol{g}(\omega) \tag{1.40}$$

and coming back to the physical displacement and force vectors

$$\boldsymbol{x}(\omega) = \boldsymbol{\phi} Diag\left[\frac{1}{m_n\left(-\omega^2 + 2j\zeta_n\omega_n\omega + \omega_n^2\right)}\right]\boldsymbol{\phi}^T\boldsymbol{f}(\omega) \tag{1.41}$$

then by definition

$$\boldsymbol{H}(\omega) = \boldsymbol{\phi} Diag\left[\frac{1}{m_n\left(-\omega^2 + 2j\zeta_n\omega_n\omega + \omega_n^2\right)}\right]\boldsymbol{\phi}^T \tag{1.42}$$

in which each element of the matrix is a complex function of the frequency variable depending by the modal parameters:

$$H_{ij}(\omega) = \sum_{n=1}^{N}\frac{\phi_i^{(n)}\phi_j^{(n)T}}{m_n\left(-\omega^2 + 2j\zeta_n\omega_n\omega + \omega_n^2\right)} \tag{1.43}$$

Actually there are multiple definitions of the FRF depending on what the type of responses are considered: receptance, mobility and accelerance (or inertance) relate the force to displacement, velocity or acceleration, respectively. In the following, $\boldsymbol{H}(\omega)$ will indicate the receptance, the mobility will be derived as $j\omega\boldsymbol{H}(\omega)$ and the accelerance as $-\omega^2\boldsymbol{H}(\omega)$, without introducing any additional notation. Nevertheless the analysis of their graphical presentation, as suggested in Ref.[13], is a powerful tool that will be used in this thesis. In particular, the Bode type of plot, consisting of the two graphics of the FRF Modulus and FRF Phase versus the Frequency, is represented in Fig.1.3 for a typical damped single degree of freedom system to highlight the relevant characteristics of such a representation. A detailed explanation of the Response model can be found in the Sec.2.2 of Ref.[13].

It is important to point out that the Response Model can be considered fully representative of the system's vibrations as well as the Spatial and the Modal models, to which it is strictly related by Eq.(1.37) in the first case and by Eq.(1.43) in the second case.

1.3.1 State-Space Model

The expression of the system's equation (1.1) can be reformulated in the so-called state-space model, which is commonly used in the control theoretical formulation, by reducing the order of the differential

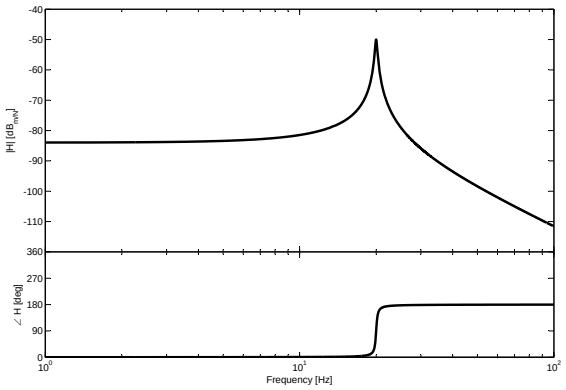

(a) Receptance

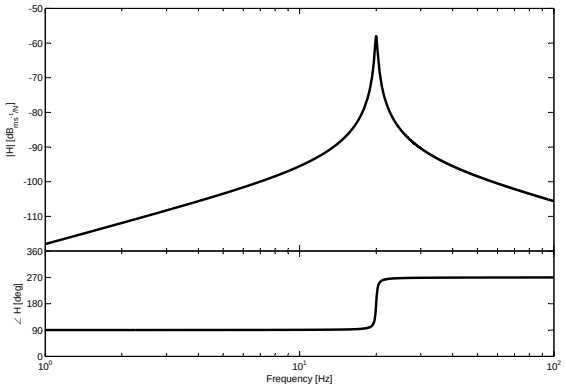

(b) Mobility

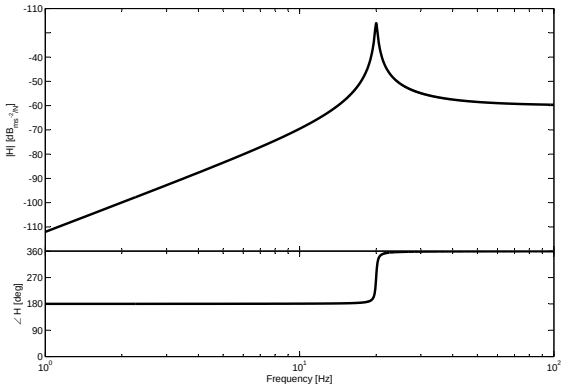

(c) Accelerance

Figure 1.3: Bode diagrams of Frequency Response Functions, Ref.[13].

equations to one. In particular, in the frequency domain by setting the new variable as follows

$$\boldsymbol{x}_1(\omega) = \begin{pmatrix} \boldsymbol{x}(\omega) \\ -j\ \omega \boldsymbol{x}(\omega) \end{pmatrix} \tag{1.44}$$

the Eq.(1.36) becomes

$$-j\ \omega \boldsymbol{x}_1(\omega) \;=\; \begin{bmatrix} 0 & \mathbf{I} \\ -\mathbf{M}^{-1}\mathbf{K} & -\mathbf{M}^{-1}\mathbf{C} \end{bmatrix} \boldsymbol{x}_1(\omega) + \begin{pmatrix} 0 \\ \mathbf{M}^{-1} \end{pmatrix} \boldsymbol{f}(\omega) \tag{1.45}$$

that yields to

$$-j\ \omega \boldsymbol{x}_1(\omega) \;=\; \boldsymbol{A}\boldsymbol{x}_1(\omega) + \boldsymbol{B}\boldsymbol{f}(\omega) \tag{1.46}$$

$$\boldsymbol{y}(\omega) \;=\; \boldsymbol{C}\boldsymbol{x}_1(\omega) + \boldsymbol{D}\boldsymbol{f}(\omega) \tag{1.47}$$

where

$$\mathbf{A} = \begin{bmatrix} 0 & \mathbf{I} \\ -\mathbf{M}^{-1}\mathbf{K} & -\mathbf{M}^{-1}\mathbf{C} \end{bmatrix} \qquad \mathbf{B} = \begin{bmatrix} 0 \\ \mathbf{M}^{-1} \end{bmatrix} \qquad \mathbf{C} = \begin{bmatrix} \mathbf{I} \\ 0 \end{bmatrix} \qquad \mathbf{D} = 0 \tag{1.48}$$

in which $\boldsymbol{A}$, $\boldsymbol{B}$ and $\boldsymbol{C}$ are called state, input and output matrices and $\boldsymbol{D}$ is usually neglected, because the effect of the excitation is fully considered in the first equations. Equation (1.47) introduces the variable $\boldsymbol{y}(\omega)$ as the output of the system and, in this case, it is related to the system's physical displacement through the output matrix. Nevertheless the system's velocities or accelerations can be also considered by modifying the output matrix. Identification algorithms based on a state-space model identify the system matrices $\boldsymbol{A}$, $\boldsymbol{B}$ and $\boldsymbol{C}$ from the measurement data. The transfer function matrix between the outputs and the inputs is then given by the following

$$\boldsymbol{H}(\omega) \;=\; \boldsymbol{C}\left[-j\ \omega \boldsymbol{I} - \boldsymbol{A}\right]^{-1} \boldsymbol{B} \tag{1.49}$$

It can be proved that the system's modal parameters can be evaluated from the eigenvalue problem associated to the state matrix

$$\boldsymbol{A}\boldsymbol{v}^{(n)} = \mu_n \boldsymbol{v}^{(n)}, \quad n = 1, 2, \ldots, 2N \tag{1.50}$$

In fact, if $\boldsymbol{v}^{(n)} = \begin{Bmatrix} \boldsymbol{v}_1^{(n)} \\ \boldsymbol{v}_2^{(n)} \end{Bmatrix}$, considering the partitions for the state matrix defined in Eq.(1.48), the Eq.(1.50) results

$$\begin{bmatrix} 0 & \mathbf{I} \\ -\mathbf{M}^{-1}\mathbf{K} & -\mathbf{M}^{-1}\mathbf{C} \end{bmatrix} \begin{Bmatrix} \boldsymbol{v}_1^{(n)} \\ \boldsymbol{v}_2^{(n)} \end{Bmatrix} = \mu_n \begin{Bmatrix} \boldsymbol{v}_1^{(n)} \\ \boldsymbol{v}_2^{(n)} \end{Bmatrix} \tag{1.51}$$

that yields

$$\boldsymbol{v}_2^{(n)} = \boldsymbol{v}_1^{(n)} \mu_n \tag{1.52}$$

$$-\mathbf{M}^{-1}\mathbf{K}\boldsymbol{v}_1^{(n)} - \mathbf{M}^{-1}\mathbf{C}\boldsymbol{v}_2^{(n)} = \mu_n \boldsymbol{v}_2^{(n)} \tag{1.53}$$

Combining the last equations and rearranging results

$$\left[\mu_n^2\mathbf{M} + \mu_n\mathbf{C} + \mathbf{K}\right] \boldsymbol{v}_1^{(n)} = 0 \tag{1.54}$$

that is the same expression of Eq.(1.19) with $\mu_n = \lambda_n$ and $\boldsymbol{v}_1^{(n)} = \boldsymbol{p}^{(n)}$. Moreover also the Eq.(1.49) can be manipulated to give the expressions obtained in Eq.(1.42).

1.4 Experimental Modal Analysis

The experimental route to vibration analysis follows a different path with respect the theoretical one. However, they share the same models, whose understanding is the driving criteria of the experimental investigations. A general description of how the test setup should be organized in order to evaluate the structure's response properties is shown in Fig.1.4. According to the definitions given in Sec.3 of Ref.[13], each block is described:

Test Structure. It represents the system under investigation. The important preliminary to the whole process is its preparation with the boundary conditions. Free or grounded conditions are usually considered for common tests although the reference condition should be the operating one.

Exciter and Power Amplifier. The structure can be excited into vibration in several ways although the two most commonly used are by an attached shaker or by a hammer blow. The main issue is the

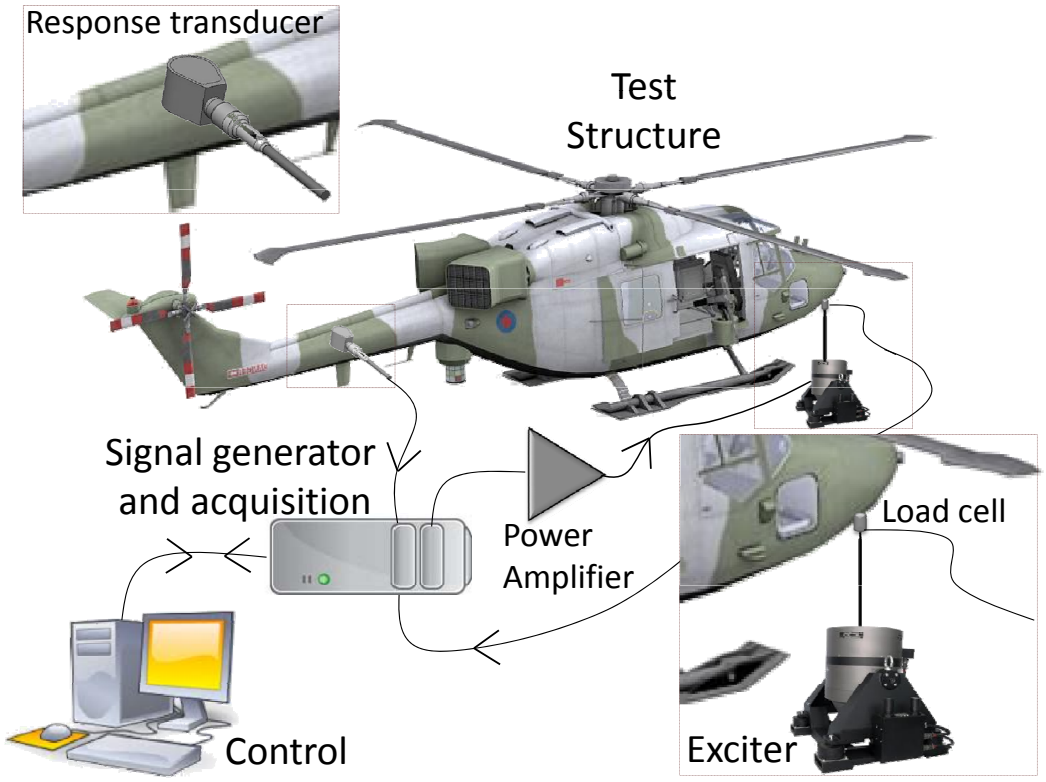

Figure 1.4: General Layout of Experimental Modal Analysis.

insertion error that can follows and the positioning. The Power Amplifier will be necessary in order to drive the actual device used to vibrate the structure

Transducers. There are many different devices available to measure the excitation forces and the various responses of interest. Common devices are piezoelectric load cells and accelerometers because of their wide frequency range of application. Nevertheless also strain gauges can be used as a less expensive solution.

Signal generator and acquisition. The structure should be excited by a loading that allows the identification of the vibration properties. The signal generator is a source for the excitation signal, *i.e.*, harmonic, random, transient (as an impact), according to the aim of the test. It is important that the generation of the signal is coordinated with the exciter and the acquisition of the transducers

responses. Therefore, the system has to take into account the issues related to the signal processing, such as the filtering in the frequency range of interest, the sampling from continuous signal to discrete values, the synchronous acquisition among the transducers, the leakage of the signal outside the acquisition time window.

Control Unit. It is in general a computer with a software that drives the test, collects the measured data and post-processes the results in order to evaluate the starting point for the modal analysis, such as the Frequency Response Functions or the Impulse Response Functions. The user expertise is fundamental to tune all the acquisition parameters, such as sampling frequency, range definitions, transducer sensitivities, filter characteristics, acquisition time, signal windowing, excitation signal.

The practice of performing modal testing requires that all the mentioned items would be thoroughly looked after. For this reason further details about the signal processing and the system's estimate procedure are given in the following.

1.4.1 Some issues on Signal Processing

The signal generator and acquisition is the component, driven by the control unit, that deals with the signal processing issues, because, as already described, it generates and acquires the analog signals that need to be converted from or to digital signals. During this process the two main concerns to deal with are the aliasing and the leakage. The first originates from the fact that the continuous time signals that have to be sampled contains a theoretically infinite spectrum. High frequency components might then cause amplitude and frequency errors in the finite and discrete spectrum of the digital signal. If the highest frequency in a base band signal to be analyzed, f_{max}, does not meet the Shannon's theorem,

$$f_{max} \leq f_s/2 \tag{1.55}$$

where f_s is the sampling frequency, frequencies above $f_s/2$, will show up as frequencies below $f_s/2$. Figure 1.5 shows as sine waves at $f_1 = 1\ Hz$, $f_2 = 4\ Hz$ and $f_3 = 6\ Hz$, sampled at $f_s = 5\ Hz$ result as three

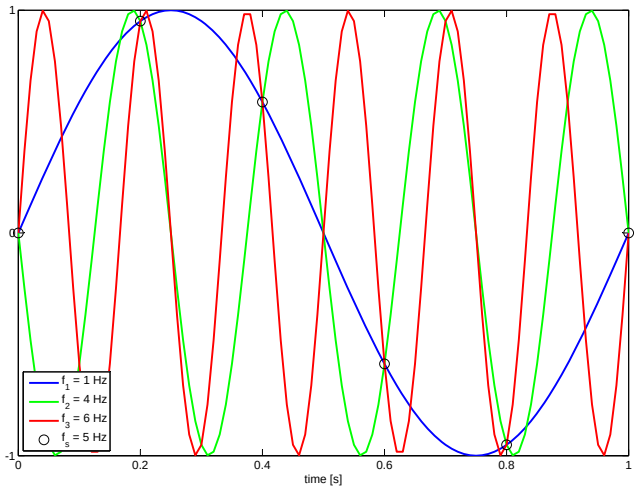

Figure 1.5: Effect of aliasing on sine waves sampled at $f_s = 5\,\mathrm{Hz}$.

identical discrete functions. Aliasing can be avoided by removing all components at frequencies higher than $f_s/2$. This can be achieved by an appropriate excitation signal (in the assumption that the system is perfectly linear), but it is generally realized by using a low pass filter with a sharp cut-off. Since filters with a perfect cut-off at $f_s/2$, *i.e.*, filters that cut all higher frequencies to zero without influencing the lower frequencies, do not exist, they are often set at $0.8 f_{max}$.

Leakage errors originate from the fact that measurements have to be taken during a finite observation time T. The discrete Fourier transform then assumes that the observed signal is periodic with period T. If this condition is not met, a leakage error occurs. The assumption of periodicity of the time signal with period T results in a discrete Fourier spectrum with samples at frequencies n/T. If a pure harmonic signal with only one component $f_1 = n_1/T$ is considered, all the frequency lines in the spectrum coincide with zeros of the continuous spectrum except for f_1. Therefore, the result is an exact reproduction of the correct spectrum. On the contrary, if the wave is not periodic within the observation window (that means that its frequency $f_2 \neq n/T$, $\forall n$), the frequency lines resulting from the periodicity assumption do not coincide with the zeros of this spectrum and, therefore, the discrete spectrum does not coincide with the exact. The real energy at frequency f_2 is spread (*leaked*) to nearby frequencies causing an amplitude error. In the time

domain the non periodicity of the signal in the observation window causes discontinuities at all multiples of T: the assumed (periodic) signal differs from the exact signal, hence errors in the spectrum can also be expected. Since any signal can be expressed as a linear combination of pure harmonic components (both sine and cosine), leakage will occur whenever a signal contains non-periodic frequency components. The only solution to the leakage problem, is to make sure that the signal is periodic or completely observed within the observation window. Generally this is very difficult to achieve. For systems with a perfect linear behaviour, it can be accomplished by exciting the structure with a periodic signal. Excitation signals as burst random also minimize this problem, because they let the damped system enough time to reach the rest within the observation window. Increasing the the observation time T has the double positive effect of improving the periodicity of the signal and decreasing the frequency step Δf. Nevertheless this usually involves long experimental test campaign adding measurement noise. Common practice is the use of time windows, other than the rectangular one, in order to fix the leakage problem. The application of time window cannot be avoided, because when measuring time signals only a part of the total signal can be considered, *i.e.*, a time record of length T. This process is equal to multiplying the actual signal with a rectangular time window. More suitable choices can reduce the leakage error by enforcing the signal to be periodic. The selection of a window is always a compromise between a good estimate of the amplitude values and a good spectral resolution. It is important to stress that the only solution to the leakage is to make sure that the signal is periodic or completely observed within the observation window. The use of widows only offers a partial solution and will yield distorted measurements. In Fig.1.6 some representative windows commonly used with random, pseudo-harmonic or impact signals are depicted. In particular, the first one is the rectangular window that corresponds to no window. When compared to the hanning window, a wider frequency range is achieved within which the function does not decrease more than 3dB.

1.4.2 Some issues on the estimate of the system

Following the experimental route the system estimate procedure starts from the experimental data coming from the tests, such as impulse or random responses to evaluate the response model. Then the modal analysis gives the directions to evaluate the modal model from the response model, such as the experimental modal analysis (EMA, also referred as Input-Output) or the operational modal analysis (OMA, also known as Output-Only). This last one constitutes the core of the thesis, so it will be addressed in the next Chapter 2. Finally, from the previous estimates, the spatial model can be reconstructed. This procedure is usually known as model updating but it will be skipped in the following for the sake of brevity.

1.4.2.1 Response Model estimate

The response model is fully characterized by the Frequency Response Function (FRF) matrix or by its inverse Fourier transform, which is the impulse response function matrix. Although they could be theoretically evaluated from direct measurements, it is experimental practice deriving them also from the system's responses in the time or frequency domain. In the first case the impulsive test has to be carried out, with the hammer as exciter, whereas the second approach allows the use of any signal that, sent to the shaker, is capable to vibrate the structure. This is the case of random tests, in which the stochastic excitation can be synthesized within the investigation frequency bandwidth. The issue of insertion error due to the exciter has been already introduced, but it should be stressed that the theoretical pure impulse, capable to excite all the investigation spectrum, is difficult to be achieved experimentally. Therefore, the procedures based on stochastic signals are widely applied in EMA and they also represent the only possibility for OMA, because its main hypothesis is a white noise excitation. The main objective is the evaluation of the FRFs $H_{ij}(\omega)$ from the system's response at the i-th experimental point with respect to the j-th excitation point within the frequency range of investigation, $\omega \in [0, f_{max}]$, being N_o the number of outputs ($i = 1, 2, \cdots, N_o$) and N_i the number of inputs ($j = 1, 2, \cdots, N_i$). From the measurements of two output responses, y_i

and y_k, $i,k = 1,2,\cdots,N_o$ in the time domain, it is possible to evaluate the output correlation function $R_{y_i y_k}(\tau)$, as a function of the time lag τ:

$$R_{y_i y_k}(\tau) = \lim_{T\to\infty} \frac{1}{T} \int_{-T/2}^{+T/2} y_i(t) y_k(t+\tau) dt \tag{1.56}$$

The Power Spectral Density (PSD) function, $G_{y_i y_k}(\omega)$, is defined as the Fourier transform of the correlation function, but according to the Wiener-Khintchine relation it can be also evaluated from the spectra of the responses Y_i and Y_k, $i,k = 1,2,\cdots,N_o$ in the frequency domain:

$$G_{y_i y_k}(\omega) = \lim_{T\to\infty} \frac{Y_i^* Y_k}{T} \tag{1.57}$$

where * denotes the complex conjugate. It is usually referred to auto or cross correlation and PSD function if $i = j$, or $i \neq j$, respectively. Identical definitions are used for the input responses, referred as $R_{f_j f_k}$ and $G_{f_i f_k}$ for correlation and PSD, respectively. By combining the output and input PSD functions two different estimates of the FRF, commonly recognized as H_1 and H_2, can be derived, Ref.[19]:

$$H_1(\omega) = \frac{G_{yf}}{G_{ff}} \tag{1.58}$$

$$H_2(\omega) = \frac{G_{yy}}{G_{fy}} \tag{1.59}$$

In practice the use of alternative ways of calculating the FRF from the auto- and cross-PSD gives advantages, as the reduction of uncorrelated noise on the input or the output signals achieved by averaging. Since those FRF estimates are least square approximations, a corresponding correlation function can be defined and it is called coherence. The latter is a measure of the least square error and, for a single input, it is defined as:

$$\gamma(\omega) = \frac{H_1}{H_2} = \frac{|G_{fy}|^2}{G_{ff} G_{xx}} \tag{1.60}$$

The coherence varies between 0 and 1, with a value of 1 indicating that a perfect linear relationship exists between the two compared signals (input and output). A coherence less than 1 can be due to uncorrelated

noise in the measurements of the input or output, nonlinearity of the system under investigation, leakage, delays in the system not compensated in the analysis. It is a good practice the use of H_2 (H_1) if a good estimate of the peak of resonance (anti-resonance) is required since extraneous noise on the input (output) do not influence the estimate. One more FRF estimate is commonly used, since its formulation is unbiased with respect to both input and output noise:

$$H_v(\omega) = \frac{G_{yy} - \kappa G_{ff} + \sqrt{[G_{ff}\kappa - G_{yy}]^2 + 4|G_{fy}|^2\kappa}}{2G_{yf}} \tag{1.61}$$

in which $\kappa = G_{n_y n_y}/G_{n_x n_x}$ is the ratio between the auto-PSD of the noise acting on the output and the auto-PSD of the noise acting on the input; if it is not known, it is usually taken to 1.

1.4.2.2 Modal Model estimate

The role of the Experimental Modal Analysis (EMA) is the identification of the vibration modes from the system's responses. Several methodologies have been developed and implemented, but their description is beyond the aim of this thesis. Therefore, a brief overview of the modal parameter estimation algorithms considered representative is presented with the suggested references as in Ref.[20]. During the last three decades the methods have evolved from very simple single degree of freedom (SDOF) techniques to methods that analyze data from multiple-input excitation and multiple-output responses (MIMO) simultaneously in a multiple degree of freedom (MDOF) approach. In the class of MDOF methods, a major grouping is usually done based on the domain in which the data are treated numerically resulting in time-domain and frequency-domain methods. One of the first MDOF time-domain algorithms specifically designed for MIMO modal parameter estimation was the Ibrahim Time-Domain (ITD) method Ref.[21]. This method uses impulse response function data to identify modal parameters by means of an eigenvalue problem. When originally proposed, it built the eigenvalue problem using free-response time data and it was adapted for an automated model order selection in order to minimize the required user-interaction, by means of the Modal Confidence Factor (MCF), Ref.[22]. Later another well-known time-domain algorithm was formulated with

the name Eigensystem Realization Algorithm (ERA) Ref.[23]. It starts from the state space formulation described in Sec.1.3.1 to derive the minimum realization of the system matrices. The original formulation requires the singular value decomposition of the so-called Hankel matrix, which is constructed from the impulse response function data, while the faster ERA/DC variant uses autocorrelation functions as data, as introduced in Ref.[24]. The theoretical background of this method is also related to the most recent Stochastic Subspace Identification (SSI) algorithms, Ref.[25], widely used also in the OMA framework, as it will be shown in the next Chapter. Another class of time-domain system identification methods, having its roots in the domain of control theory and applications, are the so-called autoregressive moving-average (ARMA) models, that provide a parsimonious description of a (weakly) stationary stochastic-process in terms of two polynomials, one for the auto-regression and the second for moving averages. The general ARMA model was described in the 1951 thesis of Peter Whittle, Ref.[26], and can be studied in Ref.[27]. A much faster time-domain method is the Least Squares Complex Exponential (LSCE) algorithm first introduced by Ref.[28] as an extension of Prony's method Ref.[29], which states that the roots of an underdamped system always occur in complex conjugate pairs and therefore can be used to form a characteristic polynomial with real coefficients. From the impulse response function data at subsequent discrete time instants, these coefficients can be computed and the roots then result in the system poles. A MIMO version of the LSCE is referred to as the polyreference-LSCE (p-LSCE) Ref.[30]. It is fast and does not require initial estimates for the modal parameters. Moreover, based on auto- and cross-correlations between output measurements, this algorithm can also be successfully applied for the modal parameter estimates from output-only measurements, as in the next Sec.2.1. The only unknown is the number of modes that must be considered in the analysis, or rather the model order, for which an iterative procedure is usually build by letting this value changing. This requires the distinction between the physical and computational modes for which a so-called stabilization chart was proposed. The stabilization diagram is a useful tool to determine the order of the system, that is the number of considered modes in the estimation

procedure. It is built by comparing the modal parameters calculated from models of consecutive order and by defining them as stable if the relative error is less than an arbitrary small fix threshold. For low noise levels the PLSCE in combination with the stabilization chart is suitable for an accurate modal parameter estimate. However, for high noise levels the estimation process becomes susceptible to errors and results can differ significantly depending on the user's experience.

In frequency-domain analysis a number of important features, such as overlap averaging, data windowing and frequency band selection, considerably reduce computation and storage requirements. A classical MDOF method is the Least Squares Frequency-Domain (LSFD) algorithm, based on the expression of the response model in term of the modal parameters as in Eq.(1.43). In the case that the poles are not known, this method is nonlinear in the parameters resulting in a nonlinear least squares problem that has to be solved using an optimization algorithm. Good starting values are required to reduce the number of iterations. This method as such never became popular, except in combination with other methods providing an estimate of the poles, because, if this is the case, it reduces to a linear Least Squares problem yielding global estimates for the mode shapes, as shown in Sec.2.1 for OMA applications. As in the time-domain, a number of frequency-domain methods use a state space parametrization. A frequency-domain version of the ERA method (ERA- FD), is presented in Ref.[31], which formulation is closely related to the time-domain algorithm. The primary data for the ERA-FD are the FRFs forming a complex block matrix from which, through an SVD, a state model is derived and transformed to the modal space. As for the ERA method, frequency-domain versions of time-domain subspace identification schemes having a reduced computation and storage requirements were proposed. Starting from MIMO frequency response function measurements, frequency-domain algorithms based on discrete-time deterministic subspace identification have been described in Ref.[25]. The Complex Mode Indicator Function (CMIF), Ref.[32], that uses a SVD of the frequency response function matrix, has gained some popularity because of its simple use. The CMIF is a plot of the log-magnitude of the singular values of the FRF matrix as a function of the

frequency. Peaks in the CMIF plot indicate the damped natural frequencies. Based on the assumption that near a resonance the FRF matrix is dominated by a single term in Eq.(1.43), it follows that the mode shape and modal participation factor vectors are found from the left and right singular vectors associated with the largest singular value. Since the CMIF is a multiple input algorithm, it can detect multiple roots resulting in several significant singular values peaking at a specific frequency. It should be noticed that, for the case of multiple poles, the singular vectors corresponding to the singular values significantly differing from zero are not the actual mode shapes. Instead, these are given by a (unknown) linear combination of the singular vectors. A similar approach, working on the output PSD functions instead of the FRFs, will be described in the next Chapter as an OMA method called Frequency Domain Decomposition (FDD). A large number of frequency-domain estimators are based on a matrix fraction description model and one of them is briefly discussed in the following, since it is the method used in this thesis as a reference for the Operational Modal Analysis. This is the PolyMAX algorithm developed by LMS and implemented in the Test.Lab software as described in Ref.[33]. The PolyMAX method is a further evolution of the Least-Squares Complex Frequency-domain (LSCF) estimation method, [34]. The most important advantage of the LSCF estimator over the available and widely applied parameter estimation techniques is the fact that very clear stabilization diagrams are obtained with a relatively small computational effort. A thorough analysis of different variants of the common-denominator LSCF method can be found in Ref.[20]. It was found that the identified common-denominator model closely fitted the measured FRF data. However, when converting this model to a modal model Eq.(1.43) by reducing the residues to a rank-one matrix using the singular value decomposition (SVD), the quality of the fit decreases. Another feature of the common-denominator implementation is that the stabilization diagram can only be constructed using pole information (eigenfrequencies and damping ratios). Neither participation factors nor mode shapes are available at first instance. The theoretically associated drawback is that closely spaced poles will erroneously show up as a single pole. These two reasons provided the motivation for a polyreference

version of the LSCF method, which is PolyMAX. Time-domain methods, such as the polyreference Least-Squares Complex Exponential (p-LSCE, Ref.[34]) method, typically require impulse responses (obtained as the inverse Fourier transforms of the FRFs) as primary data, while PolyMAX uses directly the measured FRFs as primary data. The latter estimator consider the scalar matrix-fraction description for the measured FRFs, better known as a common-denominator model:

$$\boldsymbol{H}(\omega) = \frac{\sum_{\gamma=0}^{p} z^{\gamma} \boldsymbol{\beta}_{\gamma}}{\sum_{\gamma=0}^{p} z^{\gamma} \alpha_{\gamma}} \tag{1.62}$$

where $\boldsymbol{H}(\omega) \in \mathcal{C}^{N_o \times N_i}$ is the matrix containing the FRFs between all N_i inputs and all N_o outputs; $\boldsymbol{\beta}_{\gamma} \in \mathcal{C}^{N_o \times N_i}$ are the numerator matrix polynomial coefficients; $\alpha_{\gamma} \in \mathcal{C}$ are the denominator polynomial coefficients and p is the model order. Please note that a so-called z-domain model (i.e. a frequency-domain model that is derived from a discrete-time model) is used in Eq.(1.62), with:

$$z \;=\; e^{j\omega t_s} \tag{1.63}$$

where t_s is the sampling time. Equation (1.62) can be written down for all values ω of the frequency axis of the FRF data. Basically, the unknown model coefficients α_{γ}, $\boldsymbol{\beta}_{\gamma}$ are then found as the least-squares solution of these equations (after linearization). Once the denominator coefficients α_{γ} are determined, the poles and modal participation factors are retrieved as the eigenvalues and eigenvectors of their companion matrix. This procedure is similar to what happens in the time-domain LSCE method and allows for constructing a stabilization diagram for increasing model orders and using stability criteria for eigenfrequencies, damping ratios and modal participation factors. Although theoretically the mode shapes could be derived from the model coefficients α_{γ}, $\boldsymbol{\beta}_{\gamma}$, a so-called pole-residue model is also considered:

$$\boldsymbol{H}(\omega) \;=\; \sum_{i=1}^{N} \left[\frac{\boldsymbol{\varphi}^{(i)} \boldsymbol{\psi}^{(i)T}}{j\ \omega - \lambda_i} + \frac{\boldsymbol{\varphi}^{(i)*} \boldsymbol{\psi}^{(i)H}}{j\ \omega - \lambda_i^*} \right] - \frac{\boldsymbol{LR}}{\omega^2} + \boldsymbol{UR} \tag{1.64}$$

where N is the number of modes; $\boldsymbol{\varphi}^{(i)} \in \mathcal{C}^{N_o}$ are the mode shapes; superscript $*$, T, H respectively denote complex conjugate, transpose, and hermitian of a matrix; $\boldsymbol{\psi}^{(i)} \in \mathcal{C}^{N_i}$ are the modal participation factors

and λ_i are the poles, which occur in complex-conjugated pairs and are related to the eigenfrequencies ω_i and damping ratios ζ_i as follows:

$$\lambda_i, \lambda_i^* = -\zeta_i \omega_i \pm j\ \omega_i \sqrt{1-\zeta_i^2} \tag{1.65}$$

$\boldsymbol{LR}$, $\boldsymbol{UR} \in \Re^{l \times m}$ in Eq.(1.64) are respectively the lower and upper residuals modelling the influence of the out-of-band modes in the considered frequency band. The interpretation of the stabilization diagram yields a set of poles λ_i and corresponding participation factors $\boldsymbol{\psi}^{(i)}$. Since the mode shapes $\boldsymbol{\varphi}^{(i)}$ and the lower and upper residuals are the only unknowns, they are readily obtained by solving Eq.(1.64) in a linear least-squares sense. This second step is commonly called least-squares frequency-domain (LSFD) method.

All the previously discussed estimators belong to the class of so-called deterministic algorithms, which in essence are curve fitting techniques. Using however a stochastic approach yields a more realistic description of real-life experiments. By taking knowledge about the noise on the measured data into account in the cost function, it is possible to derive estimators with significant higher accuracy compared to the ones developed in the deterministic framework. Most of the described stochastic estimators start from the Fourier transform of the input (force) and response time sequences measured using a periodic excitation signal derived in an errors-in-variables framework, from which a sample mean and sample variance can be derived as in Ref.[35]. Based on this information, the model parameters can be derived using the so-called frequency-domain Maximum Likelihood Estimator (MLE) developed by Schoukens and Pintelon, Ref.[36], and extended to multivariable systems by Guillaume, Ref.[37]. From the combination of the MLE and the PolyMAX algorithm a new identification approach has been recently developed. It is called PolyMAX plus and its description can be found in Ref.[38].

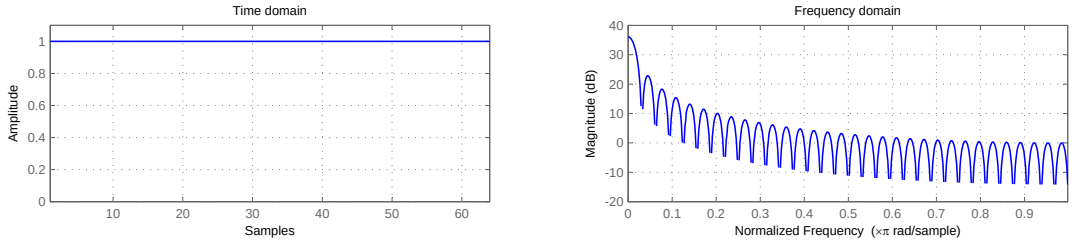

(a) rectangular

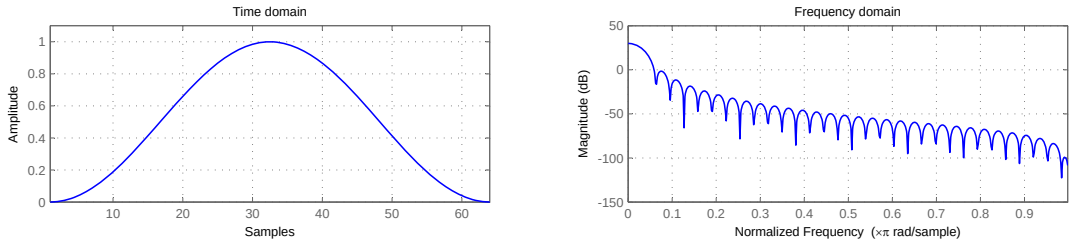

(b) hanning

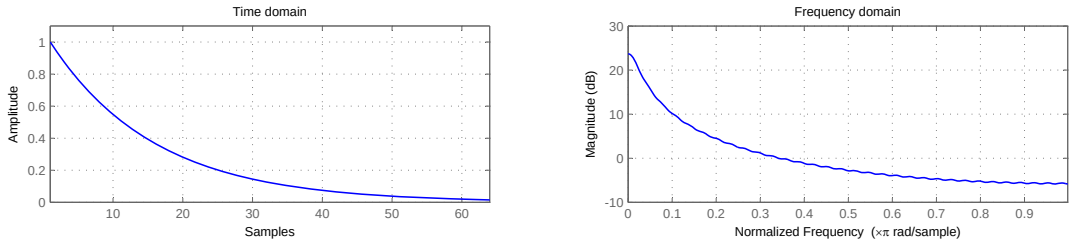

(c) exponential

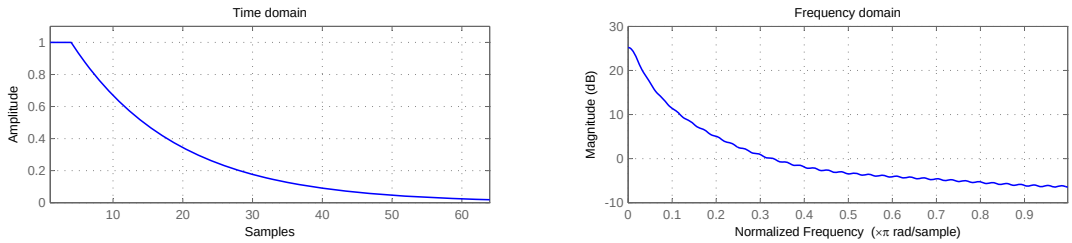

(d) force exponential

Figure 1.6: Rectangular window compared to typical windows used for random, pseudo-harmonic or impact signals.

Chapter 2

Operational Modal Analysis

The development of Operational Modal Analysis techniques allows estimating the modal parameters of a structure using vibration responses only. Thus, the costs associated to the test campaign are reduced and, in addition, an increase of the accuracy of the modal signature is achieved due to possibility to evaluate the behavior of the system under the actual boundary conditions and excitation levels, both provided from the operating conditions. Several techniques, both in frequency and in time domain, have been developed in recent years, under the main common assumption that the excitation has to be stochastic with the same spectral characteristics of the white noise. Among the methods it is worth recalling the Frequency Domain Decomposition (FDD, Ref.[3]), the Hilbert Transform Method (HTM, Ref.[39]) and two methods belonging to the Stochastic Subspace Identification (SSI, Ref.[40]), in which the state-space model is associated to the observed output responses through the so-called orthogonal projection technique in the time domain, Ref.[6], or in the frequency domain, Ref.[5].

Moreover a new method capable to deal with operational conditions in which the excitation cannot be considered as white noise has been developed starting from the HTM and it is presented as modified HTM. It is applicable when some tones are added to the shochastic broadband excitation and corrupt the system's responses. This method finds a wide application in rotorcraft as well as wind turbine technology, which are

characterized by multi-harmonic excitation embedded in a white noise loading.

Finally, for the sake of completeness, it should be noted that the mode shapes gained using the OMA are unscaled, because of the unknown excitation level, that means that also the frequency response functions gained by the only responses are biased by a scaling factor depending on the modal masses. Some procedures capable to extract these modal parameters by performing more than one test have been developed and are dealt in this chapter. They are based on the modal parameter variations induced by a mass or stiffness change and are named Constant Mode Shapes, CMS, Ref.[2], and Receptance Based Normalization, RBN, Ref.[1].

2.1 Basic Theory behind Operational Modal Analysis

The OMA bases its identification algorithms on the experimental modal analysis, by substituting the Frequency Response Functions (or the impulse response functions) with the Power Spectral Density functions (or the correlation functions). This substitution is possible thanks to the main assumption on the white noise behaviour of the excitation. The effectiveness of this practice is proven in Ref.[34]. Consider the response model in the frequency domain as introduced in Eq.(1.43), where the frequency response function is expressed as a function of the modal parameters:

$$H_{ij}(\omega) = \sum_{n=1}^{N} \left(\frac{\phi_i^{(n)} \phi_j^{(n)}}{m_n \left(j\omega - \lambda_n\right)} + \frac{\phi_i^{(n)*} \phi_j^{(n)*}}{m_n^* \left(j\omega - \lambda_n^*\right)} \right) \tag{2.1}$$

in which the complex conjugate pairs are explicit. From the measurements of the output responses, y_i, $i = 1, 2, \cdots, N_o$, (N_o being the number of measurement points) over N_t time samples, it is possible to build the output spectral density function matrix, $\mathbf{G}_{yy}(\omega_k) \in \mathcal{C}^{N_o \times N_o}$, $k = 1, \cdots, N_t/2$ from the evaluation of the spectral density functions, $G_{y_i y_j}(\omega_k)$, defined between the i-th and j-th output responses, at the k-th spectral line, as:

$$\mathbf{G}_{yy}(\omega_k) = \begin{pmatrix} G_{y_1 y_1}(\omega_k) & \dots & G_{y_1 y_{N_o}}(\omega_k) \\ \vdots & \ddots & \vdots \\ G_{y_{N_o} y_1}(\omega_k) & \dots & G_{y_{N_o} y_{N_o}}(\omega_k) \end{pmatrix} \tag{2.2}$$

For stationary stochastic processes this power spectral density function matrix among the outputs, $\mathbf{G}_{yy}(\omega)$, is

$$\mathbf{G}_{yy}(\omega) = \mathbf{H}^{H}(\omega)\mathbf{G}_{ff}(\omega)\mathbf{H}(\omega) \tag{2.3}$$

where $\mathbf{G}_{ff}(\omega)$ is the power spectral density function matrix among the inputs, Ref.[41] Sec.7.4. Under the assumption of uncorrelated and white noise inputs, $\mathbf{G}_{ff}(\omega)$ is not frequency dependent and equals a constant matrix $\mathbf{G}_{ff}$. Combining Eqs.(2.1) and (2.3) yields an expression that decomposes the output power spectral density matrix into modal components, Ref.[34]:

$$G_{y_i y_j}(\omega) = \sum_{n=1}^{N} \left(\frac{\phi_i^{(n)} \psi_j^{(n)}}{(j\omega - \lambda_n)} + \frac{\phi_i^{(n)*} \psi_j^{(n)*}}{(j\omega - \lambda_n^*)} + \frac{\psi_i^{(n)} \phi_j^{(n)}}{(-j\omega - \lambda_n)} + \frac{\psi_i^{(n)*} \phi_j^{(n)*}}{(-j\omega - \lambda_n^*)} \right) \tag{2.4}$$

where $\boldsymbol{\psi}^{(n)}$ is the output-only reference vector of the n-th mode. This reference vector is a complex function of the terms of the $\mathbf{G}_{ff}$ matrix and the system's modal parameters and, hence, does not allow the estimate of the modal participation factor (or modal masses). Equation (2.4) forms the basis for the frequency domain OMA techniques, where the unknown input is assumed to be white noise. It shows that if the terms related to unstable poles (the ones with positive real part) are not considered Eq.(2.4) reduces to Eq.2.1 and the output PSD function matrix can be decomposed into modal components, as is the case of the FRF matrix.

Taking the inverse Fourier Transform of Eq.(2.4) yields the output correlation function matrix $\mathbf{R}_{yy}(\tau)$, for positive and negative time lags τ:

$$R_{y_i y_j}(\tau) = \begin{cases} \sum_{n=1}^{N} \left(\phi_i^{(n)} \psi_j^{(n)T} e^{\lambda_n \tau t_s} + \phi_i^{(n)*} \psi_j^{(n)H} e^{\lambda_n^* \tau t_s} \right) & \text{for} \quad \tau \geq 0 \\ \sum_{n=1}^{N} \left(\psi_i^{(n)} \phi_j^{(n)T} e^{\lambda_n |\tau| t_s} + \psi_i^{(n)*} \phi_j^{(n)H} e^{\lambda_n^* |\tau| t_s} \right) & \text{for} \quad \tau < 0 \end{cases} \tag{2.5}$$

where t_s is the sampling period. Equation (2.5) forms the basis for the time domain OMA techniques, since it shows that the output correlation functions (for $\tau > 0$) can be expressed as a sum of decaying sinusoids (or pseudo-harmonic functions), as in the case with the impulse response function.

2.1.1 Frequency domain

Starting from Eq.(2.4) in the frequency domain, by varying the model order n from 2 to a certain arbitrary high value, a transfer function is evaluated by founding those polynomial expressions of the numerator ($B^{(n)}(\omega)$) and denominator ($A^{(n)}(\omega)$) of degree n that minimize the quadratic error with respect to the given complex frequency function. This procedure solves the problem of minimizing the sum of the squared error between the actual and the desired frequency function points, $F(\omega_k)$ for $k = 1, \ldots, N_f$, with N_f frequency points:

$$\min_{B,A} \sum_{k=1}^{N_f} \left| F(\omega_k) - \frac{B(\omega_k)}{A(\omega_k)} \right|^2 \tag{2.6}$$

Then the transfer function in terms of polynomial expressions is converted in the partial fraction expansion:

$$\frac{B(\omega)}{A(\omega)} = \sum_{j=1}^{n} \frac{R_j}{\omega - p_j} + K(\omega) \tag{2.7}$$

where $K(\omega)$ is the direct term. At this point, the n roots of the denominator give the system's poles. An iterative procedure is implemented so that for each model order n the results are compared with the ones coming from the previous step and the so-called stabilization diagram is built, as represented in Fig.2.1. Estimated poles corresponding to physically relevant system modes tend to appear for each estimation order with nearly identical values, while the so-called mathematical poles, i.e. poles resulting from the mathematical solution of the Eq.(2.6) but meaningless with respect to the physical interpretation tend to disperse. These mathematical poles are mainly due to the presence of noise on the measurements and can be classified as unstable if they differ from the previous ones more then an arbitrary fixed threshold (usually about 5%). The columns of 's' on the chart suggest which poles have to be selected during the identification process of the modal parameters. After that, an algorithm that evaluate the modes from the residues can be implemented in order to minimize the error between the experimental matrix of the response functions and the theoretical expression of these functions in terms of the modal parameters:

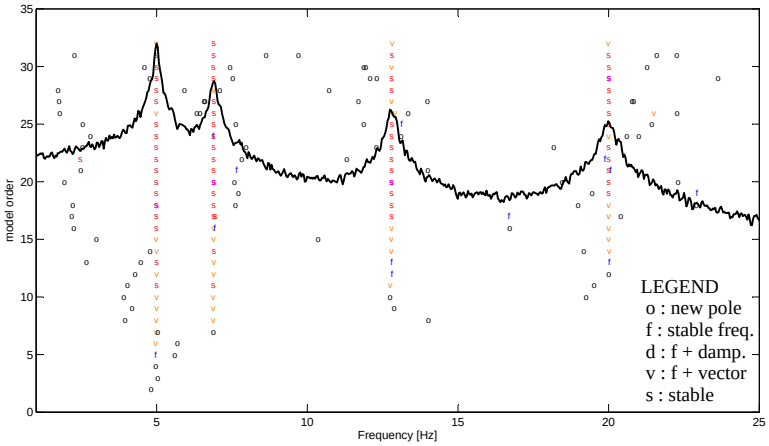

Figure 2.1: Stabilization diagram for the selection of the system's poles in NIMA.

$$\mathbf{H}(s) = \sum_{i=1}^{N_m} \left(\frac{\boldsymbol{\phi}^{(i)} \mathbf{L}^{(i)T}}{s - \lambda_i} + \frac{\boldsymbol{\phi}^{(i)*} \mathbf{L}^{(i)H}}{s - \lambda_i^*} \right) + \frac{1}{s^2}\mathbf{LR} + \mathbf{UR} \tag{2.8}$$

$$\mathbf{H}(s) = \mathbf{V}\left[s\mathbf{I} - \boldsymbol{\Lambda}\right]^{-1}\mathbf{L} + \frac{1}{s^2}\mathbf{LR} + \mathbf{UR} \tag{2.9}$$

in which $\mathbf{LR}$ and $\mathbf{UR}$ are the *Lower Residuals* and the *Upper Residuals*, respectively. Since the system's poles are known, Eq.(2.9) can be written as

$$\mathbf{b} = \mathbf{xA}$$

with the aim of putting apart the unknowns, as:

$$\mathbf{b}_{(N_o N_{ref})\times(N_f)} = \begin{bmatrix} H_{11}(s_1) & \dots & H_{11}(s_{N_f}) \\ \vdots & \ddots & \vdots \\ H_{N_o1}(s_1) & \dots & H_{N_o1}(s_{N_f}) \\ & \vdots & \\ H_{1N_{ref}}(s_1) & \dots & H_{1N_{ref}}(s_{N_f}) \\ \vdots & \ddots & \vdots \\ H_{N_oN_{ref}}(s_1) & \dots & H_{N_oN_{ref}}(s_{N_f}) \end{bmatrix} \tag{2.10}$$

$$\mathbf{x}_{(N_o N_{ref})\times(2N_m+2)} = \begin{bmatrix} R_{11}^{(1)} & \dots & R_{11}^{(N_m)} & R_{11}^{(1)*} & \dots & R_{11}^{(N_m)*} & LR_{11} & UR_{11} \\ \vdots & \ddots & \vdots & \vdots & \ddots & \vdots & \vdots & \vdots \\ R_{No1}^{(1)} & \dots & R_{No1}^{(N_m)} & R_{No1}^{(1)*} & \dots & R_{No1}^{(N_m)*} & LR_{No1} & UR_{No1} \\ & \vdots & & & \vdots & & \vdots & \vdots \\ R_{1N_{ref}}^{(1)} & \dots & R_{1N_{ref}}^{(N_m)} & R_{1N_{ref}}^{(1)*} & \dots & R_{1N_{ref}}^{(N_m)*} & LR_{1N_{ref}} & UR_{1N_{ref}} \\ \vdots & \ddots & \vdots & \vdots & \ddots & \vdots & \vdots & \vdots \\ R_{NoN_{ref}}^{(1)} & \dots & R_{NoN_{ref}}^{(N_m)} & R_{NoN_{ref}}^{(1)*} & \dots & R_{NoN_{ref}}^{(N_m)*} & LR_{NoN_{ref}} & UR_{NoN_{ref}} \end{bmatrix}$$

$$\mathbf{A}_{(2N_m+2)\times(N_f)} = \begin{bmatrix} \frac{1}{s_1-\lambda_1} & \dots & \frac{1}{s_{N_f}-\lambda_1} \\ \vdots & \ddots & \vdots \\ \frac{1}{s_1-\lambda_{N_m}} & \dots & \frac{1}{s_{N_f}-\lambda_{N_m}} \\ \frac{1}{s_1-\lambda_1^*} & \dots & \frac{1}{s_{N_f}-\lambda_1^*} \\ \vdots & \ddots & \vdots \\ \frac{1}{s_1-\lambda_{N_m}^*} & \dots & \frac{1}{s_{N_f}-\lambda_{N_m}^*} \\ s_1^{-2} & \dots & s_{N_f}^{-2} \\ 1 & \dots & 1 \end{bmatrix} \tag{2.11}$$

where N_f is the number of spectral lines of the experimental functions, N_o is the number of measurement points, N_{ref} is the number of points used as references. Taking into account that the matrices are generally

complex valued, it is more convenient to rewrite their expressions as follows:

$$\mathbf{b} = \begin{bmatrix} {}_{\Re}\mathbf{H}_{11}^{T} & + & j_{\Im}\mathbf{H}_{11}^{T} \\ & \vdots & \\ {}_{\Re}\mathbf{H}_{No1}^{T} & + & j_{\Im}\mathbf{H}_{No1}^{T} \\ & \vdots & \\ {}_{\Re}\mathbf{H}_{1N_{ref}}^{T} & + & j_{\Im}\mathbf{H}_{1N_{ref}}^{T} \\ & \vdots & \\ {}_{\Re}\mathbf{H}_{N_oN_{ref}}^{T} & + & j_{\Im}\mathbf{H}_{N_oN_{ref}}^{T} \end{bmatrix} \tag{2.12}$$

$$\mathbf{x} = \begin{bmatrix} {}_{\Re}\mathbf{R}_{11}^{T} + j_{\Im}\mathbf{R}_{11}^{T} & {}_{\Re}\mathbf{R}_{11}^{H} + j_{\Im}\mathbf{R}_{11}^{H} & LR_{11} & UR_{11} \\ \vdots & \vdots & \vdots & \vdots \\ {}_{\Re}\mathbf{R}_{No1}^{T} + j_{\Im}\mathbf{R}_{No1}^{T} & {}_{\Re}\mathbf{R}_{No1}^{H} + j_{\Im}\mathbf{R}_{No1}^{H} & LR_{No1} & UR_{No1} \\ \vdots & \vdots & \vdots & \vdots \\ {}_{\Re}\mathbf{R}_{1N_{ref}}^{T} + j_{\Im}\mathbf{R}_{1N_{ref}}^{T} & {}_{\Re}\mathbf{R}_{1N_{ref}}^{H} + j_{\Im}\mathbf{R}_{1N_{ref}}^{H} & LR_{1N_{ref}} & UR_{1N_{ref}} \\ \vdots & \vdots & \vdots & \vdots \\ {}_{\Re}\mathbf{R}_{N_oN_{ref}}^{T} + j_{\Im}\mathbf{R}_{N_oN_{ref}}^{T} & {}_{\Re}\mathbf{R}_{N_oN_{ref}}^{H} + j_{\Im}\mathbf{R}_{N_oN_{ref}}^{H} & LR_{N_oN_{ref}} & UR_{N_oN_{ref}} \end{bmatrix} \tag{2.13}$$

$$\mathbf{A} = \begin{bmatrix} \boldsymbol{\alpha}_{\Re} + j\boldsymbol{\alpha}_{\Im} \\ \boldsymbol{\beta}_{\Re} + j\boldsymbol{\beta}_{\Im} \\ \boldsymbol{\gamma}_{\Re} + j\boldsymbol{\gamma}_{\Im} \\ \boldsymbol{\epsilon}_{\Re} + j\boldsymbol{\epsilon}_{\Im} \end{bmatrix} \tag{2.14}$$

Therefore the problem results:

$$\begin{bmatrix} {}_{\Re}\mathbf{H}_{11}^{T} & {}_{\Im}\mathbf{H}_{11}^{T} \\ \vdots & \\ {}_{\Re}\mathbf{H}_{No1}^{T} & {}_{\Im}\mathbf{H}_{No1}^{T} \\ & \vdots \\ {}_{\Re}\mathbf{H}_{1N_{ref}}^{T} & {}_{\Im}\mathbf{H}_{1N_{ref}}^{T} \\ & \vdots \\ {}_{\Re}\mathbf{H}_{N_oN_{ref}}^{T} & {}_{\Im}\mathbf{H}_{N_oN_{ref}}^{T} \end{bmatrix} = \tag{2.15}$$

$$\begin{bmatrix} {}_{\Re}\mathbf{R}_{11}^{T} & {}_{\Im}\mathbf{R}_{11}^{T} & {}_{\Re}\mathbf{R}_{11}^{H} & {}_{\Im}\mathbf{R}_{11}^{H} & LR_{11} & UR_{11} \\ \vdots & \vdots & \vdots & \vdots & \vdots & \vdots \\ {}_{\Re}\mathbf{R}_{No1}^{T} & {}_{\Im}\mathbf{R}_{No1}^{T} & {}_{\Re}\mathbf{R}_{No1}^{H} & {}_{\Im}\mathbf{R}_{No1}^{H} & LR_{No1} & UR_{No1} \\ \vdots & \vdots & \vdots & \vdots & \vdots & \vdots \\ {}_{\Re}\mathbf{R}_{1N_{ref}}^{T} & {}_{\Im}\mathbf{R}_{1N_{ref}}^{T} & {}_{\Re}\mathbf{R}_{1N_{ref}}^{H} & {}_{\Im}\mathbf{R}_{1N_{ref}}^{H} & LR_{1N_{ref}} & UR_{1N_{ref}} \\ \vdots & \vdots & \vdots & \vdots & \vdots & \vdots \\ {}_{\Re}\mathbf{R}_{N_oN_{ref}}^{T} & {}_{\Im}\mathbf{R}_{N_oN_{ref}}^{T} & {}_{\Re}\mathbf{R}_{N_oN_{ref}}^{H} & {}_{\Im}\mathbf{R}_{N_oN_{ref}}^{H} & LR_{N_oN_{ref}} & UR_{N_oN_{ref}} \end{bmatrix} \begin{bmatrix} \boldsymbol{\alpha}_{\Re} + \boldsymbol{\beta}_{\Re} & \boldsymbol{\alpha}_{\Im} + \boldsymbol{\beta}_{\Im} \\ -\boldsymbol{\alpha}_{\Im} + \boldsymbol{\beta}_{\Im} & \boldsymbol{\alpha}_{\Re} - j\boldsymbol{\beta}_{\Re} \\ \boldsymbol{\gamma}_{\Re} & 0 \\ \boldsymbol{\epsilon}_{\Re} & 0 \end{bmatrix}$$

Finally, the residual terms come from the least-square resolution of the equation:

$$\tilde{\mathbf{x}} = \tilde{\mathbf{A}}^{\dagger}\tilde{\mathbf{b}}$$

where the number of spectral lines is much higher of the unknown residual terms.

2.1.2 Time domain

Classical resolution methods in the time domain for the impulse response functions can be applied to the correlation functions $R_{y_i y_j}(\tau)$ in Eq.(2.5) for $\tau > 0$ to estimate the system's poles λ_n and modes $\boldsymbol{\varphi}^{(n)}$ by rewriting the discrete functions in a more compact form:

$$R_{ij}(k\Delta\tau) = \sum_{n=1}^{2N} C_{ij}^{(n)} e^{\lambda_n k\Delta\tau} \tag{2.16}$$

in which the sum is expanded to $2N$ terms to take into account the complex conjugate pairs. The parameters of this expression can be found by applying the *Prony's method* because a polynomial of order $2N$ in terms of $e^{\lambda_n \Delta\tau}$ can be written as:

$$\beta_0 R_{ij}^k + \beta_1 R_{ij}^{k+1} + \ldots + \beta_{2N-1} R_{ij}^{k+2N-1} = -R_{ij}^{k+2N} \tag{2.17}$$

where $R_{ij}^k = R_{ij}(k\Delta\tau)$ and if $k = 1, \ldots, l$. A linear system of l equations based on the Hankel matrix can be built to determine the coefficient β_n, $n = 1, \ldots, 2N$:

$$\mathbf{R}_{ij}\boldsymbol{\beta} = \bar{\mathbf{R}}_{ij} \tag{2.18}$$

This procedure uses a single correlation function, but, since $\boldsymbol{\beta}$ are global quantities, the modal parameters can be derived from all the correlation functions. Hence, if p responses are considered and q of them are adopted as reference, the associated Eq.(2.18) for all the $q \times p$ correlation functions results into one system:

$$\begin{bmatrix} \mathbf{R}_{11} \\ \mathbf{R}_{12} \\ \vdots \\ \mathbf{R}_{qp} \end{bmatrix} \boldsymbol{\beta} = - \begin{Bmatrix} \bar{\mathbf{R}}_{11} \\ \bar{\mathbf{R}}_{12} \\ \vdots \\ \bar{\mathbf{R}}_{qp} \end{Bmatrix} \tag{2.19}$$

A solution in a least-square sense can be found for $\boldsymbol{\beta}$ using pseudo-inverse techniques, provided that $lqp \geq 2N$. Using all qp correlation functions allows to obtain more accurate modal parameters estimation. Since the order N necessary to properly represent the dynamics of the system is not known a priori, the pole identification is performed for several orders, and a stability diagram is built as previously described.

Once the system's poles have been identified, the residual terms can be evaluated. If a set of q correlation functions $R_{ij}(k\Delta\tau)$ is considered for a unique reference signal j, then Eq.(2.16) yields:

$$R_i(k\Delta\tau) = \sum_{n=1}^{2N} C_i^{(n)} e^{\lambda_n k\Delta\tau} \tag{2.20}$$

where $i = 1, \ldots, q$, $k = 1, \ldots, L-1$ and L is the number of time instances of the correlation functions considered for the mode extraction. If $V_n = e^{\lambda_n \Delta\tau}$ is defined, the previous equation can be put in the matrix form:

$$\begin{bmatrix} V_1 & V_2 & \cdots & V_{2N-1} & V_{2N} \\ V_1^2 & V_2^2 & \cdots & V_{2N-1}^2 & V_{2N}^2 \\ \vdots & & \ddots & & \vdots \\ V_1^{L-1} & V_2^{L-1} & \cdots & V_{2N-1}^{L-1} & V_{2N}^{L-1} \end{bmatrix} \begin{bmatrix} C_1^{(1)} & \cdots & C_q^{(1)} \\ C_1^{(2)} & \cdots & C_q^{(2)} \\ \vdots & & \vdots \\ C_1^{(2N)} & \cdots & C_q^{(2N)} \end{bmatrix} = \begin{bmatrix} R_1^{(1)} & \cdots & R_q^{(1)} \\ \vdots & & \vdots \\ R_1^{(L-1)} & \cdots & R_q^{(L-1)} \end{bmatrix} \tag{2.21}$$

In this expression, R_i^k are obtained from the measurements and V_n are known from the pole identification step. Equation (2.21) is a complex system of equations where the coefficients V_n and $C_i^{(n)}$ appear as complex conjugate pairs. Hence, it would be sufficient to consider $L = N$ time samples of the correlations. In practice, in order to average out numerical errors and noise, more time samples are considered R_i^k ($L >> 2M$) and the residues are computed as the least-squares solution of Eq.(2.21).

2.2 Frequency Domain Decomposition

This method starts from the Eqs.(2.2) and (2.4). Because such a response spectral matrix is Hermitian, $G_{y_i y_j}^*(\omega_k) = G_{y_j y_i}(\omega_k)$, with real positive diagonal elements, the singular value decomposition of the output spectral density matrix, for each of the k-th available spectral lines, could be written as, Ref.[3]:

$$\mathbf{G}_{yy}(\omega_k) = \mathbf{U}_k(\omega_k)\mathbf{\Sigma}_k(\omega_k)\mathbf{U}_k^H(\omega_k) \tag{2.22}$$

in which $\mathbf{U}_k(\omega_k) \in \mathcal{C}^{N_o \times N_o}$ is the matrix of left singular vectors and $\mathbf{\Sigma}_k(\omega_k) \in \mathcal{R}^{+(N_o \times N_o)}$ is the diagonal matrix of singular values. Under the hypothesis that the structure behaves as a single degree of freedom system around the peak of resonance, ω_n, the rank of $\mathbf{G}_{yy}(\omega_k)$ tends to one as the current frequency ω_k approaches one of the system's natural frequencies, ω_n.

By comparing Eq.(2.4) and Eq.(2.22) when $\omega_k = \omega_n$, a good estimate of the mode shape can be achieved from the singular vector corresponding to the only non-zero singular value.

Moreover, from Eq.(2.5), the correlation matrix can be written in terms of the modal parameters. If such correlation functions are evaluated by an inverse Fourier transform of the power spectral density matrix in the neighborhood of the identified natural frequency, and the mode shapes are well separated, then they correspond to the free decay of an equivalent SDOF system. Therefore, the logarithmic decrement technique can be applied to estimate the damping ratio, Ref.[13, 42]. This technique is based on the fact that the natural logarithm of the ratio of successive drops in the amplitude of a pseudo-harmonic signal can be used to estimate the damping. In Fig.2.2 the impulsive response of a SDOF system is shown as

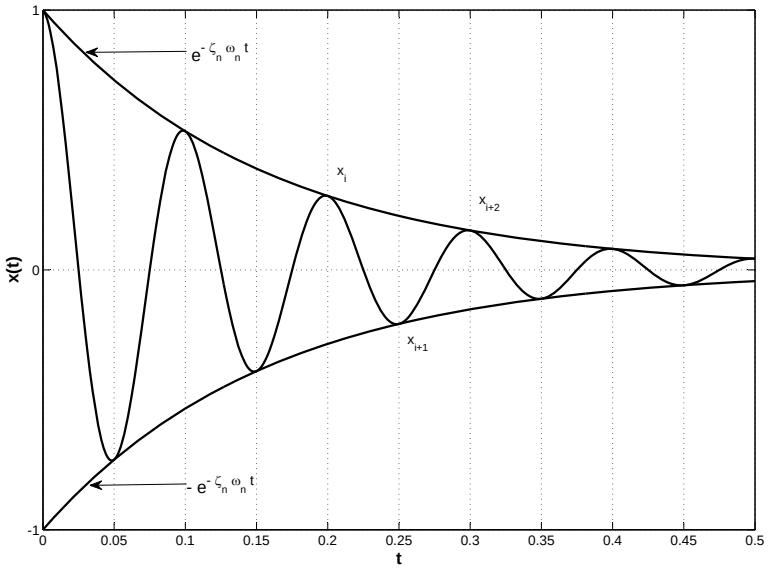

Figure 2.2: Damping estimate using the Logarithm Decrement technique.

pseudo-harmonic function with frequency ω_n and damping ζ_n. Such a function can be written as

$$x(t) = e^{-\zeta_n \omega_n t} \cos\left(\omega_n \sqrt{1-\zeta_n^2}\, t\right) \tag{2.23}$$

The function's local maxima and minima x_i correspond to those values in which the cosine function is equal to 1 or -1, therefore they lies on the natural exponential envelope represented in Fig.2.2. Moreover

they correspond to the values of the independent variable t that is equal to the integer multiples of the semi-period $T/2 = \frac{\pi}{\omega_n\sqrt{1-\zeta^2}}$. Equation (2.23) for $t = iT/2$ becomes

$$x_i = x(t = iT/2) = e^{-\zeta_n\omega_n iT/2} \tag{2.24}$$

and taking the natural logarithm, it results

$$\log x_i = -\frac{\zeta\pi}{\sqrt{1-\zeta^2}}i \tag{2.25}$$

This means that the damping ζ can be found from the angular coefficient of the linear trend obtained by plotting the logarithm of the absolute values of the maxima and minima x_i against the index i, with $i = 0$ when $t = 0$.

2.3 Stochastic Subspace Identification

The goal of the Stochastic Subspace Identification (SSI) methods is the evaluation of the dynamical behavior of the system represented by the state space formulation (Sec.1.3.1):

$$\mathbf{x}(k+1) = \mathbf{A}\mathbf{x}(k) + \mathbf{B}\mathbf{f}(k) \tag{2.26}$$

$$\mathbf{y}(k) = \mathbf{C}\mathbf{x}(k) \tag{2.27}$$

in which the state vector is $\mathbf{x} \in \Re^{2N}$, the output vector is $\mathbf{y} \in \Re^{N_o}$ and, consequently, the state matrix is $\mathbf{A} \in \Re^{2N\times 2N}$ and the output matrix is $\mathbf{C} \in \Re^{N_o\times 2N}$; for the sake of simplicity, the input belongs only to the first equation, the input matrix is $\mathbf{B} \in \Re^{2N\times N_i}$ and $\mathbf{f} \in \Re^{N_i}$ represents the white noise excitation vector, where N is the number of degrees of freedom of the system. The estimation of the system's modal parameters is easily evaluated by calculating the eigenvalues and the eigenvectors of the state matrix $\mathbf{A}$, that, in turn, can be obtained starting from the observability matrix of order p, $\mathbf{O}_p \in \Re^{pN_o\times 2N}$, that is, by definition:

$$\mathbf{O}_p = \begin{bmatrix} \mathbf{C} \\ \mathbf{CA} \\ \vdots \\ \mathbf{CA}^{p-1} \end{bmatrix} \tag{2.28}$$

Thus, the $\mathbf{C}$ matrix can be extracted from the first N_o lines of $\mathbf{O}_p$, and $\mathbf{CA}$ from the next ones. As a result the estimation of the $\mathbf{A}$ matrix is obtained by a least square procedure. Two different algorithms, Balanced Realization (BR-SSI) and frequency domain (f-SSI) methods, can be used to evaluate the observability matrix starting from the system responses in the time or in the frequency domain. In the first case the starting point is the Hankel matrix of the correlation functions evaluated with the time system responses. In the frequency approach the Vandermonde matrix is used because it is composed by the spectra of the system responses. More details could be found in Refs.[5, 6].

2.3.1 Balanced Realization

The Hankel matrix of orders p and q is computed by choosing N_{ref} outputs as references

$$\mathbf{H}_{pq} = \begin{bmatrix} \mathbf{R}_1 & \dots & \mathbf{R}_q \\ \vdots & \ddots & \vdots \\ \mathbf{R}_p & \dots & \mathbf{R}_{p+q-1} \end{bmatrix} \tag{2.29}$$

in which $\mathbf{R_m} \in \Re^{\mathbf{N_o} \times \mathbf{N_{ref}}}$ are the correlation function matrices defined as 1.56 and evaluated as follows:

$$R_{ij_k} = E[y_{i_{k+m}}, y_{j_m}] = \frac{1}{N_t - k} \sum_{m=0}^{N_t-k-1} \mathbf{y}_{i_{m+k}} \mathbf{y}_{j_m}$$

for $i = 1..N_o$ and $j = 1..N_{ref}$. It is possible to demonstrate that [6]:

$$\mathbf{H}_{pq} = \mathbf{O}_p \mathbf{C}_q \tag{2.30}$$

in which $\mathbf{C}_q \in \Re^{2N \times qN_{ref}}$ is the controllability matrix of order q:

$$\mathbf{C}_q = \begin{bmatrix} \mathbf{G} & \mathbf{AG} & \dots & \mathbf{A}^{q-1}\mathbf{G} \end{bmatrix} \tag{2.31}$$

where the elements of the matrix $\mathbf{G} \in \Re^{2N \times N_{ref}}$, G_{ij} are the expected values $E[x_{i_{k+1}}, y_{j_k}]$. The singular value decomposition of the Hankel matrix could be approximated by:

$$\mathbf{H}_{pq} = \begin{bmatrix} \mathbf{U}_1 & \mathbf{U}_2 \end{bmatrix} \begin{bmatrix} \mathbf{S}_1 & 0 \\ 0 & \mathbf{S}_2 \end{bmatrix} \begin{bmatrix} \mathbf{V}_1^T \\ \mathbf{V}_2^T \end{bmatrix} \approx [\mathbf{U}_1] [\mathbf{S}_1] [\mathbf{V}_1^T] \tag{2.32}$$

where the $\mathbf{S}_1 \in \Re^{\ell \times \ell}$ matrix contains highest ℓ singular values in decreasing order. Combining Eq.(2.30) and Eq.(2.32), the observability matrix can be estimated as follows:

$$\mathbf{O}_p = \mathbf{U}_1 \mathbf{S}_1^{1/2} \tag{2.33}$$

The illustrated procedure is repeated by increasing the number of ℓ because the system order is not known. A comparison among the poles corresponding to different iteration steps allows to plot the stabilization diagram to distinguish stable poles as structural modes.

2.3.2 Frequency domain

The Vandermonde matrix is computed from the spectral responses as follows

$$\left[\begin{array}{cccc} z_1^{-p}\mathbf{Y}_1 & z_2^{-p}\mathbf{Y}_2 & \dots & z_N^{-p}\mathbf{Y}_N \\ z_1^{-p+1}\mathbf{Y}_1 & z_2^{-p+1}\mathbf{Y}_2 & \dots & z_N^{-p+1}\mathbf{Y}_N \\ \vdots & \vdots & \ddots & \vdots \\ z_1^{-1}\mathbf{Y}_1 & z_2^{-1}\mathbf{Y}_2 & \dots & z_N^{-1}\mathbf{Y}_N \\ \hline \mathbf{Y}_1 & \mathbf{Y}_2 & \dots & \mathbf{Y}_N \\ z_1\mathbf{Y}_1 & z_2\mathbf{Y}_2 & \dots & z_N\mathbf{Y}_N \\ \vdots & \vdots & \ddots & \vdots \\ z_1^{p-1}\mathbf{Y}_1 & z_2^{p-1}\mathbf{Y}_2 & \dots & z_N^{p-1}\mathbf{Y}_N \end{array}\right] \stackrel{def}{=} \left[\begin{array}{c} \mathbf{Y}_- \\ \hline \mathbf{Y}_+ \end{array}\right] \tag{2.34}$$

It is possible to demonstrate, [5], the following equation:

$$\mathbf{Y}_+ / \mathbf{Y}_- = \mathbf{O}_p \mathbf{X} \tag{2.35}$$

in which $\mathbf{O}_p$ is the system observability matrix introduced in Eq.(2.28) and the expression $\mathbf{A}/\mathbf{B}$ is shorthand for the projection of the row space of the matrix $\mathbf{A}_{[p \times j]}$ on the row space of the matrix $\mathbf{B}_{[q \times j]}$. This projection can be performed as follows:

$$\mathbf{Y}_+ / \mathbf{Y}_- = \mathbf{Y}_+ \mathbf{Y}_-^H (\mathbf{Y}_- \mathbf{Y}_-^H)^{-1} \mathbf{Y}_- \tag{2.36}$$

otherwise by QR factorization:

$$\left[\begin{array}{c} \mathbf{Y}_+ \\ \mathbf{Y}_- \end{array}\right] = \left[\begin{array}{cc} \mathbf{R}_B^H & 0 \\ \mathbf{R}_{AB}^H & \mathbf{R}_A^H \end{array}\right] \left[\begin{array}{c} \mathbf{Q}_A \\ \mathbf{Q}_B \end{array}\right] \tag{2.37}$$

$$\mathbf{Y}_+ / \mathbf{Y}_- = \mathbf{R}_{AB}^H \mathbf{Q}_A \tag{2.38}$$

The observability matrix is estimated by considering the following approximation:

$$\mathbf{Y}_+/\mathbf{Y}_- = \begin{bmatrix} \mathbf{U}_1 & \mathbf{U}_2 \end{bmatrix} \begin{bmatrix} \mathbf{S}_1 & 0 \\ 0 & \mathbf{S}_2 \end{bmatrix} \begin{bmatrix} \mathbf{V}_1^T \\ \mathbf{V}_2^T \end{bmatrix} \approx [\mathbf{U}_1][\mathbf{S}_1]\left[\mathbf{V}_1^T\right] \tag{2.39}$$

and by using Eq.(2.33). Let varying the model order through the parameter ℓ, as for the time domain approach, the stabilization diagram is built and the structural modes are identified as the stable poles.

2.4 Hilbert Transform Method

The advantage in using the Hilbert transform is primarily the capability that it provides of estimating the imaginary part of a causal function starting from its real part, Ref.[18]. The polar representation of a driving point FRF is given by

$$H_{ii}(\omega) = |H_{ii}(\omega)|e^{-j\phi_{ii}(\omega)} \tag{2.41}$$

or, by introducing the natural logarithm, it can be expressed as

$$ln\left[H_{ii}(\omega)\right] = G_{ii}(\omega) - j\phi_{ii}(\omega) \tag{2.42}$$

in which $G_{ii}(\omega) = ln|H_{ii}(\omega)|$ is the gain function. Considering that the real part of the FRF is an even function and the imaginary part is an odd function, the gain and the phase are, therefore, even and odd, respectively. As a result, the left-hand side of the Eq.(2.42) can be expressed as the sum of a pair of Hilbert transform functions:

$$\phi_{ii}(\omega) \quad = \quad -\hat{G}_{ii}(\omega) \tag{2.43}$$

The gain function is also related to the spectral density function as:

$$\mathbf{G}_{yy}(\omega_k) = \mathbf{H}(\omega_k)\mathbf{G}_{ff}(\omega_k)\mathbf{H}^H(\omega_k) \tag{2.44}$$

The Hilbert transform of a signal $x(t)$ is defined as the Cauchy principal value of

$$\hat{x}(t) = \mathcal{H}[x(t)] = \frac{1}{\pi} \not\int_{-\infty}^{+\infty} \frac{x(\tau)}{t-\tau} d\tau \tag{2.40}$$

where the input spectral density matrix, defined between the N_i inputs, *i.e.*, $\mathbf{G}_{ff}(\omega_k) \in \mathcal{C}^{N_i \times N_i}$, is assumed to be derived from a white noise excitation. This implies that $\mathbf{G}_{ff}(\omega_k)$ is frequency independent and $\mathbf{G}_{ff}(\omega_k) = \mathbf{G}_{ff}$, where $\mathbf{G}_{ff}$ is a diagonal matrix when the input excitation is uncorrelated in the space domain. As a consequence, by applying the natural logarithm and performing the Hilbert transform, Eq.(2.44) becomes:

$$\mathcal{H}\left[\ln(G_{y_i y_i}(\omega))\right] = 2\mathcal{H}\left[\ln|H_{ii}(\omega)|\right] \tag{2.45}$$

in which the input spectral density contribution, $G_{f_i f_i}$, is null, as the Hilbert transform of a constant is zero. Combining the previous Eqs.(2.43) and (2.45) it is possible to write

$$\phi_{ii}(\omega) = -\frac{1}{2}\mathcal{H}\left[\ln(G_{y_i y_i}(\omega))\right] \tag{2.46}$$

Therefore, the FRF at the i-th driving point is achieved by evaluating the modula and the phase functions from the response Power Spectral Density, PSD, function $G_{y_i y_i}$ as:

$$|H_{ii}(\omega)|^2 =: \frac{|\tilde{H}_{ii}(\omega)|^2}{G_{f_i f_i}} = \frac{G_{y_i y_i}(\omega)}{G_{f_i f_i}} \tag{2.47}$$

$$\phi_{ii}(\omega) = -\frac{1}{2}\mathcal{H}\left[\ln(G_{y_i y_i}(\omega))\right] \tag{2.48}$$

where the unknown input PSD function $G_{f_i f_i}$ gives the bias on $|H_{ii}(\omega)|$ with respect to $|\tilde{H}_{ii}(\omega)|$. Therefore, the bias FRF in the i-th driving point is estimated by:

$$\tilde{H}_{ii}(\omega) = \sqrt{G_{y_i y_i}(\omega)} e^{j\phi_{ii}(\omega)} \tag{2.49}$$

The off-diagonal terms of the FRF are derivable from the comparison between the commonly used H1 and H2 estimators, Refs.[39]. The response of the j-th degree of freedom when a loading is applied at the i-th degree of freedom, for deterministic signals, is given by

$$H_{ji}(\omega) = \frac{X_j(\omega)}{F_i(\omega)} \tag{2.50}$$

that could be rewritten as

$$H_{ji}(\omega) = \frac{X_i^*(\omega)X_j(\omega)}{X_i^*(\omega)F_i(\omega)} \tag{2.51}$$

This equation is also equivalent to the following relationship:

$$H_{ji}(\omega) = \frac{X_i^*(\omega)X_j(\omega)}{F_i^*(\omega)F_i(\omega)\frac{X_i^*(\omega)}{F_i^*(\omega)}} \tag{2.52}$$

that is

$$H_{ji}(\omega) = \frac{G_{y_i y_j}(\omega)}{\sqrt{G_{f_i f_i}}H_{ii}^*(\omega)} \tag{2.53}$$

Therefore the off-diagonal terms of the bias FRF matrix can be obtained:

$$\tilde{H}_{ij}(\omega) = \frac{G_{x_i x_j}(\omega)}{\tilde{H}_{ii}(\omega)} \tag{2.54}$$

Obviously, the estimated functions are unbiased depending on the unknown input forces, but it is important to stress that the bias constant on the operational FRF does not affect the modal parameter estimates, because they are not dependent on the biasing level. The modal parameters are evaluated with a least square approximation, considering the expression of FRF in pole-residue terms, Eq.(1.43). In the frequency range of definition of the FRF, the number of modes, N_m, is not known, therefore a stabilization diagram is introduced to estimate it by means of an iterative procedure. It is worth remarking that the structural properties are independent from the order used to describe the system, thus stable poles are representative of natural frequencies, Ref.[34].

2.5 Modified Hilbert Transform Method

The methodology proposed in this section improves the already developed operational modal analysis method, HTM described in the previous section 2.4, to deal with harmonic excitations embedded in a stochastic white noise loading ([7, 43, 44, 45, 46]). First, it will be shown how to identify the presence of a harmonic excitation by statistically characterizing the output responses. The effects of the harmonic

components could be distinguished from the non-deterministic excitation in the output responses because of different probability density functions, detected, in turn, by the statistical function called "Entropy", Ref.[47]. Then, an approach capable to remove the effects of the harmonic excitations in the modal parameter estimate will be presented. This method starts from the availability of a parametric representation of the biased frequency response function gained by the so called Hilbert Transform method. The capability to improve the OMA procedures is initially investigated through several numerical analyses in which both the accuracy of statistical index and the effects of the harmonic removal in the modal parameter estimate are investigated. The effectiveness of the used statistical procedure will be compared with the so called "Kurtosis" index, already used in previous works, Refs.[48, 49], whereas a comparison among the modal parameter estimates achieved by different methodologies is performed for an assessment of the proposed approach.

2.5.1 Statistical tools

In this section, some background on the statistical approach used to characterize stochastic signals are briefly introduced. More details could be found in Refs.[47, 50]. Let be $p(x)$ a one dimensional probability density function, pdf, characterizing a random process of the value x, with the well known properties that $p(x) \geq 0, \ \forall x$ and $\int_{-\infty}^{\infty} p(x)dx = 1$. A measure of the uncertainty associated with this variable could be expressed in terms of the Entropy of such a pdf, S, derived from Ref.[47]:

$$S = -\int_{-\infty}^{+\infty} p(x) \log\left[p(x)\right] dx \tag{2.55}$$

When the random process is described by n discrete values of the pdf, $p_i, \ldots, p_n$, then the Entropy could be defined, in analogy with the previous expression, as:

$$S = -\sum_{i=1}^{n} p_i \log\left(p_i\right) \tag{2.56}$$

This formulation is commonly recognized as entropy as defined in physical applications of statistical mechanics, *i.e.*, in Boltzmann's thermodynamic theorem. Shannon introduced the entropy by elaborating

a model of communication, as a parameter to quantify the loss of information occurring during a data transfer process due to the presence of noise. In this thesis an application of this statistical tool to detect the presence of non-gaussianity in a stochastic process is provided. An important property of the Entropy for discrete pdf is that it is null if and only if all the p_i are zero, but one, and then this non-zero pdf has to have unitary value. Thus, the Entropy vanishes only when the occurrence is certain, otherwise it is positive. This property could be extended to a continuous distribution $p(x)$ by setting to zero the left-hand side of Eq. 2.55, when considering a uniform distribution over a unit domain. Moreover, it could be demonstrated that the Entropy has a maximum value when the random process, with standard deviation σ, is represented by a gaussian distribution of values, that is when the pdf can be written as:

$$p(x) = \frac{1}{\sqrt{2\pi}\sigma} e^{-\frac{x^2}{2\sigma^2}} \tag{2.57}$$

For this type of random process, the maximum value of the Entropy, S_G, depends only on the standard deviation and is given by:

$$S_G = \log\left(\sigma\sqrt{2\pi e}\right) \tag{2.58}$$

Therefore a pdf will always have an Entropy value belonging to the $[0, S_G]$ interval. To prove this property the function $S(x)$ has to be maximized with the constraints:

$$\sigma^2 = \int p(x)x^2 dx \tag{2.59}$$

$$1 = \int p(x)dx \tag{2.60}$$

This requires, by the calculus of variations, maximizing

$$\int \left[-p(x)\log p(x) + \lambda p(x)x^2 + \mu p(x)\right] dx \tag{2.61}$$

The condition for this is

$$-1 - \log p(x) + \lambda x^2 + \mu = 0 \tag{2.62}$$

and consequently, adjusting the constants to satisfy the constraints in Eqs.(2.59-2.60):

$$p(x) = \frac{1}{\sqrt{2\pi}\sigma} e^{-\frac{x^2}{2\sigma^2}} \tag{2.63}$$

that is the Gaussian pdf.

This statistical analysis could be also performed using time responses of a rotating structure characterized by the presence of a harmonic contribution blended in a stochastic random process. It is worth noting that the pdf of the response of a linear system to stochastic independent excitations is well approximated by the gaussian model (central limit theorem). On the contrary, the response of the system to a harmonic excitation is (practically) deterministic with the same frequency of the excitation, provided its energy level is high enough with respect to the one of the random process. In addition, it is reasonable to expect that the Entropy of the response signal evaluated at the frequency of the excitation would be non maximum because it involves deterministic realizations. Therefore, the Entropy associated to the response of a rotating structure will be maximum in all the frequency range of interest, whereas it will be lesser than the maximum at the frequency of the harmonic excitation, for a given standard deviation of the time response. The advantages of using this Entropy index to identify harmonic components acting in a random process have been validated by comparing its behavior with the Kurtosis statistical index, defined in Ref.[50], and already used in Ref.[49]. In order to give information on how a random process having a mean value μ is similar to a gaussian one, the Kurtosis index is defined as:

$$\gamma = \frac{1}{N\sigma^2} \sum_{i=1}^{N} (x_i - \mu)^4 \tag{2.64}$$

where N is the number of the realizations. It is worth noting that, for normal or gaussian distributions, the Kurtosis value is 3. Therefore, a modified Kurtosis value, γ^* is generally considered so that:

$$\gamma^* = \gamma - 3 \tag{2.65}$$

In this way, γ^* gives a measure of how far a stochastic process is from the gaussian. It is shown in Ref.[49] that this modified Kurtosis value is equal to -1.5 when a pure harmonic signal is considered.

Briefly, from the analysis of the Entropy (or the Kurtosis) index as frequency functions, the detection of the harmonic excitations is achieved. In particular, when a local minimum (or the value of -1.5) is reached for the Entropy (Kurtosis), then the frequency of the deterministic, and, hence, of the harmonic, component is identified. The last problem that has to be addressed is how the Entropy (or the Kurtosis) statistical index, associated to the responses of the system under investigation, is calculated as frequency functions. Fig.2.3 shows the methodology to follow in order to evaluate such a function. It can be divided in two steps: the first is the definition of a set of band-pass filters centered at each frequency available in the analysis, which is a running filter, the second is the statistical characterization of the filtered time responses. The importance in the definition of the filter is strictly related to the accuracy of the achieved

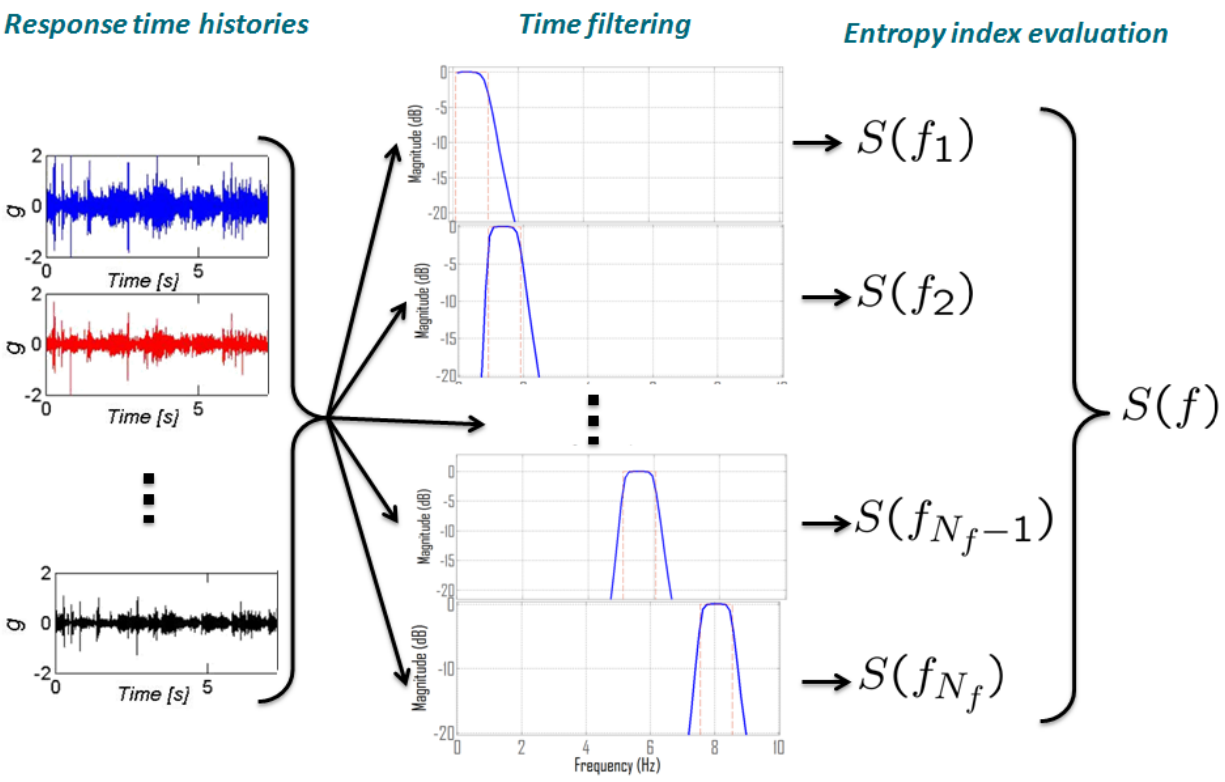

Figure 2.3: Evaluation of the entropy index as a frequency function.

entropy (or kurtosis) function. This motivation should lead to a filter with high order and narrow band, but these are conflicting with the necessary computational effort. The expertise suggests that a butterworth filter with order 6 and width around $1\ [Hz]$ leads to enough accurate entropy functions. In the following

section 3.4, some numerical examples will show the sensitivity of the results to the filter characteristics. It is important to note that the statistical properties of the time series are not affected by this filtering processing, so the pdf preserves its shape and consequently the entropy (or the kurtosis) values keep their role in identifying the deterministic corruptions in the stochastic signals.

2.5.2 Harmonic removal

The previous representation of the biased FRF gained by applying the HTM, Eqs.(2.49) and (2.54), gives an important tool for removing the effects of harmonic loadings in the considered operational data. Indeed, once the harmonic excitations (both their operational frequencies, ω_{op_n}, and their number, N_{op}), are identified from the evaluation of the frequencies where the output signal has non-gaussian behavior, as described in the previous section, it is possible to neglect their contributions to the formation of the biased FRF, $\tilde{\mathbf{H}}(\omega)$. Assuming that the number of modes M is given by the sum of the elastic modes N_m and the operational modes N_{op}, so that $M = N_m + N_{op}$, the harmonic-free frequency response function, $\overset{\emptyset}{\mathbf{H}}(\omega)$, could be expressed as:

$$\overset{\emptyset}{\mathbf{H}}(\omega) = \tilde{\mathbf{H}}(\omega) - \overset{\mathrm{O}}{\mathbf{H}}(\omega) \tag{2.66}$$

where the operational frequency response function, $\overset{\mathrm{O}}{\mathbf{H}}(\omega)$, is defined as:

$$\overset{\mathrm{O}}{\mathbf{H}}(\omega) := \sum_{n=1}^{N_{op}} \left[\frac{\mathbf{R}^{(n)}}{j\omega - \lambda_{op_n}} + \frac{\mathbf{R}^{(n)*}}{j\omega - \lambda^*_{op_n}} \right] \tag{2.67}$$

where $\lambda_{op_n} = \zeta_{op_n}\omega_{op_n} + j\omega_{op_n}\sqrt{1-\zeta^2_{op_n}}$. The matrices of the residuals, $\mathbf{R}^{(n)}$, and the equivalent damping ratios, ζ_{op_n}, are estimated using the standard residue/pole least-square technique in frequency domain from the knowledge of the operational frequency, ω_{op_n}, already estimated by analyzing the Entropy statistical index. It is worth noting this estimate takes into account possible structural couplings, responsible for dynamic energy loss, and the effects of a limited observation recording time of the output responses, which, in turn, introduces an equivalent damping on the estimate of the frequency response functions [51].

2.6 Modal Mass Estimate

In the OMA the dynamic properties of the system are identified without any measurement of the input excitation, but assuming it behaves as white noise in the frequency band of interest. All the explained methodologies can be implemented to evaluate the natural frequencies, the damping ratios and the mode shapes, except for the modal masses, because of the unknown excitation loading. A way to avoid this problem is performing more than one experimental test in which the mass or stiffness properties of the structure are perturbed. Two different approaches could be considered starting from Eq.(1.8), when a variation of the mass or stiffness is introduced:

$$(\boldsymbol{K}+\boldsymbol{\Delta K})\,\bar{\boldsymbol{\varphi}}^{(n)} \;=\; \bar{\lambda}_n\,(\boldsymbol{M}+\boldsymbol{\Delta M})\,\bar{\boldsymbol{\varphi}}^{(n)}, \quad n=1,2,\ldots,N \tag{2.68}$$

where $\bar{\boldsymbol{\varphi}}^{(n)}$ and $\bar{\lambda}_n$ represent the system's eigenvector and the eigenvalue (as in Eq.(1.35) after the perturbation. These approaches are named Constant Mode Shapes, CMS, [2], and Receptance Based Normalization, RBN, [1].

2.6.1 Constant Mode Shapes

Under the assumption that mass or stiffness variations do not induce a mode shape variation, by combining the Eqs.(1.8) and (2.68), with $\bar{\lambda}_n = \lambda_n + \Delta\lambda_n$, one gets:

$$(\boldsymbol{\Delta K}-\lambda_n\boldsymbol{\Delta M})\,\boldsymbol{\varphi}^{(n)} \;=\; \Delta\lambda_n\,(\boldsymbol{M}+\boldsymbol{\Delta M})\,\boldsymbol{\varphi}^{(n)}, \quad n=1,2,\ldots,N \tag{2.69}$$

Therefore, modal mass, m_n, could be evaluated pre-multiplying by $\boldsymbol{\varphi}^{(n)T}$ and rearranging:

$$m_n = \boldsymbol{\varphi}^{(n)T}\boldsymbol{M}\boldsymbol{\varphi}^{(n)} \;=\; \frac{\boldsymbol{\varphi}^{(n)T}\left(\boldsymbol{\Delta K}-\bar{\lambda}_n\boldsymbol{\Delta M}\right)\boldsymbol{\varphi}^{(n)}}{\Delta\lambda_n}, \quad n=1,2,\ldots,N \tag{2.70}$$

If $\boldsymbol{\Delta K}=0$, it results:

$$m_n = -\boldsymbol{\varphi}^{(n)T}\boldsymbol{\Delta M}\boldsymbol{\varphi}^{(n)}\frac{\bar{\lambda}_n}{\Delta\lambda_n}, \quad n=1,2,\ldots,N \tag{2.71}$$

The main limitation of this method is that the mode shape variation induced by the mass or stiffness variation is neglected. Therefore, if for example the system variation is induced by adding masses on the structure, particular attention is required by the positioning of the masses themselves in order to minimize the mode shape variations.

2.6.2 Receptance Based Normalization

Equation (2.68) can be rewritten as, see [1]:

$$\left(\boldsymbol{K} - \bar{\lambda}_p \left(\boldsymbol{M} + \boldsymbol{\Delta M}\right)\right) \bar{\boldsymbol{\varphi}}^{(p)} \quad = \quad 0, \quad p = 1, 2, \ldots, N \tag{2.72}$$

Rearranging this equation in order to separate the dependency on the natural frequencies of the perturbed system, $\boldsymbol{H}(j\omega = \bar{\lambda}_p)$ in Eq.(1.37), is it possible to write:

$$\bar{\lambda}_p \left(\boldsymbol{K} - \bar{\lambda}_p \boldsymbol{M}+\right)^{-1} \boldsymbol{\Delta M} \bar{\boldsymbol{\varphi}}^{(p)} \quad = \quad \bar{\boldsymbol{\varphi}}^{(p)}, \quad p = 1, 2, \ldots, N \tag{2.73}$$

By introducing the expression of the receptance in terms of the modal parameters of the system, which is Eq.(1.43) for $j\omega = \bar{\lambda}_p$, equation (2.73) becomes

$$\sum_{k=1}^{N_m} \frac{\boldsymbol{\varphi}^{(k)} \left(\boldsymbol{\varphi}^{(k)T} \boldsymbol{\Delta M} \bar{\boldsymbol{\varphi}}^{(p)}\right) \bar{\lambda_p}}{\lambda_k - \bar{\lambda_p}} \gamma_k \quad = \quad \bar{\boldsymbol{\varphi}}^{(p)}, \quad p = 1, 2, \ldots, N_m \tag{2.74}$$

where $\gamma_k = m_k^{-1}$ are the unknown scaling factors. Equation (2.74) is a linear system for each p-th normal mode. If $N_o \leq N$ system responses are available and $N_m \leq N$ modes are investigated, the overall equations are $N_m \times N_o$ and the unknown quantities are N_m. Therefore, the resolution of the Eq.(2.74) can be performed in the least square sense. Hence, it has to be noted that this method requires that $N_m \times N_o >> N_m$, otherwise the resolution of the Eq.(2.74) is not accurate.

Part II

Numerical and Experimental Validation

Chapter 3

Numerical Test Case

All the Operational Modal Analysis methodologies described in the previous Chapter 2 have been implemented in a single numerical platform called NIMA (Natural Input Modal Analysis) thanks to the work done in last years by students and Professors of the University "La Sapienza" at the Department previously known as "Aerospace and Astronautics Engineering". A reviewed version of such a code is described in this chapter together with the novel methods presented in this thesis. In order to verify the applicability of the proposed approaches and describe their implementation in the numerical platform NIMA, numerical test cases are analyzed as benchmark.

3.1 Numerical model

The main objective is the validation of the suggested methodologies and the quantification of their accuracy estimating the modal parameters without considering the input measurements. The numerical simulations are performed considering a known 4 DOF lumped parameter system, whose natural frequencies are shown in Tab.3.1, and the modal damping is constant and equal to $1.0\,\%$. The knowledge of the system parameters allows the estimate of the accuracy of the methodologies. Nevertheless the responses of the system to a white noise excitation have to be simulated numerically avoiding computational problems. The system is implemented as modal model with viscous damping using Simulink and the block diagram is represented

Table 3.1: Experimental natural frequencies for the 4 DOF numerical system.

Mode #	f_n [Hz]
1	5.0
2	6.9
3	12.8
4	20.0

in Fig.3.1, where the input is a normal distributed random in the frequency range of investigation and is applied on the second spatial DOF. Then, the transpose of the matrix of the modes is used to project the loading on the modal domain, represented by the four single transfer functions with unitary numerator and denominator depending on the poles, as in Eq.(1.42). Finally, the spatial responses are obtained from the modal ones by means of the modal matrix. All the responses are saved to the Matlab workspace together with the sampling time, but only the one corresponding to the first DOF is outputted in Simulink. The analytical modal parameters are compared with the estimates coming from the OMA approaches that

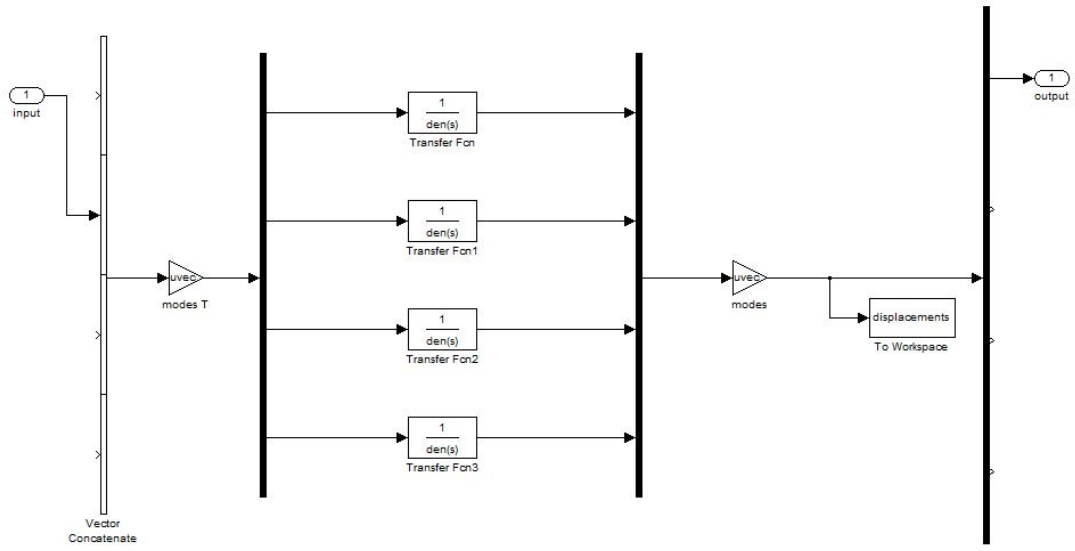

Figure 3.1: The Simulink block diagram of the 4 DOF modal model.

operate using only the responses. The Matlab *ode3* solver is used to evaluate the system's responses with a fixed time step equal to $0.0016\,\mathrm{s}$ to obtain a thorough simulation. This solver corresponds to a third-order Runge-Kutta method and the time step is chosen to ensure an accurate integration, although

it corresponds to the $625\,\mathrm{Hz}$ sampling frequency. It has to be noted that the for the experimental tests the signal's frequency bandwidth is usually chosen no wider than double the value of the maximum frequency of interest (avoiding aliasing), that is in this case around $40\,\mathrm{Hz}$. Therefore, a decimation of the system's responses can be performed to narrow the bandwidth to about $1/8$. It has to be noted that the decimation implies first a filtering of the responses and then a down-sampling. Although this process can always be performed, it is necessary in this case only to ensure that the data coming from the numerical simulation are representative of typical experimental situations. The simulation time is set to achieve 2^{18} samples, in order to have enough samples after the decimation. Therefore, the time signals analyzed with the NIMA platform are the four system's responses depicted in Fig.3.2, with sampling time equal to $0.0128\,\mathrm{s}$ and length equal to 2^{15}.

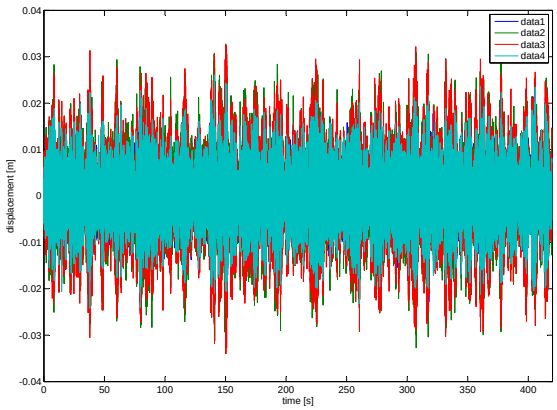

Figure 3.2: The time responses of the 4 DOF modal model with white noise excitation.

3.2 The main code

NIMA is a numerical platform developed in Matlab language with Graphical User Interface. It needs an input file with the system responses arranged in a matrix with dimensions equal to the number of samples times the number of channels times the number of the run (if a multi-run test is performed) and a scalar variable with the sampling time. Moreover, information about the geometry and the channel setup are necessary to

build the animation of the mode shapes. All the parameters requested by the methodologies are explained in the following whenever they are used to give advice on their selection. The main code, running from the Matlab workspace, starts with a first home window in which it is possible to choose the analysis to perform. In particular all the OMA methodologies are implemented as described in the following sections in addition to the presentation of the novel techniques developed to deal with the presence of harmonic components in the excitation and the evaluation of the modal masses. The flow diagram of the code is represented in Fig.3.3, in which the relations among the different subroutine are shown.

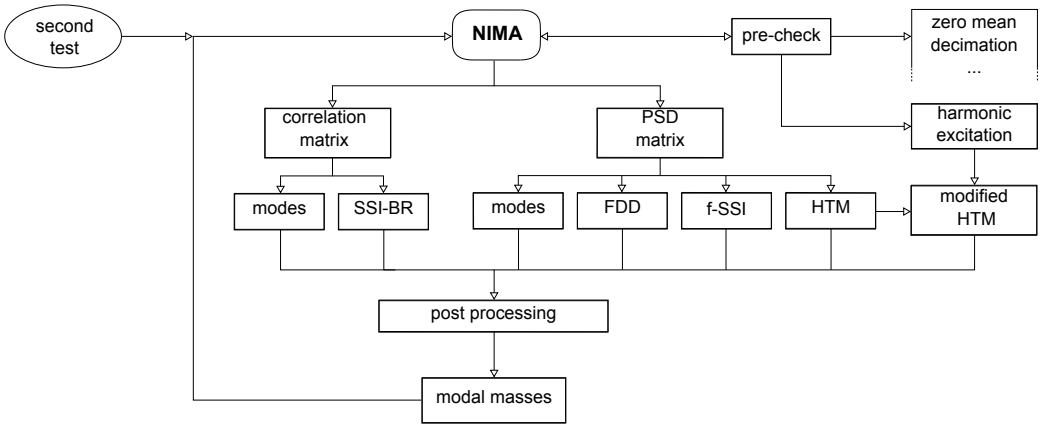

Figure 3.3: Flow diagram of the NIMA code.

Starting from the time histories, the first computational effort is the estimate of the correlation or power spectral density functions. This step involves the averaging procedure, since these functions can be computed by dividing the time series in overlapped blocks in the time or frequency domain, respectively. As Fig.3.4 shows, the higher the number of blocks, the higher is the the number of averages that can be performed on the PSD function with lower resolution, which is varying from about $0.02\,\mathrm{Hz}$ (of the blue line) to $0.15\,\mathrm{Hz}$ (of the cyan line). Once the PSD function matrix, or its inverse Fourier transform (the correlation function matrix) is evaluated, NIMA can directly estimate the modal parameters as described in Sec.2.1. This implementation in the code is depicted in Fig.3.5 in the frequency and time domain, respectively.

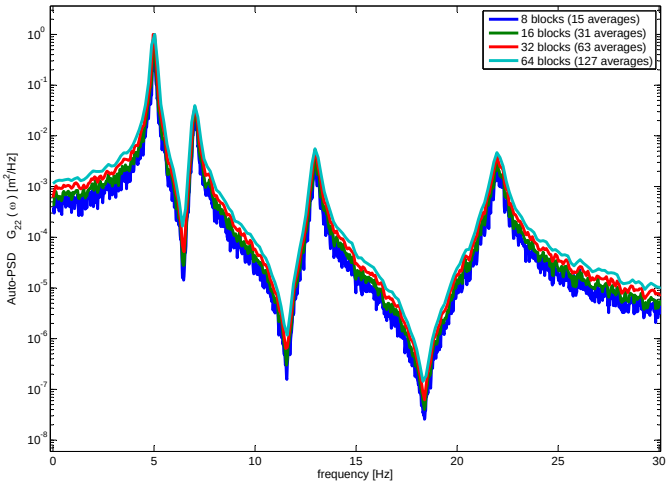

Figure 3.4: Sensitivity of the PSD function on the number of blocks.

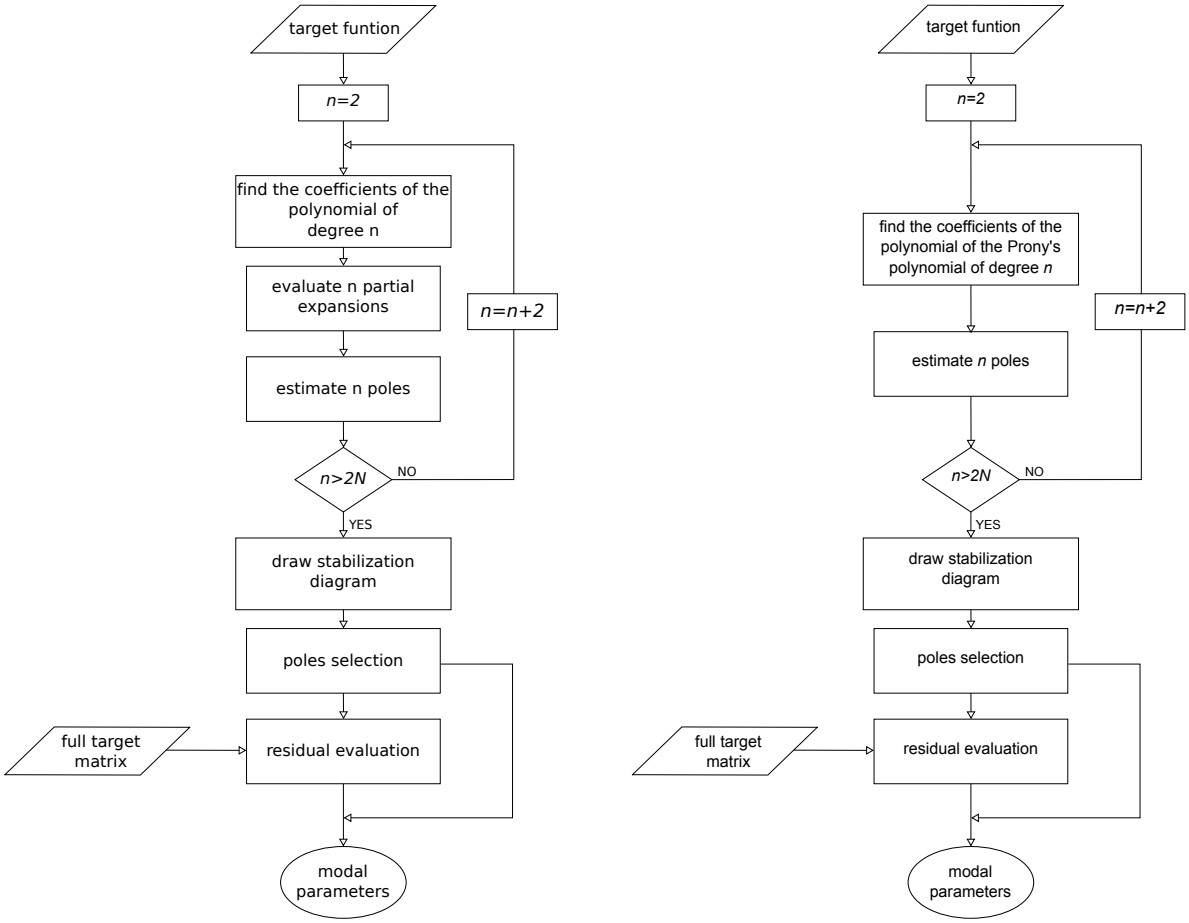

(a) frequency domain (b) time domain

Figure 3.5: Flow diagram of the pole and residue estimate procedure in NIMA.

In particular, an iterative procedure is implemented to find the best-fitting of the PSD or correlation functions in the frequency or time domain, respectively. Whereupon the stabilization diagram is build to drive the selection of the system poles and then the residual terms are evaluated as an estimate of the mode shapes. Then, the modal parameters can be used to synthesize the PSD and the correlation functions as their analytical expressions. Nevertheless the NIMA code can also use the experimental PSD and correlation matrices to implement the other OMA methods, such as Frequency Domain Decomposition (FDD), Hilbert Transform Method (HTM), Stochastic Subspace Identification (SSI) in frequency (f-) or time domain as Balanced Realization (BR-). Further details about them follow in the next sections.

There is an auxiliary branch in the NIMA's flow diagram of Fig.3.3. It performs some preliminary checks on the time histories, such as the zero mean, the resize of the data length to a power of two samples, the definition of the geometrical position of the sensors. Moreover, in this part the identification of the harmonic components in the excitation is included by means of the entropy index evaluation. The results coming from this statistical characterization of the time histories are coupled with the ones obtained by the HTM and the modified algorithm is implemented as discussed in the following.

3.3 OMA methodologies

3.3.1 Frequency Domain Decomposition

The flow chart of the subroutine FDD as implemented in NIMA is represented in Fig.3.6. This method works in the frequency domain, so it starts from the PSD function matrix. Then, in a cycle, the singular value decomposition of the PSD matrix is evaluated for each spectral line, for $k = 1, \cdots, N_f$, being N_f the overall frequency points in which the PSD matrix is known. It should be noted that, if the original time histories (of length N_t) have been divided in B blocks to average the noise, than N_f is not anymore the same of the original data, but $N_t/2B$. The trend of the singular values with respect the frequency is characterized by several peaks, since the system behaves as a SDOF nearest the resonance. Therefore,

the selection of the relative maxima gives the estimate of the natural frequencies and the corresponding singular vectors yield the mode shapes.

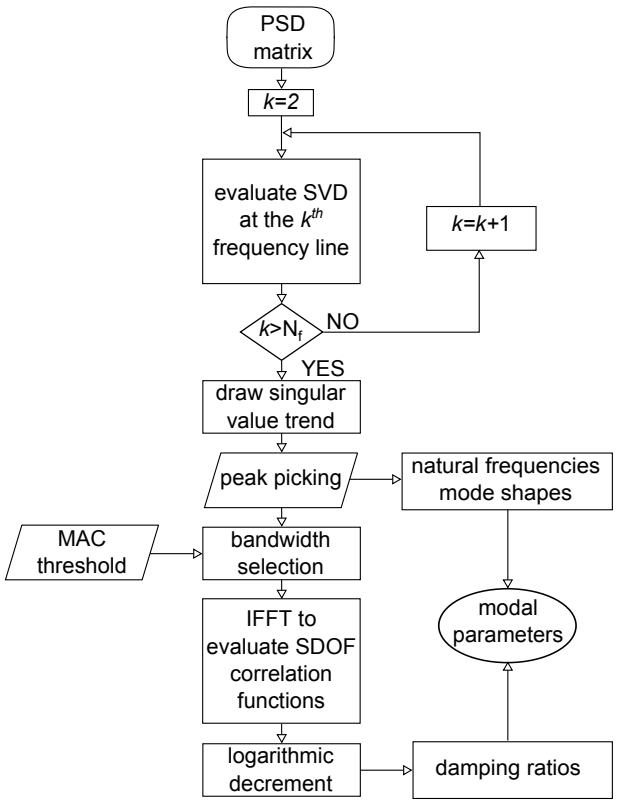

Figure 3.6: Flow diagram of the FDD code.

In Fig.3.7 the trend of the singular values in the frequency domain is shown in decibel to highlight the difference between the maximum value and the others. The picking of the peaks gives the natural frequencies and, as a consequence, the corresponding singular vector is the estimate of the mode shape. Since Eqs.(2.4) and (2.22) suggest that in the neighbourhood of the natural frequency the system behaves as a Single Degree of Freedom, the singular vectors are not expected to change; then the bandwidth around each peak is selected as the frequency range in which the MAC between the singular vectors is higher then 0.95. In Fig.3.7 these intervals are highlighted by adding the circles on the maximum singular value trend. The inverse Fourier transform of each sequence provides the SDOF correlation functions and the logarithmic decrement technique estimates the damping ratio as the exponent of the best-fitting exponential function

of the relative maxima and minima in absolute value, as it can be seen in the bottom part of the Fig.3.7. In Tab.3.2 the results are summarized. The relative error is about $0.15\,\%$ on the natural frequencies and $7\,\%$ on the damping ratio. The maximum error is related to the second mode, for which the threshold of the MAC value fixed at 0.95 is too high for the selection of the bandwidth for the use of the inverse fourier transform of the SDOF PSD, providing the SDOF correlation function. If it is lowered to 0.9, the natural frequency and mode shape estimates do not change, as expected, but the damping ratio becomes just $1\,\%$.

Table 3.2: Natural frequencies and damping ratio of the 4 DOF numerical system estimated by FDD.

Mode #	f_n [Hz]	ζ_n [%]
1	5.01	1.08
2	6.91	1.10
3	12.79	0.97
4	19.98	0.94

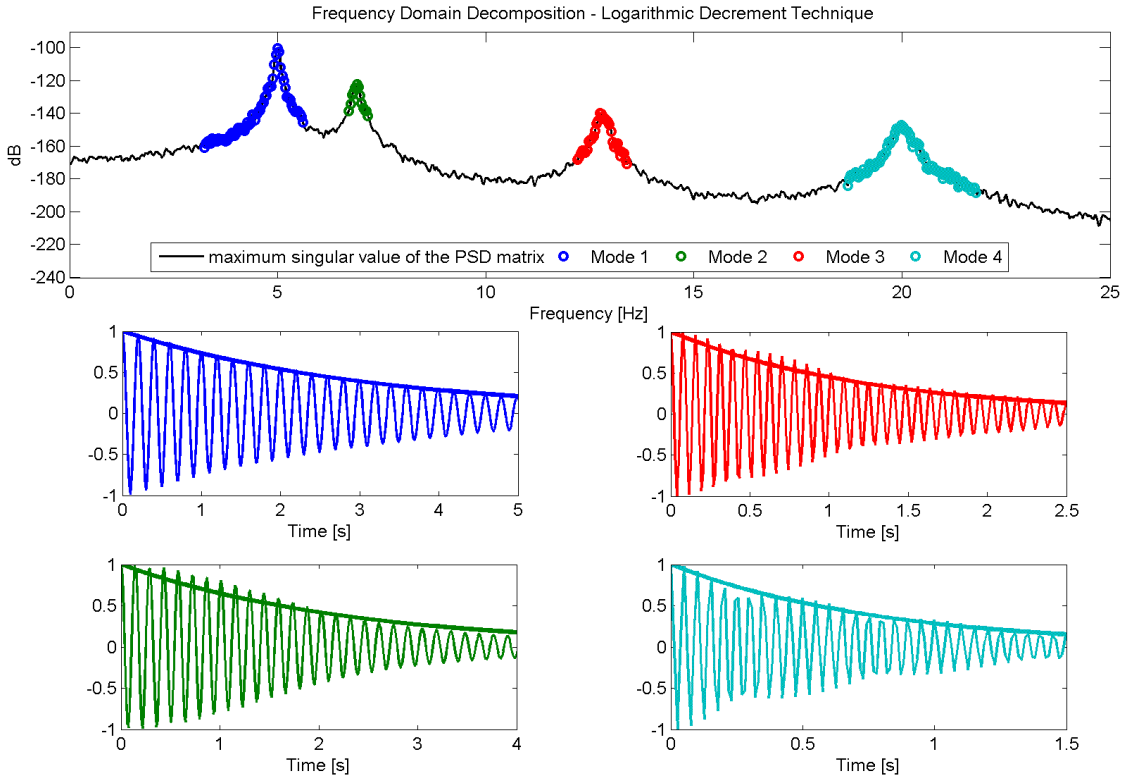

Figure 3.7: FDD estimate algorithm - frequency trend of the maximum singular value of the PSD matrix, peak picking, and SDOF pseudo-harmonic functions of the modes.

3.3.2 Balanced Realization - Stochastic Subspace Identification

The flow chart of the implementation of the code is shown in Fig.3.9, as described in Sec.2.3.1. There is a first evaluation of the Hankel matrix of orders p and q (with $p = q$ since all the measurement points are considered as references). In the selection of this parameter it has to be considered that the higher is the value, the higher can be the model order used for the stabilization diagram, but also the higher is the complexity of the mathematical model, so more spurious solutions have to be expected. In this case it is set to 12, since the system is very simple.

This approach directly estimates all the modal parameters (natural frequencies, damping ratios and mode shapes); so the stabilization diagram, as shown in Fig.3.8, is built by considering the relative error of the poles and the MAC of the shapes with the thresholds for the stable poles of $5\,\%$ and $10\,\%$, respectively. The results are summarized in Tab.3.3. It can be noted that the stabilization diagram is very clear and the

Table 3.3: Natural frequencies and damping ratio of the 4 DOF numerical system estimated by BR-SSI.

Mode #	f_n [Hz]	ζ_n [%]
1	5.00	0.91
2	6.90	1.10
3	12.80	0.90
4	20.01	0.94

selection of the columns with stable poles is easy, although some spurious solutions are found also in this numerical case.

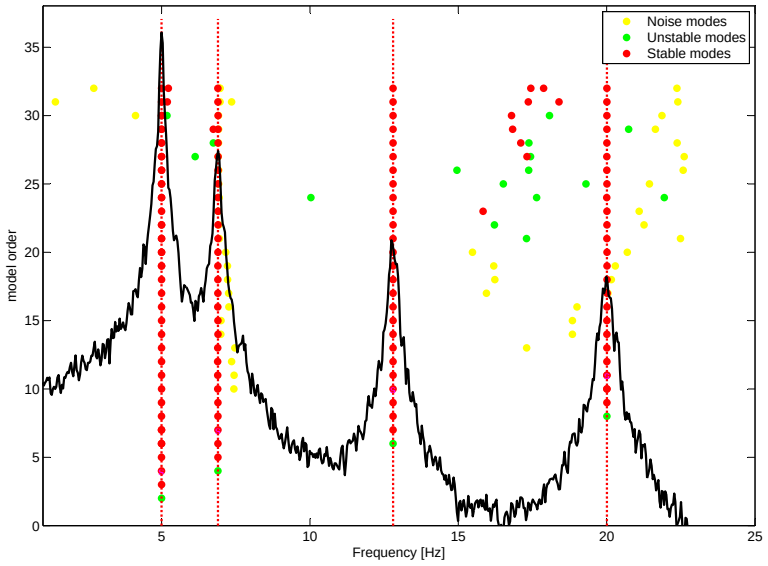

Figure 3.8: BR-SSI estimate algorithm - stabilization diagram of the system's modes.

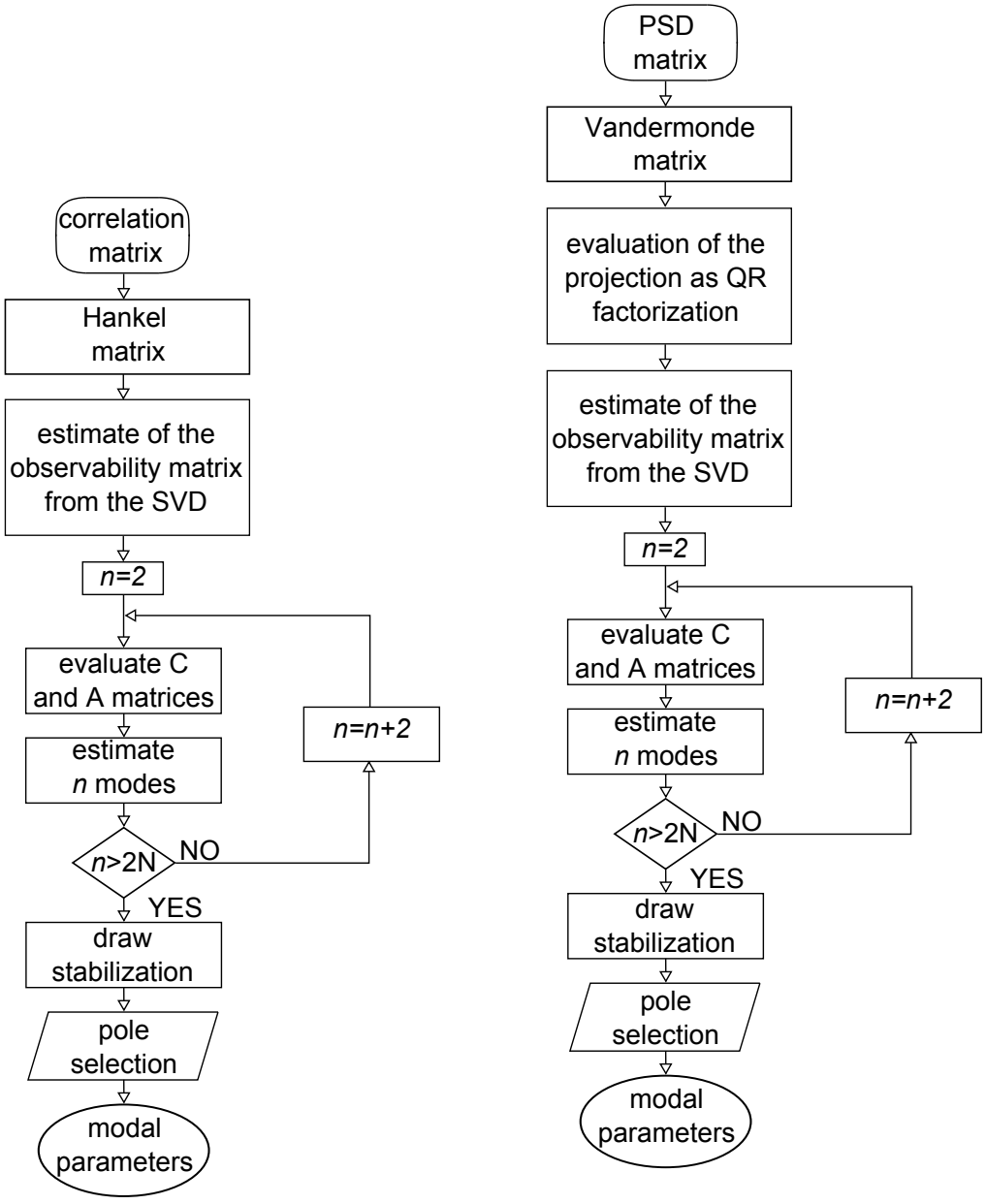

(a) BR-SSI (b) f-SSI

Figure 3.9: Flow diagram of the Stochastic Subspace Identification code in the time and frequency domain.

3.3.3 Frequency domain - Stochastic Subspace Identification

In this case, the flow chart in is very similar to the previous one. Fig.3.9 shows the presence of the extra computational effort required by the QR factorization to evaluate the projection of Eq.(2.36). Then, the algorithm goes on with the evaluation of the observability matrix and with its realization in terms of the system's matrices C and A for an increasing value of the system's order.

The stabilization diagram is drawn once the iterative procedure ends by comparing the modal parameters of consecutive iterations, as in Fig.3.10. The selected columns give the results summarized in Tab.3.4, where relative errors less than $1\,\%$ and $10\,\%$ are evalauted for the natural frequencies and damping ratios, respectively.

Table 3.4: Natural frequencies and damping ratio of the 4 DOF numerical system estimated by f-SSI.

Mode #	f_n [Hz]	ζ_n [%]
1	5.00	0.90
2	6.90	1.10
3	12.80	0.88
4	20.01	0.92

3.3.4 Hilbert Transform Method

The Hilbert Transform method is implemented as in Fig.3.11 where the evaluation of the bias Frequency Response Function matrix is achieved thanks to the Hilbert transform. Only the output responses are used to synthesize the full 4×4 bias FRF matrix, according to the procedure described in the previous section 2.4; in Fig.3.12, the $\tilde{H}_{24}$ is reported as reference with a blue line. Then, the modal parameter identification is performed as shown in Fig.3.5 and the stabilization diagram of the poles is built as in Fig.3.12. Using the selected poles and recalling the full FRF matrix among all the responses, the modes are estimated from the residual terms and the FRF functions can be re-synthesized as the green line shown in Fig.3.12. The modal parameters estimated from one column of the bias FRF matrix using the residue/pole fitting in the frequency domain, are practically the same as the reference ones, see Tab.3.5.

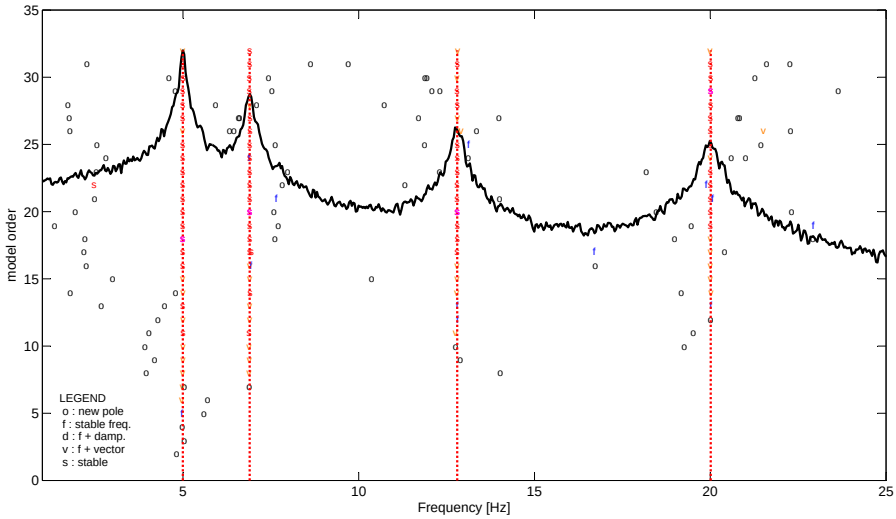

Figure 3.10: f-SSI estimate algorithm - stabilization diagram of the system's modes.

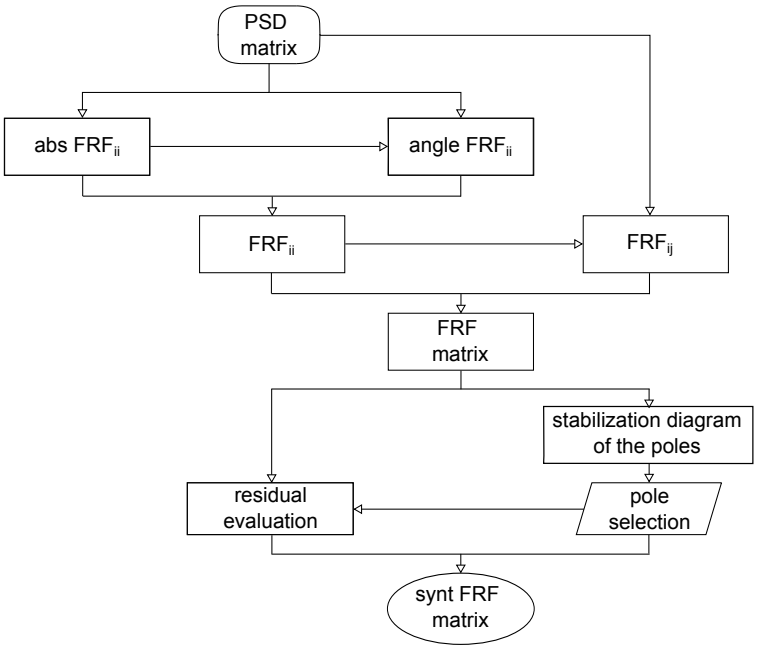

Figure 3.11: Flow diagram of the HTM code.

Table 3.5: Natural frequencies and damping ratio of the 4 DOF numerical system estimated by HTM.

Mode #	f_n [Hz]	ζ_n [%]
1	5.00	0.83
2	6.92	1.23
3	12.80	0.93
4	20.00	0.85

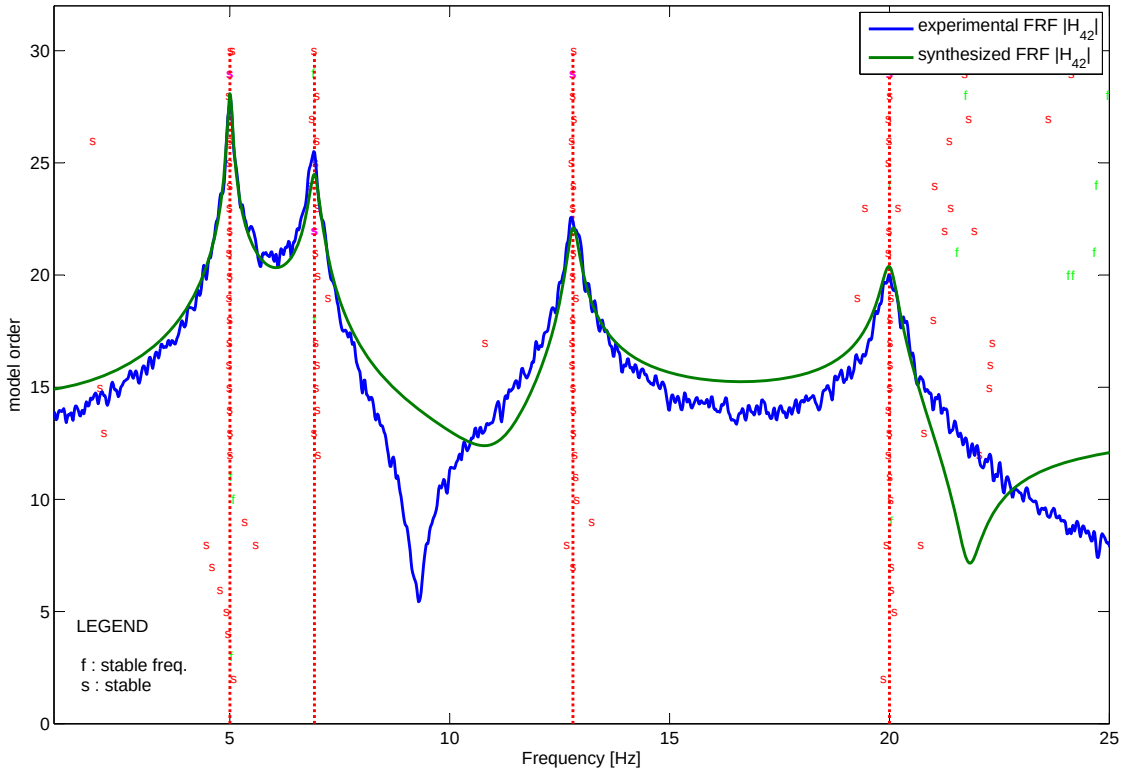

Figure 3.12: HTM estimate algorithm - stabilization diagram of the system's poles and synthesis of the FRF with the residual estimate process.

3.4 Modified Hilbert Transform Method

The previous excitation loading is enriched by adding a sinusoidal signal, with a proper amplitude, pulsating at 6.64, 9.96 and $13.28\,\mathrm{Hz}$, respectively to simulate the $2/\mathrm{rev}$, $3/\mathrm{rev}$, $4/\mathrm{rev}$ forcing frequencies of a structure rotating at nominal angular speed equal to $3.32\,\mathrm{Hz}$. As a consequence, the resulting dynamic signature of the system is modified. The presence of the operational spikes in correspondence of the three frequencies characterizing the harmonic excitations could be easily found from the "skewed" frequency response function depicted in Fig.3.13.

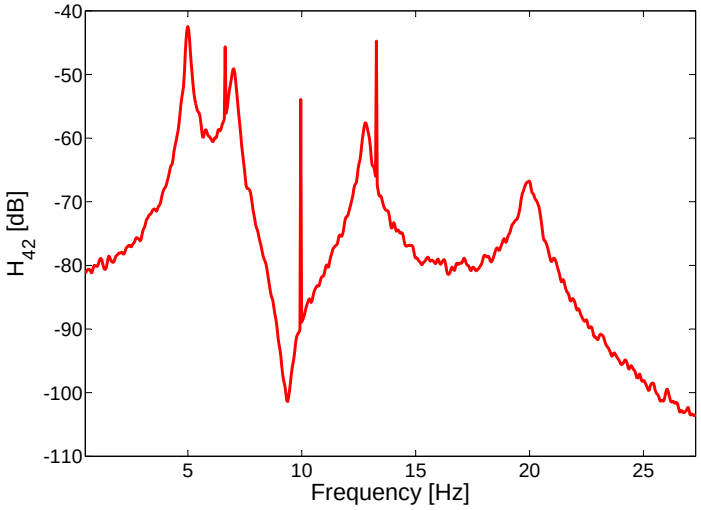

Figure 3.13: Estimate of the skewed frequency response function in the case of harmonic excitations blended with the white noise loading.

3.4.1 Identification of the harmonic loading

The capabilities of the Entropy index to identify such operational frequencies are then investigated. The non-gaussianity test is carried out on the output responses. A narrow-band filter is introduced in the time domain in order to find those frequencies to which the signals have an operational nature, that is they could not be considered as typical gaussian responses. Therefore, for all frequencies available in the test a Butterworth filtering is carried out, Ref.[48]. Then, the Entropy statistical index is calculated for each

of the running frequencies. The presence of harmonic excitations in the output signals is clearly exploited from the several minima reported in Figs.3.14 and 3.15, where the Entropy index is plotted as a function of the frequency for different widths and orders of the Butterworth filter. The sensitivity of the local

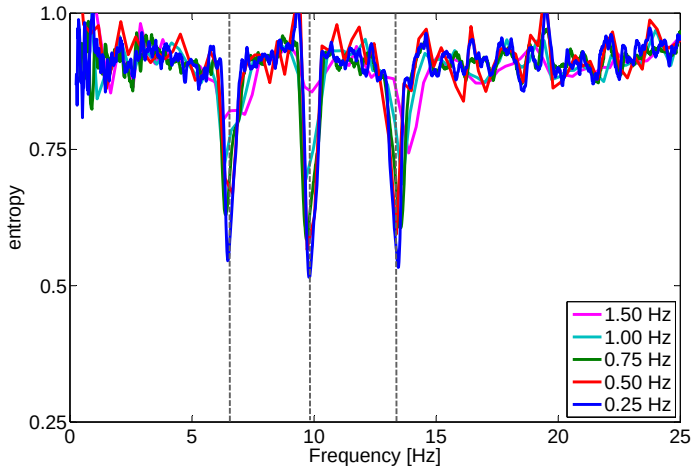

Figure 3.14: Lumped parameter system - Effects of the width of 6th order Butterworth filter in the harmonic identification by the entropy approach.

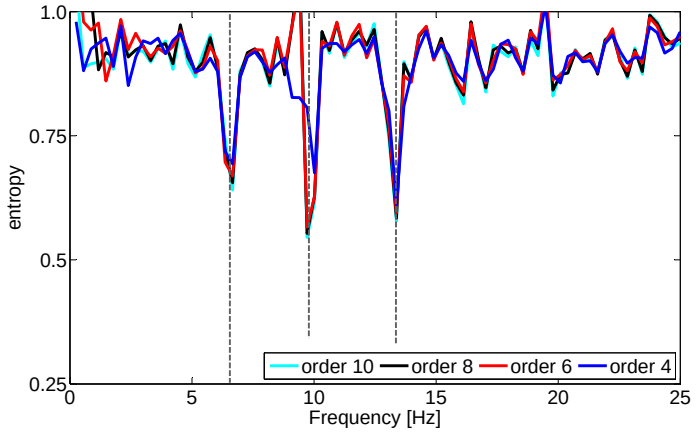

Figure 3.15: Lumped parameter system - Effects of the order of the Butterworth filter, frequency width $= 0.50\ Hz$, in the harmonic identification by the entropy approach.

minima to the width of the Butterworth filter becomes negligible as it reduces to values less than $0.5\,\mathrm{Hz}$. Concerning the effects of the order of the filter, it is shown a practical exact identification of the operational

frequencies from filter order equal or above 6. In order to validate the use of the Entropy statistical index for the identification of the harmonic components, the same signal analysis is carried out using the Kurtosis index. Both the effects of the frequency width and the order of the filter are analyzed. As reported in Figs.3.16 and 3.17, the behavior of such harmonic loading identification is similar to the previous one. Nevertheless, it seems that the Entropy index is more robust because it does not require a prescribed value for the harmonic identification, but only the minimum condition, as in case of the Kurtosis index, in which γ^* should reach the value of -1.5 when approaching the frequency of a harmonic component.

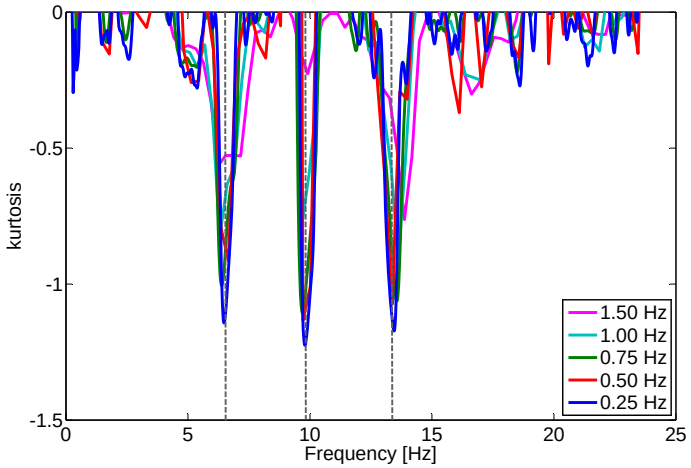

Figure 3.16: Lumped parameter system - Effects of the width of 6th order Butterworth filter in the harmonic identification by the Kurtosis approach.

3.4.2 Harmonic removal

Once the operational frequencies have been correctly identified by the proposed Entropy index, the possibility to estimate the biased frequency response functions from the skewed ones is further investigated. It is worth noting these biased FRFs do not suffer from the presence of the operational spikes, and, therefore, they are named "harmonic-free" FRFs. The accuracy of the proposed harmonic removal is shown in Fig.3.18 and Fig.3.19, where the comparison between the different estimates of the frequency response functions is depicted. The estimate of the biased $\overset{\oslash}{H}_{42}(f)$ is practically coincident with the reference biased $\tilde{H}_{42}$, as in

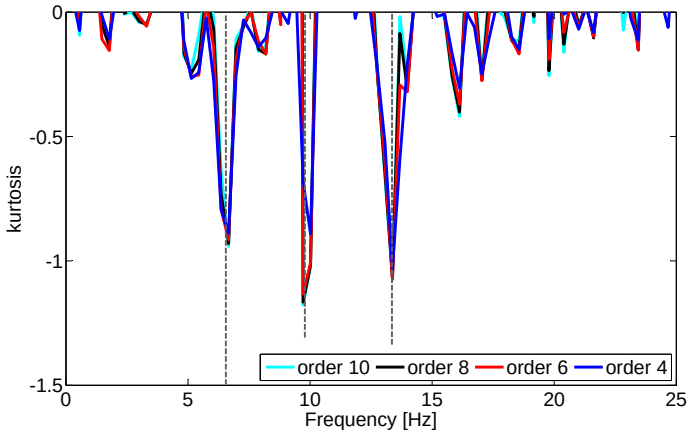

Figure 3.17: Lumped parameter system - Effects of the order of the Butterworth filter, frequency width $0.50\,\mathrm{Hz}$, in the harmonic identification by the Kurtosis approach.

Fig.3.13, here not reported for clearness of the pictures. Finally, the effects of the harmonic removal in

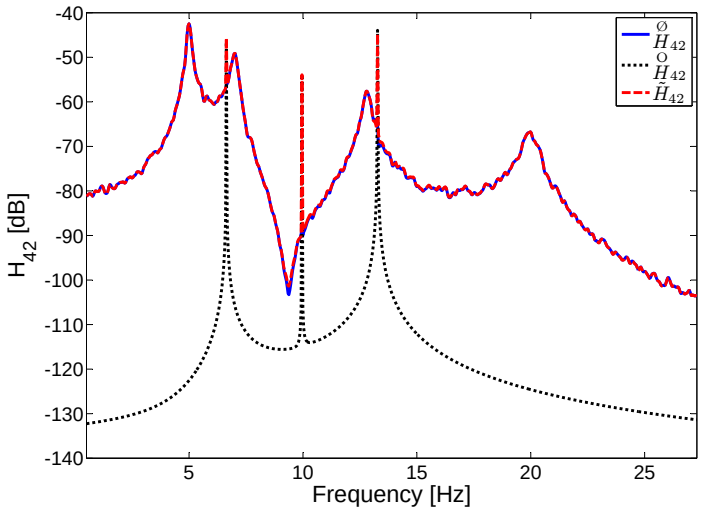

Figure 3.18: Effect of the harmonic removal from the skewed FRF.

the modal parameter estimates are analyzed. For this investigation, different operational frequencies are considered in order to assess the accuracy of the method as the operational frequency get closer to one of the natural frequencies. As expected, the estimate of the natural frequencies is not impaired by the presence of the harmonic excitation, provided they are different. On the other hand, a sensitivity of the

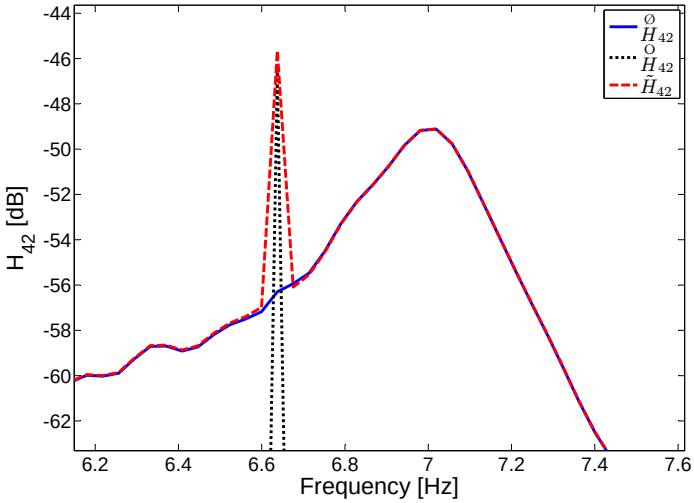

Figure 3.19: Effect of the harmonic removal from the skewed FRF, detailed view around the second mode.

Table 3.6: Lumped parameter system - Sensitivity of the damping ratio estimates to frequency of the harmonic loading. Estimates from the skewed FRF $\tilde{}$; from harmonic-free FRF $\oslash$.

Ω_{op}/Ω_n	$\Delta\tilde{\zeta}_n$ [%]	$\Delta\overset{\oslash}{\zeta}_n$ [%]
0.95	1	1
0.96	7	1
0.97	23	2
0.98	53	3
0.99	80	10
1.00	100	N.A.

damping ratio to the operating conditions is found out. For each condition, identified by the ratio between the operational frequency and the natural frequency of interest, Ω_{op}/Ω_n, the error in the damping ratio estimate from the reference, numerically set to the value $1.5\,\%$, is reported in Tab.3.6. The estimates have been carried out considering both the skewed FRF, $\Delta\tilde{\zeta}_n$, and the harmonic-free FRF, $\Delta\overset{\oslash}{\zeta}_n$. When the operational frequency is far enough from the natural frequency of the system, about $5\,\%$ in the presented numerical test case having mode shapes well separated, it seems there are no significant influences on the modal parameter estimate by the presence of the spike in the frequency response function. As the operational frequency get closer to the natural frequency, the estimate of the damping ratio could be substantially wrong, more than $80\,\%$. On the contrary, the same damping ratio estimate performed on the

harmnonic-free FRF, results practically insensitive to the presence of the spike induced by the operational working condition. Indeed, the last column of Tab.3.6 is characterized by very low values of errors. Finally, the occurrence of an operational frequency coincident with the natural frequency results in the inability to estimate the damping ratio. Considering the skewed FRF, the resulting damping ratio has an immaterial value due to the operational condition; of course there is no pole to estimate when considering the harmonic-free FRF due to its removal by the proposed procedure.

3.5 Modal Mass estimates

In this section, the effectiveness of the considered approaches to properly scale the mode shapes in operational modal analysis is evaluated by considering the model described in Ref.[1]. A 5-DOF lumped parameter system, with unitary masses, constant stiffness equal to 100 (in some consistent set of measurement unit) and with a damping ratio of $1\,\%$, equal for each mode, is considered. The reference natural frequencies for this system are reported in Tab.3.7. In order to simulate the effects of the incompleteness

Table 3.7: Experimental natural frequencies for the 5 DOF numerical system.

Mode #	f_n [Hz]
1	0.45
2	1.32
3	2.08
4	2.68
5	3.05

in both the available degrees of freedom and in the mode set (as in the experimental conditions) several combinations of such parameters have been considered. In the following numerical analyses only the first and the fifth degree of freedom and only the modes 1, 2, 3, and 5 are retained. It is worth noting that, for this simple numerical example, the modal masses estimated by the considered scaling procedures are practically coincident with the theoretical ones when modifying the structure in each of the 5 DOF and considering the complete mode set. The effects of the different modal mass estimates are evaluated in terms of the correlation between the resulting frequency response functions that could be synthesized

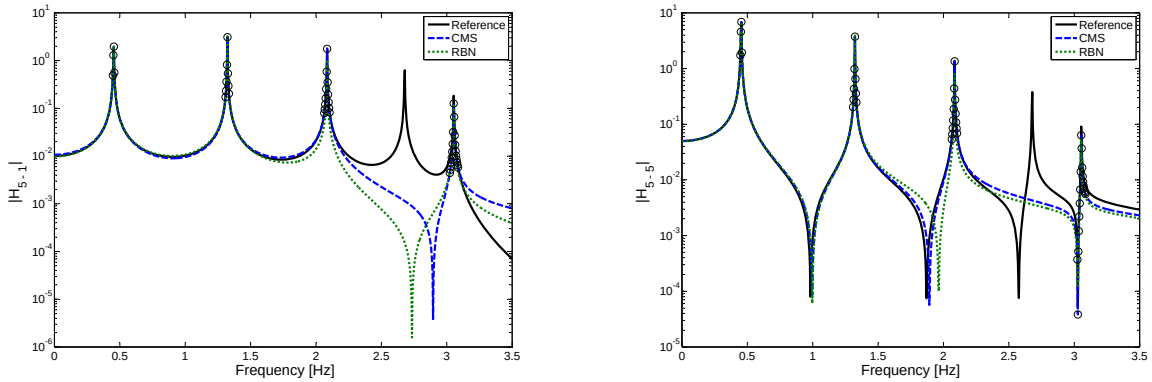

(a) H_{51} (b) H_{55}

Figure 3.20: Comparison between the FRF estimates with uniform perturbation mass of 10% of the system's mass.

by the knowledge of all the modal parameters. Following Ref.[34], this correlation is expressed in terms of the normalized complex product of the synthesized, from the Output-Only analysis (H_{CMS} or H_{RBN} where CMS refers to the constant mode shape method, whereas RBN refers to the receptance-based mass normalization method), and the measured, from the traditional Input/Output analysis (H_{IO}), frequency response functions:

$$\chi = \text{correlation} = \frac{\left|\sum_{i=1}^{N_f} H_{OO}(\omega_i) H_{IO}^*(\omega_i)\right|^2}{\left(\sum_{i=1}^{N_f} H_{OO}(\omega_i) H_{OO}^*(\omega_i)\right)\left(\sum_{i=1}^{N_f} H_{IO}(\omega_i) H_{IO}^*(\omega_i)\right)} \tag{3.1}$$

where the superscript * indicates the complex conjugate and N_f is the number of spectral lines available from the test. For the sake of brevity, only two representative cases are here reported. The first one considers a perturbation of the mass by 0.25 (consistent unit), occurring in each of the available degrees of freedom, that is DOF 1 and 5 for a total of a $10\,\%$ mass variation of the system. Then, the modal masses are evaluated by using both considered mass perturbation approaches. The resulting FRFs synthesized by the full modal model just estimated are compared with the reference ones in Figs.3.20.

As one can see, the accuracy of both approaches in estimating the frequency response functions using an incomplete modal data is excellent. Nevertheless, the CMS approach seems slightly more accurate with respect to the RBN, as reported in Table 3.8, where the average correlations, evaluated around the

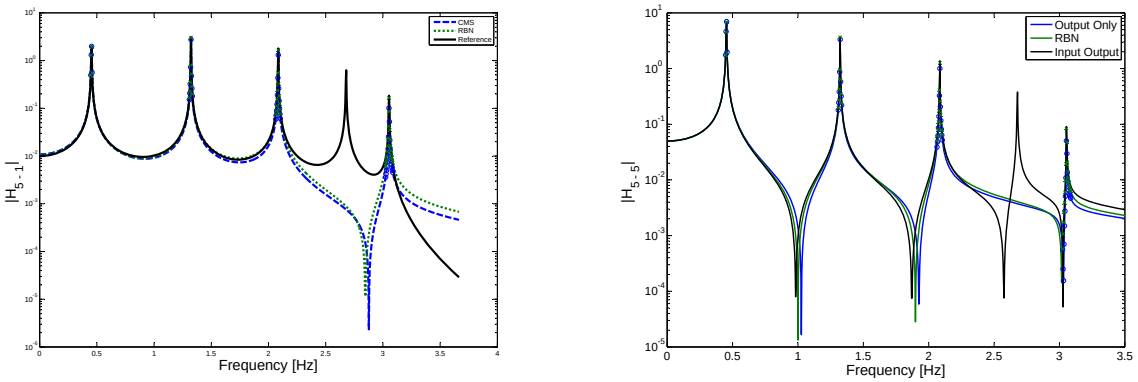

(a) H_{51} (b) H_{55}

Figure 3.21: Comparison between the FRF estimates with localized perturbation mass of 10% of the system's mass.

resonance are reported. The frequency points around the natural frequencies used to compute the average correlations are depicted with circles, in each of the considered FRFs, whereas in Eq.(3.1) the H_{IO} is equal to the reference FRF. This behaviour is probably due to the numerical approximation induced by the RBN approach, which required the solution of a least-square scheme. Indeed, the accuracy of the least square solution is affected by the lack of information due to the missing mode shape. On the contrary, the CMS method is insensitive to the completeness of the modal basis, used in the scaling process as it operates considering each mode individually.

Table 3.8: Accuracy of the scaling methods - Uniform perturbation mass.

Method	Correlation [%]		
	H_{11}	H_{51}	H_{55}
CMS	99.89	99.97	99.99
RBN	92.91	96.61	99.53

In the last numerical case, the mass perturbation is represented by the same $10\,\%$ mass change as the previous case, but this time a lumped mass of 0.5 (consistent unit) is added only to the 5th degree of freedom. As in the previous case, the overall accuracy in the estimate of the modal masses, and, in turn, the frequency response function estimates, are in excellent agreement, see Figs.3.21.

When the correlation analysis between the FRFs is performed, a slight reduction in the accuracy of

the CMS method is found. As reported in Table 3.9, the effects of the changes of the mode shapes, as a consequence of a localized mass perturbation imposed to the system, on the identification of the modal masses result in a reduction of less than $2\,\%$ in the average correlation between the synthesized FRFs. This could viewed as the limiting factor in the CMS scaling method due to the violation of the hypothesis of the insensitivity of the mode shapes to the mass perturbation.

Table 3.9: Accuracy of the scaling methods - Localized perturbation mass.

Method	Correlation [%]		
	H_{11}	H_{51}	H_{55}
CMS	98.81	98.74	99.54
RBN	99.91	99.90	99.97

Chapter 4

Ground Vibration Tests

The Operational Modal Analysis methodologies described in Chapter 2 are validated against the Experimental Modal Analysis approach as described in Sec.1.4, by performing Ground Vibration Tests on a life-expired Lynx Mk7 airframe at the Bristol Laboratory for Advanced Dynamics Engineering (BLADE) at the University of Bristol. These tests give the possibility to assess the methodologies described in this thesis with respect to the industrial standard on a real scale one structure. Moreover, the novel methodology developed to deal with harmonic components embedded in the stochastic white noise excitation has been validated by simulating in the laboratory the sine excitation as superimposed to the random broadband loading.

4.1 Experimental Setup

The structure under investigation is a life-expired Lynx Mk7 (XZ649) airframe, which is represented in Fig.4.1. It was previously used at QinetiQ as a dynamic test structure, and later transfered to the Bristol Laboratory for Advanced Dynamics Engineering, BLADE, at the University of Bristol. Results from a shake test campaign on this specific helicopter can be also found in Ref.[52]. The same airframe was also used as main test structure for the earlier GARTEUR AG14 programme whose primary aim was to explore methods and procedures for improving finite element models of helicopter type structures through the use of error

Figure 4.1: The Lynx Mark 7.

location, model updating and dynamic testing, as reported in Ref.[53]. The aircraft configuration under examination consists of the bare baseline airframe with engines and gearboxes removed. Moreover, in order to simplify the structure to a fundamental built state and to minimize any rattles that might impair the quality of the dynamic measurements, the majority of the original non-structural components and materials such as seats and avionics have been removed. In contrast to the configuration used in Ref.[53], the skids are not removed from the airframe in the present test and the boundary conditions are provided by placing the entire structure on a set of 6 deflated inner tubes (3 for each skid as in Fig.4.2), rather than suspension by bungees. This boundary configuration can be considered acceptable, the main purpose of this test being to make an EMA-to-OMA correlation rather than the validation of a finite element model against the experiments. Each skid is connected to the main cabin by means of a single hinge on the front section, while a leaf-spring suspension directly connects the two skids to the bottom of the rear cabin.

LMS SCADAS III hardware system was employed as the signal analysis tool unit with a total of 32 channels available. The airframe was spatially-discretized in 14 geometrical points, giving the wireframe shown in Fig.4.3. Each point carries the lateral and vertical (Y and Z respectively) degrees of freedom,

Figure 4.2: Boundary condition on the airframe: deflated inner tubes were used to simulate free-free condition.

for a total of 28 output (response) channels. Given the limited number of channels available, no fore-aft direction measurement were included in the acquisition. Acceleration responses at these 28 locations were recorded using PCB-ICP transducers characterized by an average $100\,\mathrm{mV/g}$ sensitivity. This specific configuration is the outcome of a pretest analysis based mainly on engineering judgement which was aimed at capturing the lowest most significant global modes of the airframe. In the Input/Output experimental modal analysis (EMA) the airframe was excited by means of two model v406 electrodynamic LDS shakers acting simultaneously. One shaker (identified by SN) was placed at the lower-port-side of the cockpit-nose junction, in order to provide loading along the vertical direction. The second shaker (ST), which excites the latter direction, was placed at the tailboom-fin junction, as shown in Fig.4.4. Special care was paid to ensure that the two sources of excitation, acting simultaneously on the system, remain uncorrelated around the resonances where structure-shaker coupling-interaction may become more evident. This Multiple-Input Multiple-Output (MIMO) configuration chosen to carry out the EMA analysis not only gives the airframe a properly space distributed input energy, but it is more likely to be the case during operational conditions, where the structure is generally exposed to both spatial and temporal stochastic loading environments (e.g. aerodynamic turbulence). In order to ensure minimum leakage error effects, a burst-random signal was

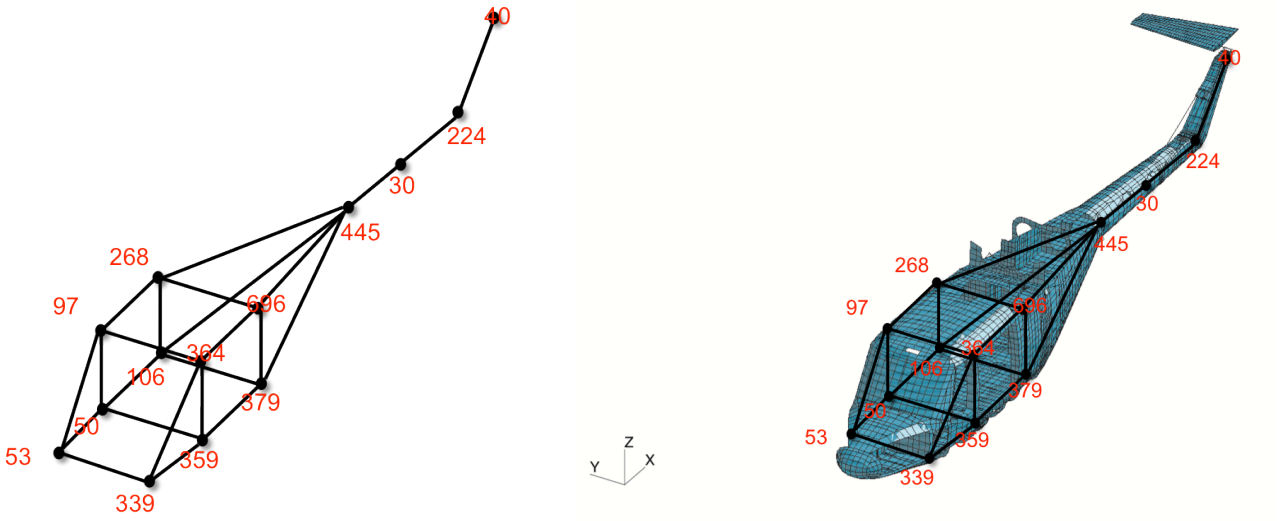

Figure 4.3: The grid of points used as spatial discretization.

chosen as the excitation input. Several loading configurations were considered to investigate the linearity of the behavior of the vibrating structure with respect to the input excitation and the reciprocity properties, Ref.[13]. Finally, the insertion error due to the shaker-stinger-structure interaction has been evaluated. The level of burst-random excitation loading, which represents the percentage of the observation time in where the random signal is active and after which the input signal is equal to zero, has been carefully selected to ensure that the responses will die away completely in the time window where the input is not active anymore. When performing an Output-Only modal analysis, the time responses due to a multiple random excitation environment (SN and ST shakers active), were collected for an estimation of the modal parameters using the operational modal analysis techniques. The responses were collected by performing two averages in the time domain, in order to reduce the presence of noise in the data. A summary of the main acquisition parameters used in the experimental investigation, both in the EMA and OMA analysis, is reported in Tab.4.1.

Furthermore, an inertial shaker is added inside the cockpit, as shown in Fig.4.5, to provide a harmonic excitation at fixed frequencies with different amplitudes, in order to investigate the effectiveness of the modified operational modal analysis methods. The performed experimental investigations considered several

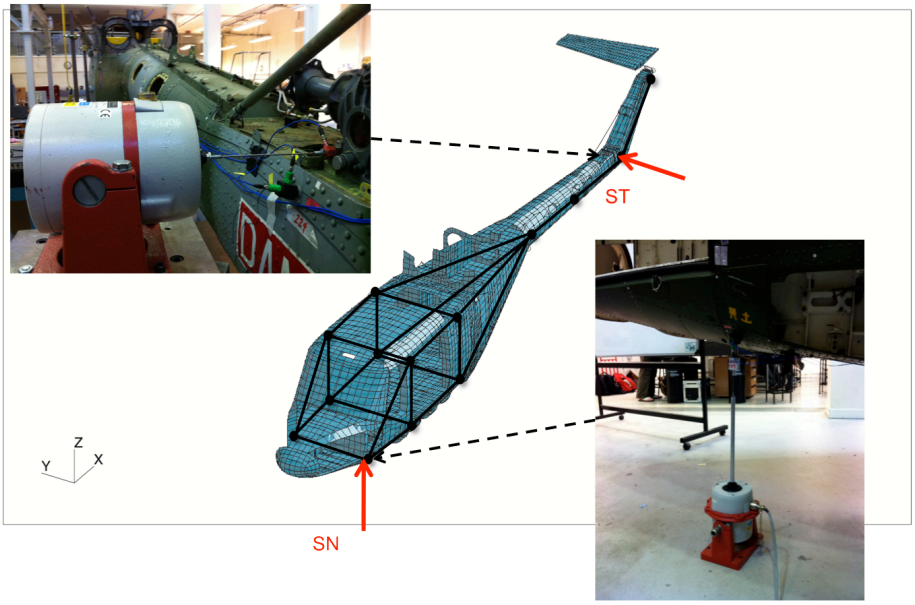

Figure 4.4: Scheme of shaker positions used on the airframe.

Table 4.1: Main parameters for Input/Ouput and Output-Only tests.

Parameter	EMA	OMA
Input signal	Burst Random 90%	Random
Input levels [V]	3	vary
Sample frequency [Hz]	128	128
Spectral lines	4096	16384
Observation time [s]	64	256
Window	Uniform	-
Averages	10	2
Estimator	Hv	-

amplitude of the harmonic (sine) excitation in order to evaluate the limits of the OMA methods to deal with harmonic excitations blended with the broad band random loading. For this purpose a sine-to-random ratio (SRR) dimensionless parameter is introduced to characterize the excitation provided to the helicopter structure. This parameter takes into account both the input energy provided as sinusoidal excitation by the inertial shaker and the random input energy from the nose and tail shakers. Such excitation energy levels are taken proportional to the measured root mean square value (σ) of the force signals recorded by the load cells placed in correspondence of the shakers. Denoting with σ_I the root mean square value of the sine excitation from the inertial shaker, and with σ_T and σ_N the root mean square value of the tail

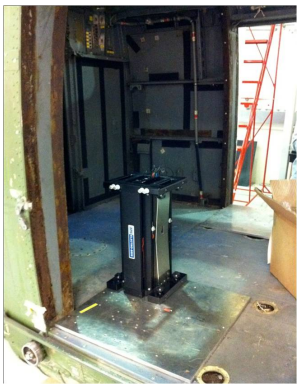

Figure 4.5: Positioning of the inertial shaker providing the harmonic excitation on the Lynx Mk7 airframe.

Table 4.2: Sine to random ratio (SSR) values .

SRR [N/N]	Nose Shaker σ_N [N]	Tail Shaker σ_T [N]	Inertial Shaker σ_I [N]
0.50	10	10	10
1.75	10	10	35
3.50	5	5	35
5.83	3	3	35
17.50	1	1	35

and the nose shaker respectively, the SRR index is given by:

$$SRR = \frac{\sigma_I}{\sigma_T + \sigma_N} \tag{4.1}$$

Several sine-to-random ratio (SRR) values are considered in order to investigate the effects of different sine excitation levels vibrating at $11\,\mathrm{Hz}$, see Tab.4.2. Then, six more tests are performed by tuning the frequency of the harmonic excitation closer and closer to the natural frequency corresponding to the second vertical mode of the structure $(23.0\,\mathrm{Hz})$. In this case only two SSRs values are considered, *i.e.*, 1.75 and 3.5, for each sine signal at $22.0\,\mathrm{Hz}$, $22.9\,\mathrm{Hz}$ and $23.12\,\mathrm{Hz}$.

4.2 Preliminary Tests

A major concern in shake test experimentation is to ensure the linearity of the system response with respect to the input amplitude level. As a general criterion, it is assumed that the level of the random signal should guarantee the responses to be an order of magnitude higher than the prevailing noise level. A linearity check can be performed later by doubling the level of the first guessed excitation level. No remarkable difference should be found when comparing the FRFs derived from different input levels. As depicted in Fig.4.6, where the FRFs corresponding to the output responses at node 30 in direction Y and Z, when exciting with the horizontal and vertical shakers, no remarkable difference in the estimates is reported for different excitation levels (represented with the two different values of the amplifier gain equal to $1\,\mathrm{V}$ and $3\,\mathrm{V}$). Also, the reciprocity properties of the whole system under investigation seem to be consistent, as shown in Fig.4.7, where a comparison between corresponding FRFs are depicted. In order to investigate the occurrence of possible inconsistencies, due to the shaker-stinger-structure interaction, a first test was run having one shaker active, while the other was attached but inactive, whereas in the second test the inactive shaker was completely detached from the structure. Cross-checks between different experiments have been performed for different point FRFs, to explore such effects. As shown in Fig.4.8, very little interaction between the structure and the excitation system is identified at frequencies above $25\,\mathrm{Hz}$. Indeed, the FRFs are practically superimposed both in the lateral and in the vertical directions, regardless the activated shaker.

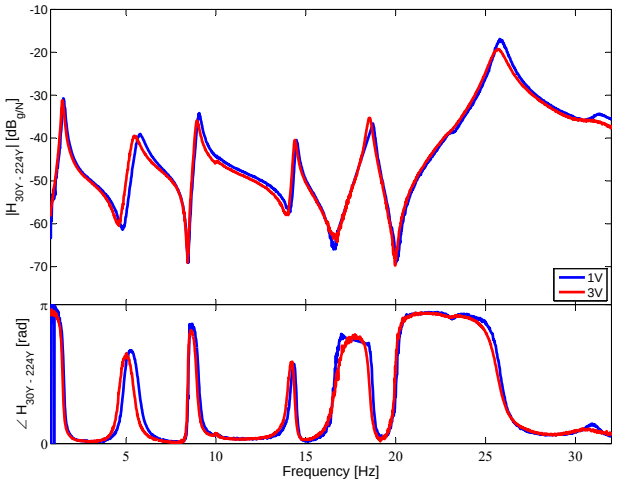

(a) Y direction

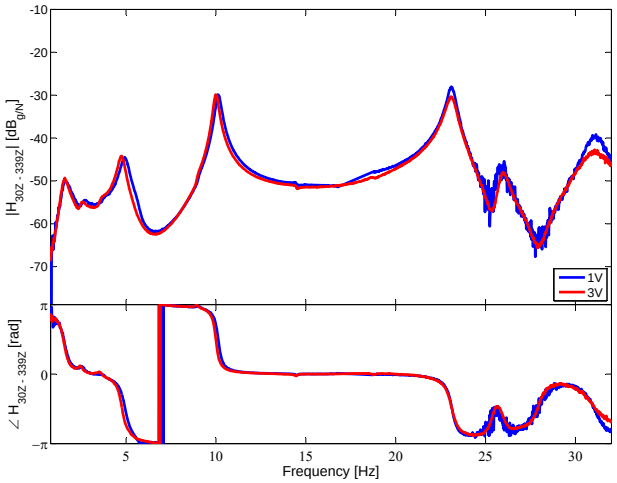

(b) Z direction

Figure 4.6: Linearity check using two different amplifier gain, denoted as 1V and 3V: FRF of a point on the tail boom.

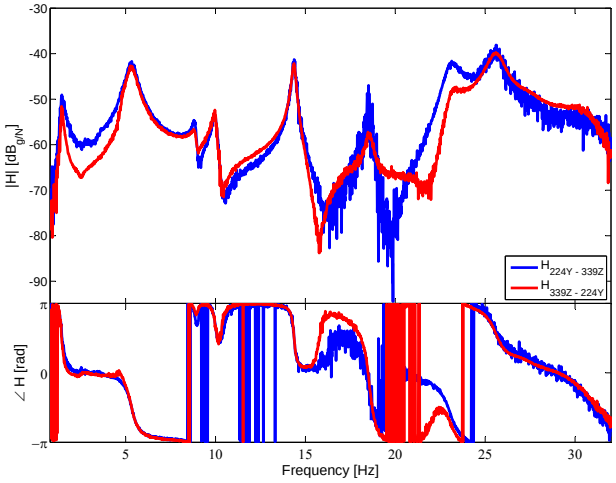

Figure 4.7: Reciprocity check.

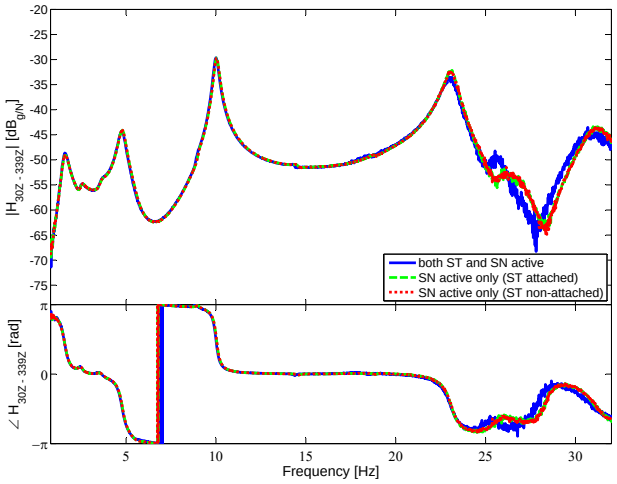

(a) Y direction

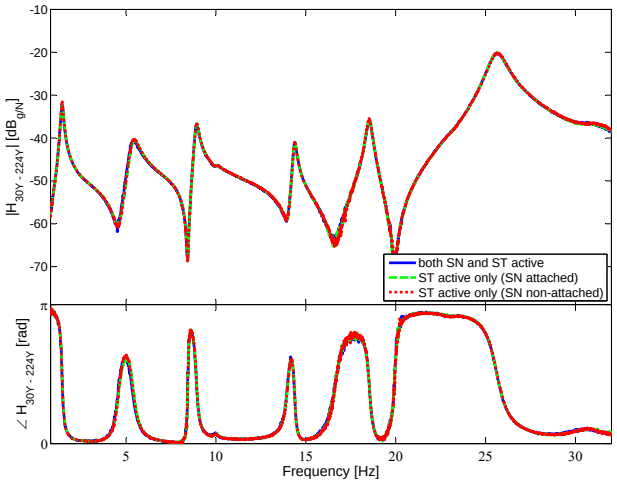

(b) Z direction

Figure 4.8: Insertion errors activating and attaching the shakers independently.

4.3 Experimental Modal Analysis Estimates

Experimental modal analysis was performed by exciting the structure with both the nose (SN) and the tail (ST) shakers, setting the amplifier level to the value of $3\,\mathrm{V}$, whereas all the other acquisition parameters are reported in Tab.4.1. Because each experimental point measured the acceleration in the lateral (Y) and in the vertical (Z) directions, a total number of $2 \times 28 = 56$ FRFs were obtained and used for the identification of the modal parameters. Using the LMS-PolyMax analysis method, 9 mode shapes were identified in the frequency band $[0 - 35]$ Hz, as reported in Tab.4.3. Specifically, two main "rigid-body"

Table 4.3: Natural frequencies, damping ratios and mode shape descriptions estimated with EMA approach.

Mode #	f_n [Hz]	ζ_n [%]	Description
1	4.8	4.6	Rigid mode vertical
2	5.4	5.0	Rigid mode roll
3	8.9	1.4	1st lateral bending
4	10.0	1.4	1st vertical bending
5	14.4	0.7	Fuselage rigid roll mode, tail boom bending
6	18.5	0.9	2nd lateral bending
7	23.0	1.8	2nd vertical bending
8	25.7	2.0	Tail boom lateral bending
9	30.6	3.6	3rd vertical bending

mode shapes were identified, at natural frequencies of 4.8 and $5.4\,\mathrm{Hz}$. These modes represent the rigid vertical plunging and rotation about the longitudinal axis, respectively, due to the coupling of the airframe structure with the inner tubes used as device to obtain the boundary condition of a quasi-free-free structure, see Figs.4.9 and 4.10. The values for such natural frequencies are quite close to the first global elastic mode shape of the structure with a natural frequency of approximately $9\,\mathrm{Hz}$, which means that the inner tubes were stiffer than had been intended and so do not provide an ideal representation of the desired free-free boundary condition. Suspending the structure by means of bungees would be a better solution and it is recommended to do this for future tests. Nevertheless, it is stressed that the final aim is to cross-correlate two sets of experiments, rather than to validate a specific finite element model for which

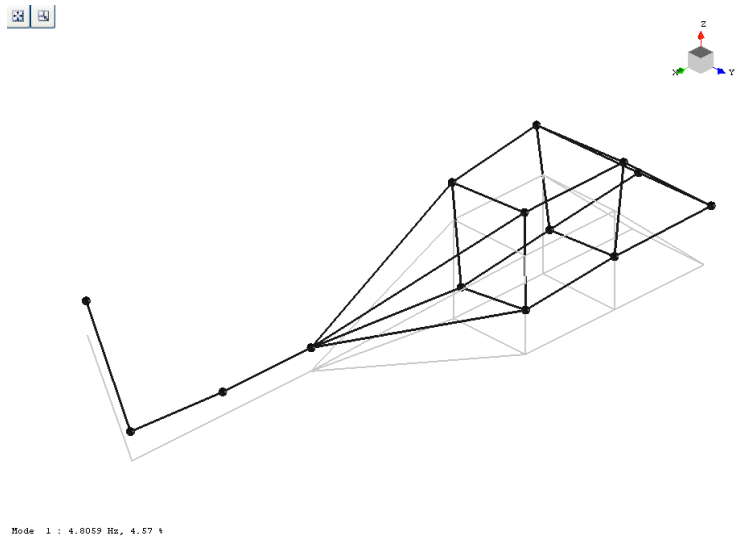

Figure 4.9: Vertical rigid mode shape due to inner tubes at $f_n = 4.8\,\mathrm{Hz}$.

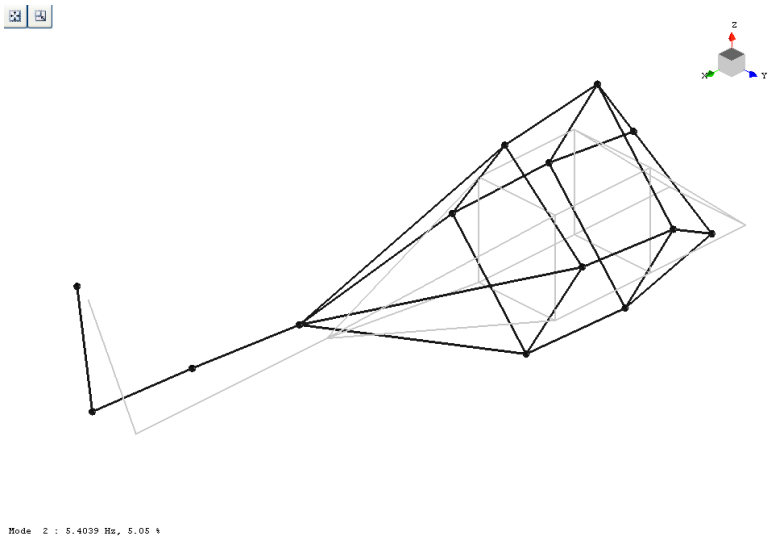

Figure 4.10: Roll rigid mode shape due to inner tubes at $f_n = 5.4\,\mathrm{Hz}$.

the choice of the boundary conditions are much more critical. In addition to the expected lateral and vertical bending modes, and the clearly identified 3rd vertical mode (at $30.6\,\mathrm{Hz}$), two more modes were identified with natural frequencies of 14.4 and $25.7\,\mathrm{Hz}$ respectively that were not predicted by independent numerical analysis. The first of these two modes, shown in Fig.4.11, exhibits a rigid rotation of the main cabin about the longitudinal axis, coupled with an elastic lateral bending motion of the tail boom. This particular motion is likely to be caused by the skids-fuselage interaction. The second mode, having a natural

frequency of $25.7\,\mathrm{Hz}$, appears to be mainly a tail boom lateral bending, which involves also a combination of the 2nd lateral-and-vertical-bending fuselage mode shapes, Fig.4.12. Finally, the consistency of the

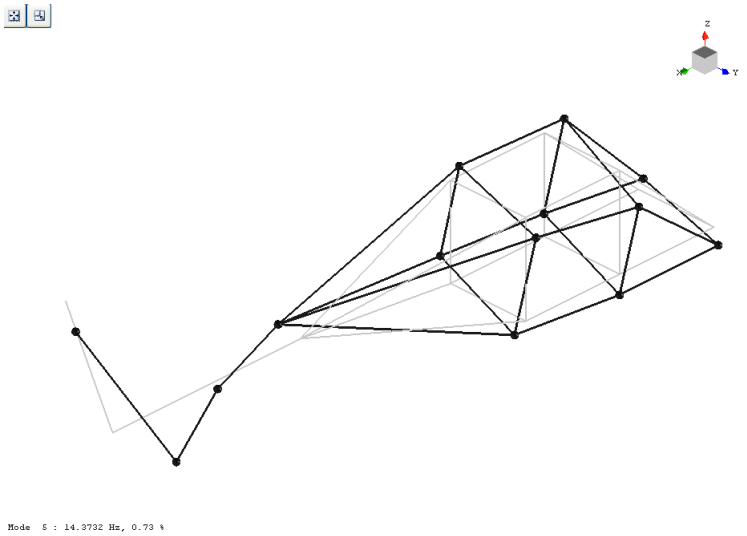

Figure 4.11: Coupling of the fuselage rigid roll with the tail boom mode due to the skids at $14.4\,\mathrm{Hz}$.

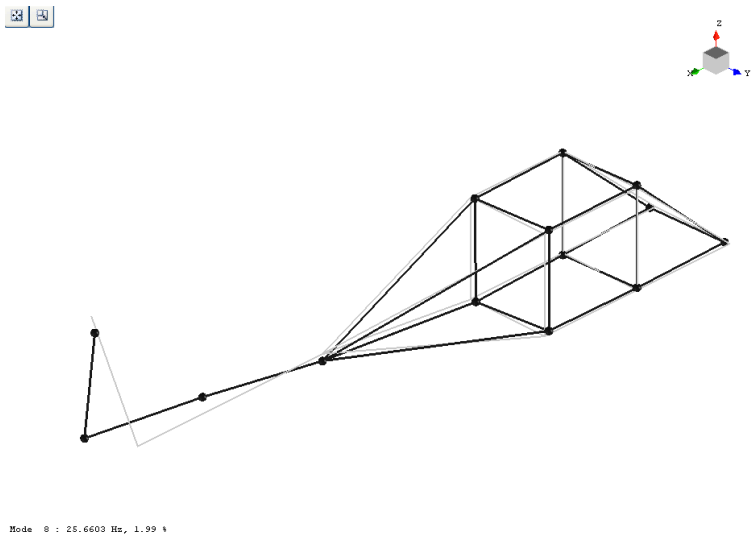

Figure 4.12: Coupling of the fuselage rigid roll with the tail boom mode due to the skids at $25.7\,\mathrm{Hz}$.

modal database identified in this EMA analysis, given by evaluating the orthogonality properties of the identified mode shapes, is presented in Fig.4.13 where the Auto Modal Assurance Criterion, AutoMAC, matrix is shown. As can be seen, the AutoMAC values are practically zero except for the diagonal elements (which should be 1.00). Thus, a weak spatial aliasing is detected, requiring then to increase the number

of the measurement points if a more accurate identification of higher order modes is required.

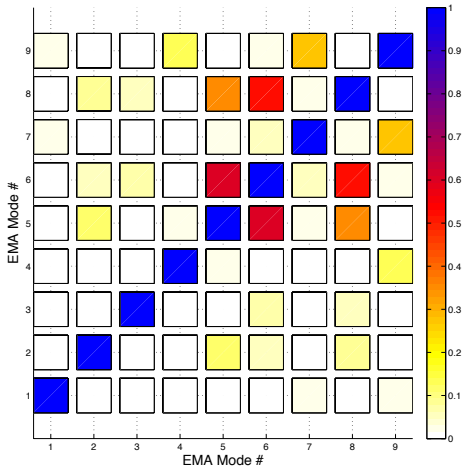

Figure 4.13: Orthogonality check with auto-MAC matrix in the EMA analysis.

4.4 Operational Modal Analysis Estimates

In this section, the estimates obtained by applying the previously-described OMA techniques to the data gathered by engaging both the nose and the tail shakers, are directly compared with the EMA findings shown previously. Both EMA and OMA tests correspond to an amplifier gain setting to 3V. The outcome of this computation is summarized in Tabs.4.4, 4.5, and 4.6. The first two tables report the estimates of the natural frequencies and damping ratios, whereas in Tab.4.6 the orthogonality of the estimated mode shape with respect to the corresponding modes identified in the EMA analysis, is reported in terms of the Modal Assurance Criterion (MAC) value. Both the natural frequencies and the damping ratios, identified by the different estimation techniques, are in very good agreement with the corresponding modal parameters evaluated with the EMA techniques. This good agreement is shown in Tab.4.7, where the average errors, defined as $\varepsilon_{f_n} = \frac{f_n^{EMA} - f_n^{OMA}}{f_n^{EMA}}$ and $\varepsilon_{\zeta_n} = \frac{\zeta_n^{EMA} - \zeta_n^{OMA}}{\zeta_n^{EMA}}$ for the natural frequencies and damping ratios respectively, are more than acceptable except for those referring to the rigid body modes. The correlation between all the modes identified by the Balance Realization OMA technique (BR-SSI), for example, with the ones from the EMA technique is given in Fig.4.14, where a qualitative indication of the good level of correlation achieved is shown. Furthermore, a qualitative comparison between the mode shapes is also

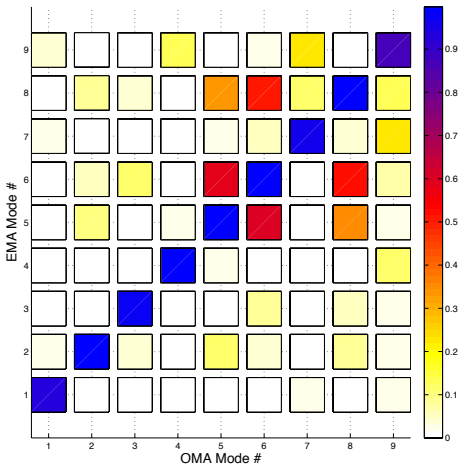

Figure 4.14: Orthogonality check with MAC matrix between the EMA and OMA experimental analysis.

Table 4.4: Comparison between the natural frequency estimates.

	f_n [Hz]				
Mode #	EMA	FDD	f-SSI	HTM	BR-SSI
1	4.8	4.6	4.7	5.0	4.9
2	5.4	5.6	5.6	5.4	5.5
3	8.9	9.0	9.0	9.0	8.9
4	10.0	10.1	10.0	10.0	10.0
5	14.4	14.4	14.4	14.4	14,4
6	18.5	18.5	18.4	18.5	18.6
7	23.0	23.1	23.0	23.1	23.1
8	25.7	25.8	25.5	25.7	25.7
9	30.6	30.5	30.6	30.6	31.1

Table 4.5: Comparison between the damping ratio estimates.

	ζ_n [%]				
Mode #	EMA	FDD	f-SSI	HTM	BR-SSI
1	4.6	2.5	3.1	2.3	5.42
2	5.0	3.8	5.1	2.9	5.98
3	1.4	1.2	1.0	1.8	1.46
4	1.4	1.4	1.2	1.8	1.49
5	0.7	0.9	0.6	0.8	1.05
6	0.9	0.9	1.0	0.9	1.31
7	1.8	1.1	1.4	1.5	1.66
8	2.0	2.8	1.8	2.3	3.01
9	3.6	1.7	2.1	2.9	2.86

Table 4.6: Comparison between the MAC values.

	MAC wrt EMA			
Mode #	FDD	f-SSI	HTM	BR-SSI
1	0.90	0.92	0.90	0.93
2	0.92	0.90	0.93	0.99
3	0.94	0.95	0.97	0.97
4	0.99	1.00	0.99	1.00
5	0.99	0.99	0.98	1.00
6	0.99	0.95	0.98	1.00
7	0.89	0.91	0.97	0.96
8	1.00	0.98	1.00	1.00
9	0.85	0.89	0.89	0.86

Table 4.7: Relative error between the natural frequencies and damping ratios across several estimation techniques.

Mode #	FDD		f-SSI		HTM		BR-SSI	
	ε_{f_n} [%]	ε_{ζ_n} [%]	ε_{f_n} [%]	ε_{ζ_n} [%]	ε_{f_n} [%]	ε_{ζ_n} [%]	ε_{f_n} [%]	ε_{ζ_n} [%]
1	5.0	45.7	1.2	32.6	4.2	50.0	2.0	17.9
2	2.8	24.0	4.1	2.3	0.0	42.0	2.5	19.7
3	0.6	14.3	0.6	32.1	1.1	28.6	0.3	4.6
4	0.9	0.0	0.4	10.8	0.0	28.6	0.5	6.6
5	0.1	23.1	0.3	14.3	0.0	14.3	0.0	49.8
6	0.2	5.3	0.6	13.0	0.0	0.0	0.3	45.4
7	0.5	38.9	0.1	21.9	0.4	16.7	0.3	7.6
8	0.3	38.2	0.8	8.0	0.0	15.0	0.2	50.5
9	0.3	52.8	0.0	41.7	0.0	19.4	1.5	20.6

given in Figs.4.15 to 4.19. In order to assess the distance between the EMA and the OMA experimental

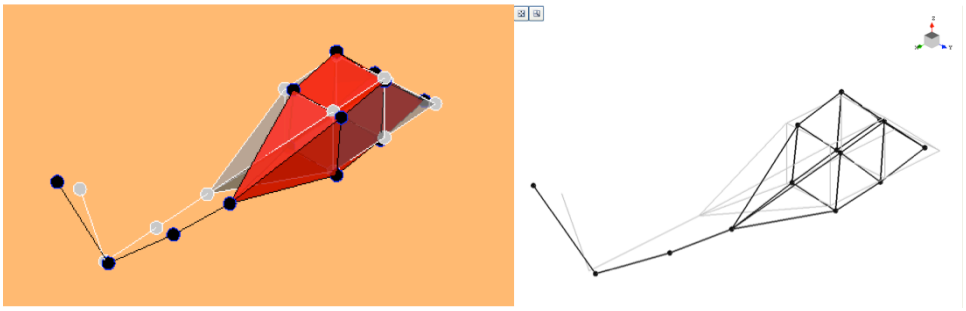

Figure 4.15: Comparison between OMA (left) and EMA (right) modes shape for 1st vertical bending.

models, an accuracy index is used, defined as:

$$\text{Accuracy Index} = \frac{|| \varepsilon ||_2}{N_m}$$

in which N_m is the number of the identified normal modes and $|| \varepsilon ||_2$ is the Euclidean norm of the relative error between the actual OMA and reference EMA for both the natural frequency and the damping ratio of each mode, as reported in Tab.4.7. This index gives a measure of the accuracy of each OMA method with respect to the EMA approach, such that lower values means an agreement between the two methods. These values are summarized in Figs.4.20(a) and 4.20(b), where the accuracy indices are reported as red bars and blue bars for the frequency-domain and the time-domain OMA approaches, respectively. As

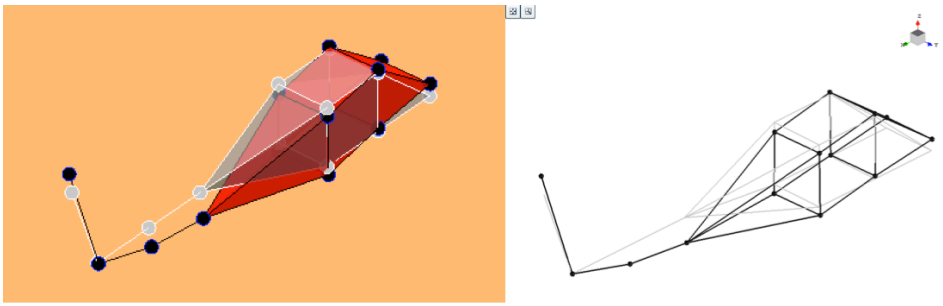

Figure 4.16: Comparison between OMA (left) and EMA (right) modes shape for 1st lateral bending.

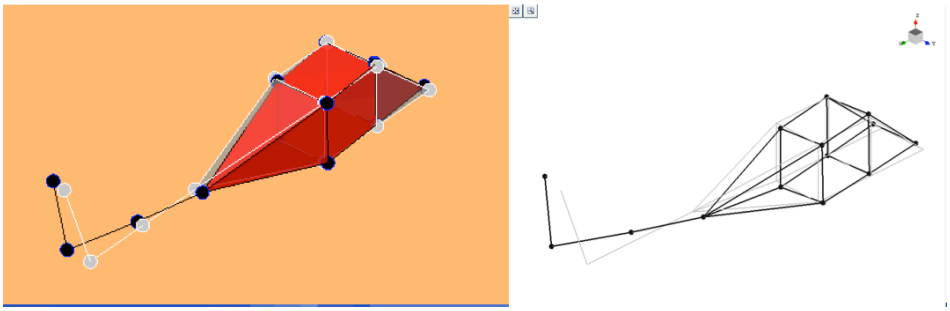

Figure 4.17: Comparison between OMA (left) and EMA (right) modes shape for 2nd vertical bending.

expected, the natural frequencies estimated by the OMA techniques are closer to the EMA estimates than the damping ratios. Specifically, the maximum discrepancy for the natural frequencies is of 0.65, which is one order of magnitude lower then that dealing with the damping ratios. Although the approaches in time- and frequency-domains behave similarly, it seems that BR-SSI (time-domain) and HTM (frequency-domain) approaches are characterised by the highest accuracy for the natural frequency estimates. The excitation corresponding to the operating flight condition could not be reproduced in the laboratory, so in order to assess the reliability of the OMA methodologies to deal with data recorded during flight tests, similar experimental analyses have been performed by varying the input level provided by the shakers. The loading conditions do not seem to influence the OMA modal parameter estimates, as long as the excitation is white noise and the system is linear. Indeed, as depicted in the Figs.4.21 and 4.22, the FRFs evaluated by the Hilbert Transform Method do not change their shape with respect to the input level, and the only appreciable variation is the scale factor due to the primary limitation of the OMA - that is, its inability

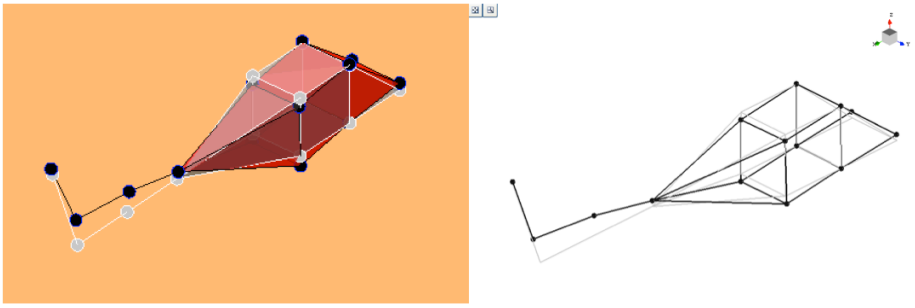

Figure 4.18: Comparison between OMA (left) and EMA (right) modes shape for 2nd lateral bending.

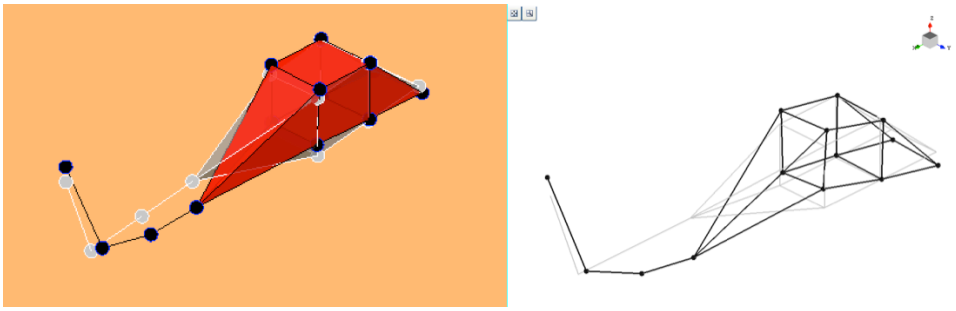

Figure 4.19: Comparison between OMA (left) and EMA (right) modes shape for 3rd vertical bending.

to evaluate the load participation factors. It is also remarkable that these analyses are able to highlight the presence of a little interaction between the shaker and the structure above the $25\,\mathrm{Hz}$, as shown in the preliminary test section by comparing the FRFs coming from EMA analyses.

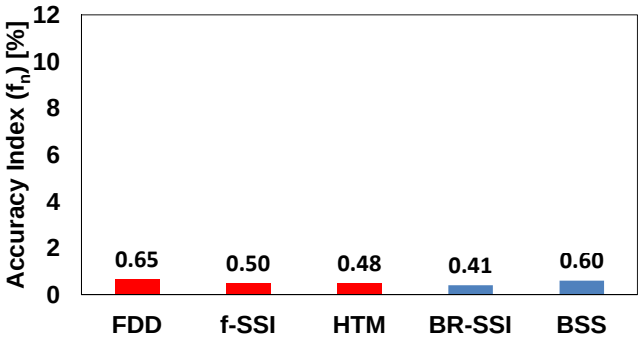

(a) natural frequencies

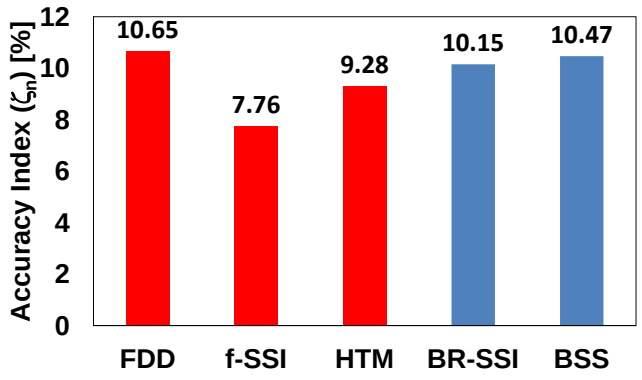

(b) damping ratios

Figure 4.20: Accuracy index - Frequency domain approaches (red bars), time domain approaches (blue bars).

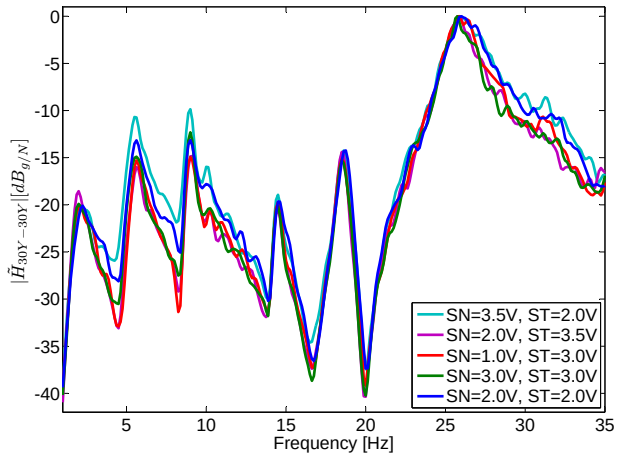

Figure 4.21: Bias frequency response function of a point on the tail boom in Y direction evaluated by the Hilbert Transform Method for different loading conditions.

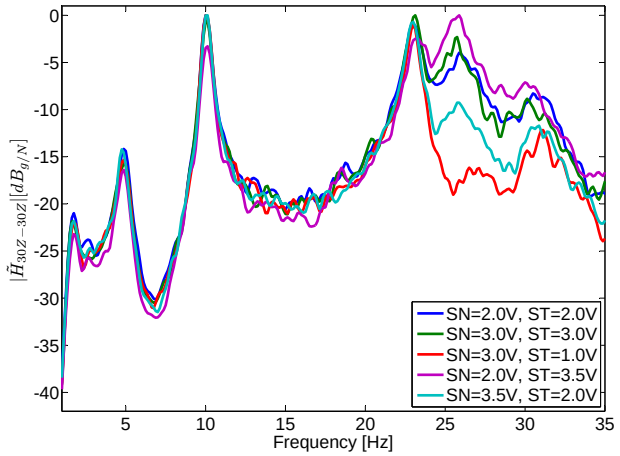

Figure 4.22: Bias frequency response function of a point on the tail boom in Z direction evaluated by the Hilbert Transform Method for different loading conditions.

4.5 OMA Methods in the Presence of Harmonic Loading

In this section, the accuracy of the OMA methods in the estimate of the modal parameters when using sine corrupted output data (as described in Sec.4.1) is investigated. At first the identification of the frequencies, at which the harmonic loading is acting, is performed with the the proposed entropy method, then the removal of their effects on the system's responses is implemented in order to evaluate the modal parameters comparable with the ones gained in the previous sections 4.3 and 4.4. Moreover, several combination of the methodologies, considered the actual state of the art, were considered and summarized as follows :

NF: Non-filtered time-histories are analysed with a traditional OMA technique (BR-SSI).

TSA: Time Synchronous Averaging Filtering Technique is implemented according to Ref.[54] and [55] in order to filter the time-histories to analyse with a traditional OMA technique (here represented by BR-SSI).

ERAH: The extension of the eigensystem realisation algorithm to the case of harmonic excitation (ERAH) is implemented according to [56] and it is applied to the non-filtered time-histories.

HTM: Hilbert Transform Method as described in Sec.2.5.

4.5.1 Harmonic identification and removal

The capability to identify the harmonic contribution blended in a random noise response is here investigated considering the approaches presented in Sec.2.5.1. By applying the entropy approach, the frequencies of the harmonic excitation are evaluated. In Fig.4.23 the entropy index is plotted as a function of the frequency, for each of the considered SRR values, when the inertial shaker provides a sine excitation at $11\,\mathrm{Hz}$. For this analysis, a filter frequency width equal to $1.5\,\mathrm{Hz}$ and a filter order equal to 6 are chosen. A clear identification of the frequency of the sine excitation blended with the random loading signal is clearly

For the sake of clarity, the bold labels here defined will be used as default notation for any figures and tables in the following sections of this chapter.

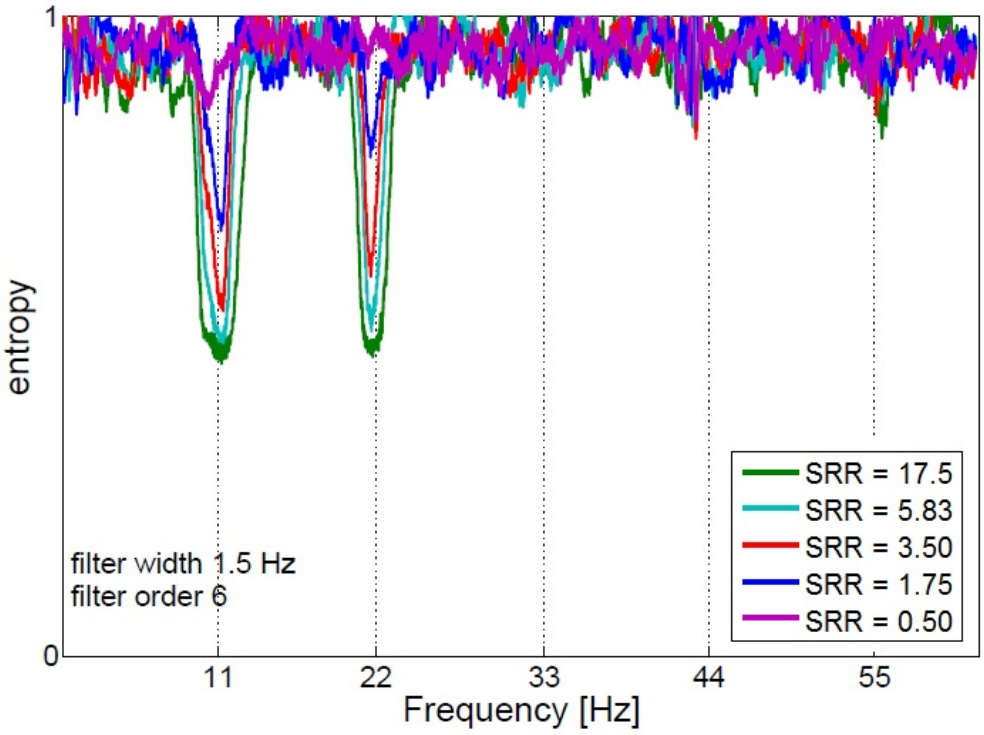

Figure 4.23: Entropy index for several Sine to Random Ratio values with $f_{sine} = 11\,\mathrm{Hz}$.

identified at $11\,\mathrm{Hz}$ corresponding to the local minima of the entropy index, regardless the considered values of the SRR. Moreover, it seems that also the $22\,\mathrm{Hz}$ harmonic excitation (multiple of the fundamental one) is characterizing the dynamic response of the airframe. Higher order harmonics are not identified probably due to the the low level of their amplitudes with respect to the random excitation. It could be noted that the lower SRR values, the lower the effects of the deterministic excitation on the responses. In fact, until the root mean square value of the harmonic force is higher then the others, two minima in Fig.4.23 can be easily distinguished at $11\,\mathrm{Hz}$ or $22\,\mathrm{Hz}$, but the last case (depicted in purple) where the presence of a weak harmonic excitation is barely identified only at $11\,\mathrm{Hz}$. The capabilities of the proposed entropy index to detect sine excitations close to a natural frequency is then investigated. The airframe structure is excited, in different runs, by the inertial shaker with a sine signal having the frequency of $22.00\,\mathrm{Hz}$, $22.90\,\mathrm{Hz}$ and $23.12\,\mathrm{Hz}$, respectively. As reported in Fig.4.24, the entropy index is capable to distinguish

the frequency of the sine excitation (marked in black) from the natural frequency (marked in red), even when such frequencies are very close. In Fig.4.24b and c the difference is less than $0.5\,\%$.

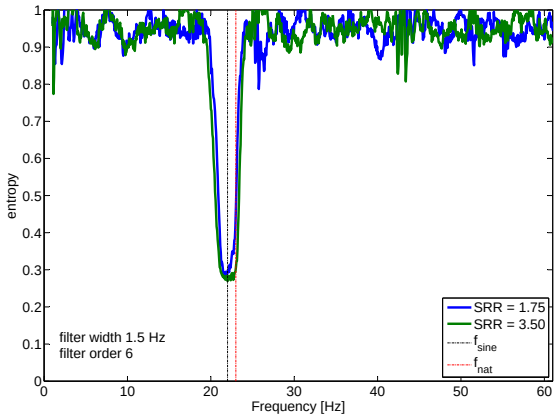

(a) $f_{sine} = 22.0\,\mathrm{Hz}$

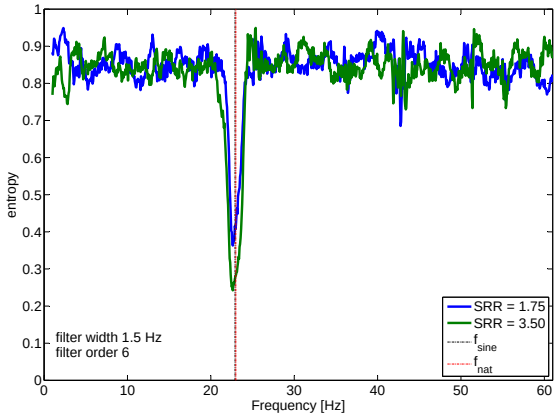

(b) $f_{sine} = 22.9\,\mathrm{Hz}$

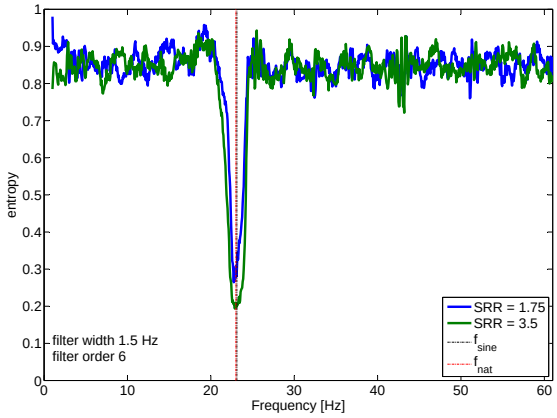

(c) $f_{sine} = 23.12\,\mathrm{Hz}$

Figure 4.24: Entropy index for several frequencies of the harmonic excitation.

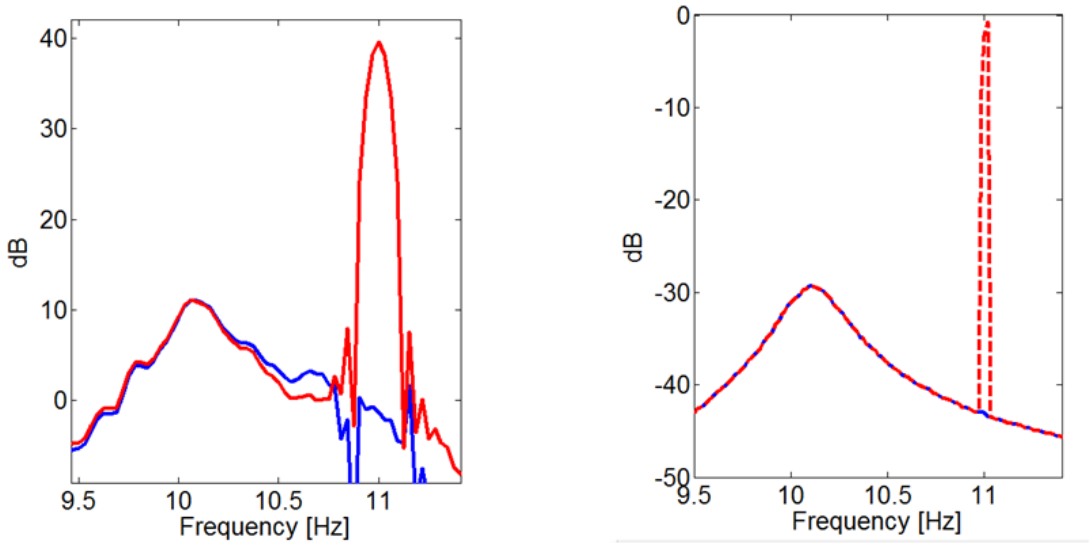

(a) OMA - HTM (b) EMA

Figure 4.25: Comparison between harmonic blended/harmonic free biased FRF in the Hilbert Transform Method, $f_{sine} = 11\,\mathrm{Hz}$.

Once the frequency of the sine excitation has been identified as in the previous section 4.5.1, its contribution is removed from the biased frequency response function, following the approach proposed in Sec.2.4. First, the effects of such harmonic removal process is reported in Fig.4.25, where a comparison between the (generical) bias FRFs blended with the harmonic excitation and the ones with such contribution removed is reported. For this case, the SRR value is equal to 1.75, whereas the harmonic excitation frequency is set equal to $11\,\mathrm{Hz}$. In the right-hand-side part of such a figure, it is shown that no remarkable differences are reported in the FRF obtained with the traditional EMA approach, except the presence of the harmonic peak corresponding to the external excitation. On the contrary, some differences in the FRFs are noticed in the operational modal analysis framework (left-hand-side part of the figure). These differences affect both the amplitude of the FRF in the neighborhood of the frequency of the harmonic excitation and (marginally) the FRF around the peak of resonance. Then, the modal parameters are derived in order to evaluate possible effects on the modal parameter estimates of the harmonic removal process. When considering the FRFs from the EMA investigation, in presence of the sine excitation at

11 Hz superimposed to the random broadband loading, the harmonic removal process does not change the FRF around the resonance peaks. This leads HTM to estimate (practically) the same modal parameters of Sec.4.4, with the same uncertainty level.

4.5.2 Estimate of the modal parameters

The effects of the harmonic component in the excitation on the modal parameters is investigated by increasing the SRR and changing the frequency, as described in Sec.4.1.

Sensitivity to the SRR on the estimates

Deriving the modal parameters using the output responses only, not only the effect of the harmonic excitation is reported, but also the sensitivity to the SRR is observed. In Fig.4.26 and 4.27 the natural frequencies, damping ratios, and the mode shapes, estimated by a standard OMA method from the harmonic blended data when SRR is set to 0.5, are compared with those corresponding to the case with SRR equal to 17.5. The differences in such modal parameters, especially the damping ratios, are practically acceptable

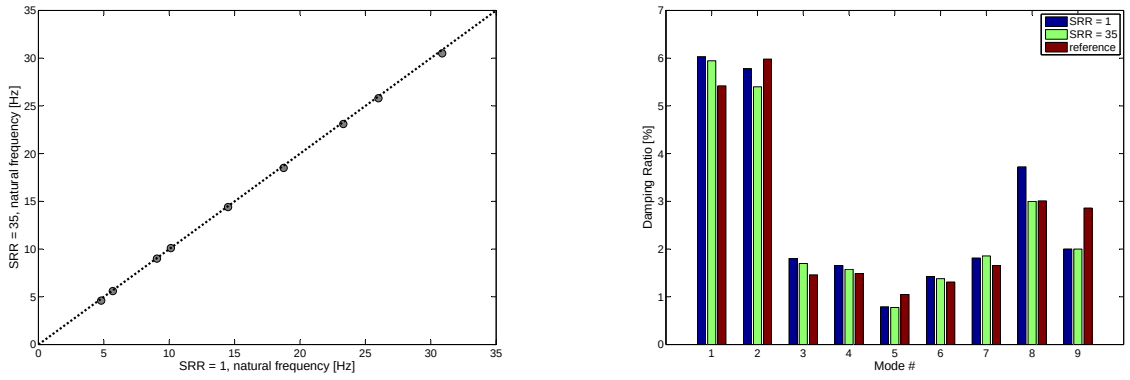

(a) natural frequency (b) damping ratio

Figure 4.26: Comparison between the natural frequency and the damping ratio estimates using the OMA method, corresponding to SRR = 0.50 and SRR = 17.50, $f_{sine} = 11\,\mathrm{Hz}$.

and they become negligible when considering the mode shapes, as reported in the MAC table of Fig.4.27 where the correlation between the two sets on mode shapes is shown. Nevertheless, it seems that the modes

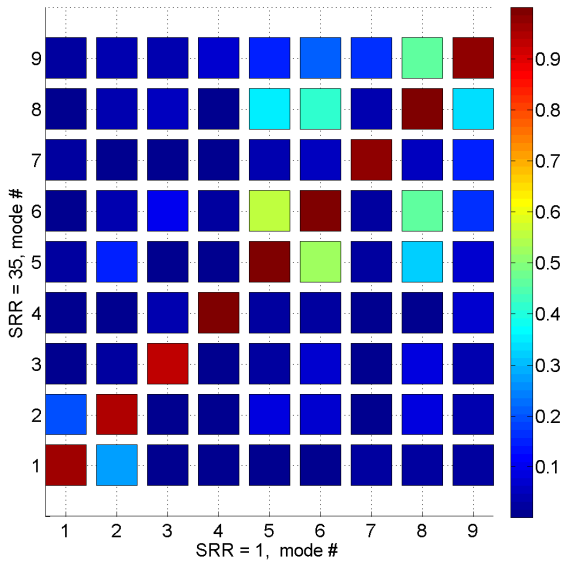

Figure 4.27: Comparison between the mode shape estimates using the ERA method, corresponding to SRR = 0.50 and SRR = 17.50, $f_{sine} = 11\,\mathrm{Hz}$.

more affected by the presence of the harmonic loading are the rigid ones. It is worthwhile to remark that the obtained estimates take advantages from the user expertise, who has to choose the modal parameters from the stabilization diagram, avoiding the so-called operational modes, as well as the numerical solutions corresponding to non-physical modes. This is the reason why the a-priory knowledge of the frequency of the harmonic excitation, as provided by applying the proposed entropy index methodology, is an important issue. A comparison between the stabilization diagrams evaluated with SRR values equal to 0.50 and 17.50 is provided in Fig.4.28, where both the structural, the operational and the spurious poles (depicted in yellow) are clearly mixed. In such a figure, the red circles correspond to those poles whose natural frequencies and damping ratios differ less than $0.5\,\%$ and $5\,\%$, respectively, and whose mode shapes does not change ($MAC \geq 0.9$), by increasing the model order. The green dots correspond to such poles that satisfy only two of the previous three comparison criteria.

A further investigation is carried out in order to evaluate the sensitivity of the considered estimating processes to the amplitude of the sine excitation. Among the several possibilities, the effects on the estimate

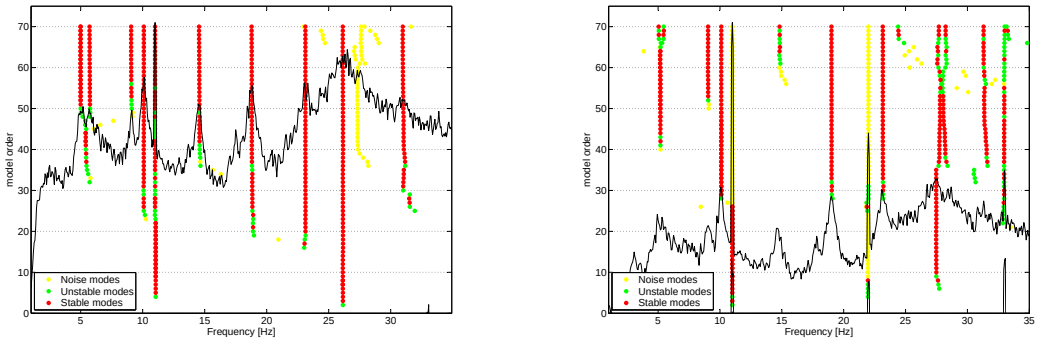

(a) SRR=0.5 (b) SRR=17.5

Figure 4.28: Comparison between the stabilization diagrams, in the BR-SSI Technique, $f_{sine} = 11\,\mathrm{Hz}$.

of the first vertical mode (whose natural frequency is estimated at about $10\,\mathrm{Hz}$) is considered. The response data are processed with all considered methodologies and compared with the modal parameters obtained from the traditional Input/Output experimental modal analysis considered, again, as references. From

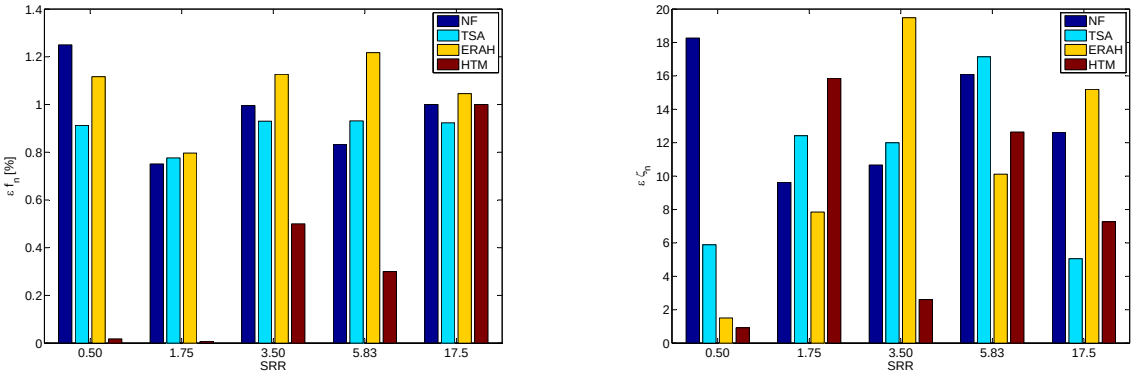

(a) natural frequency (b) damping ratio

Figure 4.29: Comparison between the natural frequency and damping ratio estimates corresponding to the 1st vertical mode at several SRRs with respect to the EMA estimates, $f_{sine} = 11\,\mathrm{Hz}$.

Fig.4.29a it is found out that an error not exceeding about $1.2\,\%$ is expected in the estimate of the natural frequencies, when not considering the effect of the harmonic loading. On the contrary, lower errors (in average) are evaluated when considering the presence of the harmonic excitation. Specifically, the ERAH approach shows higher relative errors for all the considered SRR values, whereas practical no errors are

found when considering the Hilbert Transform Method for all the SRR values, except for the higher one. Comparing the damping ratio estimates, reported in Fig.4.29b, an average error less than $20\,\%$ is obtained when the presence of the harmonic excitation is not considered. When the harmonic removal procedures are considered, the average error reduces to about $10\,\%$. Finally, from Fig.4.30, it seems that more than

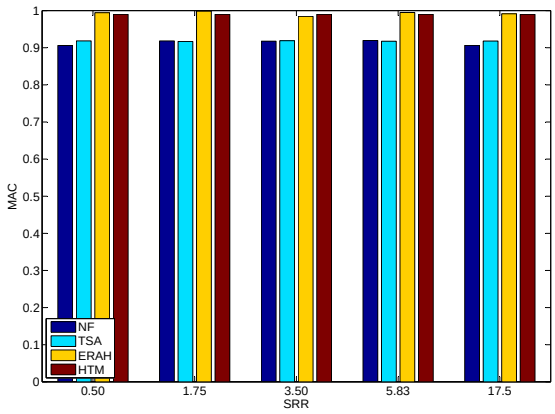

Figure 4.30: Comparison between the mode shape estimates corresponding to the 1st vertical mode at several SRRs with respect to the EMA estimates, $f_{sine} = 11\,\mathrm{Hz}$.

$90\,\%$ in the correlation between the mode shapes is achieved using the MAC value. It is shown that the ERAH and the HTM approaches give the same mode shape as the Input/Output-based estimating method.

Sensitivity to the closeness of the f_{OP} to the f_n

In this section the effects of the distance between the frequency of the harmonic excitation, f_{OP}, and the natural frequency, f_n, are reported. Among many available cases, the effects of the harmonic excitation close to the second vertical bending mode (whose reference natural frequency is $23\,\mathrm{Hz}$, from Tab.4.3) are reported. The analyses are carried out considering an operational frequency approaching the natural frequency from a distance of about $4\,\%$ and getting as close as $0.4\,\%$. Moreover, two SRRs values are considered, *i.e.*, 1.75 and 3.50 to better characterize the situation. Specifically it can be noted that when $f_{sine} = 22.00\,\mathrm{Hz}$, the errors are similar to those evaluated for $f_{sine} = 11.00\,\mathrm{Hz}$, for both considered SRR values. This means that no coupling between the excitation frequency and the system's pole is achieved.

Therefore, the OMA approaches could be applied without losing accuracy in the estimates, unless dealing with poles with very low damping ratios. Moreover, when the forcing frequency gets closer and closer to the natural frequency (no matter if approaching from lower or higher frequencies) the estimates will suffer of low accuracy, especially the damping ratios. As an example, see the values of the blue bars in Figs.4.31 and 4.32 for $f_{sine} = 22.90\,\mathrm{Hz}$ and $f_{sine} = 23.12\,\mathrm{Hz}$. Although a general improvement on such estimates is gained by applied the OMA methods, high values of the relative errors still characterize the ERAH estimates (depicted in yellow in the figures). On the other hand, very accurate estimates are achieved with HTM in evaluating the poles, but less reliability is verified in the mode shapes. The removal of the contribution of the operational FRF, from the biased FRF, allowed an estimate of the mode shape not so well correlated with the corresponding reference, yielding a MAC value about $70\,\%$, when the frequency of the harmonic excitation is practically superimposed to a resonant frequency (the frequency resolution of almost $0.06\,\mathrm{Hz}$).

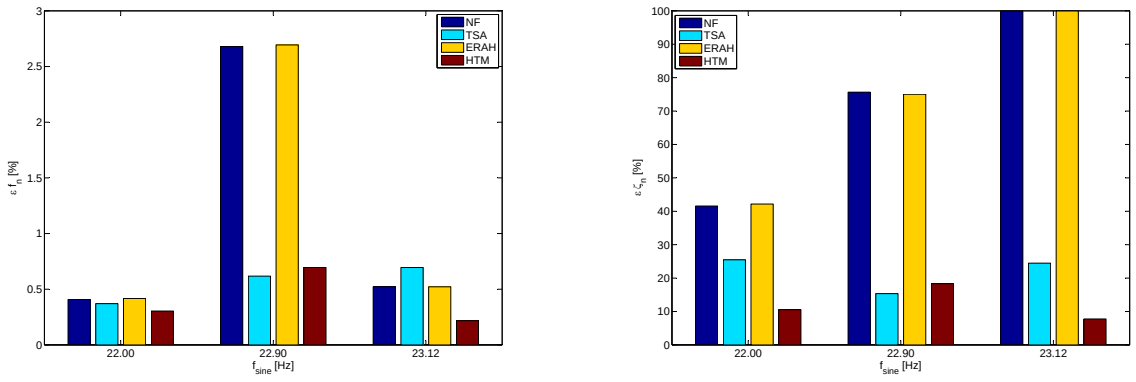

(a) natural frequency (b) damping ratio

Figure 4.31: Comparison between the natural frequency and damping ratio estimates corresponding to the 2nd vertical mode at several frequencies of the harmonic excitation with respect to the EMA estimates, $SRR = 1.75$.

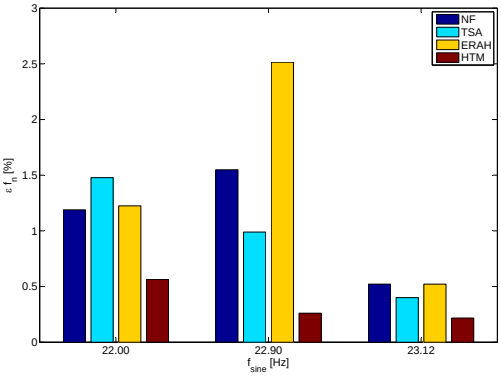

(a) natural frequency

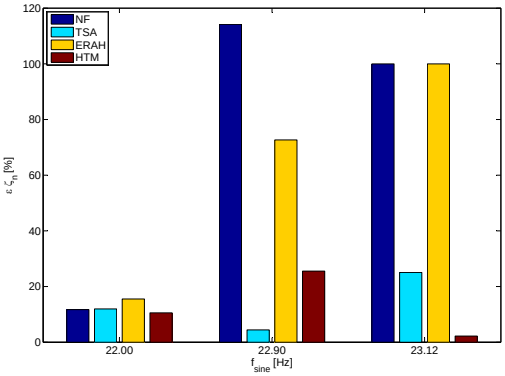

(b) damping ratio

Figure 4.32: Comparison between the natural frequency and damping ratio estimates corresponding to the 2nd vertical mode at several frequencies of the harmonic excitation with respect to the EMA estimates, $SRR = 3.50$.

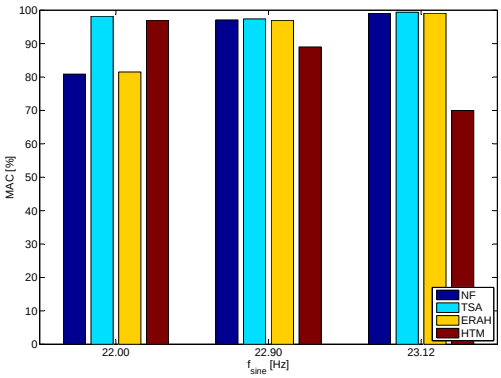

(a) SRR=1.75

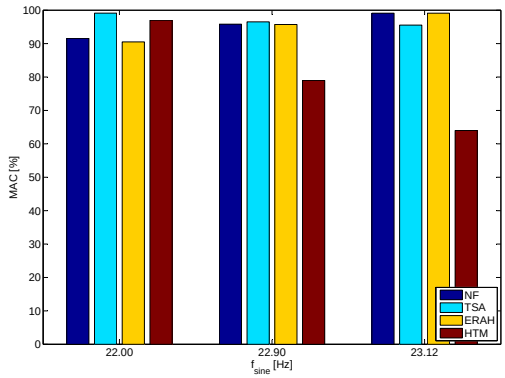

(b) SRR=3.5

Figure 4.33: Comparison between the mode shape estimates corresponding to the 2nd vertical mode at several frequencies of the harmonic excitation with respect to the EMA estimates.

Chapter 5

Whirl Tower Tests

As explained in Chapter 2 and numerically or experimentally shown in Chapters 3 and 4, the OMA methodologies have issues when dealing with structures operating with stochastic white noise loadings blended together with high amplitude, with respect to the variance of the random signal, harmonic excitations. A typical example, in the aerospace field, is the intrinsic periodic nature of the airloads acting on the rotor blade of a rotary wing aircraft. In this case, the identification of the modal parameters from the operational response could be skewed, especially the damping ratios, when a natural frequency of the structure is close to the harmonic excitation loading frequency. They could not be even estimated at all in the case of the operational and natural frequency concurrence. The improvement of OMA methods to accurately identify the modal parameters in such a frequency range, considered critical for the safe life of the structure, is therefore one of the main concern of researchers. The methodologies proposed in this thesis improve the Hilbert Transform Method to deal with such harmonic excitations. They allow the identification and the removal of harmonic excitation, acting together with a broad band stochastic loading, by statistically characterizing the output responses and improving the estimate of the FRF. This approach is applied to the data from the whirl tower experimental tests, carried out at German Aerospace Center, DLR, in Braunschweig. In these tests, the dynamic excitation of the rotating frame is provided by the perturbations

arising from the operating conditions characterized by both stochastic and harmonic contributions. It is worth remarking that the rotating speed of the system not only influences the frequencies of the harmonic input forces, but also the stiffness of the blade and, consequently, the natural frequencies of the structure. This simultaneous variation could result in a superimposition of structural and operational modes. Therefore, the identification of a rotating blade is performed by considering the so-called fan plot, that shows the natural frequencies of the blade as depending on the rotating speed, see Ref.[57]. It should be stressed that the experimental identification of the fan plot is a difficult problem to address because of the intrinsic dependance of the system spatial model parameters (in terms of the mass, damping and stiffness properties) to the operating parameters, such as the rotating speed. This is the reason why the OMA is able to fix this problem once the effects of the harmonic excitation can be evaluated and distinguished from the modal behaviour.

5.1 Test setup

The tests are carried out at the Whirl Tower Test facility of the German Aerospace Center, DLR located in Braunschweig, Germany. The test specimen consists of a rotor model blade installed on a test rig having a $30\,\mathrm{KW}$ DC shunt-wound motor and by a weight mounted on the opposite side of the rotating blade to balance the rotating system at different (clockwise) rotating speeds, Fig.5.1. The rotating blade is equipped with both strain gauges (14 full or half bridge channels) and accelerometers (2 ICP channels). The torsional deformation is recorded by two strain gauges, arranged on the opposite sides of the upper and lower blade shell in an angle of ± 45 degrees, located at 6 spanwise positions. Moreover, 3 sets of strain gages are added to record the flapwise bending deformation, Fig.5.2. The data transfer is achieved by a 24 slip rings and by a proper telemetry system. The experimental investigations have been carried out by varying the rotational speed of the system, Ω, in order to obtain the fan plots of the modal parameters of the structure. The reference value (due to the tower configuration) is $\Omega_0 = 1043\,\mathrm{RPM}$ and five speed

Figure 5.1: General view of the Whirl Tower test setup.

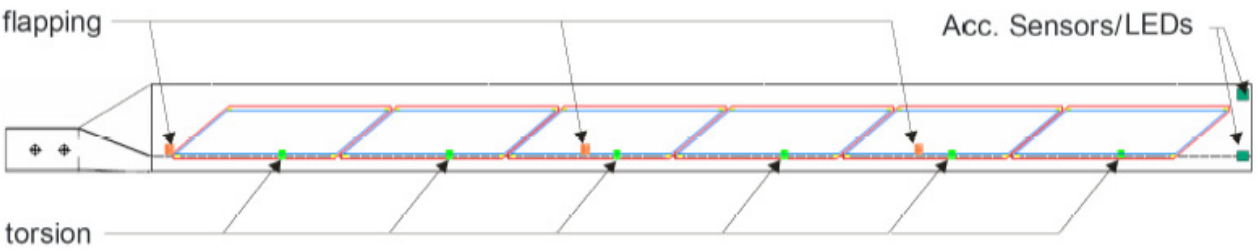

Figure 5.2: Sketch of the positions of the sensors.

ratios are considered: $\Omega/\Omega_0 = 0.00, 0.24, 0.48, 0.72, 1.00$.

5.2 Identification of the harmonic loadings

The first step of the approach requires the identification of possible harmonic loadings from the broad band white noise response characterizing the motion of the rotating blade. Therefore, the same non-gaussianity test, as described in the previous chapters for numerical and experimental tests, is performed on the output response signals (the total recording time was $80\,\mathrm{s}$). For all the frequencies, $f_j,\ j = 1, \cdots, N_f$, available in the test (being $N_f = 2^{14}$ the number of the available frequency lines), a Butterworth filtering has been carried out so that the Entropy statistical index could be calculated for each frequency f_j. From the several minima reported in Figs.5.3 and 5.4, where the Entropy index is depicted for different

widths and orders of the Butterworth filter respectively, it was possible to evaluate the frequencies of the harmonic excitation characterizing the working condition of the rotating blade. The sensitivity of the

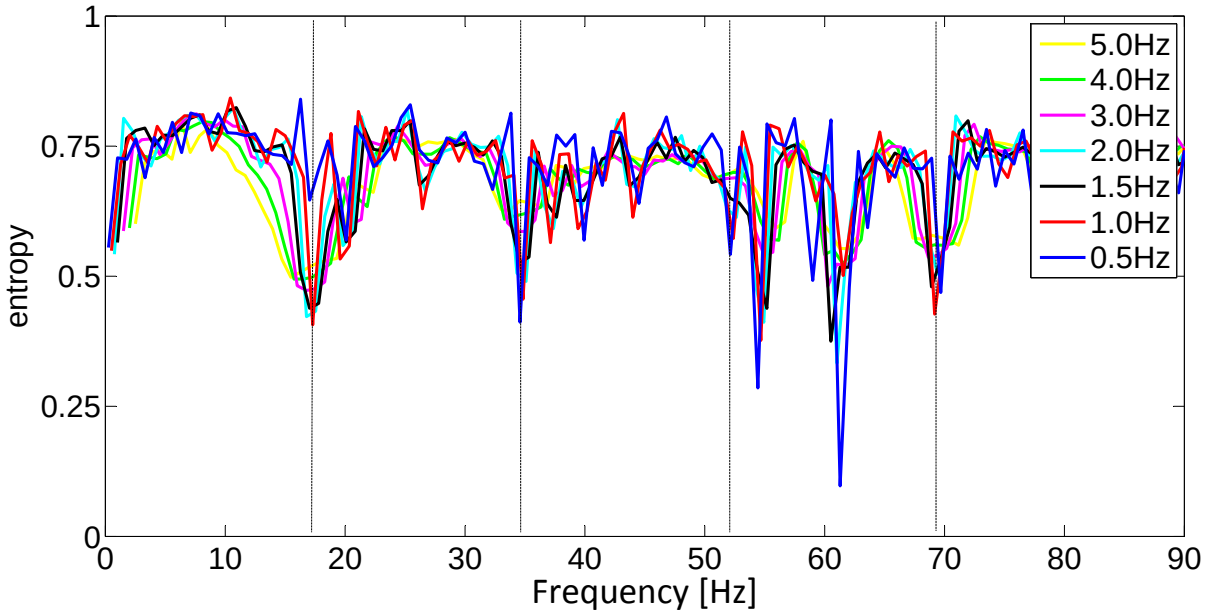

Figure 5.3: Rotating blade - Effects of the width of a 6th order Butterworth filter in the harmonic identification by the entropy approach.

local minimum to the width of the Butterworth filter becomes negligible as it reduces to values between 1 and $3\,\mathrm{Hz}$. For frequency widths less than $1\,\mathrm{Hz}$ the accuracy of the estimate of the statistical index is greatly reduced. For higher ranges smoother plots are obtained impairing an accurate identification of the frequencies of the harmonic excitations. An accurate identification of the operational frequencies is achieved with filter orders as low as 4. For higher filter orders the computational costs become too high. It is worth noting the presence in the output responses of harmonic excitations whose frequencies differ from the multiple of the fundamental angular velocity, $\Omega_0 = 109.33\,\mathrm{rad/s}$ (or $f_0 = 17.4\,\mathrm{Hz}$). The summary of the identified operational frequencies is reported in Tab.5.1. Since this is the first time that the statistical

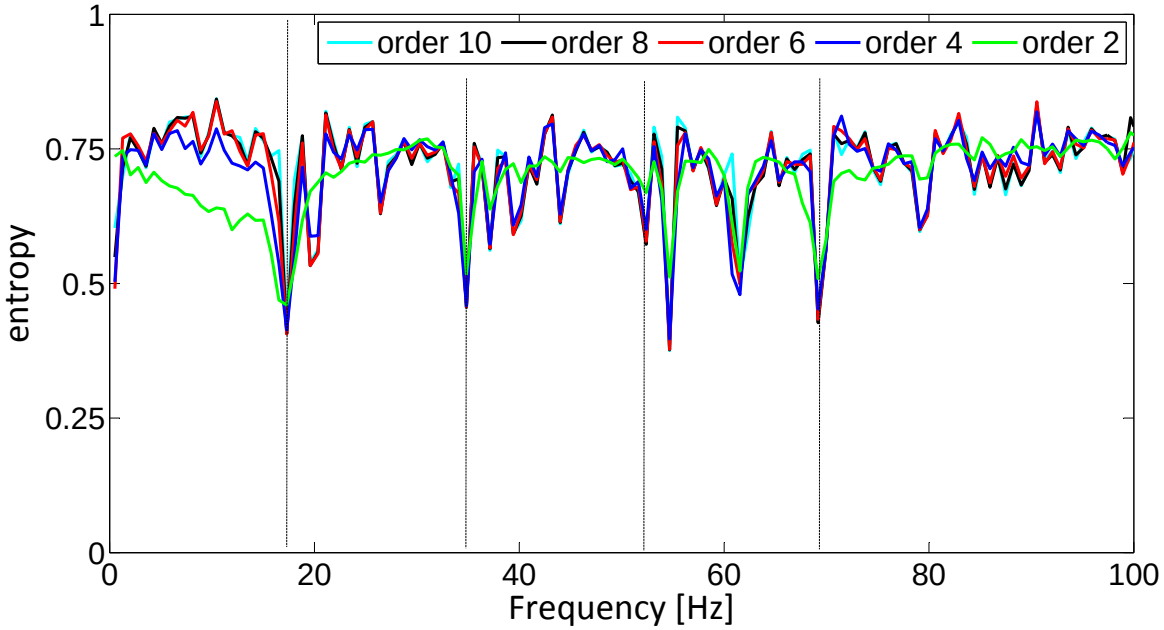

Figure 5.4: Rotating blade - Effects of the order of the Butterworth filter, frequency width $1.0\,\mathrm{Hz}$, in the harmonic identification by the entropy approach.

Table 5.1: Operational frequency estimate when $\Omega = \Omega_0$.

$\#_{op}$	1	2	3	4	5	6	7	8	9	10	11
ω_{op}/Ω_0	1.00	1.14	1.53	2.00	2.14	2.28	2.53	3.00	3.14	3.53	4.00

characterization of the responses is performed for the identification of the harmonic loading in the rotating frame, the previous findings are compared with those that could be achieved by using the Kurtosis index. As reported in Figs.5.5 and 5.6, the behavior of such harmonic loading identification give almost the same results as the Entropy index. Also using these experimental data, it seems that the Entropy index is more robust than the Kurtosis due its request for a local minima for the harmonic identification rather then the stricter request of the Kurtosis-based approach (that is the achievement of -1.5).

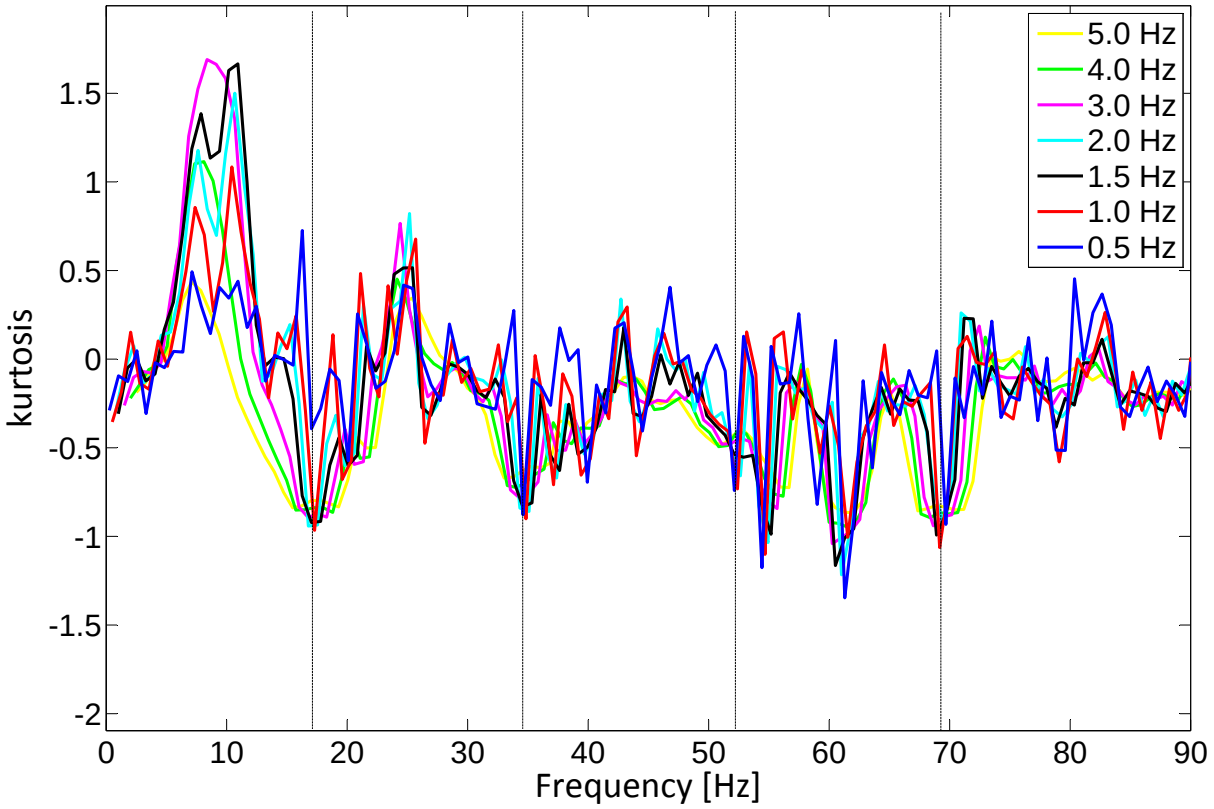

Figure 5.5: Rotating blade – Effects of the width of 6th order Butterworth filter in the harmonic identification by the Kurtosis approach.

5.3 Harmonic removal and estimate of the modal parameters

Once the frequencies of the harmonic excitations have been identified, the next step of the procedure is devoted to the identification of the biased frequency response functions of the vibrating structure by applying the Hilbert Transform method described in the previous Chapter 2. In Fig.5.7 the driving point FRF evaluated at the root of the blade rotating at the nominal angular frequency Ω_0 is depicted together with the Entropy statistical index for finding of the operational frequencies; the dashed-vertical lines correspond to frequencies multiple of Ω_0. In addition, the Kurtosis statistical index has been added to the previous picture so that a comparison between the proposed identification method and the one developed by other researchers could be carried out. The operational contributions to the structural responses are

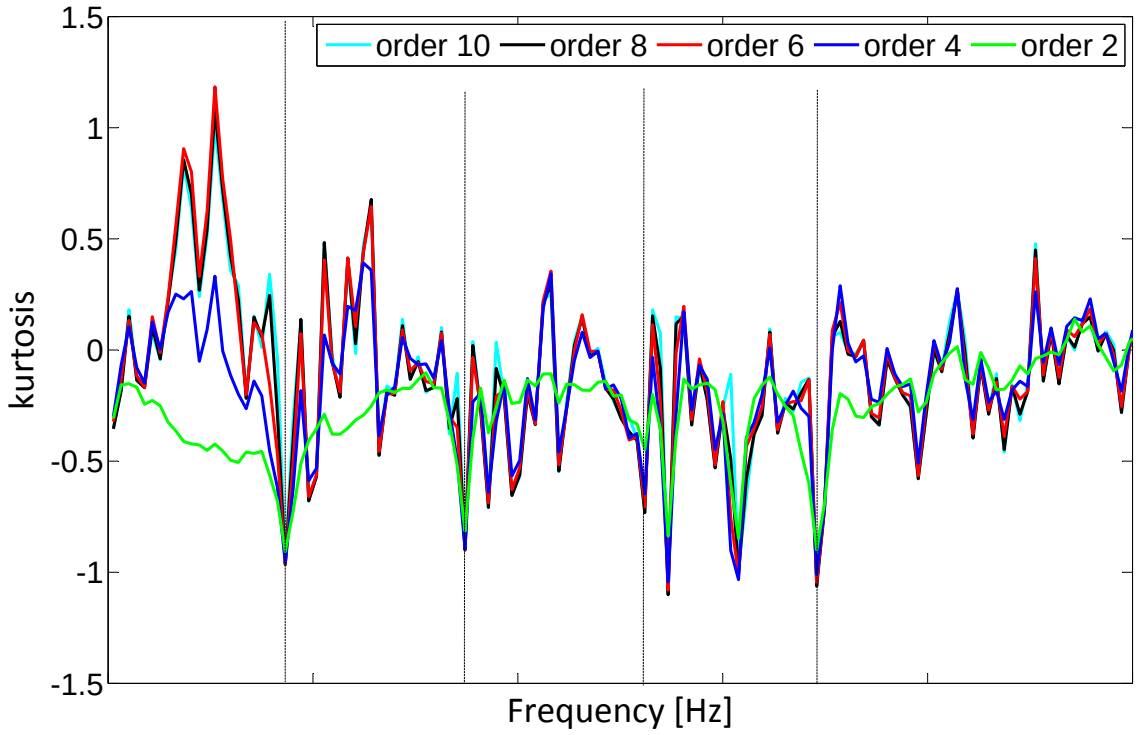

Figure 5.6: Rotating blade – Effects of the order of the Butterworth filter, frequency width $= 1.0\ Hz$, in the harmonic identification by the Kurtosis approach.

clearly identified by the several spikes superimposed to the frequency response function. These spikes are characteristic of operational modes shapes that should be viewed, in turn, as normal modes with practical null damping ratios. Furthermore, the presence of spurious, with respect to the multiple of the fundamental rotating frequency, operational frequencies can be also identified. These frequencies correspond to the spectral lines where the gaussian test, performed on the output response failed, *i.e.*, the frequencies that correspond to a local minimum value of the Entropy index or close to the value of $\gamma^* = -1.5$ for the Kurtosis index. The effect of not considering such harmonic excitations in the dynamic signature of the rotating blade is depicted in Fig.5.8, where the initial driving point frequency response function, $\tilde{H}_{ii}$, is plotted together with the operational FRF, $\overset{\mathrm{O}}{H}_{ii}$, and the harmonic-free FRF, $\overset{\oslash}{H}_{ii}$. The positive effect of the proposed procedure in estimating the dynamic properties of the rotating blade allows one a clear

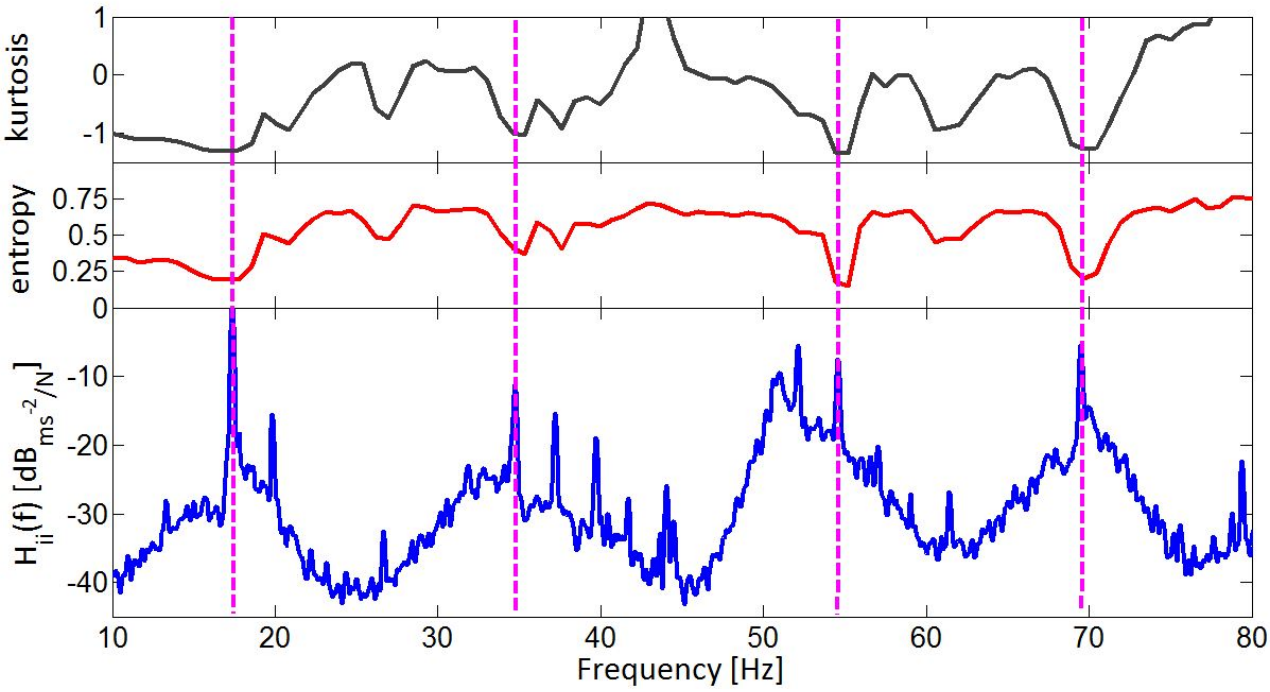

Figure 5.7: Rotating blade – Harmonic Excitation, Kurtosis, Entropy and Frequency Response Function; Flapping strain gauge at the root of the blade.

identification of the true elastic modes, by using the $\overset{\oslash}{H}_{ii}$, therefore, reducing the possibility of a wrong estimate of the operational modes. In Fig.5.9, where a zoom of the previous picture is shown, the contribution of the harmonic excitation to the frequency response function is highlighted. The behavior of the approach has been validated by identifying the dynamic characteristics at different rotating speeds of the blade. As one would expect, the estimate of the rotating natural frequencies of the blade does not exhibit any remarkable differences with respect those already identified in Ref.[58]. In Fig.5.10, it is shown how the different harmonic loads, acting at the different multiple of the fundamental frequency (namely the 1/rev, 2/rev, 3/rev etc.), interfere with the intrinsic dynamic behavior of the rotating blade. When the n/rev line ($n = 1, 2, \dots$) intersects one of the lines representing the rotating frequency of the system as a function of the rotational speed, a coarse identification of the pole of the system is expected due to the detrimental action of operating harmonic loads. Although the natural frequencies seem to be not much affected by the harmonic excitations, probably due to the fact that none of the harmonic components (practically) overlap with the rotating frequencies, the damping ratio estimates exhibit a strong influence of the rotating

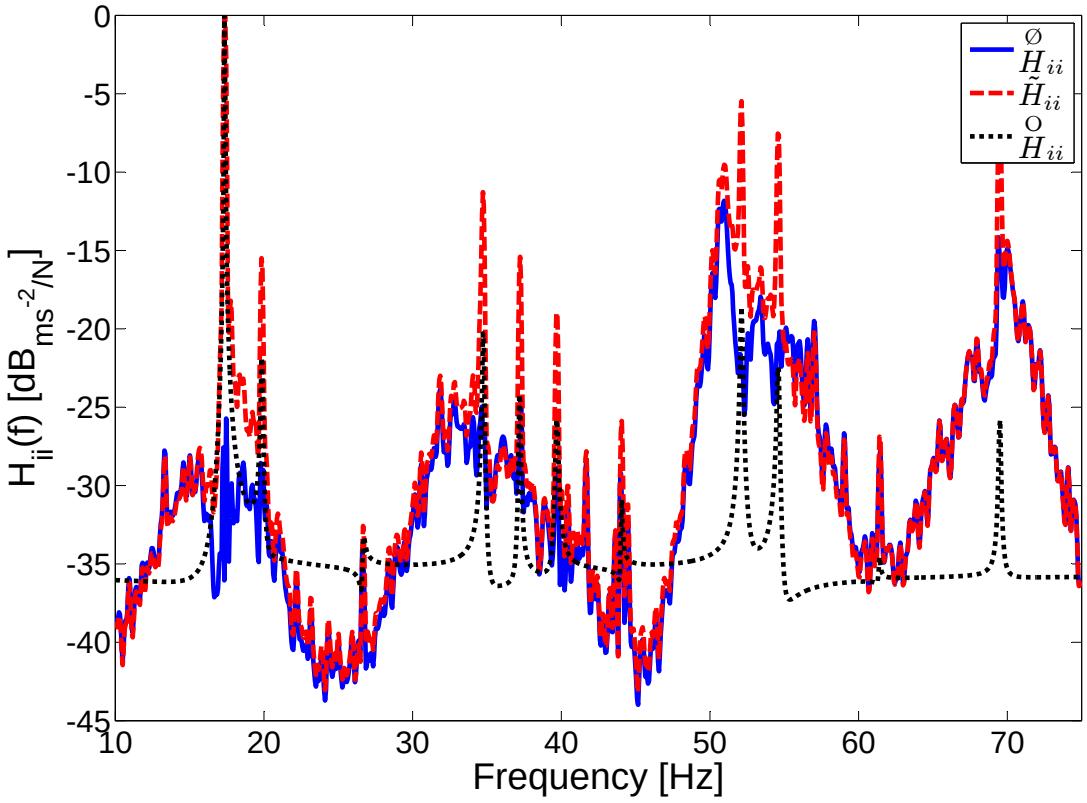

Figure 5.8: Rotating blade – Effect of the removal of the harmonic excitation in the flapping strain gauge at the blade root.

condition. As reported in Tabs.5.2 to 5.5, where the damping ratios identified in Ref.[58] (denoted with the subscript OLD) have been compared with the new estimates (subscript NEW) for each rotating speed considered in the test, remarkable differences, denoted as $\Delta\zeta = \frac{\zeta_{NEW}-\zeta_{OLD}}{\zeta_{NEW}} * 100$, are found. According to the fan plot of Fig.5.10 and to Tab.5.2, the first flapping mode, IF, suffers the 1/rev excitation in the neighborhood of the third, $\Omega/\Omega_0 = 0.48$, and fifth, $\Omega/\Omega_0 = 1.00$ rotating speed conditions. Although it is evident from the fan plot the effect of the 1/rev harmonic excitation on the damping ratio estimate

Table 5.2: Rotating blade – Damping ratio estimations - First flapping bending mode.

Ω/Ω_0	ζ_{OLD} [%]	ζ_{NEW} [%]	$\Delta\zeta$ [%]
0.00	1.97	1.97	0.00
0.24	2.38	2.40	0.83
0.48	1.50	1.74	13.79
0 .72	1.09	1.10	0.91
1.00	0.38	1.20	68.33

Table 5.3: Rotating blade – Damping ratio estimations - Second flapping bending mode.

Ω/Ω_0	ζ_{OLD} [%]	ζ_{NEW} [%]	$\Delta\zeta$ [%]
0.00	3.06	3.06	0.00
0.24	0.59	0.60	1.67
0.48	0.26	0.63	58.73
0 .72	0.28	0.45	37.78
1.00	0.57	0.57	0.00

Table 5.4: Rotating blade – Damping ratio estimations - Third flapping bending mode.

Ω/Ω_0	ζ_{OLD} [%]	ζ_{NEW} [%]	$\Delta\zeta$ [%]
0.00	0.38	0.38	0.00
0.24	0.62	0.63	1.59
0.48	0.21	0.62	66.13
0 .72	0.13	0.71	81.69
1.00	0.41	0.52	21.15

Table 5.5: Rotating blade – Damping ratio estimations - First torsional mode.

Ω/Ω_0	ζ_{OLD} [%]	ζ_{NEW} %	$\Delta\zeta$ %
0.00	0.59	0.59	0.00
0.24	0.49	1.01	51.49
0.48	0.54	0.58	6.90
0.72	0.25	0.55	54.55
1.00	0.26	0.31	16.13

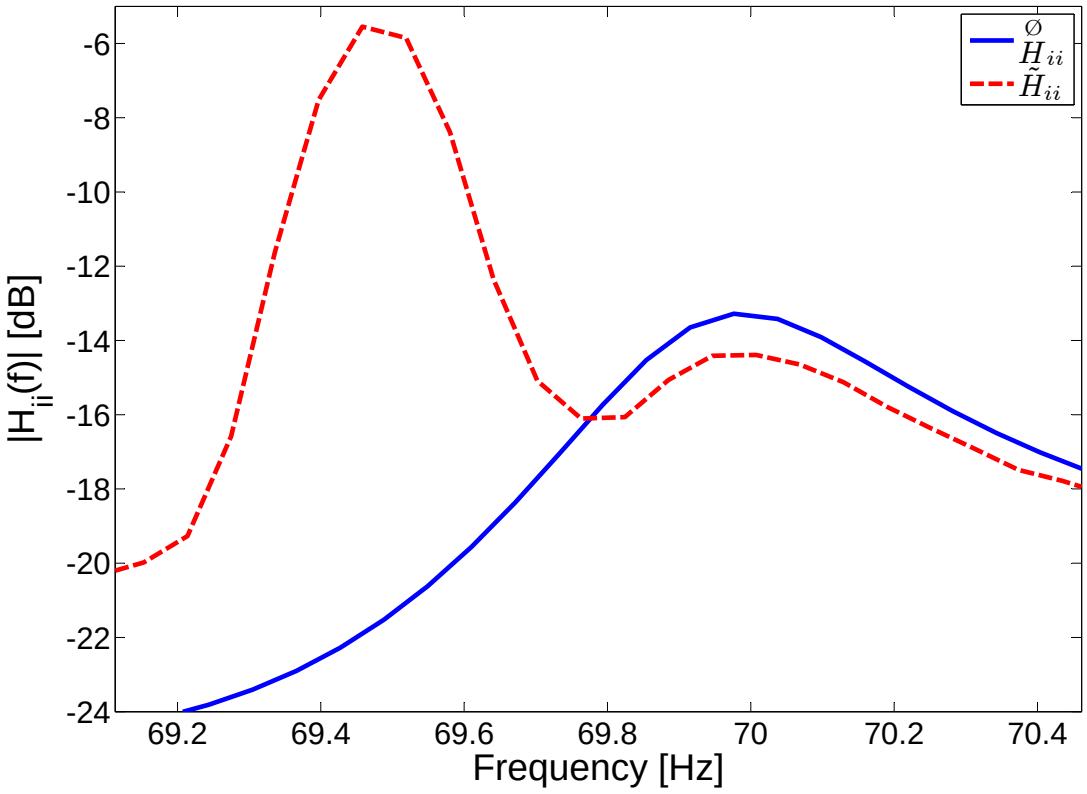

Figure 5.9: Rotating blade – Detailed view of the FRF around one mode of interest.

of the third rotating speed condition, the reason of the huge difference for the maximum rotating speed, $\Omega/\Omega_0 = 1.00$, is not so clear. Indeed, the effects of harmonics acting at non integer-multiples of the fundamental frequency, due to their completely different dynamics, should be taken into account to justify this finding. Similar considerations could be taken when dealing with the damping ratio estimates for the second and third flapping modes, IIF and $IIIF$, for which the $2/$, $3/$, and $4/$rev harmonic excitations are responsible for great differences in the estimates. The torsional mode, IT, has been found despite the interference of the $4/$rev and higher harmonic excitations, see Fig.5.10. The effect of removing the deterministic component at the $4/$rev, corresponding to a rotating angular frequency of $\Omega/\Omega_0 = 1.00$, is reported in Fig.5.9 where not only a variation of the amplitude of the peak and the shape of the FRF is detected, but also an increase of the damping ratio of about $15\,\%$ is estimated (see the last row of Tab.5.5).

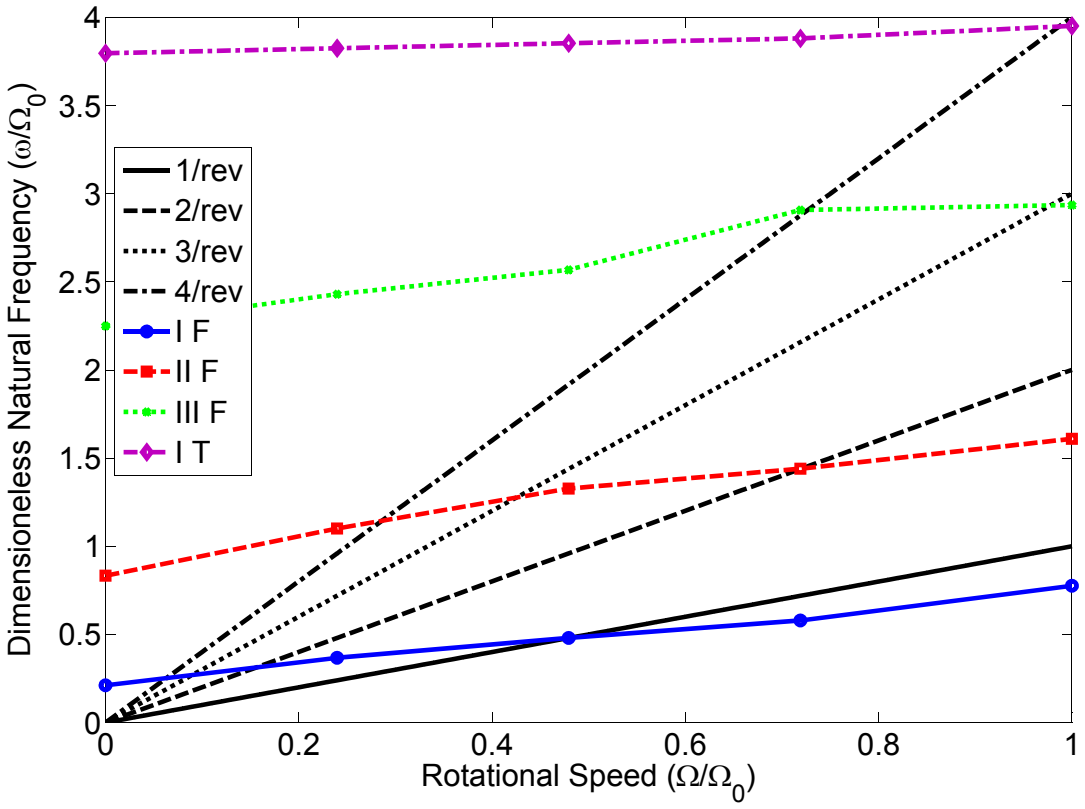

Figure 5.10: Fan Plot of the rotating blade.

A general view of the damping mechanism of the rotating blade for different rotating speeds, is depicted in Fig.5.11, where, for each mode and rotating speed, the damping ratio estimates achieved by the proposed approach (red-solid lines) are compared with those previously evaluated in Ref.[58] (blue-dashed lines). It is worth noting that the values of the damping ratios estimated by the developed approach are noticeably higher than those reported in Ref.[58] when the mode of interest approaches the frequency of the harmonic excitation. This is probably due to the fact that operational modes are characterized by (theoretical) null value of the equivalent damping ratio.

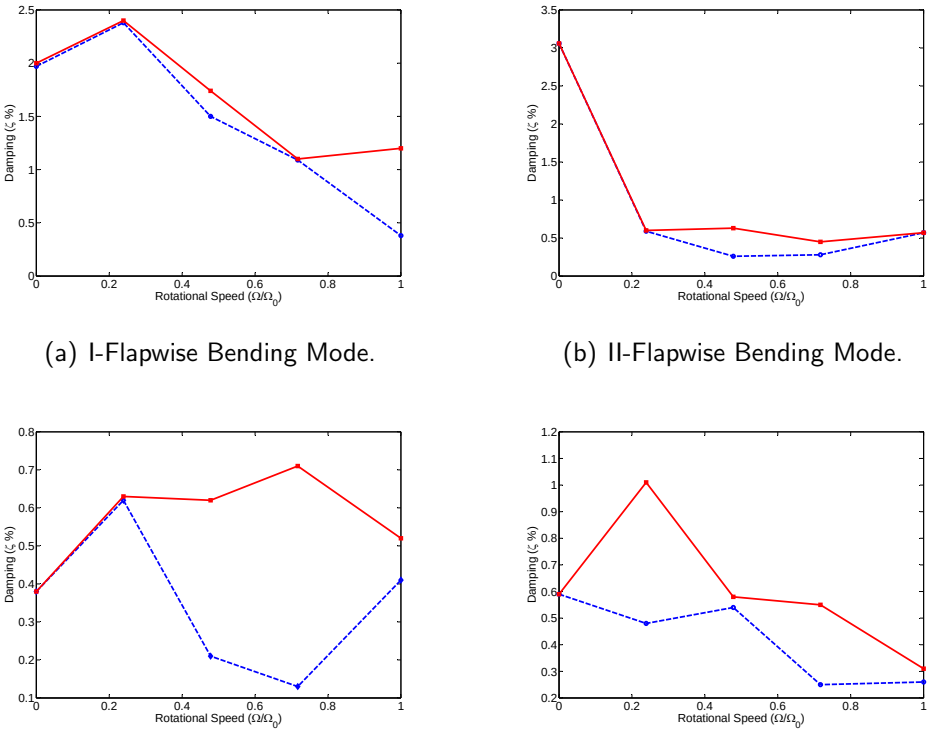

(a) I-Flapwise Bending Mode.

(b) II-Flapwise Bending Mode.

(c) III-Flapwise Bending Mode.

(d) I-Torsional Mode.

Figure 5.11: Damping Ratio Fan Plots - Red solid line: estimate from "harmonic-free" FRF. Blue dashed line: estimate from "harmonic-adultered" FRF.

Chapter 6

Wind Turbine Tests

The modified Hilbert Transform Method is here presented to identify the dynamic properties of a composite horizontal axis wind turbine blade using data recorded during its working conditions. In this case, the system is characterized by harmonic component excitations blended with white noise spectra loading so that the operational modal analysis would be not applicable. The unknown harmonic contributions are identified and their effects on the time responses removed for a clearer estimate of the modal parameters. The considered data are gained from a Fiber Bragg Grating (FBG) integrated with the wind turbine blade. The FBG transducers have many advantages over other conventional sensors. Providing real-time information about structural integrity and operational load they can be used in conjunction with appropriate methods to decrease the costs of wind turbines by optimizing their maintenance schedule for service life. This chapter discusses the capabilities of the proposed operational modal analysis procedure included in the Natural Input Modal Analysis (NIMA) code. It can be jointly used with data from FBG transducers to track the changes in the natural frequencies, damping ratios and mode shapes of the rotating wind turbine blade for structural health monitoring. Experimental data are provided by the wind tunnel test campaign carried out at the Mechanical and Aeronautical Engineering Department of Clarkson University in Potsdam (NY-USA). The dynamic of the wind energy generator are experimentally estimated using the FBG transducers

at different rotating blade speed and upstream wind velocity.

6.1 Introduction

The trend to minimize the Cost-of-Energy (COE) and increase efficiency is leaning towards increasing the swept area of the wind turbine.[59] However, this growth leads to an increase in the operational structural loads involved and necessitates a reliable method for monitoring the wind turbine blades. It is quite difficult and costly to perform inspection and maintenance work on turbines, primarily due to their height and their installation location, often remote such as in the case of offshore sites. Monitoring the health of these structures is paramount to improve safety, minimize down time and lower frequency of sudden break downs,[60] and to move from a costly schedule-based maintenance towards a more cost-effective condition-based maintenance. The capabilities to monitor the state and health of the structure might also help to fabricate lighter and/or larger blades by providing more conservative margins of safety,[61] and by allowing to harvest more energy.[62] With respect to conventional resistive strain gauge, Fiber Bragg Grating (FBG) transducers are not affected by electromagnetic interference, potentially reducing the external noise in signal and monitoring larger structures. Fiber optic signal also removes the need for localized signal amplification and signal conditioning. Furthermore, this kind of sensors have an increased lighting safety due to the fact that fiber optics are strong conductors of electricity.[63] A distribution of FBGs over a structure has been successfully used to detect transverse crack evolution.[64] The FBG can also be used to detect impact damage in a composite structure.[65] An FBG array can be Wavelength Division Multiplexed, which creates an expected characteristic wavelength range for each FBG in a fiber array.[66] This scheme of sensing allowed up to 64 FBG sensors per interrogator on our hardware, however the practical limit is about 100 per channel.[67]

In the present experimental study, the effectiveness of FBG sensors to provide real-time wind turbine strain measures in field operation is investigated. The experiment involves pseudo-operational wind tunnel

testing, in order to validate the effectiveness of using FBGs as practical transducers useful for operational modal analysis, hence, for a possible use in structural health and load monitoring of wind turbines. The wind tunnel test facility allows the rotation of a wind turbine blade at different angular speeds in order to achieve different operating conditions of the rotating structure as well as different upstream wind velocities. Since it is not possible to measure the input excitation during the experimental tests, *i.e.*, the aerodynamic forces applied to the rotor, then the standard modal analysis techniques cannot be applied. Since the considered wind turbine blade is rotating in the wind tunnel under the action of uncertain flow conditions, all the standard identification procedures based on EMA or OMA may be corrupted by operational frequencies, at least at the frequencies equal to multiples of the blade rotating speed times the number of blades of the wind turbine rotor, in this case three. Nevertheless, the advantages of the Entropy index statistical analysis and the capabilities of the harmonic removal strategy provide a method to investigate the modal behaviour of such a system.

6.2 Fiber Bragg Grating Principles of Operation

The Fiber Bragg Grating is made by periodic etching of an optic fiber resulting in a sensor with the same diameter as the original fiber and marginally changing its structural properties [66]. The etched areas have a changed refractive index compared to the remaining silica glass fiber.[67] Depending on the characteristics, FBG acts as a filter of specific wavelengths. The equation to calculate the FBGs characteristic wavelength is:

$$\lambda_B = 2n_e\Lambda \tag{6.1}$$

with λ_B being the characteristic wavelength, n_e being the effective refractive index of fiber core and Λ being the grating period. The wavelength that is filtered from the spectrum by the FBG, is reflected back toward the light source. In the used scheme, the reflected light spectrum is measured.

To correlate the change in wavelength with the strain, the following equation is used:

$$\Delta\lambda_B = \lambda_B \left[(\alpha_f + \xi_f) \Delta T + (1 - p_e) \varepsilon \right] \tag{6.2}$$

where α_f is the coefficient of thermal expansion, ξ_f is the thermo-optic coefficient, and p_e is the strain-optic coefficient of the optical fiber, whereas ΔT is the change in temperature, and ε is the strain. It is worthwhile to remark that the response of the FBG to strain and temperature are linear and additive requiring less calibration.[67] The equation for finding p_e is:

$$p_e = \left(\frac{n_e^2}{2} \right) \left[p_{12} - \nu \left(p_{11} + p_{12} \right) \right] \tag{6.3}$$

where p_{11} and p_{12} are the components of the strain-optic tensor, and ν is Poisson's ratio. Generally germano-silicate glass has a strain-optic coefficient of 0.22 [68] With the assumption that there is no change in temperature during the experiments, the strain are computed as

$$\varepsilon = \frac{1}{1 - p_e} \frac{\Delta\lambda_B}{\lambda_B} \tag{6.4}$$

6.3 Test setup

The dynamic properties of a small wind turbine, manufactured by ARI Green Energy, are experimentally identified in the lab with the aid of the developed operational modal analysis method. The first objective is the verification of the capability of the measurements from FBG coupled with the operational modal analysis technique to estimate the modal parameters when exciting the structure with a random signal both in time and in the space domain, keeping the wind turbine blade in non-rotating conditions. This experiment is quite useful because it proves the capability of the operational modal analysis to estimate the modal parameters directly from the FBG output response measurements only; it provides the necessary background to develop the knowledge needed for the dynamic identification of the blade properties during the wind tunnel tests and during its real operational conditions. Once the use of the FBG transducers is assessed, the effects of the operating conditions are evaluated in the rotating frame.

The test setup is shown in Fig.6.1. The blade is three feet in length and it is molded from Short

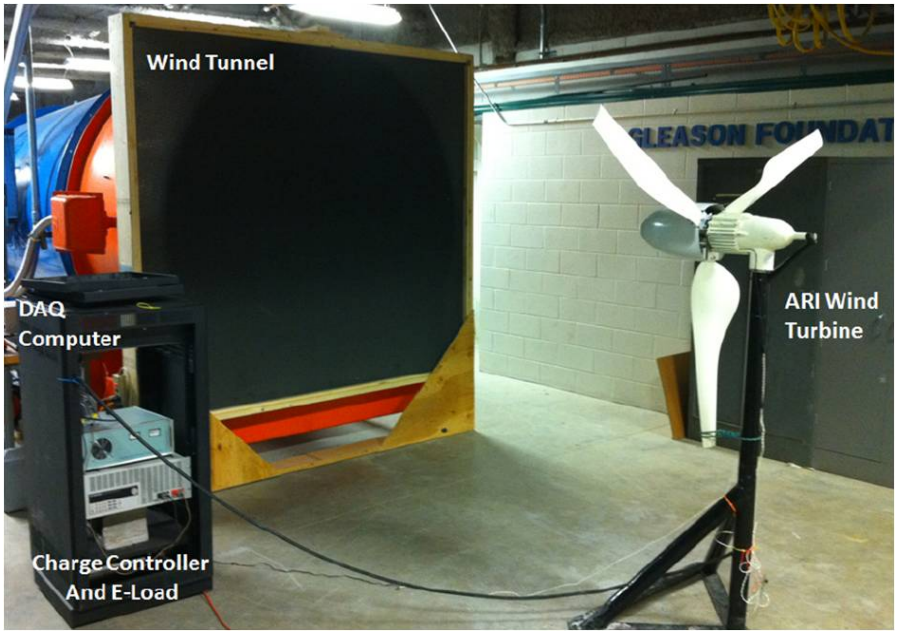

Figure 6.1: Wind tunnel test setup for the ARI Green Energy wind turbine rotor.

Glass Fiber Reinforced Plastic, SGFRP. The ARI wind energy rotor with its supporting truss, made by steel bars, is located at the open-section wind tunnel outlet. By the use of the charge controller and E-load, it is possible to control the electrical load of the generator, thus the angular speed of the rotor. For the non-rotating tests the dynamic excitation is provided by crawling fingers to have a dynamic identification of the whole rotor-tower system. One optic fiber is glued at each blade for a total of three FBG measuring lines. The locations of the strain measurements vary from four to eight, depending on the blade, for a total of 20 degrees of freedom, see Fig.6.2.

Moreover, as a reference case in the non-rotating configuration, a multi-run test is carried out using three accelerometers of sensitivities around $10\,\mathrm{mV/g}$. Two of them are placed on the supporting truss in the wind and lateral directions and are used as references for 21 different runs. The last one is moved in 7 different locations for each of the 3 blades and a roving accelerometer test is performed.

The considered sampling frequency of both FBG and accelerometer transducers is $625\,\mathrm{Hz}$, whereas the length of the data is 2^{15} time samples.

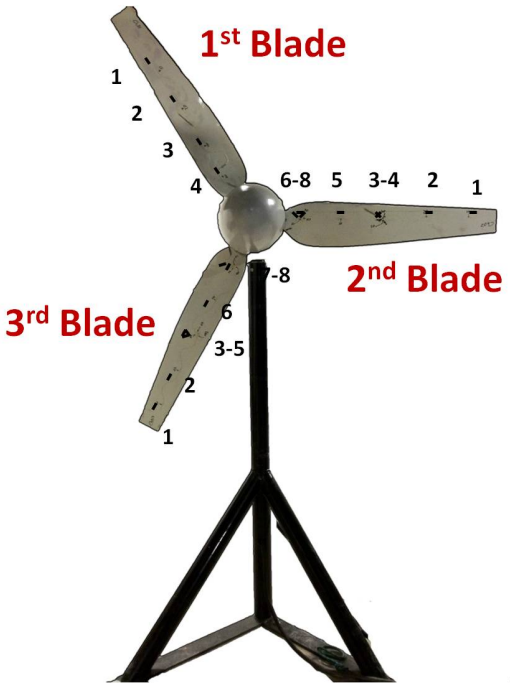

Figure 6.2: Detailed view of the ARI Green Energy wind turbine rotor with blade and sensor position numbering.

6.4 Dynamics of the non-rotating system

The simultaneous acquisition of the data measured by the accelerometers and the FBG allows the identification of the system's modal signature in the non-rotating condition. The identified natural frequencies and damping ratios are reported in Tab.6.1 as they are evaluated by the OMA for both the kind of sensors. No remarkable differences can be highlight in the system's poles identification proving that the results are not sensitive to the transducer, at least in terms of the natural frequencies and damping ratios. This consideration is not valid if the mode shapes were considered. In fact, the mode shapes can be easily identified by considering the results provided by the accelerometers, as represented in Fig.6.3. On the other hand, the FBG sensors give a measure of the strain along the surface in the fiber axial direction and the displacement modes cannot be reconstructed in this case, as the structure has a full 3D strain tensor and the sensors follow different local coordinate frames. Nevertheless, the strain shapes achieved in the non-rotating test case are used as a reference also for the rotating conditions. From their comparison with the displacement shapes (provided by the accelerometers) a characterization of the modes is then obtained.

Table 6.1: Natural frequency and damping estimates of the wind generator rotor.

Mode #	$f_n\ [Hz]$	$\zeta_n\ [\%]$	Description
1	4.58	1.20	1st bending/torsion
2	10.68	0.60	1st collective bending mode
7	47.30	1.00	2nd collective bending/torsion mode
9	78.74	0.13	3rd collective bending mode

The rotor dynamics is well correlated with the isolated blade dynamics. The first and the second collective bending modes originate from the corresponding bending modes of the isolated blades. A third collective mode can be identified as the fourth main mode of the rotor, whereas the third bending mode of the blades is coupled with the torsion mode.

In addition to the modes associated to the vibration of the blades of the rotor, it is also possible to identify the dynamic properties of the supporting truss structure. This is possible by taking advantage of the accelerometers mounted on the truss structure and the nacelle of the rotor since the FBG sensor are distributed only on the rotor blades. Both lateral, LAT, and longitudinal, LONG (with respect to the flow direction) bending modes, whose natural frequencies and damping ratios are reported in Tab.6.2, are identified.

Table 6.2: Natural frequency estimates of the supporting truss.

Mode #	$f_n\ [Hz]$	$\zeta_n\ [\%]$	Type
3	12.51	0.54	LAT
4	15.87	1.90	LONG
5	39.37	0.51	LAT+LONG
6	43.64	0.52	LONG+LAT
8	50.05	0.20	LONG

6.5 Wind turbine dynamics in the rotating frame

The dynamic behavior of the wind turbine is evaluated at different wind speeds and different operating angular speeds of the rotor. The flow speed of the wind tunnel is controlled by the rotating speed of its fan,

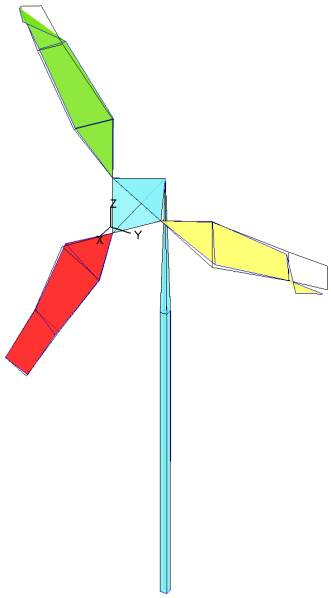

(a) First bending/torsion mode $f_n = 4.58\,\mathrm{Hz}$; $\zeta_n = 1.20\,\%$

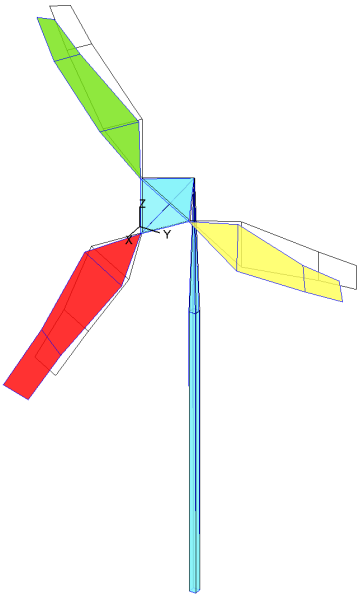

(b) First collective bending mode - $f_n = 10.68\,\mathrm{Hz}$; $\zeta_n = 0.60\,\%$

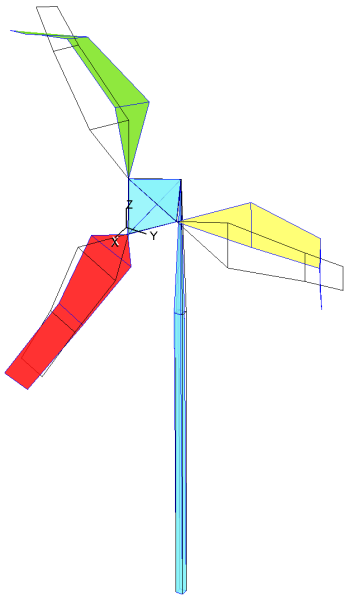

(c) Second collective bending/torsion mode - $f_n = 47.30\,\mathrm{Hz}$; $\zeta_n = 1.00\,\%$

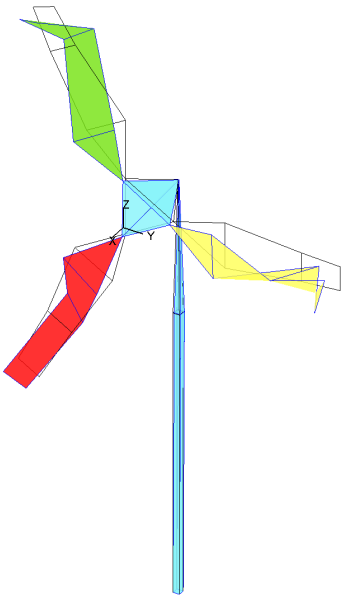

(d) Third collective bending mode - $f_n = 78.74\,\mathrm{Hz}$; $\zeta_n = 0.13\,\%$

Figure 6.3: Mode shapes of the wind generator assembly.

whereas the angular speed of the wind generator is controlled by the electrical current flowing in a given (constant current mode) electronic load (E-Load) bank, and by the flow field itself. Three rotating speeds of the wind tunnel fan are selected, *i.e.*, $345, 400,$ and $450\,\mathrm{RPM}$. For each of the considered fan speeds, three electrical loading conditions are considered, *i.e.*, 2.00, 1.00 and $0.28\,\mathrm{A}$ for a total of 9 test conditions. It is worthwhile observing that the rotor angular speed increases as the electrical load current decreases. Moreover, because of the presence of the electrical controller, the rotor angular velocity cannot be set constant. In these operating conditions a measure of the performances of the energy generator, in terms of electrical power, are recorded and summarized in Tab.6.3. Moreover, the non-rotating frame vibration

Table 6.3: Electrical power generated by the ARI wind turbine in the reference conditions.

FAN [RPM]	Current [A]	Voltage [V]	Power [W]	Rotating frequency [Hz]
345	2.00	18.3	36.6	4.73
345	1.00	22.0	22.0	5.42
345	0.28	24.6	6.89	5.87
400	2.00	25.4	50.8	6.33
400	1.00	28.5	28.5	6.87
400	0.28	30.6	8.57	7.25
450	2.00	31.5	63.0	7.71
450	1.00	34.3	34.3	8.16
450	0.28	36.2	10.14	8.47

levels of the hub in the lateral and wind directions are measured, taking advantages of the non-rotating accelerometers on the supporting truss. The estimate of the vibration levels corresponding to the main harmonic excitations is carried out by evaluating the Power Spectral Density (PSD) functions for each operating condition. It should be noted that the supporting system is excited by the wind turbine rotor and also by the blowing wind. Therefore the time signals are stochastic and the PSD functions need to be evaluated instead of the Fourier Transform, in order to estimate the frequency responses of the system. Moreover the noise effect is reduced by averaging the functions about 24 times. The rotating speed of the wind turbine rotor is calculated using the Hall sensor located between the rotating and the non-rotating systems. The considered harmonic components are integer multiples (from 1 to 6) of such rotating speed,

since the rotor has three blades. As expected the vibration coming from the wind turbine rotor is mainly due to the first, the third and sometimes the sixth multiple of the rotational speed, see Fig.6.4. The vibration in the lateral direction is usually much higher than in the wind direction, with the exception of the second and the third condition (fan speed equal to 345RPM, electric load equal to 1.00A and 2.00A).

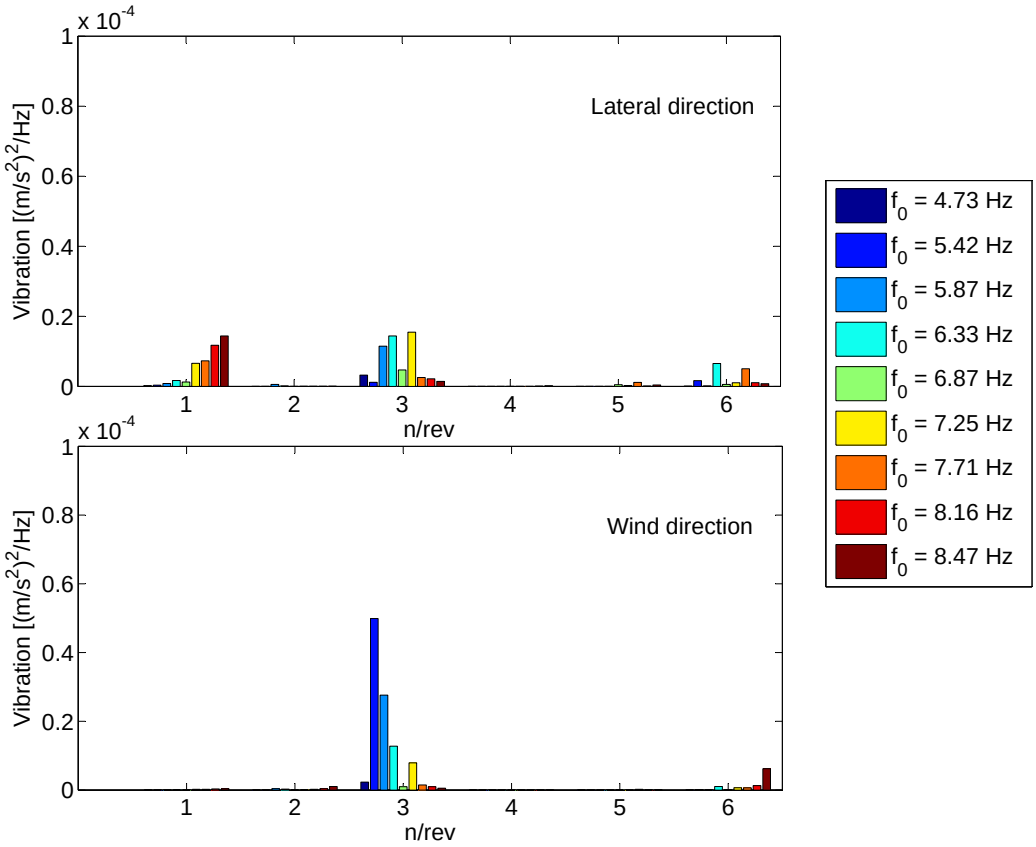

Figure 6.4: Vibration level in the non rotating frame in lateral and wind directions for several operating conditions in the reference operating conditions.

The identification of the modal parameters of the rotating blades corresponding to the nine operating conditions, identified by the value of the rotating speed of the wind tunnel fan (Fan), the electrical current flowing in the wind generator load (Load) and the corresponding operational rotating speed of the rotor (Ω_0), is reported in Tabs.6.4 (natural frequencies) and 6.5 (damping ratios) respectively. Only the dependency of the first modes of the rotor is shown, as one can see from the mode index reported in the previous tables.

The corresponding root loci are shown in Figs.6.5 and 6.6, displaying each real/imaginary pair corre-

Table 6.4: Natural frequency estimates of the wind energy rotor for different operating conditions.

Fan [RPM]	Load [A]	$\Omega_0\ [Hz]$	$f_{n_1}\ [Hz]$	$f_{n_2}\ [Hz]$	$f_{n_7}\ [Hz]$	$f_{n_9}\ [Hz]$
345	2.00	4.73	4.88	11.29	47.61	79.20
345	1.00	5.49	4.96	11.75	48.83	79.45
345	0.28	5.95	5.10	11.90	49.00	80.26
400	2.00	6.41	5.60	12.30	49.59	80.26
400	1.00	7.02	5.95	12.51	49.74	80.50
400	0.28	7.32	6.10	12.82	49.90	80.70
450	2.00	7.76	6.41	13.50	50.10	80.60
450	1.00	8.24	6.71	13.73	50.50	80.90
450	0.28	8.55	6.50	14.30	51.30	81.60

Table 6.5: Damping ratio estimates of the wind energy rotor for different operating conditions.

Fan [RPM]	Load [A]	$\Omega_0\ [Hz]$	$\zeta_{n_1}\ [\%]$	$\zeta_{n_2}\ [\%]$	$\zeta_{n_7}\ [\%]$	$\zeta_{n_9}\ [\%]$
345	2.00	4.73	1.20	2.50	1.80	1.10
345	1.00	5.53	1.60	2.00	1.70	0.60
345	0.28	5.95	1.50	1.80	1.50	0.65
400	2.00	6.41	1.80	1.20	1.50	0.80
400	1.00	6.98	1.80	0.60	1.80	0.80
400	0.28	7.32	1.90	0.50	1.40	0.80
450	2.00	7.78	0.70	0.60	1.50	0.90
450	1.00	8.24	0.60	0.60	1.00	1.20
450	0.28	8.58	0.80	0.70	1.20	0.80

sponding to each pole of the system evaluated at each working condition with the electrical Load and the Fan speed as parameters, respectively. The imaginary parts (and then the natural frequencies) of the poles of the wind energy generator associated to the dynamics of the rotor blades increase as the rotational speed increases due to the stiffening effects of the centrifugal force. On the contrary, the imaginary parts of the poles corresponding to the truss dynamics (modes #3 and #4, depicted in red and cyan, respectively) are marginally affected by the rotating speed, because, as expected, there is no stiffness contribution of the centrifugal force to the non-rotating part of the structure. Therefore, the corresponding natural frequencies remain practically unchanged. Nevertheless, due to the different energy dissipation mechanisms associated to the different working conditions, a change in the real part of the poles of the truss structure is reported.

Furthermore, potential wind turbine system instabilities are analyzed from the fan plot, depicted in Fig.6.7. In this picture, the previously identified natural frequencies (normalized with respect to the

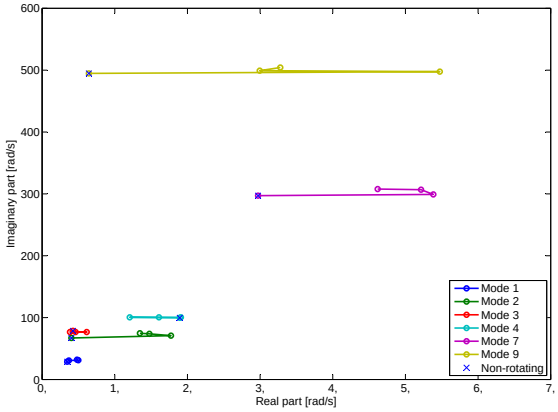

(a) 345 RPM

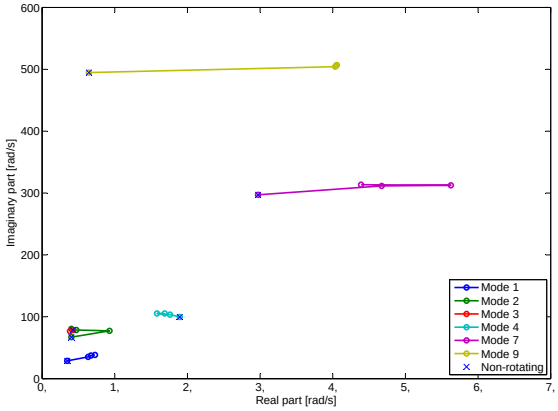

(b) 400 RPM

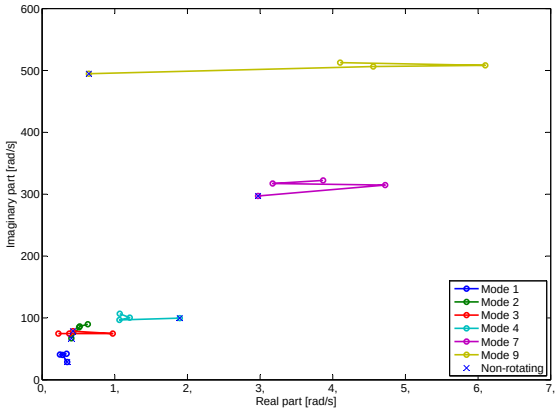

(c) 450 RPM

Figure 6.5: Experimental root loci of the ARI wind generator with respect to the electrical load at fixed Fan speed. In the non rotating condition (depicted by the blue crosses) the electrical load has to be considered infinity.

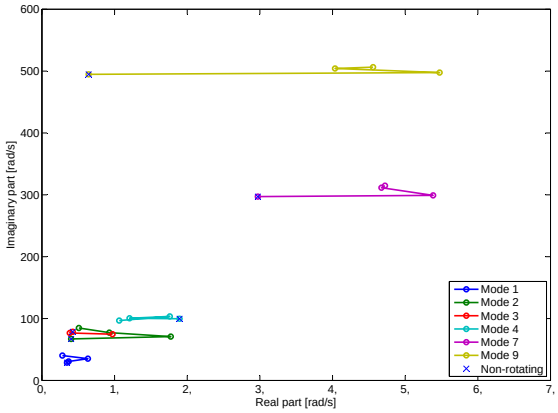

(a) 2.00 A

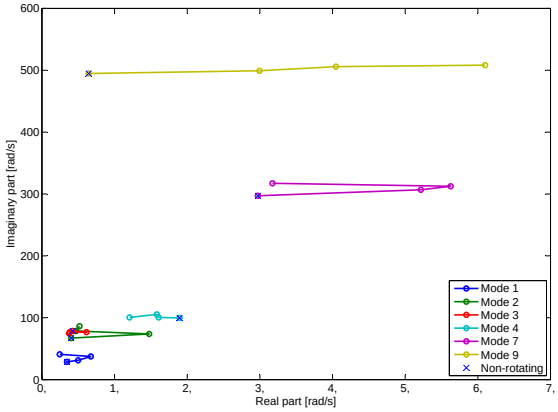

(b) 1.00 A

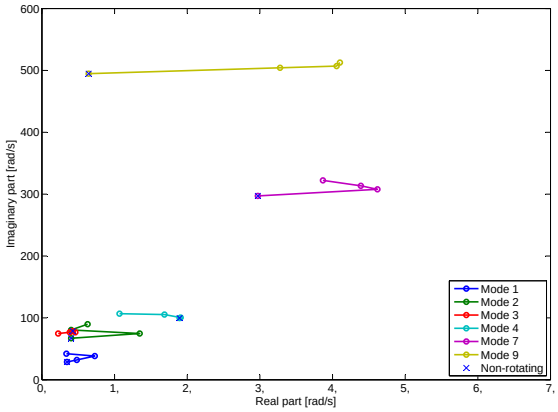

(c) 0.28 A

Figure 6.6: Experimental root loci of the ARI wind generator with respect to the Fan speed at fixed electrical load conditions.

maximum operating angular frequency) and those corresponding to the ones characterizing the dynamics of the truss structure, are reported as functions of the (normalized) average angular speed, Ω_0. Also, straight lines representing constant angular velocities, for different multiple values of the actual angular speed, rev, *i.e.*, $1/, 3/,$ and $6/$ rev, are added to the picture with black marks. In the event that one of the natural frequencies of the rotating system is close to one of these straight lines (to be viewed as the frequency lines corresponding to the frequencies of the forcing -aerodynamic- loads exciting the rotor blade) possible instabilities are expected leading then to unavoidable structural failure.

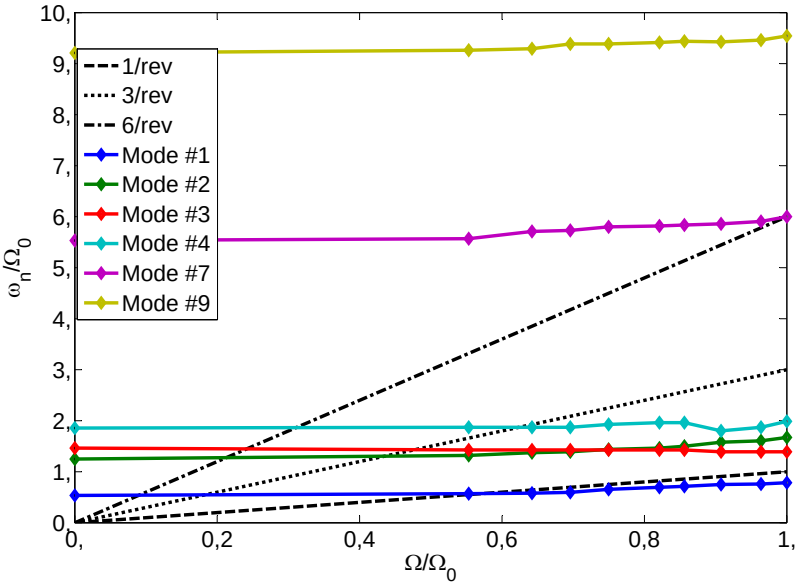

Figure 6.7: Experimental fan plot of the ARI wind generator.

The most critical operating conditions, identified in Fig.6.7, are those corresponding to the coupling of mode #1 (see Tabs.6.1 and 6.2 for details on mode numbering) with the loading exciting the structure at the frequency 1/rev, mode #4 with the 3/rev, and mode #7 with the 6/rev, respectively. These critical operating conditions are considered to check the capabilities of the proposed harmonic removal approach to deal with wind turbine systems whose dynamics is monitored by FBG sensors. First, the operational frequencies are checked by the entropy index. The operational frequencies, f_{op}, of Tab.6.6 are identified for each of the performed test by using a band-pass filter, of order 6 with a width equal to $1.0\,\mathrm{Hz}$, applied to

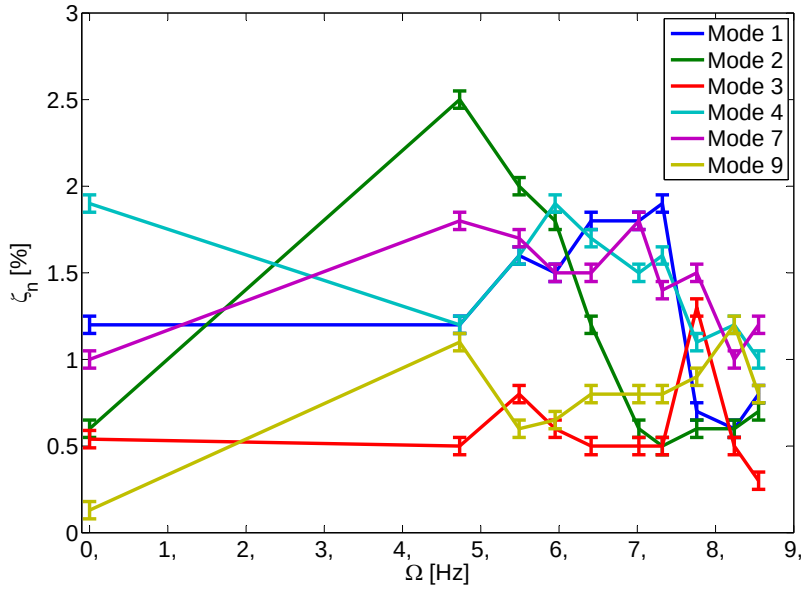

Figure 6.8: Experimental damping ratio behaviour with respect to the rotating speed of the ARI wind generator.

the time histories recorded for all FBG sensors. As the E-Load controller is responsible of the electrical load applied to the wind energy generator, the rotor blade is characterized by a non-constant rotational speed, as detected by the entropy index and indicated in Tab.6.6. Several operational frequencies are absent. Indeed, although the average values Ω_0 of the operating frequencies could be identified by the Hall RPM sensor and is used as reference in the previous Tabs.6.1 and 6.2, the change in the rotating conditions of the rotor do not introduce a practical deterministic contribution detectable by the entropy index when merged with the non-deterministic response of the rotating rotor.

Table 6.6: Estimate of the operational frequencies using the Entropy index for different operating conditions.

Fan [RPM]	Load [A]	f_{op} $[Hz]$					
345	2.00	4.9	-	-	-	-	208.2
345	1.00	5.7	10.7	-	21.9	27.8	-
345	0.28	6.2	11.3	12.3	17.9	23.9	-
400	2.00	6.6	13.2	19.6	25.8	-	-
400	1.00	6.7	7.4	14.4	-	-	-
400	0.28	7.7	14.6	22.0	29.7	-	-
450	2.00	7.2	8.1	15.8	-	-	-
450	1.00	7.8	8.6	16.2	-	-	-
450	0.28	8.0	8.9	16.8	17.6	-	-

Moreover, other operational loads are exciting the wind turbine other then those due to the aerodynamic load at frequencies equal to multiples of the fundamental $1/\text{rev}$. This is the case, for example, of the working condition corresponding to the wind tunnel fan rotating at $345\ RPM$ with an electrical load of $0.28\,\text{A}$ in which two operational frequencies are detected at $11.3\,\text{Hz}$ and $12.3\,\text{Hz}$. Finally, Fig.6.9 shows the biased FRF corresponding to FBG located at the root of one blade (blade number 2), obtained from time histories corresponding to wind tunnel fan operated at $450\,\text{RPM}$ and an electrical loading of $0.28\,\text{A}$ applied to the wind energy generator (red curve). As discussed earlier, the contribution of the operational frequency response function, $\overset{\text{O}}{\mathbf{H}}(\omega)$ (black dotted curve), is removed from the biased FRF, $\tilde{\mathbf{H}}(\omega)$, to obtain the harmonic-free FRF, $\overset{\varnothing}{\mathbf{H}}(\omega)$, depicted in blue.

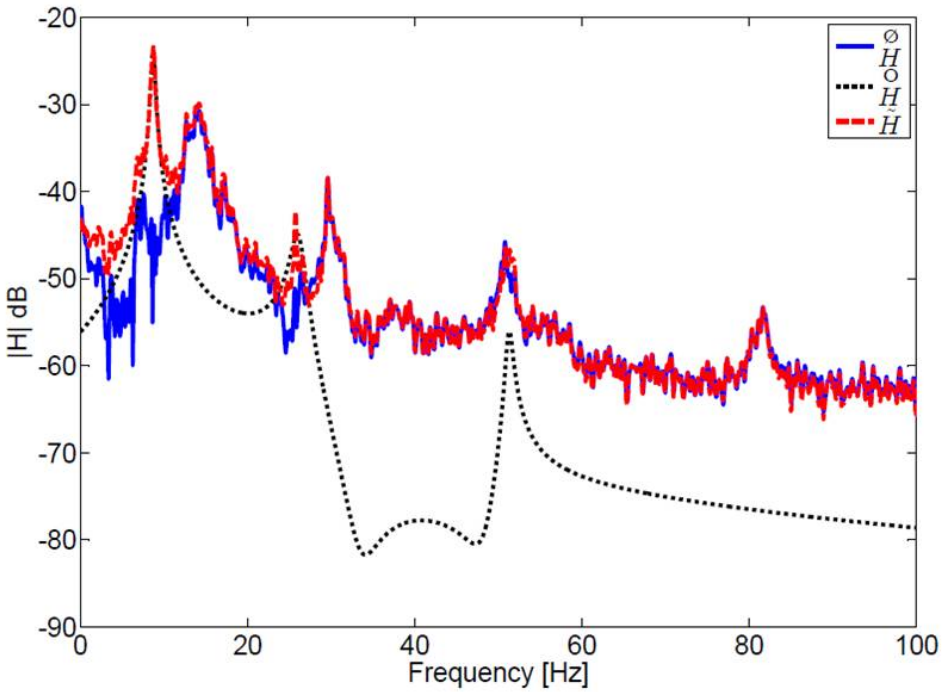

Figure 6.9: Harmonic removal process - FBG located at the root of blade 2, wind tunnel fan operated at $450\,\text{RPM}$, load $0.28\,\text{A}$.

The major effect of the harmonic removal process consists in a better identification of the pick of resonance and a more accurate damping ratio estimate. However, for the case under investigation, the coupling between the mode shapes and the operational modes does not appear so critical as the changes in the poles of the system are practically immaterial. Nevertheless, the previously identified changes in

the operational frequencies noticed during the recording phase and for different operating conditions are responsible for a low accuracy identification due to the fact that the system under investigation is not in steady-state working conditions. On the other hand, the actual capability of the proposed identification procedure applied to the FBG sensor technology to monitor the dynamic behavior of the wind energy generator working under actual operating is properly demonstrated. This justify their use in successive tests to be performed in real field operations.

Chapter 7

In-Flight Tests

The Operational Modal Analysis (OMA) can be used for the identification of the dynamics of aerospace vehicles, in terms of natural frequencies, damping ratios and mode shapes, during flight tests, using only the output responses due to the aerodynamic environment. The loading acting on the flying helicopter is composed by the contributions of both the white noise excitation and the aerodynamic harmonics acting at discrete operational frequencies equal to the multiple of the fundamental angular velocity of the rotor. As a result, the system cannot be considered excited by a pure white noise input and then the OMA methodologies cannot be theoretically applied to the output responses to estimate the dynamical behavior of the helicopter. The approach developed in this thesis is capable to deal with this problem, since the Entropy index is introduced to identify such operational frequencies, and then the effects of the removal of the harmonic contributions from the Frequency Response Functions (FRF) can be evaluated. In order to assess the overall accuracy in the modal parameter estimates, an experimental investigation, carried out on a helicopter UAV flying at different conditions, i.e. in- and out-of-ground effect hovering and forward flight at several advance ratios, is presented. The modified HTM is applied to the acceleration responses recorded on the helicopter fuselage during the flight and the improvements of this OMA method are investigated in evaluating the modal parameters of the helicopter, especially in the frequency range

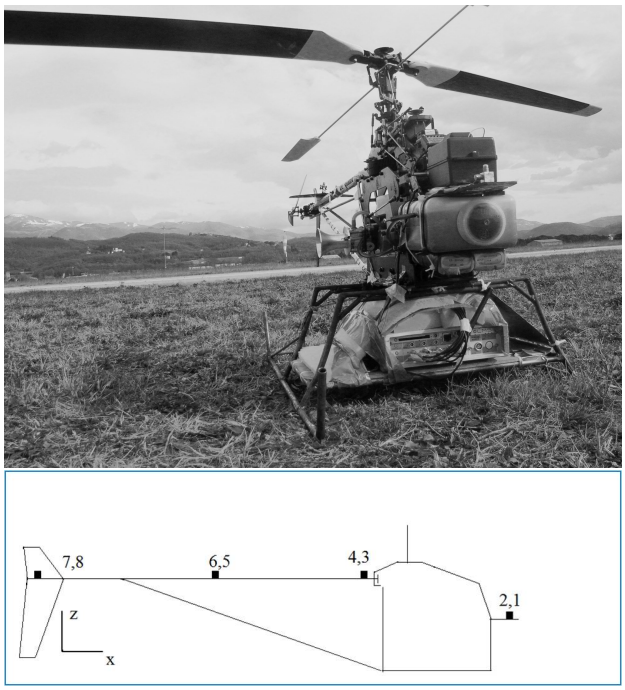

Figure 7.1: Experimental Setup of the Flight tests on the helicopter UAV.

that could be considered critical for the safe life of the structure, i.e. when the resonance is close to the harmonic excitation.

7.1 Experimental Setup

The objective of the experimental investigations is a sensitivity analysis of the effects of the flying conditions on the modal parameters of the fuselage of the Bergen "Industrial Twin" rotorcraft. Different flight conditions are experienced, i.e. in- and out-of-ground effect hovering and forward flight at several advance ratios, for at least $30\,\mathrm{s}$ each. This UAV helicopter, see Fig.7.1, is capable to complete missions lasting about 30 minutes carrying an $11\,\mathrm{Kg}$ payload. The helicopter is propelled by a two-stroke 52 cc. bi-cylinder engine developing about $8\,\mathrm{Hp}$ useful to drive both the two-bladed main rotor and the two-bladed tail rotor. The main and the tail rotor blades are made by a carbon fiber composite material. Their dimensions are $810 \times 94\,\mathrm{mm}$ and $130 \times 36\,\mathrm{mm}$ respectively. The main fuselage structure is made by an aluminum alloy and bakelite. The flight test data are measured using the LMS SCADAS Mobile hardware, which allows

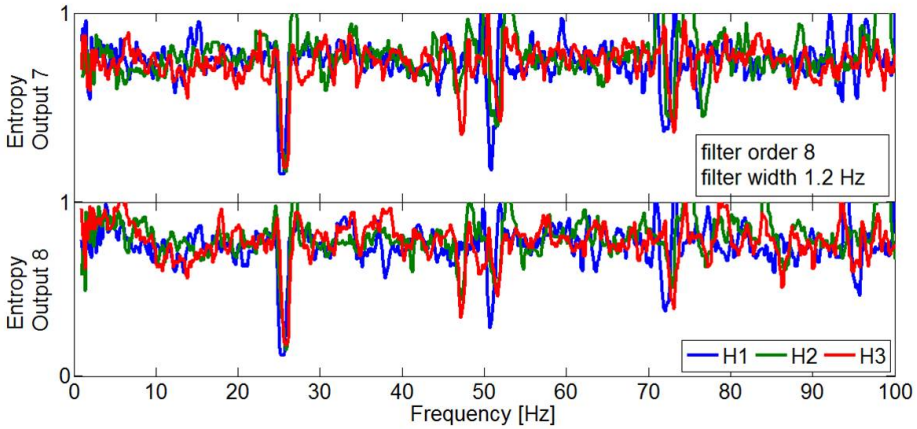

Figure 7.2: Entropy index for different Hovering conditions.

the simultaneous acquisition of 8 accelerometer signals and the record of data about position and speed of the helicopter measured by the GPS. Two different experimental setups are considered in order to analyze hovering and forward flight conditions. In the first case, the overall mass of the rotorcraft with the payload is about $14\,\mathrm{Kg}$; the sensors are located at four positions on the tail boom and on the fuselage along the vertical and lateral directions. In the second case, the overall mass was about $11\,\mathrm{Kg}$ and the accelerometer sensors were placed only along the vertical direction. The location of the accelerometers is illustrated in Fig.7.1, in which the sensors are indicated with the number used during the test: the numbers refer to the lateral and vertical direction.

7.2 Hovering conditions

During the flight tests the helicopter experiences three hovering at different altitudes, $2\,\mathrm{m}$, $10\,\mathrm{m}$ and $15\,\mathrm{m}$, among which the first one is in-ground-effect (IGE) and the others are out-of-ground-effect (OGE). The overall recorded accelerometer signals are subdivided in three time intervals of about $60\,\mathrm{s}$ with 215 samples. A sixth order Butterworth filtering, centered at each frequency available in the test, is carried out, so that the Entropy statistical index can be calculated as a frequency function for each measurement point and flight conditions. In Fig.7.2 the Entropy index is depicted for the different hovering conditions for the accelerometers at the end of the tail boom in vertical and lateral direction. From the several minima it

Table 7.1: Operational frequencies during the hovering flight conditions.

$\#f_{op}$	1/rev [Hz]	1.8/rev [Hz]	2 [Hz]	2.8/rev [Hz]	3/rev [Hz]
Hovering 1 (IGE)	25.5	45.9	51.0	71.4	76.5
Hovering 2 (OGE)	25.8	46.6	51.6	72.2	77.4
Hovering 3 (OGE)	26.0	46.8	52.0	72.8	78.0

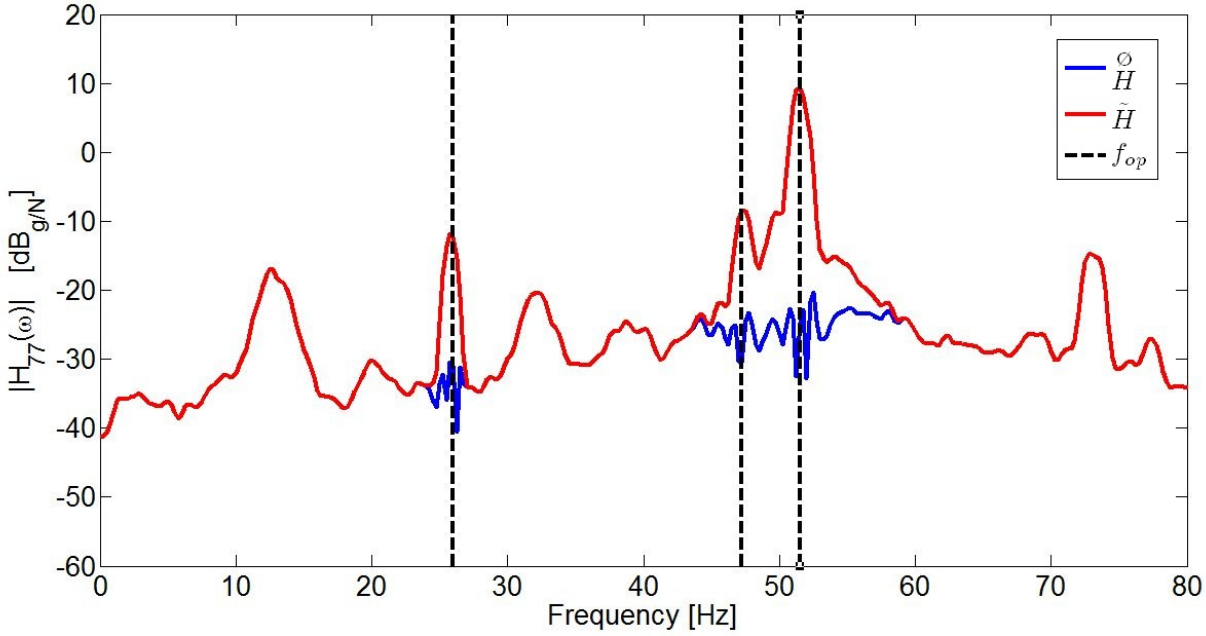

Figure 7.3: Third Hovering: Effect of the removal of the harmonic excitation in the FRF corresponding to the lateral accelerometer at the end of the tail boom.

is possible to evaluate the frequencies of the harmonic excitation characterizing the working condition of the rotorcraft, see Tab.7.1. It is worth noting the presence of spurious, with respect to the multiple of the fundamental rotating frequency, operational frequencies. There are not remarkable differences between the output accelerometer signals, as a consequence the harmonic excitation spread around all the structure. The operational frequencies are affected by the weak variation of the rotational speed of the rotor with the altitude. The evaluation of the biased frequency response functions of the vibrating structure, skewed by the presence of the harmonic loading, is performed by applying the Hilbert Transform method described in the theoretical part. Once the operational frequencies are identified using the non-gaussianity test, their contribution can be removed to achieve the so-called harmonic-free FRF. In Fig.7.3, the driving point FRF, evaluated at the end of the tail boom is depicted to put in evidence the effects of the harmonic removal;

the dashed-vertical lines correspond to the operational frequencies. These contributions to the structural responses are usually represented by the spikes superimposed to the frequency response function and they could be viewed, in turn, as normal modes with practical null values of the associated damping ratios. Finally, the modal analysis is performed to evaluate the true normal modes of the helicopter in terms of natural frequencies, damping ratios and shapes, see Tab.7.2. The natural frequencies of the first lateral and

Table 7.2: Normal modes of the helicopter during the hovering flight conditions.

Mode #	1		2		3		4		5	
	f_n [Hz]	ζ_n [%]	f_n [Hz]	ζ_n [%]	f_n [Hz]	ζ_n [%]	f_n [Hz]	ζ_n [%]	f_n [Hz]	ζ_n [%]
Hovering 1 (IGE)	12.2	2.1	18.8	2.1	32.3	1.0	—	—	63.9	1.2
Hovering 2 (OGE)	12.5	1.9	20.0	1.6	32.3	0.8	38.7	1.9	64.0	1.2
Hovering 3 (OGE)	12.5	1.5	20.0	1.8	32.3	0.7	38.7	1.9	64.7	1.0

vertical bending modes of the helicopter, that are the first and the third ones in Tab.7.2, are not influenced by the flight condition, while the correspondent damping ratios decreases of about the $30\,\%$ from the first to the third hovering. On the contrary, the second and the fourth mode seems to suffer from the ground effect. In the first case, the IGE natural frequency is lesser by about $6\,\%$ from the corresponding OGE hovering values. Moreover, in the second case, the normal mode cannot be estimated as it was not excited by the operating conditions.

7.3 Forward Flight conditions

The helicopter flew for $400\,\mathrm{s}$ performing the same flight path at different velocities. The whole recorded signals are divided into 14 data blocks corresponding to different flight phases, see Tab.7.3. The last condition corresponds to out-of-ground effect hovering flight and has been performed to collect the data for a reference null advance speed. The statistical analyses of all the accelerometer responses allow the evaluation of the frequencies in which the harmonic loading is acting at each flight configuration, see Fig.7.4. An accurate investigation of such operational frequencies is carried out by changing the characteristics of

Table 7.3: Forward flight conditions.

#	1	2	3	4	5	6	7
Speed [m/s]	1.7	4.7	4.6	6.4	7.9	11.4	12.7
Advance ratio	0.013	0.036	0.035	0.049	0.061	0.087	0.098
#	8	9	10	11	12	13	14
Speed [m/s]	16.1	14.6	20.8	12.5	13.5	7.5	0.00
Advance ratio	0.124	0.113	0.160	0.096	0.104	0.058	0.00

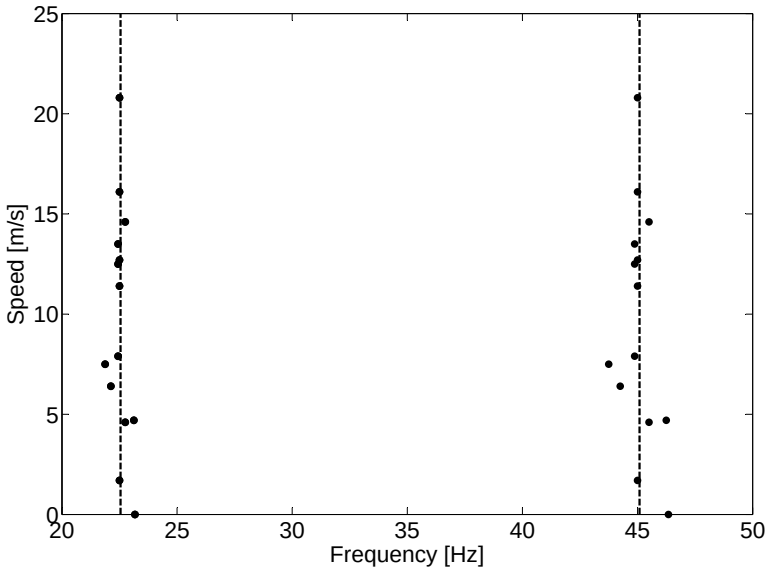

Figure 7.4: Evaluation of the harmonic excitation loading using the Entropy index for different forward flight conditions.

the Butterworth filter in terms of its order, from 4 to 10, and frequency width, from 0.5 to $3.0\,\mathrm{Hz}$. For the sake of brevity, only the results coming from the analyses of the fifth flight configuration are shown in Fig.7.5, in which it is worth noting that the approach is not so sensitive to Butterworth filter parameters provided. For the performed experimental tests, the filter frequency width greater than $0.5\,\mathrm{Hz}$ centered in each frequency line of the analysis and a filter order at least of 4 is seen to be satisfactory. Then, the harmonic-free FRFs are obtained by removing the effects of the operational frequencies. In Fig.7.6, the results of the harmonic removal are presented for the 13th flight configuration. In particular, the driving point FRF of the vertical accelerometer located at the end of the tail boom is depicted before and after

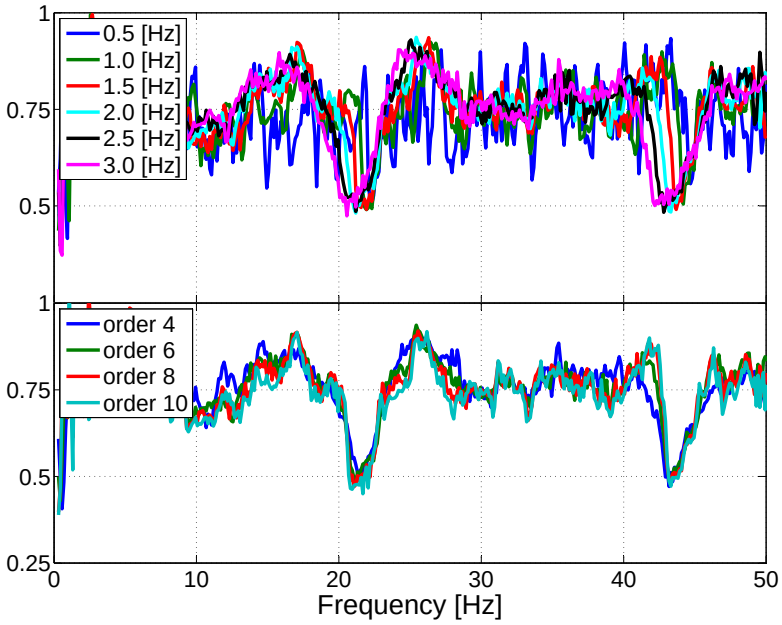

Figure 7.5: Forward Flight with advance ratio 0.061: Effects of the order of the Butterworth filter, frequency width equal to $2.0\,\mathrm{Hz}$, in the harmonic identification by the Entropy approach.

the application of the removal procedure. The harmonic-free FRF, $\overset{\oslash}{\mathbf{H}}(\omega)$, is depicted by the blue line and it is obtained from the difference between the HTM skewed FRF, $\tilde{\mathbf{H}}(\omega)$, and the harmonic FRF, $\overset{\mathrm{O}}{\mathbf{H}}(\omega)$, represented by the red and the dotted black line, respectively. Because only the vertical accelerometers are recorded, a modal analysis on a such complex structure is quite difficult. Nevertheless, the estimate of the variation of the natural frequency and the damping ratio of the first vertical bending mode of the fuselage with respect to the speed are reported in Fig.7.7. The modal parameter variation seems to linearly vary with respect to the speed of the helicopter; in particular, the natural frequency increases about $4\,\%$ and the damping ratio decreases about $40\,\%$. Similar trend can be highlighted by examining the normal modes of the tail boom in the frequency range of the analysis, see Fig.7.8: the natural frequencies increase about $6\,\%$ and $7\,\%$, the damping ratios decreases about $90\,\%$ and $30\,\%$, respectively.

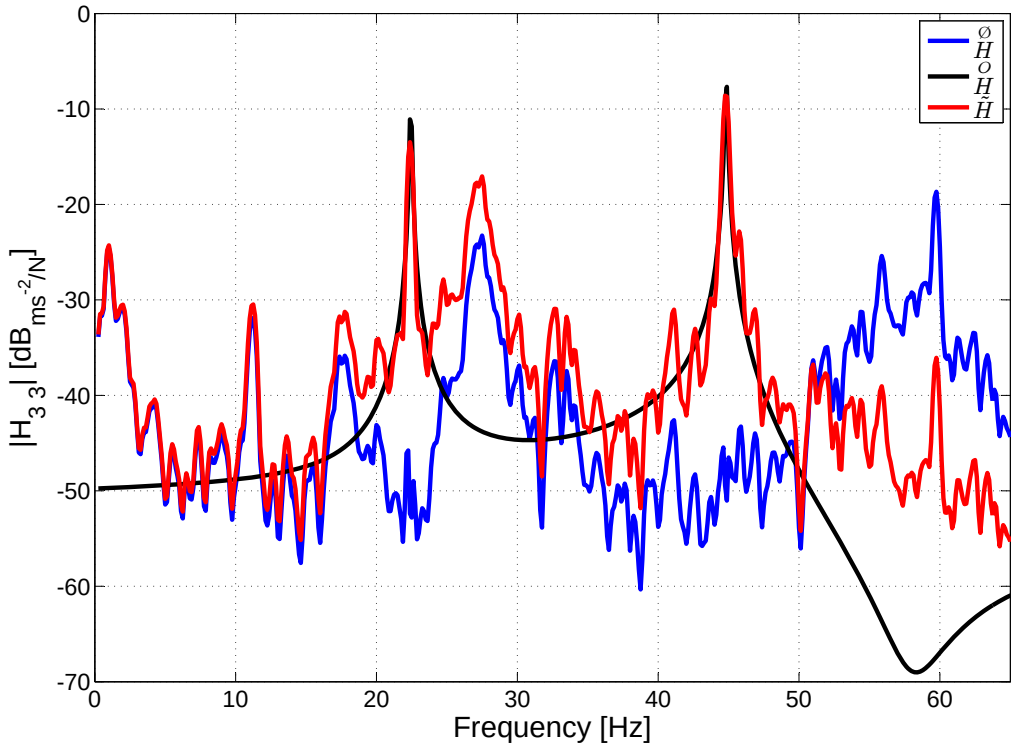

Figure 7.6: 13th Forward Flight: Effect of the removal of the harmonic excitation in the FRF corresponding to the vertical accelerometer at the end of the tail boom.

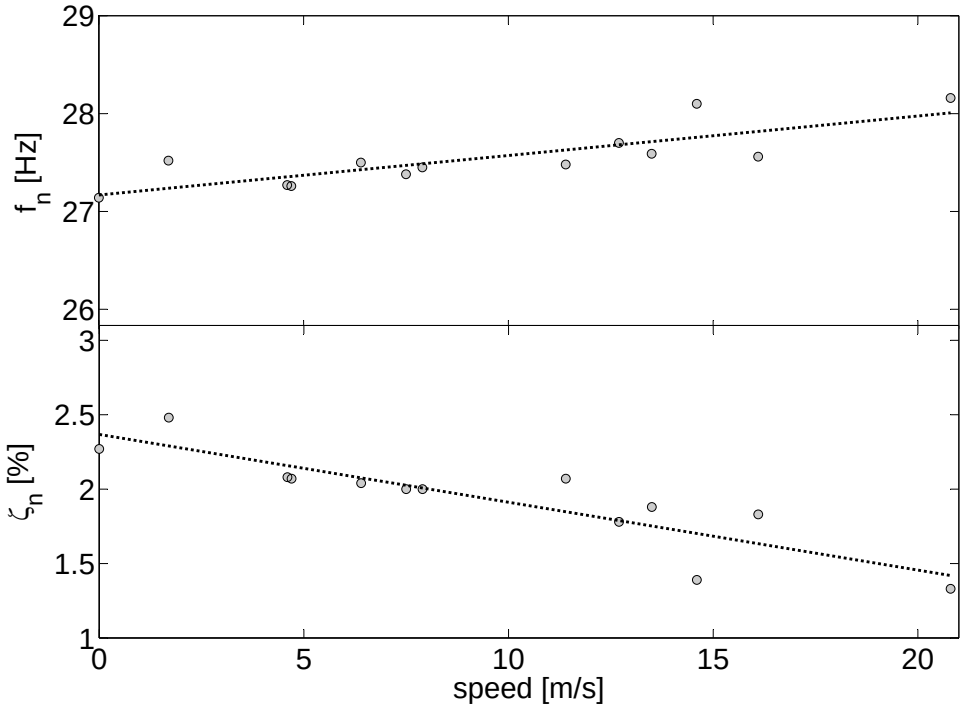

Figure 7.7: First vertical bending mode natural frequency and damping ratio with respect to the advance ratio of the forward flight.

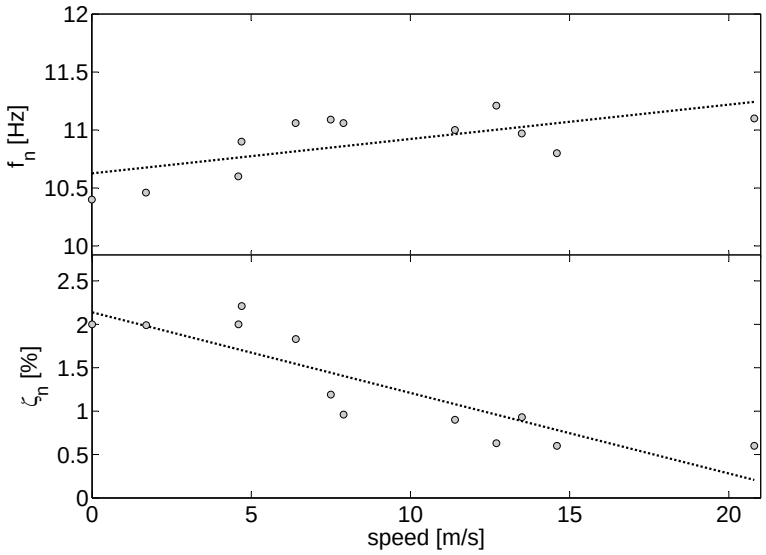

(a) 1st vertical mode

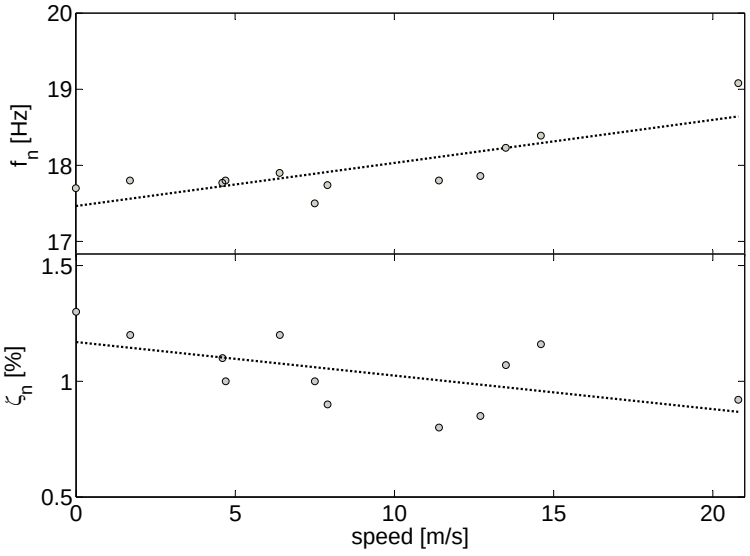

(b) 2nd vertical mode

Figure 7.8: Natural frequencies and damping ratios of the normal modes of the tail boom with respect to the advance ratio of the forward flight.

Chapter 8

Environmental Tests

Environmental tests are widely used to qualify structures for space missions, because the benchmark test facilities allow the replication of the loading conditions acting on a system during the different phases of the mission. In this chapter, an Output-Only-based technique is proposed to estimate the full modal parameters, in the frame of the environmental test-ing, to increase the accuracy of the dynamic identification and to reduce the overall time and cost associated to the qualification process. The Hilbert Transform Method is applied for the estimate of the "biased" Frequency Response Functions, FRFs, whereas the evaluation of the modal masses associated to each mode is carried out by the application of various mass perturbation methods as described in Sec.2.6. The robustness of these approaches will be assessed through environmental tests carried out on spacecraft structures, such as a robotic arm intended for space applications and a tank prototype of the Vega launcher. The accuracy of the proposed method will be finally evaluated by comparing the FRF estimates, obtained with the Output-Only approach, with the ones gained using the standard Input/Output technique.

8.1 Introduction

Space structures are requested to undergo environmental testing in order to be qualified for flight. During these tests, the capability of the structures to withstand the rigors of structural and airborne vibrations are

verified. These tests are carried out to check that when exciting the base of the structure with a known acceleration profile, the output accelerations, evaluated at selected points of the structure, are below a prescribed level and that the lower peak of resonance is at a higher frequency than a prescribed value. Both the maximum acceleration responses and the minimum resonance frequency are launcher dependent, see Launcher User's Manuals belonging to Arianespace. Generally, two main tests are provided during the environmental testing, which are the design qualification tests, and the acceptance tests. The first test campaign, allows the designer to demonstrate that the structural model is capable to withstand the vibration levels characterizing the launch. In addition, by estimating the natural frequencies of the system and by measuring the corresponding output responses, the mathematical model validation could be carried out. The last type of tests, performed on the flight model, are essentials to prove that the equipments, considered in their flight conditions, safely operate without any degradations when subjected to the high level vibration environment characterizing the first phase of the launch. Both the qualification and acceptance tests consider three type of base excitations, Ref.[69]. In the so called sine tests, the structure is excited by a progressive sweep of frequencies and amplitudes, whereas in the random tests such a harmonic base excitation is randomized. Finally, in the third type of excitation, shock test, the base gives the system a sharp and severe excitation in order to simulate the shocks felt during the separation stages and/or the engine firings. Referring to the qualification tests, the developments of the Operational Modal Analysis methods give a new prospective to the theoretical model validation, because of their capabilities to estimate the modal parameters only from the measurements of the system outputs. Therefore, recalling the main hypothesis of all the OMA approaches concerning the input excitation, which is a broad band white noise excitation, and considering the random vibration tests, it should be possible to derive the modal parameters of the vibrating structures in their actual operating conditions, directly from the environmental testing. The test article is fixed to a supporting base, which provides the required random base excitation. This base motion is assumed to stochastically excite the structure with a frequency independent spectra.

Under this hypothesis the Hilbert Transform Method is applied for the estimate of the "biased" Frequency Response Functions, FRFs, between the unknown excitation loading and the corresponding response accelerations. As a result, it is possible to derive the natural frequencies, damping ratios and mode shapes by means of residue/pole least-squared technique in the frequency domain. Nevertheless, because the intrinsic impossibility of the OMA approaches to estimate the modal masses, and because of no input excitations are measured, the full modal model could not be available from these tests. In this thesis, a novel test procedure is proposed to overcome this limitation, by taking advantages of previous works, Refs.[70], [2] and [71], available in literature. This novel possibility allows the designer to obtain the full modal model of the structure directly from random tests, that, in turn, could be used to improve the accuracy in the theoretical/numerical validation phase in structural updating problems, in model synthesis, not considering the overall cost reduction that could be achieved by optimizing this novel test procedure. The proposed approach is based on the estimate of the modal masses, by applying the mass-change methodologies to obtain the complete set of the dynamic parameters of the tested structure in terms of frequency response functions. This modal scaling techniques, already applied to a lumped parameter numerical model as in Sec.3.5, is performed on spacecraft structures such as the tank prototype of VEGA launcher and a model of a robotic arm intended for space operations.

8.2 AVUM tank prototype

The experimental investigations described in this section are performed during a test campaign at the AVIO facilities in the establishment of Colleferro (Rome, Italy). The AVUM tank prototype filled with a inert liquid propellant is put up the vibration bench as shown in Fig.8.1 with 42 accelerometers placed along two meridians at 0 deg and 90 deg with respect to the reference system and indicated with G00 and G90 in Fig.8.2. Several OMA approaches are used to estimate the modal parameters of the structure in which the random excitation is provided by tapping fingers as a first experimental investigation. In addition,

Figure 8.1: Experimental layout of the AVUM tank prototype.

a traditional hammer test is performed to the structure in order to have a reference set of FRFs. The input loading excites the system at the North Pole, in the x-direction, and measured by a load cell, with sensitivity equal to 2.3mV/N. Both the input and output signals are recorded and processed using the LMS Scadas III and the LMS Test.Lab Impact Testing. In order to assess the accuracy of the modal parameters, estimated using the OMA approaches, a comparison with those gained with the Input/Output testing is performed. As reported in Tab.8.1, a good correlation is obtained between the different estimates except for the damping ratios, where major differences, but acceptable, are identified. Then, the structure is

Table 8.1: Relative errors between the Output-Only Random and hammer test of the AVUM tank prototype.

Output-Only Method	Mode 1		Mode 2		Mode 3	
	ε_{f_n} [%]	ε_{ζ_n} [%]	ε_{f_n} [%]	ε_{ζ_n} [%]	ε_{f_n} [%]	ε_{ζ_n} [%]
FDD	0.15	0.91	0.15	41.91	0.15	49.86
HTM	0.14	11.36	0.03	10.64	0.12	21.62
BR-SSI	0.15	6.36	0.08	3.83	0.01	11.76
f-SSI	0.15	8.18	0.04	1.49	0.12	5.41

tested with a random base excitation in the vertical axis. In this case, the time responses were are recorded by the LDS-Dactron acquisition system, available at the AVIO laboratories, during the random excitation

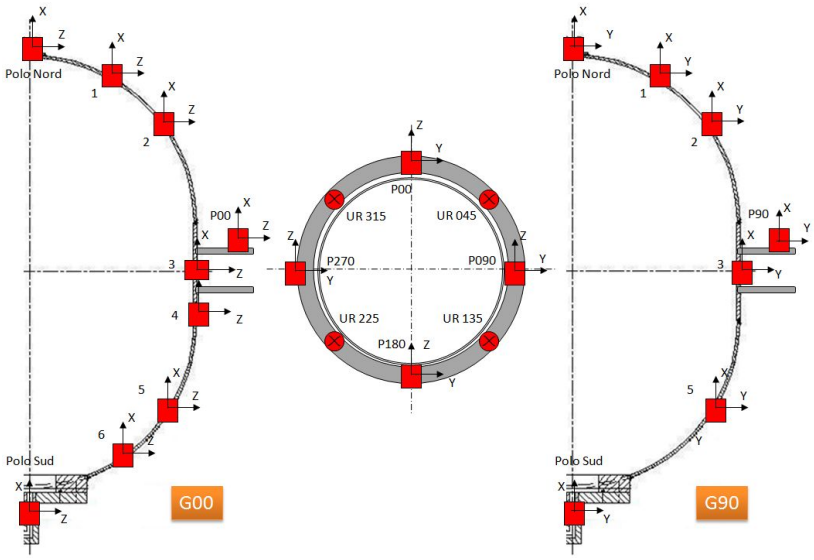

Figure 8.2: Location of the measurement points of the AVUM tank prototype.

provided by the shaker. The length of the time histories was about 51s corresponding to $2^{16} = 65536$ samples. The natural frequencies and damping ratios estimated by the OMA approaches differ from the previous ones, as a reduction of about $3.86\,\%$ and $1.13\,\%$ for the natural frequencies and an increase of the damping ratios of about $172.73\,\%$ and $33.33\,\%$, for the first axial and lateral modes respectively are found. This is probably due to the interaction of the AVUM tank prototype structure with the shaker that provides the base excitation and due to an higher participation of the liquid contained in the vibrating tank with respect to the previous tests where the system was kept at rest in the test configuration. Both these phenomena contribute to increase the mass of the system and to dissipate the elastic energy.

The experimental setup allows also to perform a sine sweep test in vertical direction to detect the resonance frequencies of the AVUM tank prototype . The observed natural frequencies perfectly agree with the last random test, proving not only the effectiveness of the OMA analysis, but also the interaction between the tested structure and the moving shaker. It is worth noting that, thanks to the OMA, it is possible to identify the damping coefficients directly from data recorded during the environmental random test with the structure configuration much closer to the operating conditions than the configuration traditionally used for the standard Input/Output experimental modal analysis. Then, the behaviour of the mode scaling

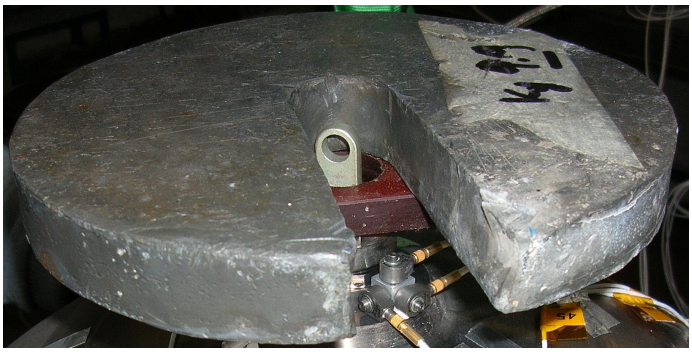

Figure 8.3: Mass perturbation for the mode scaling of the AVUM tank prototype.

procedures is tested by perturbing the AVUM tank prototype with a lumped mass of $9.9\,\mathrm{Kg}$ placed on the North Pole, along the symmetry axis, as shown in Fig.8.3. It has to be noted that this concentrated mass perturbation was the only experimentally achievable during the test campaign, although it is intrusive and did not allow to perform a complete second test campaign. Therefore, only one more test is performed with few sensors to evaluate the variation of the poles. The robustness of the scaling procedures to the accuracy of mode estimating process is here reported. This task has been pursued by introducing some uncertainties in the modified mode shapes, that is the mode shapes corresponding to the mass perturbed structure. Specifically, the reference mode shapes, identified by the OMA method, are randomly modified by using a normal with zero-mean value probabilistic density function, pdf, with a prescribed value of the variance. Therefore, the perturbed modal parameters were achieved by exciting the structure with a random load carried out with tapping fingers. The resulting frequency response functions are then compared

Table 8.2: Natural frequency shifts due to mass perturbation of the AVUM tank prototype.

	Mode 1	Mode 2	Mode 3
$\Delta f_n/f_n$ %	5.88	22.20	6.82

with the corresponding ones obtained with the traditional Input/Output method. Obviously, by referring to this specific test setup, the generality of the findings is not impaired because of the already demonstrated capability of the OMA approaches to identify the modal parameters directly from the environmental testing

setup. As a consequence of the mass perturbation, an average natural frequency shift of about is $10\,\%$, with a maximum value of more than $20\,\%$, corresponding to the second mode, is obtained, as reported in Tab.8.2. Two different uncertainty scenarios of the mode shapes are reported for brevity. In the first one, the variance of the pdf is set to $1/30$, to which corresponds a random variation of each component of the considered modes less than $10\,\%$ of the maximum displacement (equal to 1). This could be considered as a practically immaterial change in the modal base as the correlation between the reference and the modified modes is almost unitary when evaluated with the MAC value. The FRFs derived by these modal data are depicted in Fig.8.4, where the one estimated with the well known H2 algorithm (denoted with IO - Experimental) in the experimental Input/Output testing is compared with the one synthesized with the modal basis from Input/Output analysis (IO - Synthesized) together with those achieved in the OMA (denoted as OO - CMS and OO - RBN for the two Output-Only methods respectively). The same analysis

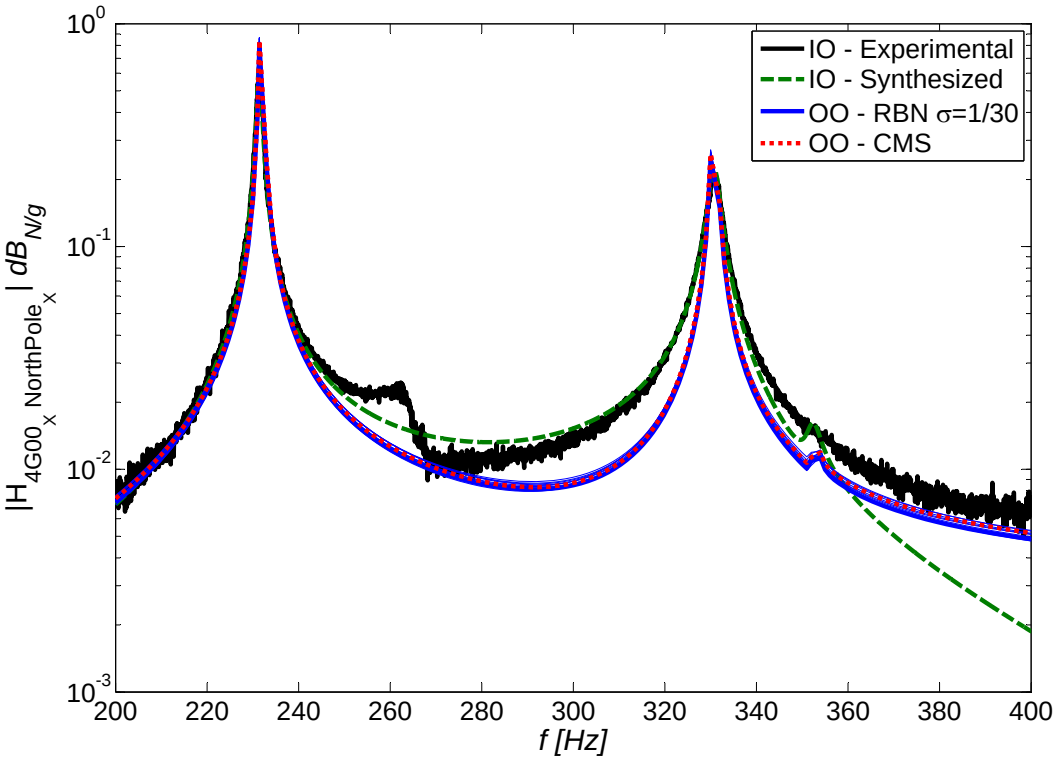

Figure 8.4: Comparison between the different FRF estimates for the AVUM tank prototype (variance $1/30$).

is carried with the last uncertainty scenario which considers an higher variance of the pdf value that is set equal to 5/30, see Fig.8.5. In this case, the random uncertainties involve a mode variation of about 80% in terms of the MAC value. Both approaches are capable to correctly estimate the FRFs directly from

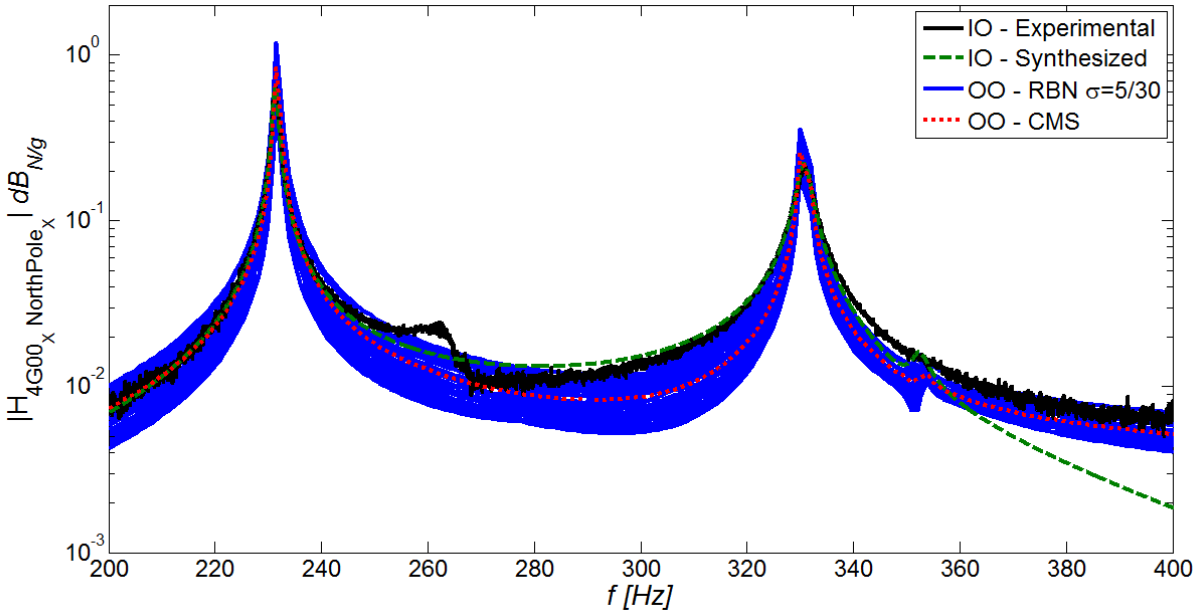

Figure 8.5: Comparison between the different FRF estimates for the AVUM tank prototype (variance 5/30).

operational data. The CMS method is more robust with respect to the RBN approach due to the choice made on the type of the mass perturbation. Nevertheless, this last method showed a more than acceptable behaviour in the FRF estimate, especially in the neighbourhood of the peak of resonance.

8.3 Robotic Arm

The tested manipulator is a part of a set-up built in the Guidance and Navigation Lab at the Università di Roma "La Sapienza" to simulate (in 2d) the behavior of robotic arms devoted to grasping missions and to validate the relevant guidance and control laws. Palmerini et al. gave more rationale and theoretical aspects of this project in Ref.[72].

Figure 8.6 provides a sketch of a preliminary set-up with (a) the arms, (b) the stepper motors, (c) the gear, equipping the shoulder motor to limit the speed and increase the torque, (d) the cradle to host the

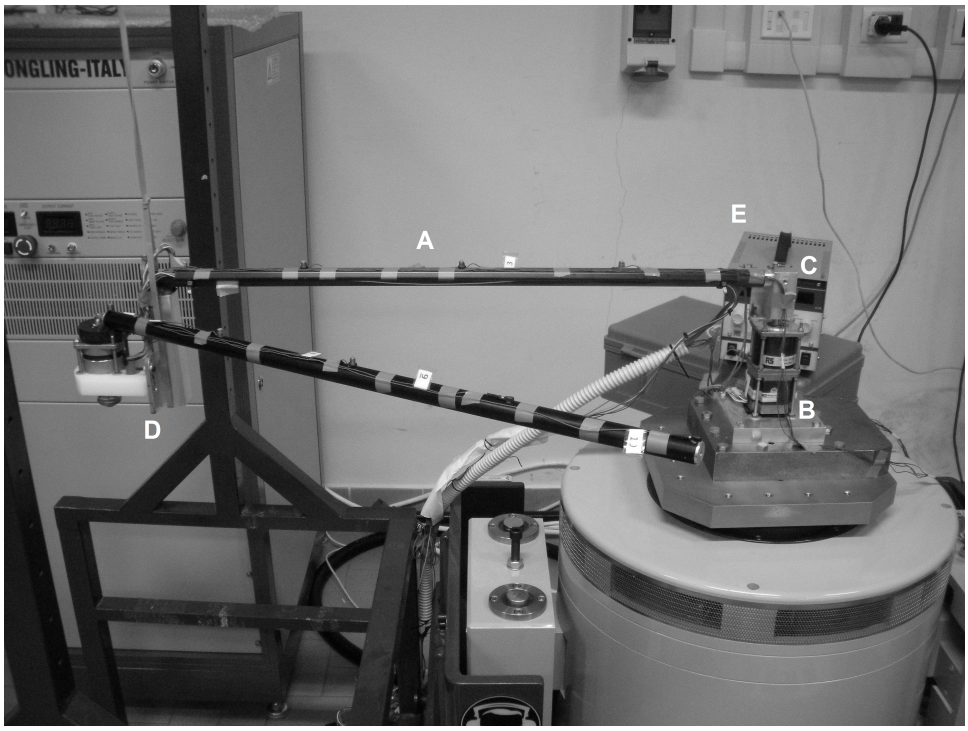

Figure 8.6: Vertical axis test setup of the robotic arm.

elbow motor, (e) the power supplies. The overall set-up includes also the limited friction table, the printed circuit boards to drive the stepper motors, a dissipating section to distribute the heat generated by the motor circuitry, and an electronic board introduced to decouple the high current power section form the PC used to control and command the set-up. In this experimental analysis, the environmental test facility, run by the Department of Mechanical and Aerospace Engineering of the University of Rome "La Sapienza", was used to excite the structure with a prescribed random base excitation and to record the required time histories. It is formed by an electro-dynamic shaker (Dong Ling, model ES-6-200 capable to provide $6\,\mathrm{kN}$ random force, $12\,\mathrm{kN}$ shock force, and $6\,\mathrm{kN}$ (peak) sine force. The system is completed with a slip table of size $700 \times 700\,\mathrm{mm}$ for horizontal vibrations and with a $300 \times 300\,\mathrm{mm}$ square head expander for the vertical excitation. The test operations are fully controlled within the environmental testing tool available in the LMS - Test.Lab software. Also for the robotic arm, an accuracy analysis has been performed by carrying out both the Input/Output and the operational modal analysis with data directly recorded during the random-base vibration tests, carried out in the vertical direction, as shown in Fig.8.6. Ten accelerometers

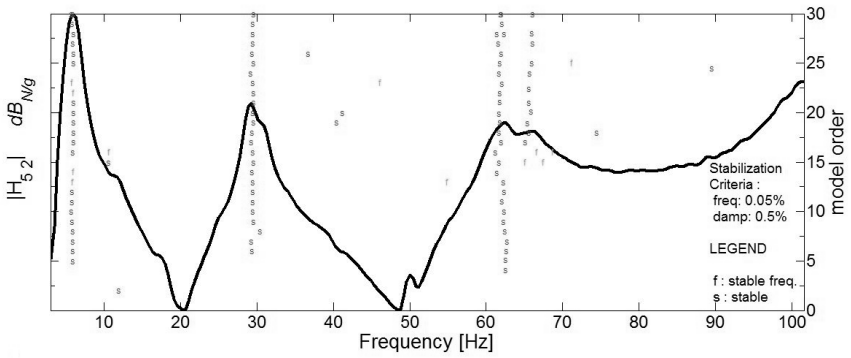

Figure 8.7: Stabilization diagram with HTM.

Table 8.3: Effects of the mass perturbation of in the robotic arm.

Mode #	$f_n\ [Hz]$	$\tilde{f}_n\ [Hz]$	$\Delta f_n\ [\%]$
1	5.86	5.46	7.3
2	29.1	28.3	2.8
3	61.8	59.5	3.9

are uniformly spaced on the arms with the control placed on the head expander. During the random environmental test, the shaker provides a constant base excitation from 5 to $2000\,\mathrm{Hz}$ with rms equal to $1\,\mathrm{g}$. In the Input/Output test, the experimental setup is the same but the shaker do not provide excitation; the FRFs are measured by hitting the structure with the hammer on the inner arm.

The HTM is capable to clearly identify the modal parameters from the bias FRFs coming from the accelerometer responses, as shown in Fig.8.7 where the stabilization diagram together with one normalized FRF is plotted. The effects of the operating conditions on the dynamic characteristics of the robotic arm is summarized in Fig.8.8, where the changes in the first three poles are shown in the root locus plot. Both the effects of the increase of the moving weight and the increase of the energy dissipation are found as the natural frequencies reduce and the damping ratios exhibit an increase of their values in a similar fashion as in the previously considered test case.

Then, the mass of the system is perturbed by adding $17\,\mathrm{gr}$ at each node, for a total of about $1\,\%$

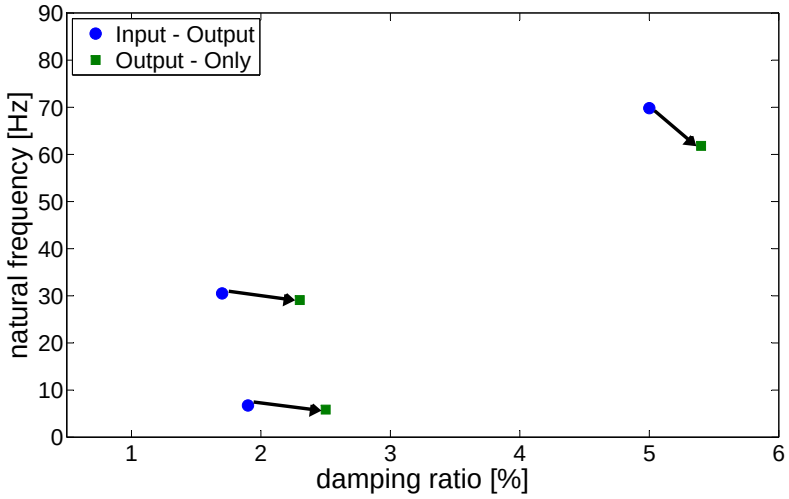

Figure 8.8: Sensitivity of the poles of the robotic arm to the operating conditions.

increase of the mass of the vibrating structure. The corresponding natural frequency shifts are reported in Tab.8.3, whereas the mode shapes are practically un-changed, according to the average MAC value of about $90\,\%$. Finally, the modal masses were estimated with the two methods and then the frequency response functions synthesized. As one can see from Fig.8.9, the considered approaches gave almost the same representation of the dynamic behavior of the structure, confirming their robustness also in this test case. From the same picture, it is evident the detrimental effects on the system identification process of not considering the structure under its actual operating working conditions. Indeed, the shifts of the poles reported in Fig.8.9 have the consequence of a poor correlation between the OMA and Input/Output analyses both with respect to the pole placement, and with respect to the level of vibrations.

8.4 Concluding Remarks

Environmental tests are widely used to validate the theoretical (and/or numerical) model and to qualify structures for space missions. Due to the relevant costs associated to this task, the novel application of

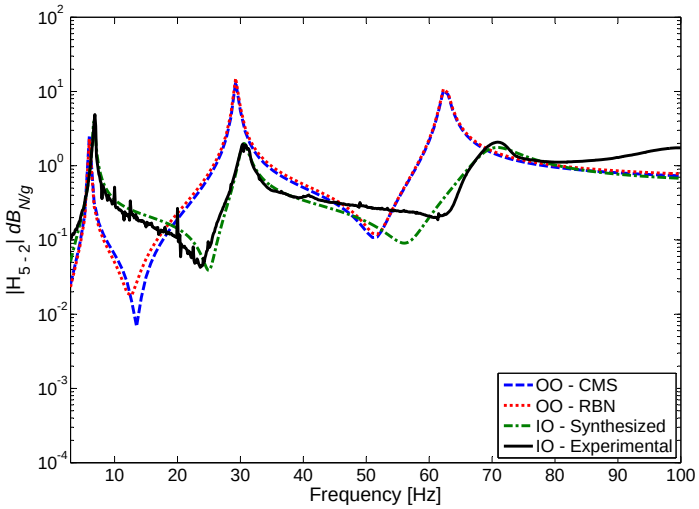

Figure 8.9: Comparison between the FRFs for the robotic arm.

the operational modal analysis is of great interest from the point of view of the industries because not only a reduction of the cost is foreseen, but also an optimization of the design phase could be achieved. The proposed approach, based on the identification of the biased frequency response functions using the OMA and the mass perturbation approach, for the mode shape scaling, is capable to identify a full set of modal parameters, i.e. natural frequencies, damping ratios, mode shapes, and modal masses. The method has been already tested using a numerical model in Sec.3.5 and in this chapter it is implemented for two different experimental tests carried out both in the AVIO laboratories and in the laboratories of the Department of Mechanical and Aerospace Engineering of the University of Rome "La Sapienza". The presented test activities, one related to the AVUM tank system, and the other related to the robotic arm intended for space applications allowed the assessment of the proposed approach highlighting the effects of the shaker-structure coupling, and the effects of incompleteness of the estimated modal basis. The overall good agreement of the frequency response functions obtained with the proposed approach with those estimated with the "traditional" Input/Output method is an important evidence of the robustness of the OMA methods.

Part III

Application in State-of-the-art Rotorcraft Technology

Introduction

In helicopters, Ref.[9], the main source of vibration is due to the unsteady aerodynamic loads produced by blade vortex interaction and dynamic stall effects in the forward flight condition. These nonlinear aerodynamic effects generate the periodic forced vibration of the blades that is characterized by a broad band spectrum. In steady-state forward flight, due to the "filtering" characteristics of the hub, vibration is mainly characterized by a higher harmonic excitation of the helicopter airframe at the frequencies nN_b/rev, where n is an arbitrary integer number and N_b is the number of the blades. This excitation, generated by higher harmonic loading of the blades in the rotating frame, cannot be suppressed easily. In general, the vibration level is low in hover flight and increases with the forward flight, in fact limiting the maximum speed of the aircraft.

Different designs been suggested for the control of helicopter vibration, either passive or active. In particular two approaches belonging to the latter group are known as higher harmonic control (HHC) and individual blade control (IBC), according to their philosophy. In the first group, the time-dependent pitch control is introduced in the non-rotating frame through the helicopter swashplate. In the second, group each blade is individually controlled in the rotating frame. Following this control strategy, the Smart Hybrid Active Rotor Control System (SHARCS) project was conceived to demonstrate the feasibility of such "hybrid" control system for the simultaneous reduction of vibration and noise on helicopters, Ref.[11]. The objective is to design and build a scaled rotor for whirl tower and wind tunnel testing featuring three active control subsystems:

- Active Pitch Link (APL) to change the blade's modal frequencies and/or damping;

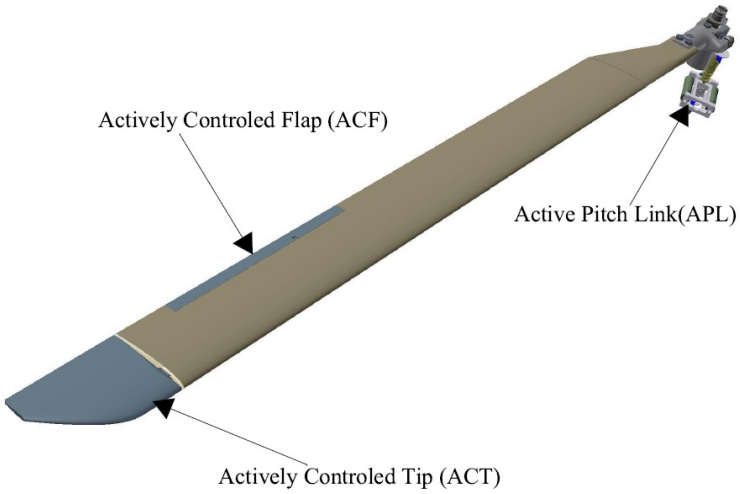

Figure 8.10: The SHARCS blade with three individual control means [11].

- Actively Controlled Flap (ACF) to actively modify the flow;
- Actively Controlled Tip (ACT) to alter the strength and the location of vortices at the blade's tip to control Blade Vortex Interaction.

The first two systems are primarily used to reduce vibration, whereas the third to reduce noise. Figure 8.10 illustrates the SHARCS blade with the three IBC systems.

The present work focuses in the APL subsystem, which is based on the idea that by actively changing the dynamic stiffness of the pitch link it is possible to control the vibration transmitted into the airframe. Within the SHARCS project, the achievement of an actively controlled pitch link has been supported by the development of the Smart Spring, as a spring with variable stiffness controlled by a piezoelectric device, Ref.[73]. The Smart Spring patented concept, as represented in Fig.8.11, allows to change the stiffness of a system adaptively in the range of $[k1, (k1 + k2)]$ by activating the smart material (piezoceramic) actuator. The main advantage of such configuration is that despite the small stroke, the large force of a piezoelectric actuator can be efficiently utilized. As described in Ref.[74], in Fig.8.11, the primary spring designated by k_1 is attached to a moving structure that has a built-in sleeve. An external vibratory force $F(t)$ is applied to the structure having mass m_1. A piezoelectric actuator is attached to the secondary spring designated by

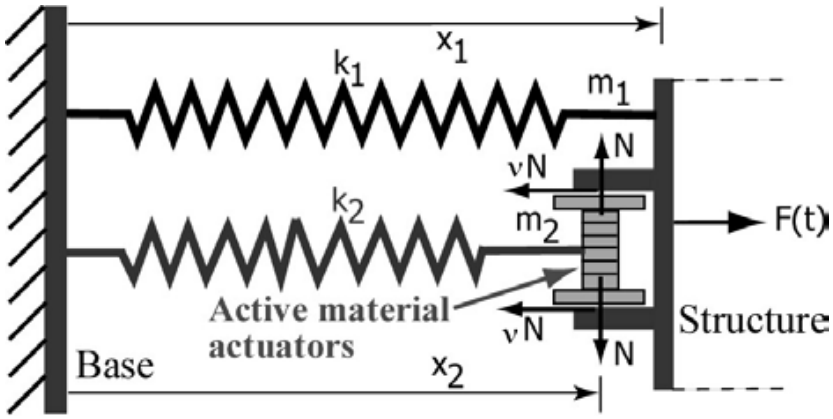

Figure 8.11: The Smart Spring concept [73].

k_2, which is inserted into the sleeve. When the actuator is off, the sleeve can move freely and the dynamic response is determined by the single primary mass-spring system consisting of m_1 and k_1. When the actuator is powered, a normal force $N(t)$ is generated to engage to the structure the secondary mass-spring system, consisting of m_2 and k_2. If the resultant friction force $\mu N(t)$ is sufficiently large, the two springs become fully coupled and a combination of two springs in parallel is obtained. Therefore, the stiffness of the system increases from its original value k_1 to the final value $k_1 + k_2$ and the mass of the system increases from m_1 to the final value $m_1 + m_2$. The dynamic friction force $\mu N(t)$ applied on the sleeve can be controlled by an external voltage stimulus to the actuator, forcing the secondary mass and spring designated by m_2 and k_2 to become increasingly coupled with the primary mass-spring system. If sliding of the secondary mass against the contact surfaces of the sleeve in the primary mass is present, the resulting change in stiffness is coupled with an increase of effective mass and damping as seen by the structure designated as m_1. As a result, the voltage applied to the piezoelectric actuator could continuously control the combinations of stiffness, damping, and mass. It is important to stress that the Smart Spring concept does not use actuators to perform work against the inertial and excitation loads but is only required to adaptively vary the effective structural impedance properties at the boundary condition. It is this change of the flexural characteristics that allows the control of the dynamic response of a structure. The primary advantage in the Smart Spring system, compared to other piezoelectric actuator based approaches, is that the Smart

Spring does not rely on the piezoelectric actuators to achieve high stroke and force simultaneously. Rather, the device only requires the actuators to produce micro displacement to generate relatively high actuation forces. The Smart Spring is suitable to be used as APL since it can be electrically controlled and can operate as a solid conventional pitch link in the event of the failure of power supply, actuator or spring.

In this thesis the APL concept is addressed from the theoretical, numerical and experimental point of view, taking advantages of the SHARCS project. In particular a reduced-scale model helicopter blade has been designed, produced and instrumented to be tested in the non-rotating and rotating conditions. The identification of its dynamical behaviour is performed as means of experimental and operational modal analysis in free-free, cantilever and rotating conditions, using several pitch links in the whirl-tower facility of the Carleton University, which has been also modified to simulate in a simplified way forward flight conditions. Two theoretical models, developed within the SHARCS project, are presented. The first, implemented in the GAST numerical tool, has an accurate formulation of the rotating beam model and is used in this contest to numerically achieve the fan plot of the SHARCS blade. The other model implements the Individual Blade Control approach for the pitch link. In this latter case the structural model can be seen as a simplified model of the previous one, but its results are representative of the vibration reduction achievable with the APL. The numerical findings are compared with the results obtained from the extensive experimental test campaign that brought to satisfactory, also if still preliminary, vibration reduction though an open-loop control strategy.

Chapter 9

The rotating beam model in the GAST code

An aeroelastic model has been developed within the SHARCS project for the prediction of the dynamical properties of the helicopter rotor in order to be able to take into account the effects of both the flow and the structure on the noise and vibration. Starting from the original model, developed by National Technical University of Athens and Centre for Renewable Energy Sources, Ref.[75], some improvements have been added in order to model the actively controlled smart helicopter rotor, Ref.[76]. In this aeroelastic tool, named GAST, the structural dynamics of the flexible helicopter blade undergoing significant elastic displacements has been described by the second order nonlinear flap-lag-torsion slender-beam differential model introduced by Hodges and Dowell, Ref.[77]. The dynamic and structural coupling of the different components is performed in the context of a multi-body analysis. Therefore, in addition to their structural deflections, each deformable component is allowed to undergo rigid body motions under kinematic and load constraints specified by its connection to the remaining structure. The main purpose of this code is the simulation of the dynamics of the full actively controlled system, which includes the Active Pitch Link and the flow control surfaces, such as blade flap and tip. In this chapter, a description of the model of the rotating blade is given as it is implemented in GAST.

9.1 Strain-displacement relations expressed in second order

The second order nonlinear beam model is formulated as described in the following. First the field of displacement for the arbitrary point on the beam is defined. Let $[O_G XYZ]$ be the inertial frame and $[Oxyz]$ be the local co-ordinate system of a beam, with its y axis lying along the un-deformed beam axis (shear centre axis) and x and z defining the two bending directions of the beam. As shown in Fig.9.1, a local

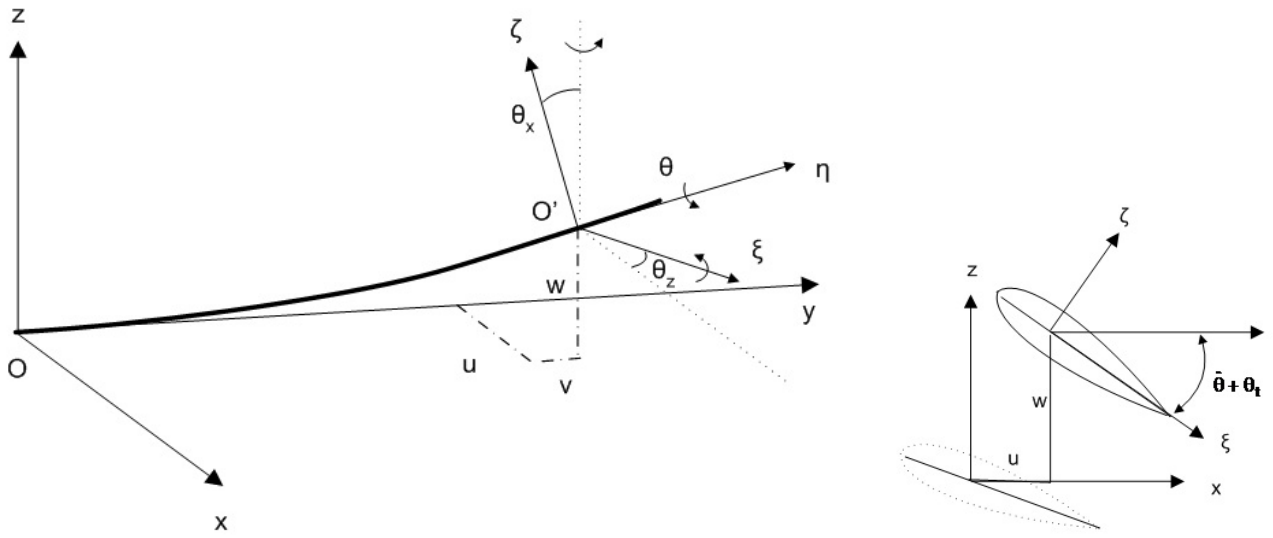

Figure 9.1: Beam coordinate system definition.

co-ordinate system $[O'\xi\eta\zeta]$ is also defined, that follows the section's pre-twist and elastic deflections. The η axis of this co-ordinate system is tangential to the deformed beam axis at any radial position, whereas ξ and ζ define the local principle axes of the section. The blade model is formulated as an Euler-Bernoulli beam where the plane defined by ξ and ζ axes (cross-section plane at the deformed state) will be perpendicular to the deformed beam axis. At the undeformed state y and η coincide, whereas ξ and ζ differ from x and z, respectively, by the value of the angle that defines the principal axes of each section. The position vector of any arbitrary point on the deformed beam, with respect to the inertia frame, is given by:

$$\boldsymbol{r} = \boldsymbol{\rho} + \boldsymbol{A}\left(\begin{Bmatrix} u \\ y+v \\ w \end{Bmatrix} + \boldsymbol{E}\begin{Bmatrix} \xi \\ -\lambda\theta' \\ \zeta \end{Bmatrix}\right) \tag{9.1}$$

where $\lambda(\xi,\zeta)$ is the warping function of the cross section, u, v, w the local deflections, θ the torsion angle about y axis, $\boldsymbol{E}$ is the transformation matrix between $[Oxyz]$ and $[O'\xi\eta\zeta]$, $\boldsymbol{A}$ is the transformation matrix between $[O_GXYZ]$ and $[Oxyz]$ and $\boldsymbol{\rho}$ is the position vector of the origin of $[Oxyz]$ with respect to $[O_GXYZ]$. $\boldsymbol{A}$ and $\boldsymbol{\rho}$ are associated with the motion that the local system of the beam undergoes with respect to the inertial frame. Thereby, they consist of rigid body motions (e.g. azimuth rotation and pitching) or motions of preceding bodies attached to the body considered. It can be shown that, up to a second order approximation, $\boldsymbol{E}$ is given by the expression:

$$\boldsymbol{E}=\begin{bmatrix} \cos\left(\theta_t+\hat{\theta}-u'w'\right)\left(1-\frac{u'^2}{2}\right) & u' & \sin\left(\theta_t+\hat{\theta}-u'w'\right)\left(1-\frac{u'^2}{2}\right) \\ -u'\cos\left(\theta_t+\hat{\theta}\right)+w'\sin\left(\theta_t+\hat{\theta}\right) & 1-\frac{u'^2}{2}-\frac{w'^2}{2} & -u'\sin\left(\theta_t+\hat{\theta}\right)-w'\cos\left(\theta_t+\hat{\theta}\right) \\ -\sin\left(\theta_t+\hat{\theta}\right)\left(1-\frac{w'^2}{2}\right) & w' & -\cos\left(\theta_t+\hat{\theta}\right)\left(1-\frac{w'^2}{2}\right) \end{bmatrix} \tag{9.2}$$

where the prime denotes differentiation with respect to y, θ_t denotes the local twist angle and $\hat{\theta}$ the local torsion angle about η axis that is equal to:

$$\hat{\theta}=\theta+\int_0^y u''w'dy \tag{9.3}$$

The Green's strain tensor ε_{ij} can, then, be defined according to:

$$\boldsymbol{dr}^T\boldsymbol{dr}-\boldsymbol{dr}_0^T\boldsymbol{dr}_0 \;=\; 2\begin{Bmatrix} d\xi & d\eta & d\zeta \end{Bmatrix}\boldsymbol{\varepsilon}\begin{Bmatrix} d\xi \\ d\eta \\ d\zeta \end{Bmatrix} \tag{9.4}$$

where $\boldsymbol{r}$ and $\boldsymbol{r}_0$ are the position vectors of the same point on the deformed and the un-deformed beam, respectively. The above expression yields the strain-elastic displacements relations (second order accuracy):

$$\begin{aligned} \varepsilon_{22} &= v'+\frac{u'^2}{2}+\frac{w'^2}{2}-\lambda\theta''+(\xi^2+\zeta^2)\left(\theta_t'+\frac{\theta'^2}{2}\right)+ \\ &\quad -u''\left(\xi\cos(\theta_t+\hat{\theta})+\zeta\sin(\theta_t+\hat{\theta})\right)+w''\left(\xi\sin(\theta_t+\hat{\theta})-\zeta\cos(\theta_t+\hat{\theta})\right) \end{aligned} \tag{9.5}$$

$$\varepsilon_{21} = \frac{1}{2}\theta'(\zeta-\partial_\xi\lambda) \tag{9.6}$$

$$\varepsilon_{23} = -\frac{1}{2}\theta'(\xi+\partial_\zeta\lambda) \tag{9.7}$$

From Eq.(9.5-9.7), the stress-elastic displacements relations can be obtained through application of Hooke's law, which in the assumption of a homogenous and isotropic material takes the form:

$$\begin{Bmatrix} \sigma_{\eta\eta} \\ \sigma_{\eta\xi} \\ \sigma_{\eta\zeta} \end{Bmatrix} = \begin{bmatrix} E & 0 & 0 \\ 0 & G & 0 \\ 0 & 0 & G \end{bmatrix} \begin{Bmatrix} \varepsilon_{\eta\eta} \\ \varepsilon_{\eta\xi} \\ \varepsilon_{\eta\zeta} \end{Bmatrix} \tag{9.8}$$

where $\varepsilon_{\eta\eta} = \varepsilon_{22}$, $\varepsilon_{\eta\xi} = 2\varepsilon_{21}$ and $\varepsilon_{\eta\zeta} = 2\varepsilon_{23}$. Integration of the normal and shear stresses, over the cross section surface A, provides the resultant loads of the section with respect to the local deformed beam co-ordinate system. Under the assumption that terms up to second order are retained (with the exception of some higher order terms that are not always negligible), the following relations are obtained:

Axial Force

$$\begin{aligned} F_\eta &= \int_A \sigma_{\eta\eta} d\xi d\zeta = \\ &= EA\left(v' + \frac{u'^2}{2} + \frac{w'^2}{2}\right) - u''\left(EA_\zeta \cos(\theta_t + \hat{\theta}) + EA_\xi \sin(\theta_t + \hat{\theta})\right) + \\ &\quad + EI_t\left(\theta_t'\theta' + \frac{\theta'^2}{2}\right) + w''\left(EA_\zeta \sin(\theta_t + \hat{\theta}) - EA_\xi \cos(\theta_t + \hat{\theta})\right) \end{aligned} \tag{9.9}$$

Bending Moment

$$\begin{aligned} M_\xi &= -\int_A \zeta\sigma_{\eta\eta} d\xi d\zeta = \\ &= -EA_\xi\left(v' + \frac{u'^2}{2} + \frac{w'^2}{2}\right) - EI_{t\xi}\left(\theta_t'\theta' + \frac{\theta'^2}{2}\right) + EC_\xi\theta'' + \\ &\quad + EI_{\xi\xi}\left(u'' \sin(\theta_t + \hat{\theta}) + w'' \cos(\theta_t + \hat{\theta})\right) \end{aligned} \tag{9.10}$$

$$\begin{aligned} M_\zeta &= \int_A \xi\sigma_{\eta\eta} d\xi d\zeta = \\ &= EA_\zeta\left(v' + \frac{u'^2}{2} + \frac{w'^2}{2}\right) - EI_{t\zeta}\left(\theta_t'\theta' + \frac{\theta'^2}{2}\right) - EC_\zeta\theta'' + \\ &\quad - EI_{\zeta\zeta}\left(u'' \cos(\theta_t + \hat{\theta}) - w'' \sin(\theta_t + \hat{\theta})\right) \end{aligned} \tag{9.11}$$

Torsion Moment

$$
\begin{aligned}
M_\eta &= \int_A (\zeta\sigma_{\eta\xi} - \xi\sigma_{\eta\zeta})\, d\xi d\zeta + (\theta_t + \theta)' \int_A (\xi^2 + \zeta^2)\sigma_{\eta\eta} d\xi d\zeta + \left(\int_A \lambda\sigma_{\eta\eta} d\xi d\zeta \right)' = \\
&= GI_t\theta' + EI_t(\theta_t + \theta') \left(v' + \frac{u'^2}{2} + \frac{w'^2}{2} \right) + EI_{t2}\theta_t'^2\theta' - (EC^*\theta'')' + \\
&\quad + (\theta_t + \theta)' EI_{t\xi} \left(u'' \sin(\theta_t + \hat{\theta}) + w'' \cos(\theta_t + \hat{\theta}) \right) + \\
&\quad + (\theta_t + \theta)' EI_{t\zeta} \left(u'' \cos(\theta_t + \hat{\theta}) - w'' \sin(\theta_t + \hat{\theta}) \right) + \\
&\quad - \left(u'' \left(EC_\zeta \cos(\theta_t + \hat{\theta}) + EC_\xi \sin(\theta_t + \hat{\theta}) \right) \right)' + \\
&\quad + \left(w'' \left(EC_\xi \cos(\theta_t + \hat{\theta}) - EC_\zeta \sin(\theta_t + \hat{\theta}) \right) \right)'
\end{aligned} \tag{9.12}
$$

where the beam structural properties involved in the above relations are defined as follows,

$$
\begin{aligned}
&EA = \int_A E d\xi d\zeta, \quad EA_\xi = \int_A E\zeta d\xi d\zeta, \quad EA_\zeta = \int_A E\xi d\xi d\zeta \\
&EI_{\xi\xi} = \int_A E\zeta^2 d\xi d\zeta, \quad EI_{\zeta\zeta} = \int_A E\xi^2 d\xi d\zeta, \quad GI_t = \int_A G(\xi^2 + \zeta^2) d\xi d\zeta \\
&EI_t = \int_A E\left(\xi^2 + \zeta^2\right) d\xi d\zeta, \quad EI_{t2} = \int_A E\left(\xi^2 + \zeta^2\right)^2 d\xi d\zeta \\
&EI_{t\xi} = \int_A E\zeta\left(\xi^2 + \zeta^2\right) d\xi d\zeta, \quad EI_{t\zeta} = \int_A E\xi\left(\xi^2 + \zeta^2\right) d\xi d\zeta \\
&EC^* = \int_A E\lambda^2 d\xi d\zeta, \quad EC_\xi = \int_A E\lambda\zeta d\xi d\zeta, \quad EC_\zeta = \int_A E\lambda\xi d\xi d\zeta
\end{aligned} \tag{9.13}
$$

9.2 Equations of structural equilibrium

Consider a differential element of the beam with cross section A and width dy (see Fig.9.2) and let $\boldsymbol{\delta P}$ denote the linear density of the external aerodynamic forces exerted on it, $\boldsymbol{dF}$ the net elastic internal forces, $\boldsymbol{g}$ the acceleration of gravity. Then, the balance of forces with respect to the blade local co-ordinate system $[Oxyz]$ takes the form:

$$
\underbrace{\int \rho \boldsymbol{A}^T \ddot{\boldsymbol{r}} dA\, dy}_{\boldsymbol{p}^i} = \boldsymbol{dF} + \underbrace{\int_A \rho \boldsymbol{g} dA dy + \boldsymbol{\delta P} dy}_{\boldsymbol{p}^e dy} \tag{9.14}
$$

where the dot denotes differentiation in time, ρ is the mass density of the beam structure. The left hand side of Eq.(9.14) is the total inertial forces $\boldsymbol{p}^i$ and the second and the third term of the right hand side

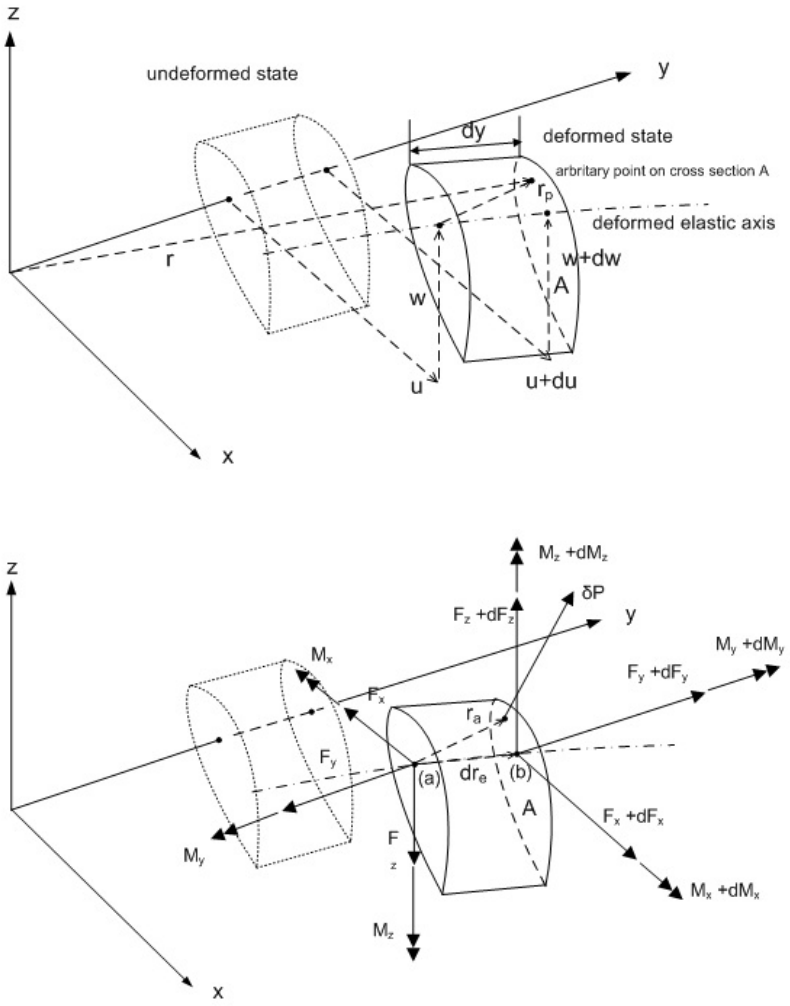

Figure 9.2: Kinematics and dynamics of deformable beams.

are the external forces $\boldsymbol{p}^e$ (aerodynamic and gravitational). Similarly the balance of the moments with reference to the origin of the differential element dy takes the form:

$$\underbrace{\int \rho \boldsymbol{A}^T \boldsymbol{r}_p \times \boldsymbol{A}^T \ddot{\boldsymbol{r}} dA\, dy}_{\boldsymbol{q}^i} = \boldsymbol{dM} + \boldsymbol{dr}_e \times (\boldsymbol{F} + \boldsymbol{dF}) + \underbrace{\int_A \rho \boldsymbol{r}_p \times \boldsymbol{g} dA dy + \boldsymbol{r}_a \times \boldsymbol{\delta P} dy}_{\boldsymbol{q}^e dy} \tag{9.15}$$

where $\boldsymbol{r}_a$ is the local position of the aerodynamic center, $\boldsymbol{r}_p = \boldsymbol{r} - \boldsymbol{r}_e^a$, and $\boldsymbol{dr}_e = \boldsymbol{r}_e^b - \boldsymbol{r}_e^a$, with $\boldsymbol{r}_e$ the position vector of point on the deformed elastic axis given by Eq.(9.1) for $\zeta = 0$ and $\xi = 0$. The left hand side of Eq.(9.15) is the total inertial moment $\boldsymbol{q}^i$ and the last two terms of the right hand side are the external moment $\boldsymbol{q}^e$. The vector equations of equilibrium (9.14) and (9.15) are written in component

form relative to the undeformed axes x, y and z. The equilibrium equations of the forces are:

$$\begin{aligned} p_x^i &= F_x' + p_x^e \\ p_y^i &= F_y' + p_y^e \\ p_z^i &= F_z' + p_z^e \end{aligned} \tag{9.16}$$

Similarly, the equilibrium equations of the moments are:

$$\begin{aligned} q_x^i &= M_x' + F_z - F_y w' + q_x^e \\ q_y^i &= M_y' - F_z u' + F_x w' + q_y^e \\ q_z^i &= M_z' - F_x + F_y u' + q_z^e \end{aligned} \tag{9.17}$$

The balance of moments in the z and x directions are used for eliminating the shear internal forces F_x and F_z appearing in the force equilibrium equations in x and z directions, respectively. In this way, the six equilibrium equations can be reduced to four equations for the four independent deflections u, v, w and θ:

$$\begin{aligned} p_x^i + (q_z^i)' &= M_z'' + (F_y u')' + p_x^e + (q_z^e)' \\ p_y^i &= F_y' + p_y^e \\ p_z^i + (q_x^i)' &= -M_x'' + (F_y w')' + p_z^e + (q_x^e)' \\ q_y^i + q_x^i u' + (q_z^i)' &= M_y' + M_x' u' + M_z' w' + q_y^e + q_x^e u' + q_z^e w' \end{aligned} \tag{9.18}$$

The internal loads provided by Eqs.(9.9)-(9.12) are expressed in $[O'\xi\eta\zeta]$. Therefore, before substituted in Eq.(9.18) they have to be transformed in $[Oxyz]$. This is done through the rotation matrix E in Eq.(9.2):

$$\begin{bmatrix} M_x & \\ M_y & F_y \\ M_z & \end{bmatrix} = E \begin{bmatrix} M_\xi & F_\xi \\ M_\eta & F_\eta \\ M_\zeta & F_\zeta \end{bmatrix} \tag{9.19}$$

Finally, substituting Eqs.(9.19) into Eqs.(9.18) and retaining terms up to second order, the following beam equations are obtained:

Force x

$$
\begin{aligned}
p_x^i + (q_z^i)' - p_x^e - (q_z^e)' &= \Big(M_\zeta \cos(\theta_t+\hat\theta) - M_\xi \sin(\theta_t+\hat\theta)\Big)'' + (F_\eta u')' = \\
&= \Big(\Big(EA_\zeta \cos(\theta_t+\hat\theta) + EA_\xi \sin(\theta_t+\hat\theta)\Big)\Big(v' + \frac{u'^2}{2} + \frac{w'^2}{2}\Big) + \\
&\quad + \Big(EI_{t\zeta} \cos(\theta_t+\hat\theta) + EI_{t\xi} \sin(\theta_t+\hat\theta)\Big)\theta_t'\theta' + \\
&\quad - \underline{\Big(EC_\zeta \cos(\theta_t+\hat\theta) + EC_\xi \sin(\theta_t+\hat\theta)\Big)\theta''} + \\
&\quad - \Big(EI_{\zeta\zeta} \cos^2(\theta_t+\hat\theta) + EI_{\xi\xi} \sin^2(\theta_t+\hat\theta)\Big)u'' + \\
&\quad - \frac{1}{2}(EI_{\xi\xi} - EI_{\zeta\zeta}) \sin(2(\theta_t+\hat\theta))w''\Big)'' + (F_\eta u')'
\end{aligned}
\tag{9.20}
$$

Force y

$$
\begin{aligned}
p_y^i - p_y^e &= F_y' = \\
&= \Big(EA\Big(v' + \frac{u'^2}{2} + \frac{w'^2}{2}\Big) + \underline{\underline{EI_t\Big(\theta_t'\theta' + \frac{\theta'^2}{2}\Big)}} + \\
&\quad + \Big(EA_\zeta \cos(\theta_t+\hat\theta) + EA_\xi \sin(\theta_t+\hat\theta)\Big)u'' + \\
&\quad + \Big(EA_\zeta \sin(\theta_t+\hat\theta) - EA_\xi \cos(\theta_t+\hat\theta)\Big)w''\Big)'
\end{aligned}
\tag{9.21}
$$

Force z

$$
\begin{aligned}
p_z^i + (q_x^i)' - p_z^e - (q_x^e)' &= -\Big(M_\xi \cos(\theta_t+\hat\theta) + M_\zeta \sin(\theta_t+\hat\theta)\Big)'' + (F_\eta w')' = \\
&= \Big(\Big(EA_\xi \cos(\theta_t+\hat\theta) - EA_\zeta \sin(\theta_t+\hat\theta)\Big)\Big(v' + \frac{u'^2}{2} + \frac{w'^2}{2}\Big) + \\
&\quad - \frac{1}{2}(EI_{\xi\xi} - EI_{\zeta\zeta}) \sin(2(\theta_t+\hat\theta))u'' + \\
&\quad - \Big(EI_{\xi\xi} \cos^2(\theta_t+\hat\theta) + EI_{\zeta\zeta} \sin^2(\theta_t+\hat\theta)\Big)w'' + \\
&\quad + \Big(EI_{t\xi} \cos(\theta_t+\hat\theta) - EI_{t\zeta} \sin(\theta_t+\hat\theta)\Big)\theta_t'\theta' + \\
&\quad - \underline{\Big(EC_\xi \cos(\theta_t+\hat\theta) + EC_\zeta \sin(\theta_t+\hat\theta)\Big)\theta''}\Big)'' + (F_\eta w')'
\end{aligned}
\tag{9.22}
$$

Moment y

$$
\begin{aligned}
& q_y^i + q_x^i u' + (q_z^i)' - q_y^e - q_x^e u' - q_z^e w' = \\
& = M_\eta' - M_\xi' \left(\cos(\theta_t + \hat{\theta}) u'' - \sin(\theta_t + \hat{\theta}) w'' \right) - M_\zeta' \left(\sin(\theta_t + \hat{\theta}) u'' + \cos(\theta_t + \hat{\theta}) w'' \right) = \\
& = \Bigg(GI_t \theta' + \underline{\underline{EI_t(\theta_t + \hat{\theta}) \left(v' + \frac{u'^2}{2} + \frac{w'^2}{2} \right)}} + EI_{t2} \theta_t'^2 \theta' + \\
& - \left(\left(EI_{t\zeta} \cos(\theta_t + \hat{\theta}) + EI_{t\xi} \sin(\theta_t + \hat{\theta}) \right) u'' \right) (\theta_t + \theta)' + \\
& + \left(\left(EI_{t\xi} \cos(\theta_t + \hat{\theta}) - EI_{t\zeta} \sin(\theta_t + \hat{\theta}) \right) w'' \right) (\theta_t + \theta)' \Bigg)' + \\
& - \Bigg(\underline{EC^* \theta'' + \left(EC_\zeta \cos(\theta_t + \hat{\theta}) + EC_\xi \sin(\theta_t + \hat{\theta}) \right) u'' + } \\
& \underline{+ \left(EC_\xi \cos(\theta_t + \hat{\theta}) - EC_\zeta \sin(\theta_t + \hat{\theta}) \right) w'' \Bigg)''} + \\
& \underline{\underline{+ \left(EA_\xi \cos(\theta_t + \hat{\theta}) - EA_\zeta \sin(\theta_t + \hat{\theta}) \right) \left(v' + \frac{u'^2}{2} + \frac{w'^2}{2} \right) u'' + }} \\
& \underline{\underline{- \left(EA_\zeta \cos(\theta_t + \hat{\theta}) + EA_\xi \sin(\theta_t + \hat{\theta}) \right) \left(v' + \frac{u'^2}{2} + \frac{w'^2}{2} \right) w'' + }} \\
& \underline{\underline{-\frac{1}{2}(EI_{\xi\xi} - EI_{\zeta\zeta}) \sin(2(\theta_t + \hat{\theta}))(u''^2 + w''^2) - (EI_{\xi\xi} - EI_{\zeta\zeta}) \cos(2(\theta_t + \hat{\theta})) u'' w''}}
\end{aligned}
\tag{9.23}
$$

As compared to the equations of the standard first order beam model, the right hand side of Eqs (9.20)-(9.23) (which corresponds to the internal loads of the beam and it is therefore associated with its stiffness characteristics) contains additional nonlinear higher-order terms. The terms related to the warping of the cross sections are underlined with a single solid line. Terms $(F_\eta u')'$ and $(F_\eta w')'$ in force x and force z equations are also nonlinear. However, they are considered first order since the traction force is expected to be high for a rotating blade. These terms correspond to the blade bending softening due to the centrifugal loads. Additional nonlinear second-order terms also appear in the right hand side of the equations which are related to the inertial and external loads. Especially with regard to the inertial loads, nonlinearities are associated with the rigid body dynamics of the system, defined through the matrices $\boldsymbol{A}$ and $\boldsymbol{\rho}$ in Eq.(9.1), as well as the structural dynamics of the highly deflected beam, as it is expressed through the nonlinear rotation matrix $\boldsymbol{E}$. Among the different second-order structural terms appearing in

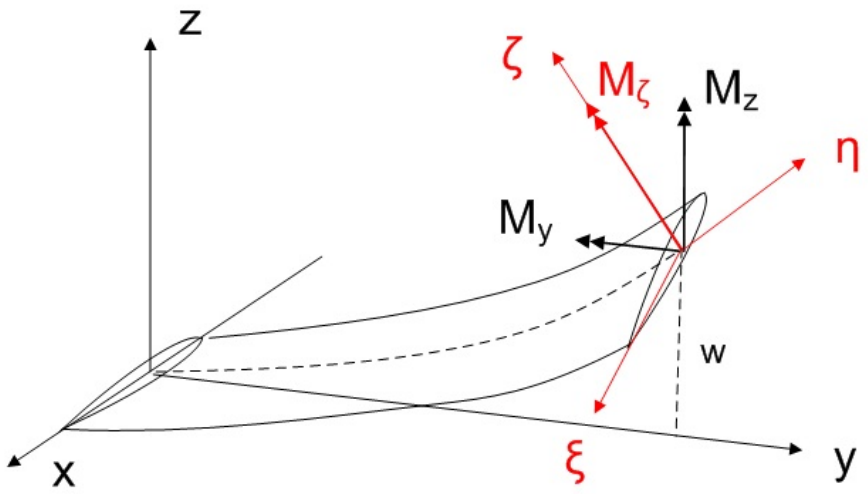

Figure 9.3: Explanation of bending-torsion coupling effect in case of large flapping deflection.

Eqs.(9.20)-(9.23) those expected to be of higher significance as the blades become more and more flexible are the ones underlined with a double solid line. The term in Eq.(9.21) and the first term in Eq.(9.23) correspond to the coupling of the blade torsion with the blade tension. As indicated by Eq.(9.5), the torsion of the blade generates axial strains $\varepsilon_{\eta\eta}$ and stresses $\sigma_{\eta\eta}$ and vice versa (see Eq.(9.12)), the axial stresses contribute to the pitching moment M_η. The last terms in Eq.(9.23) are related to the bending-torsion coupling. As the bending displacements of the blade increase, the local bending moments M_ξ and M_η generate torsion moment about the undeformed blade axis y (see Fig.9.3). The magnitude of this pitching moment primarily depends on the bending curvatures u'' and w''. It also depends on the offset of the cross section tension axis from the elastic axis.

Equations (9.20)-(9.23) are a system of four differential equations in the four variables u, v, w, θ with derivative till the fourth order with respect to y. Moreover, the inertial forces and moments on the left hand side are expressed as a second order derivative in time of the state variable. Also the external aerodynamic forces and moments contain a dependency on the state variables and their derivative in space and time. As a consequence, these contributions add more nonlinear and coupling terms among the equations. This resulting aeroelastic system of equations can be integrated in the space domain using the

Galerkin approach adopting the in-vacuum non-rotating modes of the blade as shape functions. If q is the vector of the modal amplitudes (Lagrangian coordinates), $\hat{M}$, $\hat{C}$ and $\hat{K}$ are the linear time-invariant mass, damping and stiffness structural and aerodynamic contributions, and $\hat{f}$ represents the set of all nonlinear and/or time-dependent coefficient terms, then the set of the nonlinear ordinary differential equation is written as:

$$\hat{M}\ddot{q} + \hat{C}\dot{q} + \hat{K}q = \hat{f}\left(q, \dot{q}, \ddot{q}, \psi\right) \tag{9.24}$$

where the azimuthal position of the blade ψ has been considered time dependent: $\psi = \Omega t$. Because a periodic solution is sought, the harmonic balance approach can be used to solve these equations in the time domain. An iterative numerical procedure was set up for this purpose, due to the intrinsic nonlinear nature of the considered system of equations.

Chapter 10

Individual Blade Control approach to attenuate rotor vibration

In this chapter, the mathematical linear model of a single beringless blade modeled as a flexible rotating beam with two degrees of freedom (flapwise bending and torsion) is described as in Ref.[78]. A simplified aeroelastic model of a helicopter rotor subjected to unsteady aerodynamic loads is described and implemented in order to show the capability in the vibration reduction of a control strategy acting on the boundary condition of each blade. In the first part, the linearized structural dynamics of a blade for which the stiffness of the boundary conditions may be actively changed is presented. In the second part, an unsteady aerodynamic model for the forward flight condition based on Theodorsen's theory is introduced. According to this model, the airloads are divided into two sets: the motion-dependent and the disturbance airloads. Then, the assembly of the aeroelastic model is performed and its resolution is described.

10.1 Simplified blade structural dynamic model

A linear mathematical model of a single rotating blade including only the vertical displacement w and torsion angle θ degrees of freedom (DOF) can be derived by the system of Eqs.(9.20)-(9.23) if terms up to the first order accuracy are retained and if the terms related to the warping of the cross section are

neglected:

$$F_w + F_i = (K_{11}w'' + K_{21}\theta')'' + (F_\eta w')' \tag{10.1a}$$

$$M_\theta + M_i = (K_{21}w'' + K_{22}\theta')' \tag{10.1b}$$

in which F_w and M_θ are the applied force and moments and will be obtained in the next section, F_i and M_i are the inertial force and moments and the symmetric matrix $\mathbf{K}$ is

$$\mathbf{K} = \begin{bmatrix} EI_{\xi\xi}\cos^2\theta_t + EI_{\zeta\zeta}\sin^2\theta_t & (EI_{t\xi}\cos\theta_t - EI_{t\zeta}\sin\theta_t)\theta_t' \\ (EI_{t\xi}\cos\theta_t - EI_{t\zeta}\sin\theta_t)\theta_t' & GI_t + EI_{t2}\theta_t'^2 \end{bmatrix} \tag{10.2}$$

The aeroelastic dimensionless equations are cast in the state-vector form, according to the Hellinger-Reissner-Washizu formulation, Ref.[79]:

$$M' = H + \nu F_\eta \varphi \tag{10.3a}$$

$$H' = \nu m\ddot{w} - F_w \tag{10.3b}$$

$$\varphi' = D_{11}M + D_{12}\tau \tag{10.3c}$$

$$w' = -\varphi \tag{10.3d}$$

$$\tau' = \nu m r_\theta^2(\theta + \ddot{\theta}) - M_\theta \tag{10.3e}$$

$$\theta' = D_{21}M + D_{22}\tau \tag{10.3f}$$

in which the structure compliance coefficients D_{ij} come from the inversion of the matrix $\mathbf{K}$ as expressed in Eq.(10.2) and the independent variables are the spanwise coordinate and time. The equations (10.3a-10.3f) are written in a non-dimensional form (bars were omitted for sake of simplicity), using the normalization shown in Tab.10.1. The rotational parameter ν in Eqs.(10.3) is defined as $m\Omega^2R^4/(EI_{ref})$.

The boundary conditions associated with the above set of six first-order differential equations in space

Table 10.1: Dimensionless parameter definition.

Parameter	Normalization	Description
$C_{\varphi,\theta}$	$C_{\varphi,\theta}(EI_{ref})/R^2$	flexibility constants of the boundary conditions
D_{ij}	$D_{ij}R(EI_{ref})$	compliance coefficients $i,j=1,3$
F_w	$R^3F_w/(EI_{ref})$	applied forces per unit of length
H	$R^2H/(EI_{ref})$	cross-section shear force resultant
M	$RM/(EI_{ref})$	cross-section flapwise bending moment
M_θ	$R^2M_\theta/(EI_{ref})$	applied moments per unit of length
F_η	$F_\eta/(m_{ref}R^2)$	cross-section tension
m	$m/(m_{ref})$	running mass
r	r/R	spanwise coordinate
r_θ	r_θ/R	cross-section radius of gyration about the elastic axis
w	w/R	cross-section flapwise bending displacement
τ	$R\tau/(EI_{ref})$	cross-section torque

are listed in Eqs.(10.4) , where they are normalized for the interval $0 \leq r \leq R$:

$$M(0) = 1/C_\varphi\varphi(0) \tag{10.4a}$$

$$M(1) = 0 \tag{10.4b}$$

$$H(1) = 0 \tag{10.4c}$$

$$w(0) = 0 \tag{10.4d}$$

$$\tau(1) = 0 \tag{10.4e}$$

$$\tau(0) = 1/C_\theta(\theta(0)-\theta_c) \tag{10.4f}$$

in which the the collective (θ_0) and cyclic (θ_{1c} and θ_{1s}) pitch control are introduced as a function of the azimuth angle ψ:

$$\theta_c = \theta_0 + \theta_{1c}\cos\psi + \theta_{1s}\sin\psi \tag{10.5}$$

The lumped flexibility constants of the elastic springs in flapwise bending and torsion appear explicitly

in Eqs.(10.4a) and (10.4f), respectively. By varying these constants (C_φ and C_θ) from zero to infinity, boundary conditions spanning from the perfect cantilever to the hinged blade can be simulated. More interesting, IBC can be introduced via the latter two parameters. According to this method proposed in Ref.[78], the mechanical impedance of the boundary conditions is actively controlled to tailor the blade aeroelastic response. In order to accomplish this task, the flexibility parameters are adapted by a function dependent on the azimuth angle:

$$\begin{Bmatrix} C_\varphi \\ C_\theta \end{Bmatrix} = \begin{Bmatrix} C_{\varphi 0} \\ C_{\theta 0} \end{Bmatrix} + k(\psi) \begin{Bmatrix} \Delta C_\varphi \\ \Delta C_\theta \end{Bmatrix} \tag{10.6}$$

The integrating-matrix method (Ref.[80]) offers a systematic means of integration for the governing equations in space. According to this method, the equations are discretized at N equally-spaced co-location points taken along the integration path. An $N \times N$ matrix operator $\boldsymbol{J}$ based on polynomial interpolation is introduced. If $f(x)$ is a non-dimensional function defined on the interval $0 \leq x \leq 1$, the operator $\boldsymbol{J}$ has the property:

$$\{f\} = \boldsymbol{J}\,\{\partial f/\partial x\} + f(0)\{1\} \tag{10.7}$$

where $\{f\}$ is a $N \times 1$ vector of discrete quantities. The boundary conditions are introduced with additional $N \times N$ matrix operators such that:

$$\boldsymbol{B}_0\{f\} = f(0)\{1\}; \quad \boldsymbol{B}_0\boldsymbol{J} \equiv 0 \tag{10.8}$$

$$\boldsymbol{B}_1\{f\} = f(1)\{1\} \tag{10.9}$$

$$\boldsymbol{J}_1 = (\boldsymbol{B}_1 - \boldsymbol{I})\boldsymbol{J} \tag{10.10}$$

Each one of Eqs.(10.3a-10.3f) is pre-multiplied by $\boldsymbol{J}$, resulting in a set of algebraic equations where the unknowns are the constants of integration in Eq.(10.7). Next, the latter equations are successively pre-multiplied by $\boldsymbol{B}_0$ and $\boldsymbol{B}_1$ and the boundary conditions in Eqs.10.4 are used to solve for the constants of

From here on, the notation $\{\cdot\}$ represents a $N \times 1$ vector of discrete quantities coming from the application of the integrating-matrix method.

integration, yielding :

$$\{M(0)\} = -\boldsymbol{B}_1\boldsymbol{J}\{H\} - \nu\boldsymbol{B}_1\boldsymbol{J}\mathrm{diag}\{F_\eta\}\{\varphi\} \tag{10.11a}$$

$$\{H(0)\} = -\nu\boldsymbol{B}_1\boldsymbol{J}\mathrm{diag}\{m\}\{\ddot{w}\} + \boldsymbol{B}_1\boldsymbol{J}\{F_w\} \tag{10.11b}$$

$$\{\varphi(0)\} = C_\varphi\{M(0)\} \tag{10.11c}$$

$$\{w(0)\} = \{0\} \tag{10.11d}$$

$$\{\tau(0)\} = -\nu\boldsymbol{B}_1\boldsymbol{J}\mathrm{diag}\{mr_\theta^2\}\{\theta+\ddot{\theta}\} + \boldsymbol{B}_1\boldsymbol{J}M_\theta \tag{10.11e}$$

$$\{\theta(0)\} = C_\theta\{\tau(0)\} + \{1\}\theta_c \tag{10.11f}$$

where the diagonal matrices ($\mathrm{diag}\{\cdot\}$) are constructed with the discrete values of the corresponding parameters defined at the N location points taken along the blade. In Eq.(10.11a), the geometric stiffness term due to the blade local tension can be readily calculated:

$$\nu\mathrm{diag}\{F_\eta\} = \mathrm{diag}\{\nu F_\eta\} = \mathrm{diag}\{\nu\mathbf{J}_1\mathrm{diag}\{m\}\{r\}\} \tag{10.12}$$

The constants of integration are substituted in these algebraic equations:

$$\{M\} = -\boldsymbol{J}_1(\{H\} + \nu\mathrm{diag}\{F_\eta\}\{\varphi\}) \tag{10.13a}$$

$$\{H\} = -\boldsymbol{J}_1\nu\mathrm{diag}\{m\}\{\ddot{w}\} - \{F_w\}) \tag{10.13b}$$

$$(\mathbf{I} + \nu C_\varphi\mathbf{B}_1\mathbf{J}\mathrm{diag}\{F_\eta\})\{\varphi\} = \mathbf{J}\mathrm{diag}\{D_{11}\}\{M\} - C_\varphi\mathbf{B}_1\mathbf{J}\{H\} + \mathbf{J}\mathrm{diag}\{D_{12}\}\{\tau\} \tag{10.13c}$$

$$\{w\} = -\mathbf{J}\{\varphi\} \tag{10.13d}$$

$$\{\tau\} = -\boldsymbol{J}_1(\nu\mathrm{diag}\{mr_\theta^2\}\{\theta+\ddot{\theta}\} - \{M_\theta\}) \tag{10.13e}$$

$$\left(\mathbf{I} + \nu C_\theta\mathbf{B}_1\mathbf{J}\mathrm{diag}\{mr_\theta^2\}\right)\{\theta\} = \mathbf{J}\mathrm{diag}\{D_{21}\}\{M\} - C_\theta\mathbf{B}_1\mathbf{J}(\nu\mathrm{diag}\{mr_\theta^2\}\{\ddot{\theta}\} - \{M_\theta\}) + \\ + \mathbf{J}\mathrm{diag}\{D_{22}\}\{\tau\} + \{1\}\theta_c \tag{10.13f}$$

From the six dependent variables in Eqs.(10.13), only two (associated with the primary degrees of freedom) are sufficient to close the formulation of the problem. Here, the Nx1 vectors defining the flapwise bending slope ($\{\varphi\}$) and torsion angle ($\{\theta\}$) distribution along the blade are chosen as the dependent variables. After straight-forward algebra, the remaining states are solved in terms of the chosen ones, yielding:

$$\nu \boldsymbol{DM}\ddot{\boldsymbol{x}} + (\boldsymbol{I} + \nu \boldsymbol{DZ})\boldsymbol{x} + \boldsymbol{DJ}_2\boldsymbol{q} + k(\psi)\boldsymbol{\Delta D}(\nu \boldsymbol{M}\ddot{\boldsymbol{x}} + \nu \boldsymbol{Z}\boldsymbol{x} + \boldsymbol{J}_2\boldsymbol{q}) = \boldsymbol{E}\theta_c \tag{10.14}$$

where

$$\boldsymbol{x}^T = \left[\{\varphi\}^T \ , \ \{\theta\}^T\right] \tag{10.15}$$

$$\boldsymbol{q}^T = \left[\{F_w\}^T \ , \ \{M_\theta\}^T\right] \tag{10.16}$$

$$\boldsymbol{E}^T = \left[\{0\}^T \ , \ \{1\}^T\right] \tag{10.17}$$

$$\boldsymbol{D} = \begin{bmatrix} \boldsymbol{J}\mathrm{diag}\{D_{11}\}\boldsymbol{J}_1 + C_{\varphi 0}\boldsymbol{B}_1\boldsymbol{J} & \boldsymbol{J}\mathrm{diag}\{D_{12}\}\boldsymbol{J}_1 \\ \boldsymbol{J}\mathrm{diag}\{D_{21}\}\boldsymbol{J}_1 & \boldsymbol{J}\mathrm{diag}\{D_{22}\}\boldsymbol{J}_1 + C_{\theta 0}\boldsymbol{B}_1\boldsymbol{J} \end{bmatrix} \tag{10.18}$$

$$\boldsymbol{M} = \begin{bmatrix} \boldsymbol{J}_1\mathrm{diag}\{m\}\boldsymbol{J} & 0 \\ 0 & \mathrm{diag}\{mr_\theta^2\} \end{bmatrix} \tag{10.19}$$

$$\boldsymbol{Z} = \begin{bmatrix} \mathrm{diag}\{F_\eta\} & 0 \\ 0 & \mathrm{diag}\{mr_\theta^2\} \end{bmatrix} \tag{10.20}$$

$$\boldsymbol{\Delta D} = \begin{bmatrix} \Delta C_\varphi \boldsymbol{B}_1\boldsymbol{J} & 0 \\ 0 & \Delta C_\theta \boldsymbol{B}_1\boldsymbol{J} \end{bmatrix} \tag{10.21}$$

$$\boldsymbol{J}_2 = \begin{bmatrix} \boldsymbol{J}_1 & 0 \\ 0 & -\boldsymbol{I} \end{bmatrix} \tag{10.22}$$

10.2 Blade Aerodynamics

The unsteady aerodynamic loads can be divided into two sets; the first set represents the airloads dependent on the airfoil motion (flapwise bending and torsion); the second set collects airloads that can be considered motion-independent due to effects such as Blade-Vortex-Interaction and dynamic stall. However, other airloads that are due to non-modeled effects could also be included in the second set, as the objective of the proposed IBC system is basically "disturbance rejection" under an unknown (broadband) spectrum of exogenous excitation.

10.2.1 Motion-dependent Airloads

The present model is based on the classical unsteady aerodynamic theory for two dimensional thin airfoils in incompressible flow due to Theodorsen (Ref.[81]). An approximation is also introduced in the lift deficiency function due to the time varying free stream velocity in forward flight. For relatively small variations in the free stream velocity (small advance ratio or radial stations not very close to the hub), the lift deficiency function is nearly the same as the original Theodorsen function $C(k)$ if the reduced frequency $k = \omega b/U$ is based on the local velocity U, being b the semichord. The Theodorsen function is represented in Fig.10.1 and can be expressed as

$$C(k) = \frac{H_1^{(2)}(k)}{H_1^{(2)}(k) + jH_0^{(2)}(k)} \tag{10.23}$$

in which $H_n^{(2)}$ are the Hankel functions of the second kind and can be written in terms of the Bessel functions as

$$H_n^{(2)}(k) = J_n(k) - iY_n(k), \quad n = 0, 1 \tag{10.24}$$

The non-dimensional motion-dependent lift ($\bar{L}^M$) and pitch moment ($\bar{M}_a^M$)(about a point distant ab

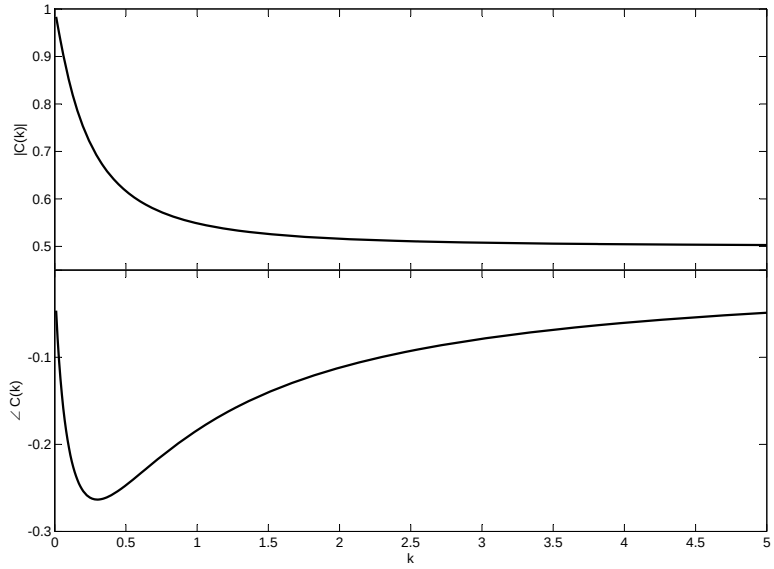

Figure 10.1: Theodorsen's function of the quasisteady circulatory lift.

from the mid-chord position, Fig.10.2) per unit of blade span can be expressed by (Ref.[9]):

$$\bar{L}^M = \bar{L}^C + \bar{L}^{NC} = C(k)\bar{L}^Q + \bar{L}^{NC} \tag{10.25}$$

$$\bar{M}_a^M = \left(\frac{1}{2}+a\right)\bar{L}^C + \pi\bar{b}\left(a\ddot{\bar{w}} - \left(\frac{1}{2}-a\right)\bar{U}\dot{\theta} + \dot{\bar{U}}\theta - \bar{b}\left(\frac{1}{8}+a^2\right)\ddot{\theta}\right) \tag{10.26}$$

where $C(k)$ is the Theodorsen's function as in Fig.10.1 and the quasi-steady circulatory lift is

$$\bar{L}^Q = a_0\left(\bar{U}^2\theta + \bar{U}\dot{\bar{w}} + \bar{b}\left(\frac{1}{2}-a\right)\bar{U}\dot{\theta}\right) \tag{10.27}$$

with a_0 the blade section lift slope, and the non circulatory lift is

$$\bar{L}^{NC} = \pi\bar{b}\left(\dot{\bar{U}}\theta + \bar{U}\dot{\theta} + \ddot{\bar{w}} - a\bar{b}\ddot{\theta}\right) \tag{10.28}$$

In forward flight, the velocity is the U_T component shown in Fig.10.3

$$\bar{U} = \bar{r} + \mu\sin\psi \tag{10.29}$$

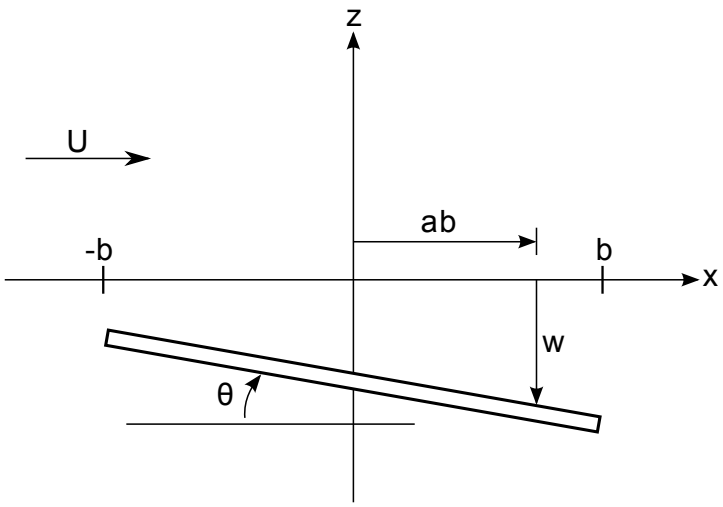

Figure 10.2: Unsteady pitching and heaving motion of the airfoil.

giving

$$\bar{U}^2 = (\bar{r}^2 + \mu^2/2) + 2\mu\bar{r}\sin\psi - \mu^2/2\cos(2\psi) \tag{10.30}$$

$$\dot{\bar{U}} = \mu\cos\psi \tag{10.31}$$

According to the previously stated justification, the reduced frequency is based on the local velocity

$$k = \omega b/U = n\bar{b}/\bar{U} \approx n\bar{b}/\bar{r} \tag{10.32}$$

The latter approximation is satisfactory for the blade radial stations such that $0 \leq \mu R/r \leq 0.7$. For the plausible advance ratio of $\mu = U\cos\alpha/\Omega R = 0.14$, this restriction is such that the airloads produced at stations less than $r/R = 0.2$ are inaccurate, and, thus, will be neglected.

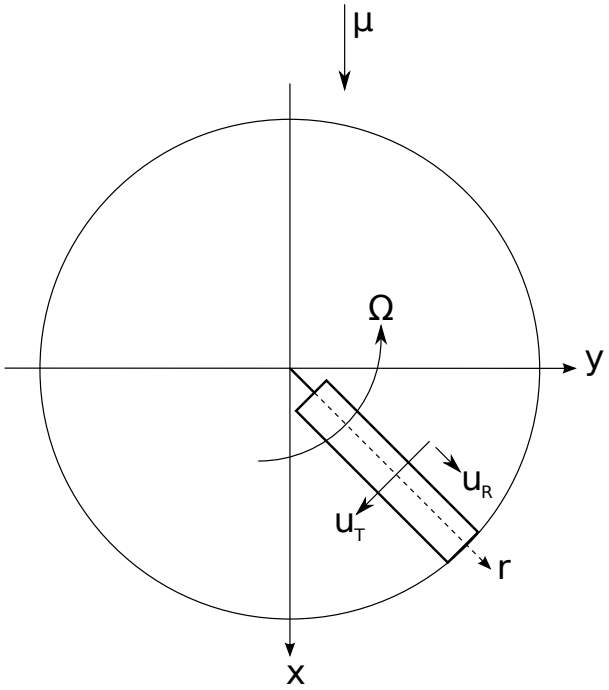

Figure 10.3: In-plane velocity components in forward flight; $U_T = r + \mu \sin\psi$ and $U_R = \mu \cos\psi$.

10.2.2 Motion-independent (Disturbance) Airloads

At this point, the only assumption that is made about the disturbance airloads is that they may be expressed as a Fourier series of the harmonics of the blade revolution:

$$\left\{ \begin{array}{c} \bar{L} \\ \bar{M}_a \end{array} \right\}^D = \sum_{n=-\infty}^{\infty} \left\{ \begin{array}{c} \bar{L} \\ \bar{M}_a \end{array} \right\}_n^D e^{in\psi} \tag{10.33}$$

where

$$\left\{ \begin{array}{c} \bar{L} \\ \bar{M}_a \end{array} \right\}_n^D = \frac{1}{2\pi} \int_0^{2\pi} \left\{ \begin{array}{c} \bar{L} \\ \bar{M}_a \end{array} \right\}^D (\psi, Mach, \mu, k, \cdots) e^{-in\psi} d\psi \ , \quad n = 0, \pm 1, \cdots, \pm\infty \tag{10.34}$$

10.3 Aeroelastic Model Assembly

In Eqs.(10.25) and 10.26, the lift is defined positive upwards, and the pitch moment positive nose-up. Following the sign convention adopted in the previous section 10.1, $F_w = -L$ and $M_\theta = M$. Therefore

the term expressed in Eq.10.16 can be rewritten as follows

$$\boldsymbol{q} = \boldsymbol{q}^M + \boldsymbol{q}^D = \frac{\nu\gamma}{2} I_b \begin{bmatrix} -\boldsymbol{I} & 0 \\ 0 & \bar{b}\boldsymbol{I} \end{bmatrix} \left(\frac{1}{a_0} \begin{Bmatrix} \bar{L} \\ \bar{M}_a \end{Bmatrix}^M + \begin{Bmatrix} \bar{L} \\ \bar{M}_a \end{Bmatrix}^D \right) \tag{10.35}$$

where the normalization shown in Tab.10.2 has been used and the Lock number $\gamma = \rho a_0 2bR^4/I_b$ and the rotational parameter $\nu = m\Omega^2 R^4/(EI_{ref})$ have been introduced. Recalling Eq.(10.3d), and using

Table 10.2: Dimensionless parameter definition.

Parameter	Normalization	Description
b	b/R	blade semi-chord
I_b	I_b/mR^3	blade mass moment of inertia
L	$L/\Omega^2 R^2 \rho b$	Lift per unit of length
M_a	$M_a/\Omega^2 R^2 \rho b^2$	Aerodynamic pitch moment per unit of length
s	s/Ω	Laplace variable
U	$U/\Omega R$	airflow local velocity

Eqs.(10.25)-(10.30), after the discretization procedure Eq.(10.35) yields a set of 2N differential equations where the values of φ and θ at the discretization points are the dependent variables (Eq.10.36). These equations can be appended to Eq.10.14 to obtain the complete set of aeroelastic governing equations. The nondimensional time (azimuth angle $\psi = \Omega t$) is the remaining independent variable.

$$\boldsymbol{J}_2\boldsymbol{q} = \frac{\nu\gamma}{2} I_b \left(\mathbf{Q}_2^L \ddot{\mathbf{x}} + (\mathbf{Q}_1^L + \mathbf{Q}_{1s}^{NL} \sin\psi)\dot{\mathbf{x}} + (\mathbf{Q}_0^L + \mathbf{Q}_{0s}^{NL} \sin\psi + \mathbf{Q}_{02c}^{NL} \cos 2\psi + Q_{01c}^{NL} \cos\psi)\mathbf{x} + J_2 \mathbf{q}^D \right) \tag{10.36}$$

where

$$\mathbf{Q}_2^L = \pi/a_0\, \mathbf{J}_2\, \mathbf{Q}_2^{NC} \mathbf{J}_3 \tag{10.37}$$

$$\mathbf{Q}_1^L = \mathbf{J}_2\, \left(\mathrm{diag}\{C_k\}\, \mathbf{Q}_1^C + \pi/a_0\, \mathbf{Q}_1^{NC}\right) \mathrm{diag}\{r\}\, \mathbf{J}_3 \tag{10.38}$$

$$\mathbf{Q}_0^L = \mathbf{J}_2\, \mathrm{diag}\{C_k\}\, \mathbf{Q}_0^C \mathrm{diag}\left(\{r^2\} + 1/2\{\mu^2\}\right)\, \mathbf{J}_3 \tag{10.39}$$

$$\mathbf{Q}_{1s}^{NL} = \mathbf{J}_2\, \left(\mathrm{diag}\{C_k\}\, \mathbf{Q}_1^C + \pi/a_0\, \mathbf{Q}_1^{NC}\right) \mathrm{diag}\{\mu\}\, \mathbf{J}_3 \tag{10.40}$$

$$\mathbf{Q}_{0s}^{NL} = 2\, J_2 \mathrm{diag}\{C_k\} \mathbf{Q}_0^C \mathrm{diag}\{\mu\} \mathrm{diag}\{r\}\, \mathbf{J}_3 \tag{10.41}$$

$$\mathbf{Q}_{02c}^{NL} = -\,\mathbf{J}_2 \mathrm{diag}\{C_k\} \mathbf{Q}_0^C\, 1/2\, \mathrm{diag}\{\mu^2\}\, \mathbf{J}_3 \tag{10.42}$$

$$\mathbf{Q}_{01c}^{NL} = \pi/a_0\, \mathbf{J}_2\, \mathbf{Q}_0^{NC} \mathrm{diag}\{\mu\}\, \mathbf{J}_3 \tag{10.43}$$

$$\mathbf{Q}_2^{NC} = \begin{bmatrix} \mathrm{diag}\{\bar{b}\} & \mathrm{diag}\{a\,\bar{b}^2\} \\ -\mathrm{diag}\{a\bar{b}^2\} & -\mathrm{diag}\{(1/8 + a^2)\bar{b}^3\} \end{bmatrix} \tag{10.44}$$

$$\mathbf{Q}_1^{NC} = \begin{bmatrix} 0 & -\mathrm{diag}\{\bar{b}\} \\ 0 & -\mathrm{diag}\{(1/2 - a)\bar{b}^2\} \end{bmatrix} \tag{10.45}$$

$$\mathbf{Q}_0^{NC} = \begin{bmatrix} 0 & -\mathrm{diag}\{\bar{b}\} \\ 0 & \mathrm{diag}\{\bar{b}^2\} \end{bmatrix} \tag{10.46}$$

$$\mathbf{Q}_1^C = \begin{bmatrix} \mathbf{I} & -\mathrm{diag}\{(1/2 - a)\bar{b}\} \\ -\mathrm{diag}\{(1/2 + a)\bar{b}\} & \mathrm{diag}\{(1/4 - a^2)\bar{b}^2\} \end{bmatrix} \tag{10.47}$$

$$\mathbf{Q}_0^C = \begin{bmatrix} 0 & -\mathbf{I} \\ 0 & \mathrm{diag}\{(1/2 + a)\bar{b}\} \end{bmatrix} \tag{10.48}$$

$$\mathrm{diag}\{C_k\} = \begin{bmatrix} \mathrm{diag}\{C(n\,\bar{b}/\bar{r})\} & 0 \\ 0 & \mathrm{diag}\{C(n\,\bar{b}/\bar{r})\} \end{bmatrix} \tag{10.49}$$

$$\mathrm{diag}\{r\} = \begin{bmatrix} \mathrm{diag}\{\bar{r}\} & 0 \\ 0 & \mathrm{diag}\{\bar{r}\} \end{bmatrix} \tag{10.50}$$

$$\mathrm{diag}\{\mu\} = \begin{bmatrix} \mathrm{diag}\{\mu\} & 0 \\ 0 & \mathrm{diag}\{\mu\} \end{bmatrix} \tag{10.51}$$

$$\mathbf{J}_3 = \begin{bmatrix} \mathbf{J} & 0 \\ 0 & \mathbf{I} \end{bmatrix} \tag{10.52}$$

In the former equations, it is worthwhile to note that when the advance ratio equals to zero (hover condition), the "nonlinear" terms (denoted by the superscript NL) reduce to zero, resulting in a set of linear, constant coefficient differential equations.

The state vector can be expanded into complex Fourier series of the harmonics of the blade revolutions:

$$\mathbf{x} = \sum_{n=-\infty}^{\infty} \mathbf{x}_n e^{in\psi} \tag{10.53}$$

where the complex coefficients, given by

$$\mathbf{x}_n = \frac{1}{2\pi} \int_0^{2\pi} \mathbf{x}(\psi) e^{-in\psi} d\psi, \quad n = 0, \pm 1, \cdots, \pm\infty \tag{10.54}$$

are related to the coefficients of the sine (subscript 's') and cosine (subscript 'c') Fourier expansions:

$$\mathbf{x}_n = \frac{1}{2}(\mathbf{x}_{nc} - i\mathbf{x}_{ns}) \tag{10.55}$$

$$\mathbf{x}_{-n} = \mathbf{x}_n^* \tag{10.56}$$

The Fourier series expansion (Eq.(10.53)) is substituted into Eqs.(10.14) and (10.36). Moreover the control signal is expressed as Fourier series and substituted in Eq.10.14:

$$k(\psi) = \sum_{p=-\infty}^{\infty} k_p e^{ip\psi} \tag{10.57}$$

where a phase lag is incorporated in the complex constant:

$$k_p = \kappa_p e^{ip\Delta\psi} \tag{10.58}$$

The harmonic balance technique is used to eliminate the time dependence. A set of algebraic equations is obtained after some algebra:

$$\begin{aligned} &\mathbf{x}_n + \mathbf{D} \sum_{j=-2}^{2} \mathbf{G}_j(n) \mathbf{x}_{n+j} + \mathbf{\Delta D} \sum_{p=-\infty}^{\infty} k_p \sum_{j=-2}^{2} \mathbf{G}_j(n-p) \mathbf{x}_{n+j-p} = \\ &= \mathbf{E}\boldsymbol{\theta}_c + \mathbf{D}\mathbf{J}_2 \mathbf{q}_n^D + \mathbf{\Delta D}\mathbf{J}_2 \sum_{p=-\infty}^{\infty} k_p \mathbf{q}_{n-p}^D \quad , \quad n = 0, \pm 1, \cdots, \pm\infty \end{aligned} \tag{10.59}$$

where

$$\mathbf{G}_0(n) = -\nu n^2\mathbf{M} + \nu\mathbf{Z} + \frac{\nu\gamma}{2}I_b(-n^2Q_2^L + in\mathbf{Q}_1^L + \mathbf{Q}_0) \tag{10.60}$$

$$\mathbf{G}_1(n) = \frac{\nu\gamma}{4}I_b(-(n+1)\mathbf{Q}_{1s}^{NL} + i\mathbf{Q}_{0s}^{NL} + \mathbf{Q}_{01c}^{NL}) \tag{10.61}$$

$$\mathbf{G}_{-1}(n) = \frac{\nu\gamma}{4}I_b((n-1)\mathbf{Q}_{1s}^{NL} - i\mathbf{Q}_{0s}^{NL} + \mathbf{Q}_{01c}^{NL}) \tag{10.62}$$

$$\mathbf{G}_2(n) = \mathbf{G}_{-2}(n) = \frac{\nu\gamma}{4}\mathbf{Q}_{02c}^{NL}) \tag{10.63}$$

A clear way of achieving control authority at the critical frequency $n = n_b$ is to set p=j in Eq.(10.59). In this case, the useful harmonics of the control signal are limited to the first 2 ($-2 \leq p \leq 2$):

$$\kappa_p = \frac{1}{2\pi}\int_0^{2\pi}\kappa(\psi)e^{-ip\psi}d\psi, \quad n = 0, \pm1, \pm2 \tag{10.64}$$

where $\kappa(\psi)$ is the signal driving the actuator device. Moreover, at the critical frequency the collective and cyclic control inputs are not affected by the IBC input (as suggested in Eq.(10.59)). Hence,

$$\left[\mathbf{I} + \mathbf{D}\mathbf{G}_0(n) + \mathbf{\Delta}\mathbf{D}\sum_{j=-2}^{2}k_j\mathbf{G}_j(n-j)\right]\mathbf{x}_n + \mathbf{D}\sum_{j=-2}^{2}\mathbf{G}_j(n)\mathbf{x}_{n+j} =$$

$$= \mathbf{D}\mathbf{J}_2\mathbf{q}_n^D + \mathbf{\Delta}\mathbf{D}\mathbf{J}_2\sum_{j=-2}^{2}k_j\mathbf{q}_{n-j}^D \quad , \quad n = 0, \pm1, \cdots, \pm\infty \tag{10.65}$$

The complete solution of the problem demands the infinite set of algebraic equations to be solved. Of course, the set can be truncated at a finite number of harmonics, but because one is only interested in obtaining results for a determined harmonic ($n = n_b$), Eq.(10.65) needs to be solved for a reduced set of frequencies ($n_b - 2 \leq n \leq n_b + 2$). It is worthwhile to point out that this procedure yields a set which is complete only for the critical frequency, and inaccurate results are obtained for the remaining harmonics. Hence, the $10N$ algebraic equations involving the central, and the neighboring upper two and lower two harmonics of the state vector are cast into a matrix form:

$$\mathbf{A}\mathbf{z} = \mathbf{b} \tag{10.66}$$

where

$$\mathbf{z}^T = [\mathbf{x}^T_{n_b-2}, \mathbf{x}^T_{n_b-1}, \mathbf{x}^T_{n_b}, \mathbf{x}^T_{n_b-1}, \mathbf{x}^T_{n_b+2}] \tag{10.67}$$

$$\mathbf{b}^T = [\mathbf{b}^T_{n_b-2}, \mathbf{b}^T_{n_b-1}, \mathbf{b}^T_{n_b}, \mathbf{b}^T_{n_b-1}, \mathbf{b}^T_{n_b+2}] \tag{10.68}$$

$$\mathbf{A} = \begin{bmatrix} \mathbf{A}_0(n_b-2) & \mathbf{A}_1(n_b-2) & \mathbf{A}_2(n_b-2) & 0 & 0 \\ \mathbf{A}_{-1}(n_b-1) & \mathbf{A}_0(n_b-1) & \mathbf{A}_1(n_b-1) & \mathbf{A}_2(n_b-1) & 0 \\ \mathbf{A}_{-2}(n_b) & \mathbf{A}_{-1}(n_b) & \mathbf{A}_0(n_b) & \mathbf{A}_1(n_b) & \mathbf{A}_2(n_b) \\ 0 & \mathbf{A}_{-2}(n_b+1) & \mathbf{A}_{-1}(n_b+1) & \mathbf{A}_0(n_b+1) & \mathbf{A}_1(n_b+1) \\ 0 & 0 & \mathbf{A}_{-2}(n_b+2) & \mathbf{A}_{-1}(n_b+2) & \mathbf{A}_0(n_b+2) \end{bmatrix} \tag{10.69}$$

with

$$\mathbf{b}_n = \mathbf{D}\mathbf{J}_2\mathbf{q}^D_n + \mathbf{\Delta}\mathbf{D}\mathbf{J}_2 \sum_{j=-2}^{2} k_j \mathbf{q}^D_{n-j} \tag{10.70}$$

$$\mathbf{A}_0 = \mathbf{I} + \mathbf{D}\mathbf{G}_0(n) + \mathbf{\Delta}\mathbf{D} \sum_{j=-2}^{2} k_j \mathbf{G}_j(n-j) \tag{10.71}$$

$$\mathbf{A}_j(n) = \mathbf{D}\mathbf{G}_j(n), \quad j = \pm 2, \pm 1 \tag{10.72}$$

It should be noted that $\mathbf{A}$ is a $10N \times 10N$ band matrix that can be always inverted and, since the equations are still written in physical coordinates, the solution of the Eq.(10.66) gives directly the two dependent variables φ and θ at the target harmonic $n = n_b$.

Chapter 11

Design and Validation of a reduced-scale model helicopter blade

A description of the design, instrumentation and identification of the SHARCS blade is summarized in this chapter. The original design of the SHARCS scaled rotor can be found in Ref.[11]. In this thesis only the APL is considered and, for this reason, the blade and also the rotor are not exactly the same as in the complete project. What described in the previous chapters from the theoretical point of view is here numerically and experimentally achieved on a mock-up. The main characteristics of the blade are given, as they reflect the real structure and its numerical model. Then, a numerical procedure is implemented to extract the inertial and stiffness properties of different cross sections and to build the 1D model suitable to be implemented in the GAST numerical procedure as illustrated in Chapter 9. Some simulations are performed in order to evaluate the natural frequencies of the blade rotating at several speeds and the numerical fan plot is obtained. Concurrently in this chapter also the experimental activities carried out at Ottawa (Ontario, Canada) in the laboratories of the Rotorcraft group of the Carleton University and of the Canadian National Research Council are presented. A first identification of the blade's modal properties is performed by considering free-free boundary conditions. The hammer test is described as well as the results with the aim of understanding the behavior of such a component itself. Then the blade is mounted

on the whirl tower and the effect of the actual boundary conditions is investigated. Two aspects have to be taken into account in this analysis: the definition of the boundary condition of the blade with respect the hub in the rotating frame in a reference condition and the effects of changing the pitch link on this condition. Moreover, the rotating tests are performed at different rotating speed and the root locus of the system's poles is estimated by applying the developed operational modal analysis methodology. The capabilities of the modified HTM to track the changes in the natural frequencies, damping ratios and mode shapes of the rotating scaled helicopter blade are investigated in order to asses the overall efficiency of the OMA methodology. Furthermore, the experimental findings are compared to those numerically achieved using the reference solution provided by GAST in solving the dynamics of a rotating blade.

11.1 The Blade

The importance in projecting a blade can be found in the necessity of having a test specimen full instrumented in order to be able to measure its responses in the operating conditions and then identify its dynamical behavior. The design of the blade is performed taking into account that the blade should reflect stiffness and inertial properties of a real blade in a reduced scale because it has to be coupled with a reduced-scale prototype of the APL. Moreover, it has to be tested in the whirl tower facility available at the Carleton University, so the rotor radius is set to $0.86\,\mathrm{m}$. The blade section is a NACA0015 airfoil, with a constant chord of $81\,\mathrm{mm}$ along the blade, with the exception of the sections next to the root. The $15\,\%$ thickness airfoil was selected to maximize the internal space inside the blade, so that the blade interior could contain the sensors and their wires. Another parameter that must be considered, at this point, is the Lock number, which represents the ratio of inertial and aerodynamic forces and is defined as

$$\gamma = \rho a_0 2 b R^4 / I_b \tag{11.1}$$

where, ρ is the freestream density, a_0 is the lift curve slope of the blade airfoil, $2b$ is the chord-length, R is the radius and I_b is the mass moment of inertia of the blade around the flapping hinge,

$$I_b = \int_0^R mr^2 dr \tag{11.2}$$

where m is the mass per unit length and r is the radial location. If the Lock number is set to 5, which is typical for scaled helicopter rotors, a condition to evaluate the mass moment of inertia of the blade around the flapping hinge is found. The blade has a linear pre-twist distribution with a total twist of 6.75 degrees, and a zero twist distribution between $65\,\%$ and $90\,\%$ of rotor radius. The original SHARCS rotor is defined to have 4 blades, with a root cut-out of $126\,\mathrm{mm}$.

To satisfy the design requirement of aerodynamic cleanness, the sensors and all their wires should be housed inside the blade. This leads to a C-shaped spar, monocoque composite blade design as shown in Fig.11.6. The composite skin is made of carbon fibre laminas with varying lay-ups along the chord. Thus, the lay-up from the leading edge to the $13\,\%$ of the chord length consists of 10 symmetric layers oriented as $[0°|0°|-45°|90°|+45°]$ from the outside with respect to the radial direction; while from the $35\,\%$ of the chord length to the trailing edge it consists of 6 symmetric layers oriented as $[0°|-45°|+45°]$. Leading edge ballast made of Tungsten is added at the nose of the blade to move forward the center of gravity of the section. The blade root is reinforced by introducing a composite structure spanning the whole blade thickness, called the *root coupon*. This enables the smooth distribution of the loads between the upper and lower skins (Fig.11.1). The root coupon consists of 78 layers (39 for each half-blade) that progressively decrease from the root to about the $10\,\%$ of the span [1].

The blade is manufactured in two shells: the upper and lower part of the profile, starting from pre-impregnated plies of carbon fibres, cut and molded into the NACA profile. Figure 11.2 shows a representative cutting scheme and the molds. Once the two parts are cured in the autoclave, they are instrumented as described in the next section and then they are bonded together, including the balancing masses and

[1] The stacking sequence at the root is $[0°|0°|0°|-45°|90°|+45°|+45°|90°|-45°|0°|0°|0°|+45°|0°|0°|+45°|90°|-45°|-45°|90°|+45°|0°|0°|+45°|0°|0°|0°|-45°|90°|+45°|+45°|90°|-45°|0°|0°|0°|0°|0°|0°]$.

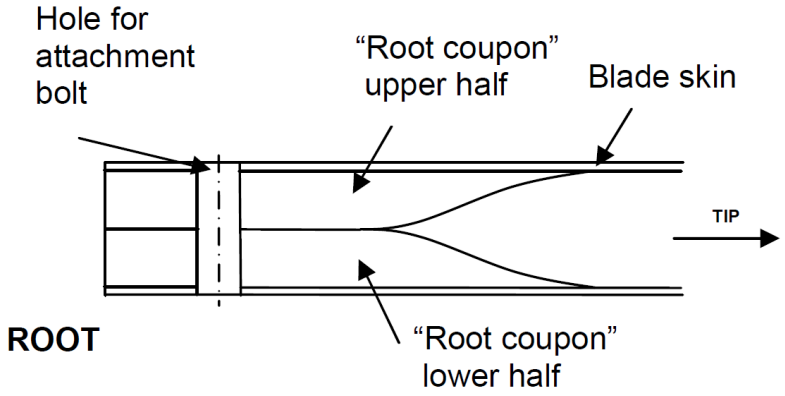

Figure 11.1: Illustration of the *root coupon* reinforcement of the blade root.

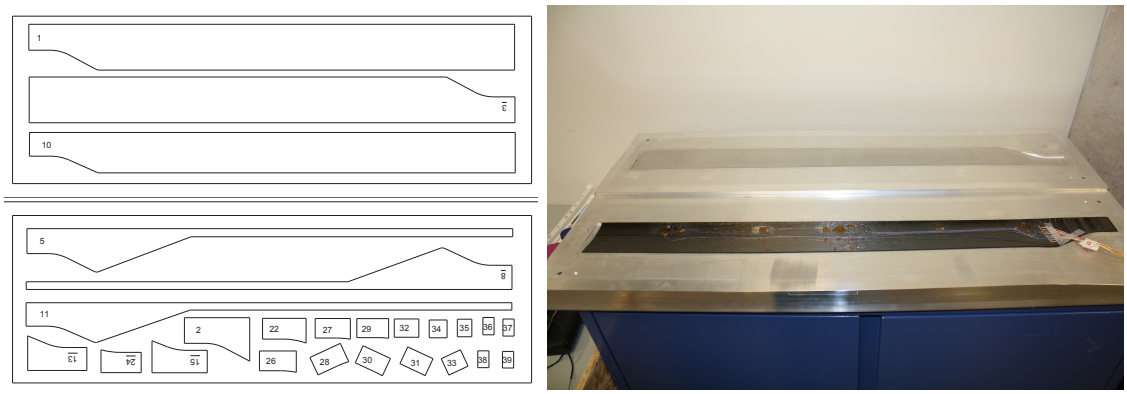

Figure 11.2: Template and molds of the SHARCS blade.

the foam. In the end the tip is filled with resin and the full blade is machined to make fixing holes at the root and to smooth the edges.

11.1.1 Sensor positioning

In order to monitoring the behavior of the blade during the tests, it is equipped with strain gauges along the flap, torsion and lead-lag direction at several spanwise positions: 3 for the first two directions and 2 for the last one, Fig.11.3. All sensors are arranged in a full-bridge configuration in order to maximize the signal to noise ratio and achieve the temperature compensation. Therefore, the deformations are measured by four strain gauges arranged on the opposite sides of the upper and lower blade shell, as shown in Fig.11.4, with an angle of $\pm 0^o$ degree for the flap and lead-lag and an angle of $\pm 45^o$ degree for the torsion with respect to the span direction of the blade. The labels of the wire connections follows the convention explained in

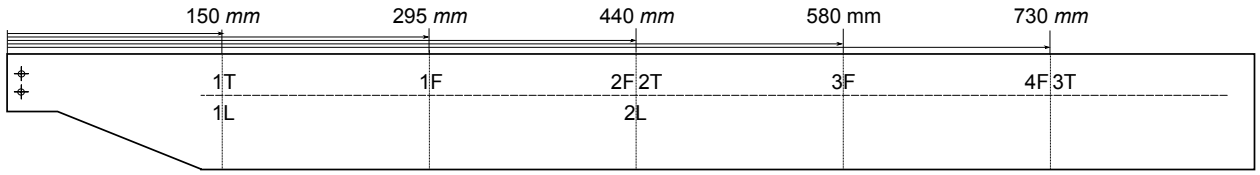

Figure 11.3: Strain gauges positioning inside the blade - F for flap, T for torsion and L for lead-lag degree of freedom.

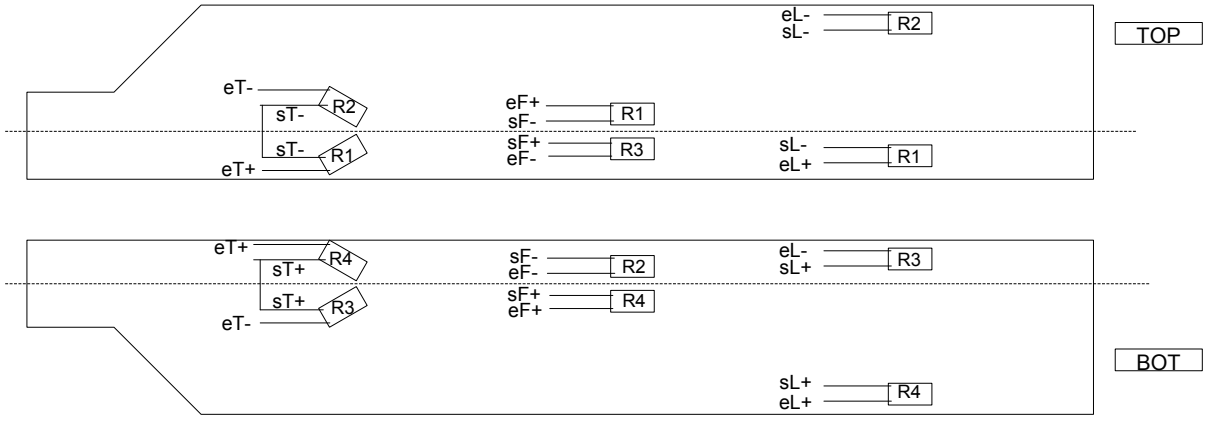

Figure 11.4: Strain gauges mounting scheme inside the blade.

Fig.11.5.

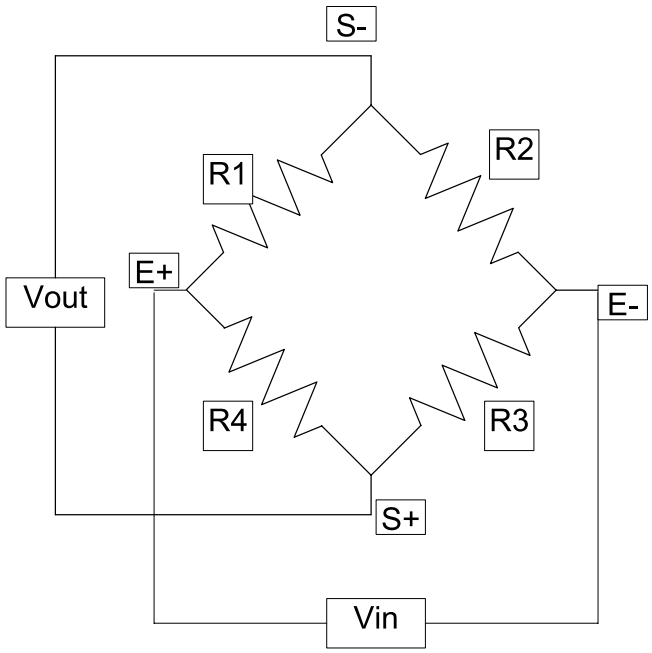

Figure 11.5: Strain gauges full bridge configuration.

11.2 Numerical model

An accurate model of some cross sections of the blade is performed starting from the described layout. The 2D profile of the characteristic section is represented in Fig.11.6. The geometrical discretization, the

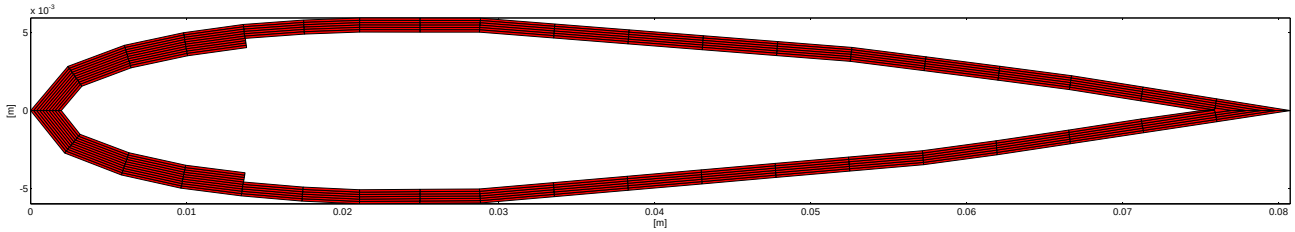

Figure 11.6: Blade's constant cross section geometry.

staking sequence and the material properties are used to write the input file suitable for the Variational Asymptotic Beam Section (VABS) analysis program, as developed at the School of Aerospace Engineering of the Georgia Institute of Technology, Ref.[82]. VABS is a code implementing various beam theories based on the concept of simplifying the original nonlinear three-dimensional (3D) analysis of slender structures into a two-dimensional (2D) cross-sectional analysis and a one-dimensional (1D) nonlinear beam analysis using a powerful mathematical method: the variational asymptotic method. VABS takes a finite element mesh of the cross section including all the details of geometry and material as inputs to calculate the sectional properties: structural and inertial. The sectional properties, such as the mass and stiffness matrices, are given in an output file. The elements in the mass matrix are arranged as follows:

$$\begin{bmatrix} \mu & 0 & 0 & 0 & \mu x_{m3} & -\mu x_{m2} \\ 0 & \mu & 0 & -\mu x_{m3} & 0 & 0 \\ 0 & 0 & \mu & \mu x_{m2} & 0 & 0 \\ 0 & -\mu x_{m3} & \mu x_{m2} & i_{22}+i_{33} & 0 & 0 \\ \mu x_{m3} & 0 & 0 & 0 & i_{22} & i_{23} \\ -\mu x_{m2} & 0 & 0 & 0 & i_{23} & i_{33} \end{bmatrix} \tag{11.3}$$

The system of coordinate in VABS is defined with x_1 along the direction of the span and points to the tip, x_2 is along the direction of the leading-edge to the trailing edge and points to the direction of the leading edge, and x3 can be determined by the right hand rule.

It can be seen that the first three elements of main diagonal of the mass matrix represent the mass per unity length μ of the section of the blade. Then from the 2×2 sub-matrix at the bottom-right corner, the mass momentum of inertia about the two axes i_{22} and i_{33} can be extracted as well as the product of inertia i_{23}. Moreover, the location of the mass center (x_{m2}, x_{m3}) is given by the bottom-left 3×3 corner (or top-right 3×3 corner, since the matrix is symmetric). The sum of the two in-plane cross-sectional mass moments of inertia is the square of the mass-weighted radius of gyration, r_θ^2.

The 4×4 stiffness matrix expresses the following constitutive relation for the classical beam model, which can be compared with the ones obtained in Eqs.(9.9-9.12) for $\theta_t = 0$ since the twist angle of the cross section is not considered here:

$$\begin{Bmatrix} F_\eta \\ M_\eta \\ M_\xi \\ M_\zeta \end{Bmatrix} = \begin{bmatrix} EA & EI_t & EA_\xi & -EA_\zeta \\ EI_t & GI_t & EI_{t\xi} & -EI_{t\zeta} \\ EA_\xi & EI_{t\xi} & EI_{\xi\xi} & -EI_{\xi\zeta} \\ EA_\zeta & -EI_{t\zeta} & -EI_{\xi\zeta} & EI_{\zeta\zeta} \end{bmatrix} \begin{Bmatrix} v' \\ \theta' \\ w'' \\ u'' \end{Bmatrix} \tag{11.4}$$

From the main diagonal of the stiffness matrix the tensional, torsional, out-of-plane and in-plane bending coefficients can be extract: EA, GI_t, $EI_{\xi\xi}$ and $EI_{\zeta\zeta}$ as introduced in Eq.(9.13). Moreover, the out of diagonal terms not equal to zero indicate the presence of coupling among tension torsion and bending coming from the non coincidence of the section tension center (on the neutral axes) and the shear center (on the elastic axis).

The results in terms of the equivalent 1D inertial and stiffness properties are indicated in Tabs.11.1 and 11.2. They are used to generate the 1D model of the blade used in the next sections 11.6 and 12.3,

Table 11.1: The 6×6 mass matrix of the constant cross section of the blade evaluated by VABS.

$$\begin{bmatrix} 2.49E-01 & 0.00E+00 & 0.00E+00 & 0.00E+00 & -5.19E-06 & 8.81E-03 \\ 0.00E+00 & 2.49E-01 & 0.00E+00 & 5.19E-06 & 0.00E+00 & 0.00E+00 \\ 0.00E+00 & 0.00E+00 & 2.49E-01 & -8.81E-03 & 0.00E+00 & 0.00E+00 \\ 0.00E+00 & 5.19E-06 & -8.81E-03 & 4.53E-04 & 0.00E+00 & 0.00E+00 \\ -5.19E-06 & 0.00E+00 & 0.00E+00 & 0.00E+00 & 3.79E-06 & -2.83E-07 \\ 8.81E-03 & 0.00E+00 & 0.00E+00 & 0.00E+00 & -2.83E-07 & 4.49E-04 \end{bmatrix}$$

together with similar results obtained for other 2D cross sections, characterizing the root region.

Table 11.2: The 4×4 stiffness matrix of the constant cross section of the blade evaluated by VABS.

$$\begin{bmatrix} \text{Extension} & \text{Twist} & \text{Out-of-plane Bending} & \text{In-plane Bending} \\ 9.07E+06 & 1.02E+02 & 1.66E+02 & -3.03E+05 \\ 1.02E+02 & 1.73E+02 & 4.38E-03 & -3.29E+00 \\ 1.66E+02 & 4.38E-03 & 1.37E+02 & -9.42E+00 \\ -3.03E+05 & -3.29E+00 & -9.42E+00 & 1.53E+04 \end{bmatrix}$$

11.3 Experimental Modal Analyses of the blade

The blade is suspended by means of bungee chords and it is excited by an instrumented hammer (with a sensitivity of $2.25\,\mathrm{mV/N}$) along the normal direction in order to minimize the coupling among the rigid and the elastic modes. Two sets of tests are carried out to evaluate the modal dynamics in terms of the out-of-plane bending and torsion degrees of freedom (described by the Z direction) and in terms of the in-plane bending degree of freedom (described by the Y direction), by turning the blade inside the elastic suspensions and by keeping the same position (next to the root, point 5 according to the geometry in Fig.11.7) and direction of the hammer when hitting the blade. In the first case, three measuring runs are repeated by changing the position of four accelerometers (with an average sensitivity of $10\,\mathrm{mV/g}$) for a total of 12 measured channels along the Z direction (by means of roving technique). Then, after a rotation of 90 degrees of the blade, one more run is performed in the Y direction with the same accelerometers. All tests are performed using the LMS Scadas 3 acquisition system and the LMS Test.Lab software. The acquisition parameters are summarized in Tab.11.3 for the two cases. The modal parameters are evaluated

Table 11.3: Main parameters for the experimental modal tests of the full blade.

Parameter	Z direction	Y direction
Input signal	Impulse along Z	Impulse along Y
Input window	Force exponential	Force exponential
Sample frequency [Hz]	1024	2048
Spectral lines	4096	4096
Observation time [s]	8	8
Output Window	Exponential	Exponential
Averages	10	10
Estimator	Hv	Hv

by applying the LMS Polymax algorithm and the results are described in Tab.11.4, where the out-of-plane and in-plane bending modes are indicated with the label flap and lead-lag, respectively, according to the nomenclature used for the blade in the operating conditions. It should be noted that the rigid modes are more than one order of magnitude lower than the elastic ones, then it is reasonable to assume that the

Table 11.4: Free-Free full-blade natural frequencies, damping ratios and mode shape descriptions.

Mode #	f_n [Hz]	ζ_n [%]	Description
1	1.4	4.6	Rigid Lead-Lag mode
2	3.9	1.9	Rigid Pitch mode
3	39.0	5.0	1st flap-torsion mode
4	66.3	3.13	local tip flap mode
5	79.0	5.0	local root flap mode
6	193.3	4.9	1st torsion 2nd flap mode
7	204.1	11.0	2nd flap mode
8	291.3	6.13	1st torsion mode
9	375.7	5.1	3rd flap mode
10	431.8	1.2	1st Lead-Lag mode
11	523.0	1.4	2nd Lead-Lag mode

boundary conditions do not affect the estimates and the blade can be considered in the free-free condition. Strong coupling of the flap and torsion mode shapes is found. This can be seen as a consequence of the layer stacking sequence of the composite material, described in Sec.11.1. The 3rd and 6th mode shapes are represented in Fig.11.7, where the 1st torsional mode is coupled with the 1st and 2nd flap mode, in (a) and (b) respectively. Moreover, it should be noted that the leading edge exhibits less displacements than the trailing edge, as expected, because of the presence of the distributed masses inside the blade, which are placed next to the leading edge, and the extra-layers of the composite material, as shown in Fig.11.6. This effect can be noted also in Fig.11.8 for the pure torsional mode, by considering that the marker with label *root* is placed next to the leading edge of the root.

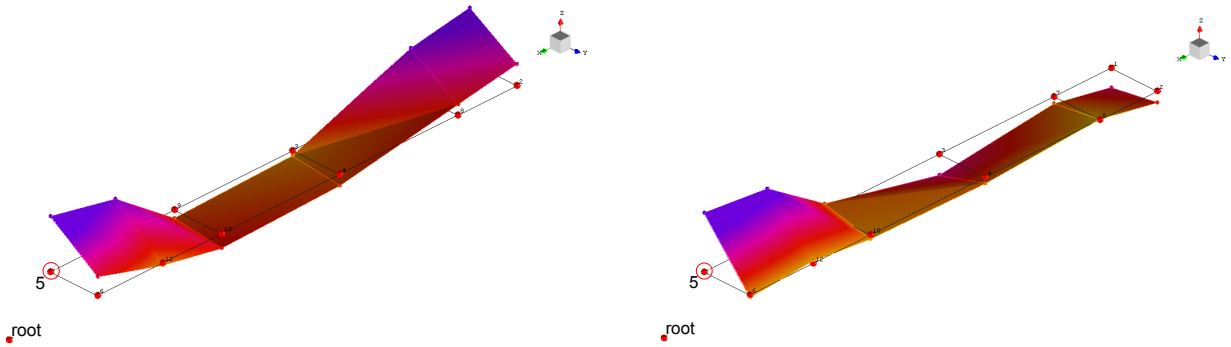

(a) 3rd Mode (b) 6th Mode

Figure 11.7: Coupling between torsion and the 1st or 2nd flap mode of the full blade.

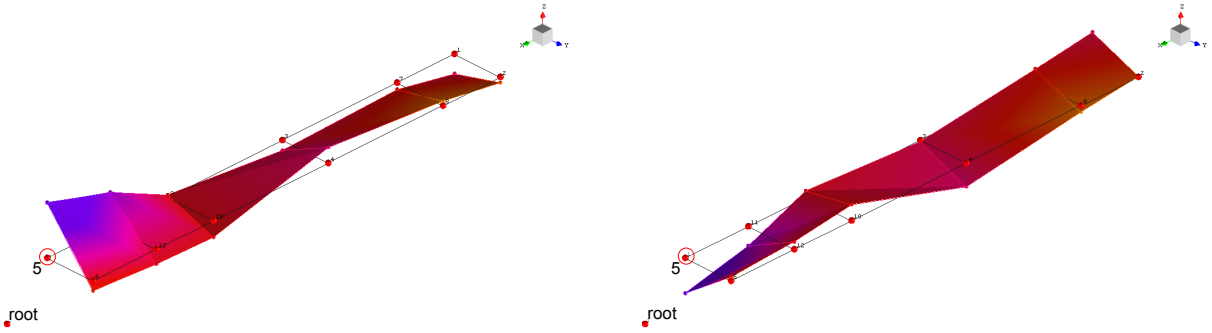

(a) (b)

Figure 11.8: 1st torsional mode of the full blade.

Figure 11.9: General view of the Whirl Tower test chamber with the blade.

Figure 11.10: The Whirl Tower Monitor and Control Room.

11.4 Whirl Tower Test Setup

The rotating tests are carried out at the Whirl Tower Test facility of the Carleton University in Ottawa, Canada, Ref.[83]. The test specimen consists of the blade described in the previous sections installed on a test rig, as depicted in Fig.11.9. The tower is driven by a $60\,\mathrm{HP}$, $575\,\mathrm{V}$ 3-phase, $1800\,\mathrm{RPM}$ motor, which is controlled via a variable frequency drive/transformer. The whirl tower is located in a test chamber with a diameter of $15\,\mathrm{ft}$. The protective walls were constructed from Armorcore level 3 panels, a glass-fibre based protective panel developed for withstanding gunshots. The whole whirl tower facility is monitored by live video and live data collection viewed from an isolated control room, see Fig.11.10. The whirl tower is deliberately designed in a way so that the lowest natural frequency is beyond the nominal rotating speed

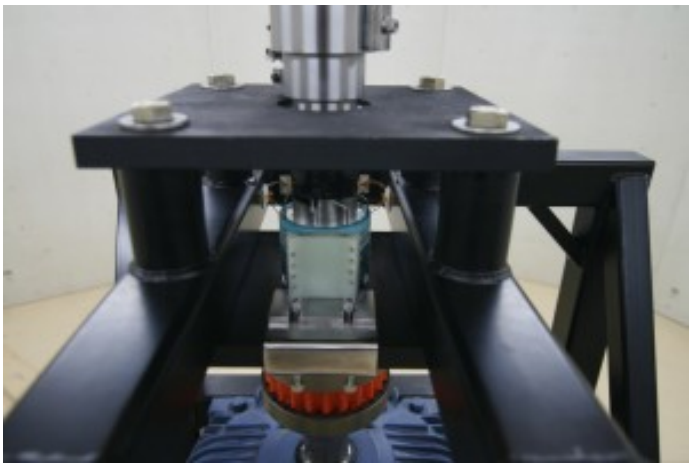

Figure 11.11: The Whirl Tower flexible coupling and 8-channel slip ring assembly.

(a) V-link (b) USB Base Station

Figure 11.12: Microstrain V-link acquisition system.

of $1550\,\mathrm{RPM}$. This allows continuous testing without any *blackout periods* in terms of the rotational frequency. To achieve low baseline vibration, the main shaft is driven directly via a flexible coupling. The rotor hub houses both a wireless telemetry system as well as an 8-channel slip ring assembly from Shleifring, see Fig.11.11.

The wireless system consists of three Microstrain V-link (Wireless Voltage) Nodes, each capable of transmitting data from 9 differential and 12 strain gauge channels. The nodes are able to store and stream all data gained from the measurement channels simultaneously. The sampling frequency is set at $512\,\mathrm{Hz}$, according to the range of measurement of the strain gauges. The experimental tests are carried out by varying the angular velocity of the system, Ω, in order to investigate the influence of the rotating speed on

the modal parameters of the blade. The reference value is $\Omega_0 = 1550\,\mathrm{RPM}$ and seven speed ratios were considered besides the arrest, that are $\Omega/\Omega_0 = 0.00, 0.26, 0.39, 0.52, 0.65, 0.77, 0.90, 1.00$. The acquisition time for each rotating condition is $128\,\mathrm{s}$.

11.5 Fan plot estimate

The approach described in the Sec. 2.5 is used for the identification of the dynamic properties of the rotating structure through tests in which the input excitation cannot be measured. The identification procedure to be followed for the experimentally evaluation of the fan-plot is the same adopted in Chapter 5 where, for the first time, the Operational Modal Analysis has been applied with this purpose on data recorded during whirl tower tests. In particular the presence of harmonic components in the excitation loading requires a first identification of the so-called operational frequencies and then their removal from the operating frequency response functions according to the modified Hilbert Transform Method. Finally, the modal parameters can be estimated for each rotating condition and the fan plot of the natural frequencies and damping ratios can be built.

11.5.1 Identification of the harmonic loadings

The first step for the characterization of the rotating blade dynamics is the identification of the harmonic components blended in the white noise excitation. The non-gaussianity test was performed from the output response signals, as described in a previous section, in order to identify possible harmonic loadings blended in the broad band white noise response, mainly originated from the air turbulence during the motion of the rotating blade.

Following the approach described at the end of Sec.2.5.1, a narrow-band filter is introduced in the time domain in order to find those frequencies to which the signals have an operational nature, *i.e.*, they could not be considered as typical gaussian responses. For all the frequencies, $f_j,\ j = 1, \cdots, N_f$, available in the test (being $N_f = 2^{16}$ the number of the available frequency lines), the entropy statistical index is calculated by applying a Butterworth filter.[48] The presence of harmonic excitations in the output signals is clearly observable from the several minima reported in Fig.11.13, where the entropy index is plotted as a function of the frequency for different orders of the Butterworth filter. From the previous analyses, it is observed

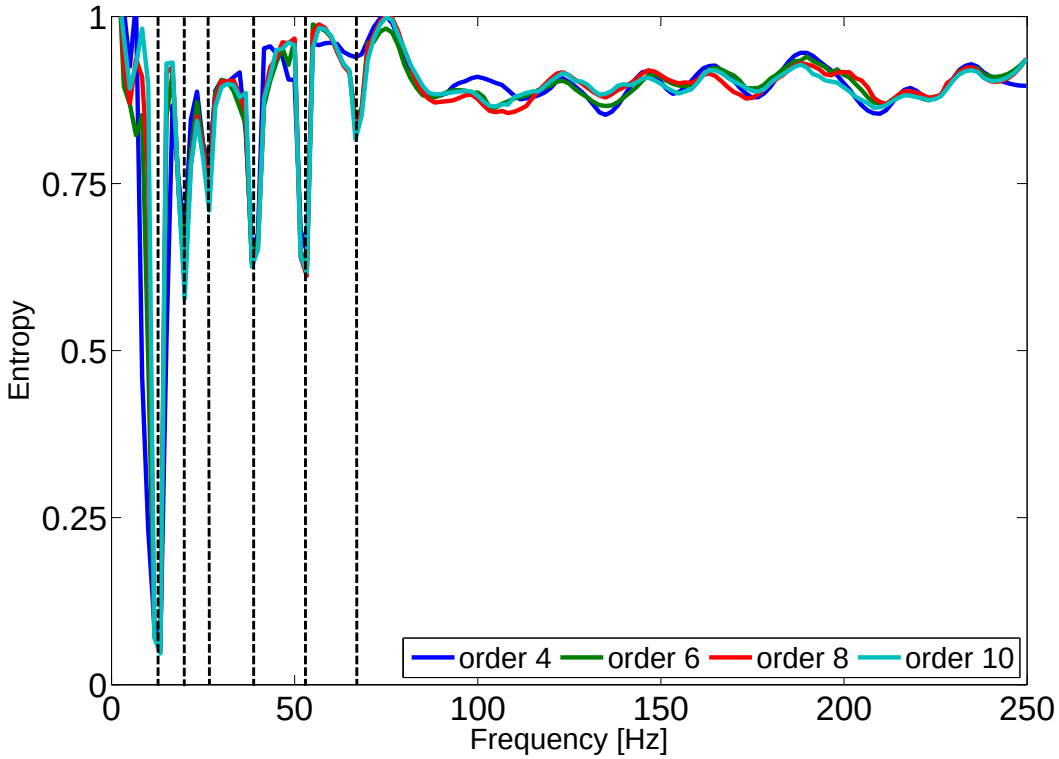

Figure 11.13: Identification of the harmonic excitation occurring at $\Omega = 0.26\Omega_0$ by the entropy approach using Butterworth filters with different orders.

that the local minimum does not depend on the order of the Butterworth filter used to obtain the entropy index as a frequency function. An accurate identification of the operational frequencies is achieved with filter orders as low as 4, thus keeping low the computational costs. The identified operational frequencies are found matching the n/rev excitation components for each of the considered rotational speed, that is $\Omega = 0.26\ \Omega_0 = 400\,\mathrm{RPM} = 41.89\,\mathrm{rad/s}$ (or $f_0 = 6.67\,\mathrm{Hz}$) in the Fig.11.13. In Tab.11.5 all the harmonic loading estimates (f_{op}^n) are summarized with the corresponding rotating speed of the system (Ω), the n/rev excitations measured at each test. It could be noted that not all multiples of the rotating speed are founded for each configuration, that means that sometimes those harmonic energy contributions are not high enough with respect to the random noise excitation, so their influence on the time responses of the system can be neglected.

Table 11.5: Operational frequency estimates f_{op}, for each rotating condition Ω.

Ω/Ω_0	0.26	0.39	0.52	0.65	0.77	0.90	1.00
f_{op}^1/Ω	-	-	1.00	1.00	1.00	1.00	-
f_{op}^2/Ω	2.00	2.00	2.00	2.00	2.00	2.00	2.00
f_{op}^3/Ω	3.00	3.00	3.00	3.00	3.00	3.00	-
f_{op}^4/Ω	4.00	4.00	4.00	4.00	4.00	4.00	4.00
f_{op}^5/Ω	-	5.00	5.00	-	5.00	-	-
f_{op}^6/Ω	6.00	6.00	6.00	-	-	-	6.00
f_{op}^7/Ω	-	-	7.00	-	-	-	-
f_{op}^8/Ω	8.00	-	8.00	-	8.00	8.00	8.00
f_{op}^9/Ω	-	-	9.00	-	-	-	-
f_{op}^{10}/Ω	10.00	-	10.00	-	10.00	-	10.00

11.5.2 Estimate of the modal parameters

Once the harmonic excitations characterizing the operating conditions of the rotating blade are identified, the operational modal analysis method is applied to estimate the modal parameters. The Hilbert Transform Method is used to calculate the biased frequency response functions of the vibrating structure as described in the previous section. In Fig.11.14, the driving point FRF $\tilde{H}$, evaluated at the root of the blade rotating at the nominal angular frequency Ω_0, is depicted in red together with the harmonic-free FRF $\overset{\oslash}{H}$ in blue and in black the FRF $\overset{\mathrm{O}}{H}$ coming from the operational frequencies evaluated using the entropy index, as in the last column of Tab.11.5 for $\Omega/\Omega_0 = 1.00$. These operational contributions to the structural response are removed and then the modal parameters are estimated by using $\overset{\oslash}{\mathbf{H}}$, evaluated from Eq. 2.67.

The positive effect of the proposed procedure in estimating the dynamic properties of the rotating blade by using the $\overset{\oslash}{H}_{ii}$ allows a clear identification of the true elastic modes, reducing the possibility of a wrong estimate of the operational modes. Fig.11.15 shows the sensitivity of the natural frequencies to the rotor speed, for each identified mode (F is for flapwise bending mode, L is for lagwise bending mode, whereas T is for torsional mode). The poles corresponding to the null rotating velocity are evaluated by performing the operational modal analysis of the time responses recorded by randomly exciting the structure with crawling fingers. In addition, straight lines, corresponding to different integer multiples of the fundamental

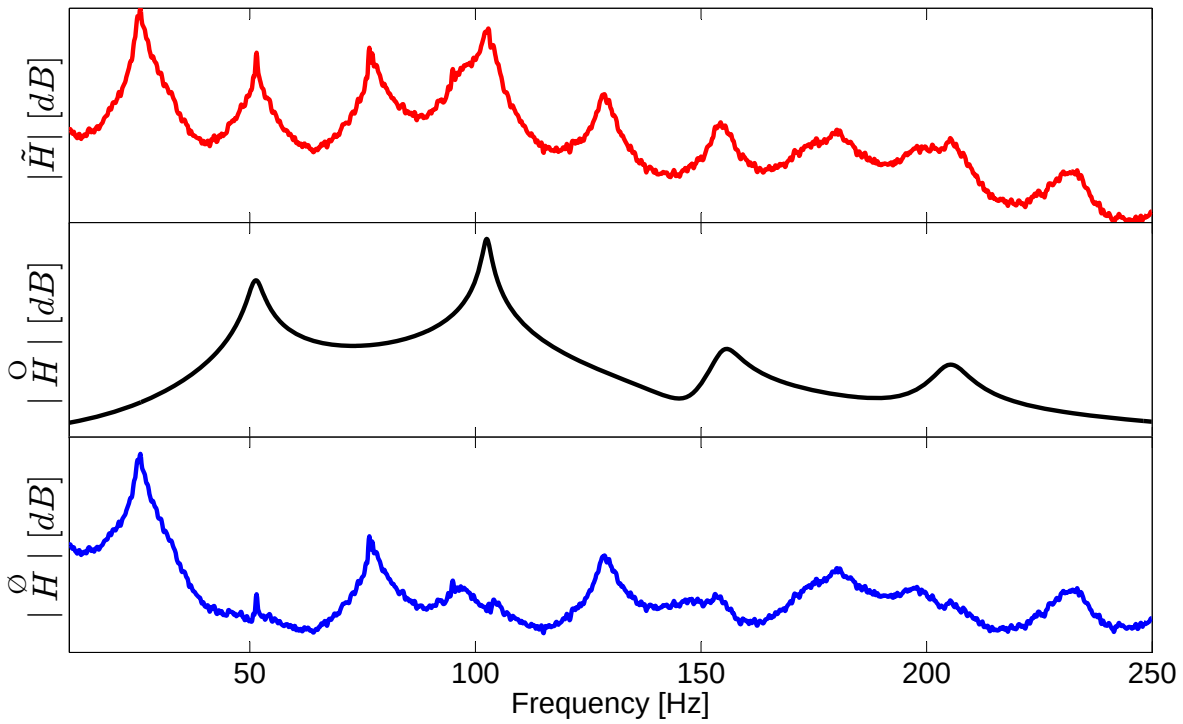

Figure 11.14: Frequency Response Function of the flapwise strain gauge at the root of the blade for $\Omega_0 = 1550RPM$.

frequency (namely the 1/rev, 2/rev, 3/rev etc.), are reported so that possible intersection between the natural frequencies and the operating frequencies could be detected. When the n/rev line ($n = 1, 2, \dots$) intersects one of the line representing the dependency of the rotating frequency of the system as a function of the rotational speed, then a coarse identification of the pole of the system is expected due to the detrimental action of operating harmonic loads.

From the analysis of the strain gauge sensors, the first consideration about the modal signature of the rotating blade involves the strong coupling between the torsion and the in- and out-of-plane bending. In fact, with the exception of the first flapping and the first torsion modes (depicted with the blue and the orange lines, respectively), all the modes are detectable by the flap, lead-lag and torsion sensors although with different participation that allows the definition of the type of the modes. The reason for this behavior can be found in the composition of the blade, which determines the complex behaviour, as seen also in

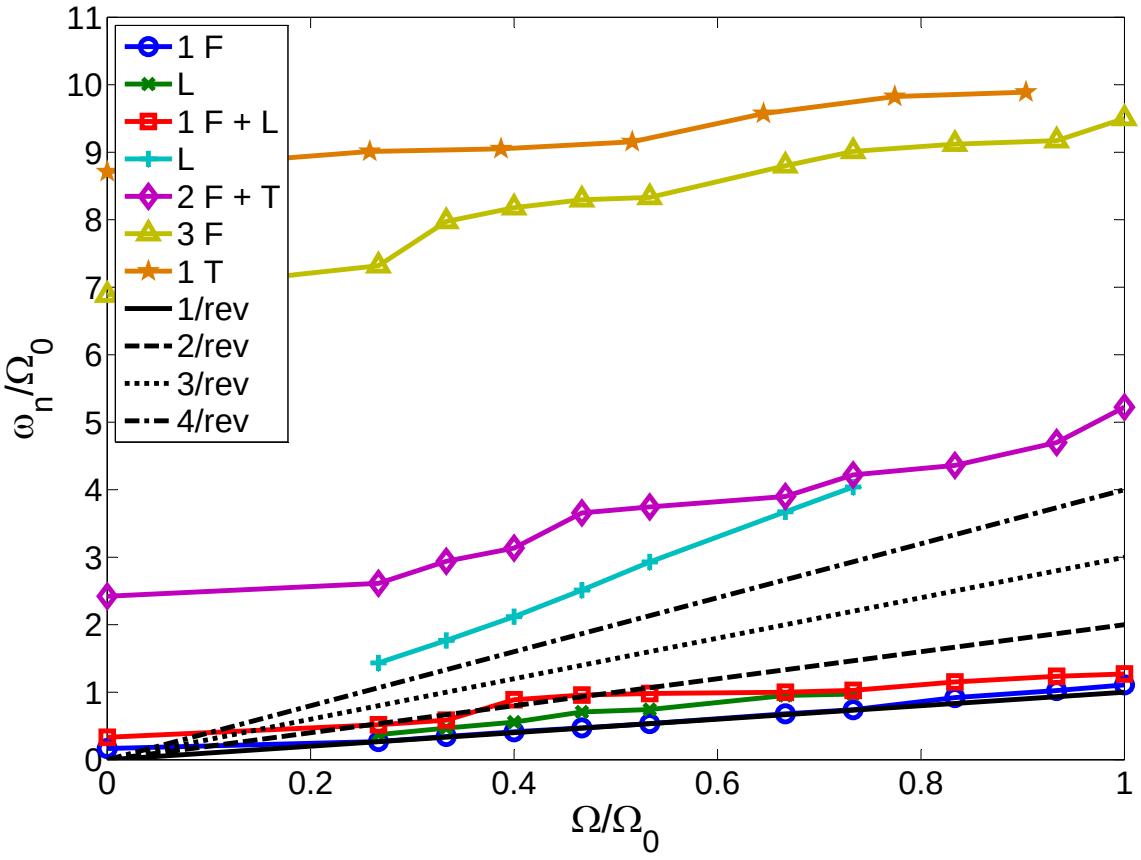

Figure 11.15: Experimental Fan Plot of the rotating blade for the natural frequencies.

the free-free boundary conditions in Sec.11.3. It should be stressed that the sensor sensitivity is likewise important because the strain gauges measure an equivalent bending or torsional strain at each position with four sensors, by assuming that the stiffness properties are locally constant. This does not take into account the possible discontinuities along the inner surface and the thickness. Nevertheless, the estimated modes are characterized by different relative amount of strain in each degree of freedom and they can be classified as torsional or bending modes according to the deformation with higher contributions. Therefore, the fan plot in Fig.11.15 shows the increase of the natural frequencies due to the rotating speed as major effect of the increase of the stiffness of the blade due to the rotation. Unfortunately, the number of lead-lag sensors is only two and during the test they experienced lack of accuracy as they presented a drift, shown in Fig.11.17. Therefore, the identification of the in-plane bending modes is not possible.

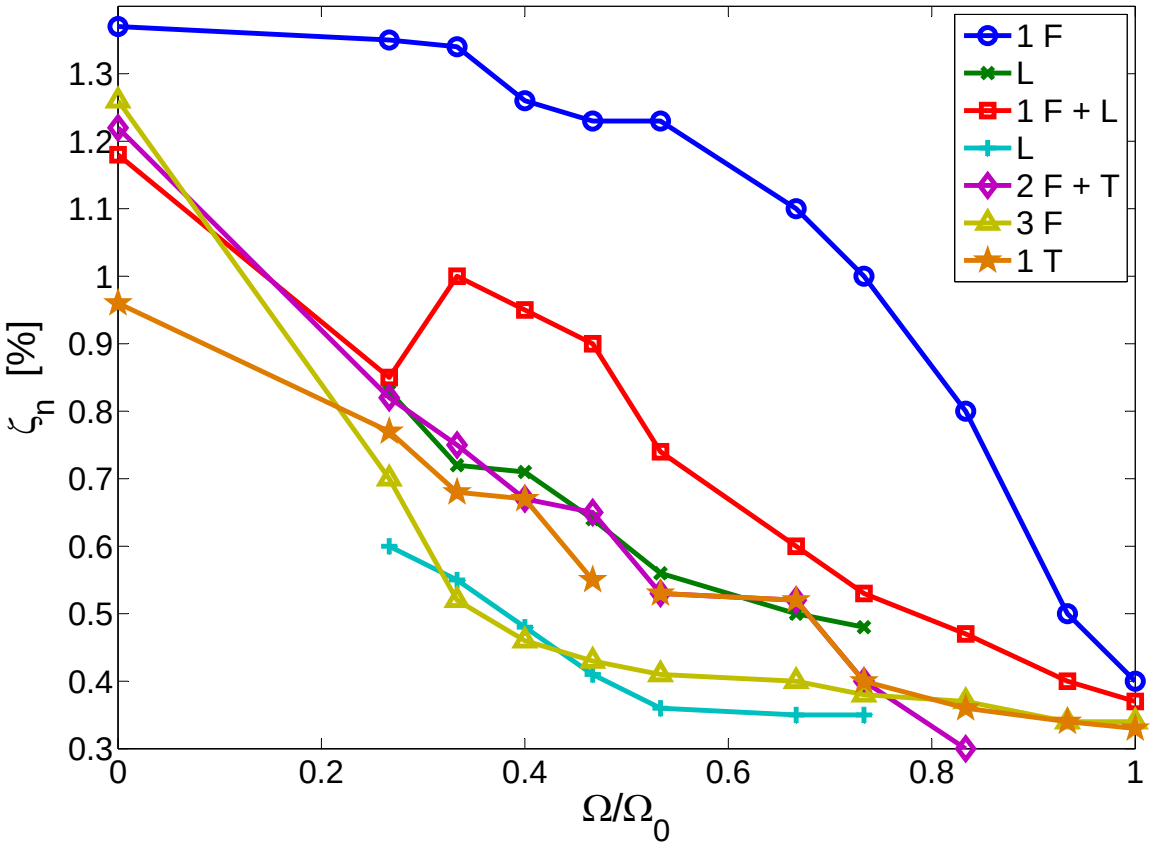

Figure 11.16: Experimental Fan Plot of the rotating blade for the damping ratios.

A final remark has to be made on the fan plot showing the damping. The rotor speed interferes with the intrinsic dynamic behavior of the rotating blade by changing the real part of the system poles. According to the fan plot of Fig.11.16, the damping ratios seem to decrease as a consequence of the growing angular velocity, hence, the system tends to reduce the stability margin with the increase of the rotor speed.

11.6 Numerical simulations of a rotating blade

The GAST code is used in order to obtain a reference solution of the fan plot and comparisons with the experimental results coming from the whirl tower tests. The investigations are performed on the model of the rotating blade with a second-order accuracy described in the Chapter 9, with the characteristics obtained using VABS, described in Sec.11.1. In particular, an eigenvalue problem of the Eq.(9.24) is

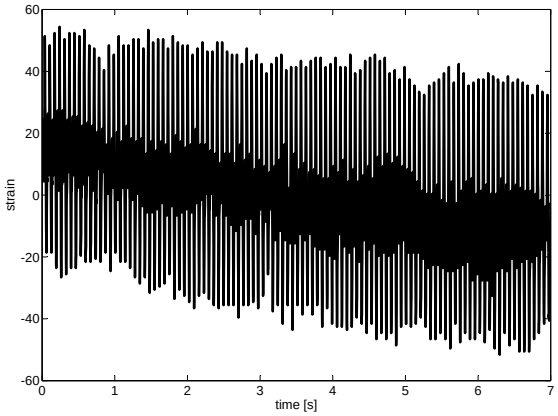

Figure 11.17: Experimental time history of the Lead-Lag sensor.

performed for each rotating speed, neglecting the aerodynamics.

The effects of the rotating speed on the natural frequencies of the blade is presented in the fan plot of Fig.11.18, where the values of the natural frequencies (along the y axis) and of the rotating velocity (along the x axis) are divided by the reference angular speed, that is $\Omega_0 = 1550RPM$, in consistent units. The label of the modes have been chosen according to the shapes evaluated in the non-rotating condition . In particular the flapping, lead-lag and torsional modes have been denoted with the letters F, L and T respectively. The added black straight lines correspond to different integer multiples of the fundamental frequency (namely the 1/rev, 2/rev, 3/rev etc.). The proximity of the natural frequencies with these lines can result in an unstable condition since they represent the frequencies of the forcing -aerodynamic- loads exciting the rotor blade. The rotational speed affects not only the natural frequencies of the blade but also the coupling among the modes. This effect is highlighted for the fourth mode in Fig.11.19, where the torsion is coupled with the out-of-plane bending.

11.6.1 Numerical - Experimental Comparison

The fan plot experimentally evaluated with the application of the modified Hilbert Transform Method to the strain gage measurements in the rotating frame can be compared with the numerical simulations performed using the GAST numerical platform. It is worth to remark that this comparison can be done

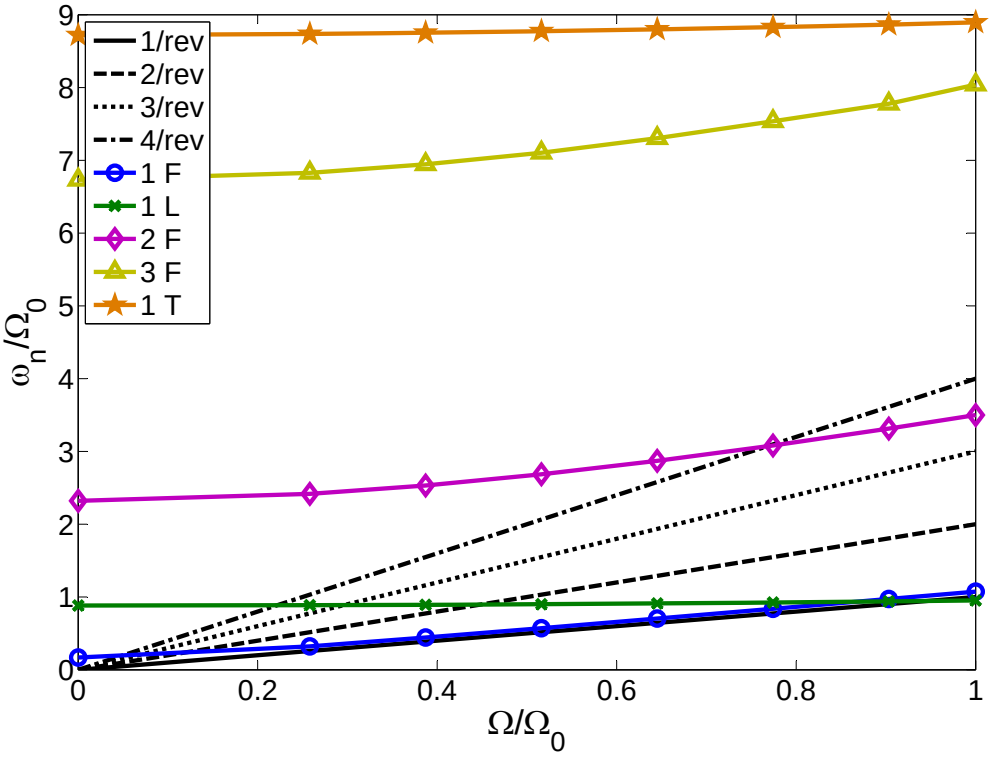

Figure 11.18: Numerical Fan Plot of the natural frequencies of the rotating beam.

only between the fan plot of the natural frequencies, since the numerical simulations do not consider a structural modal damping.

By comparing the experimental with the numerical fan plot, it can be noted a different number of the natural frequencies of the blade. A richer and more complex scenario characterizes the experimental tests with respect to the numerical simulations. Nevertheless, a very good correlation in the non rotating condition is obtained for the flapping as well as for the torsional modes. The lack of accuracy in the lead-lag estimation is due to a very poor quality of the signals recorded from the only two lead-lag sensors. A good correlation can also be noted in the evaluation of the evolution of the natural frequencies for the effect of increasing the rotating speed for $\Omega/\Omega_0 < 0.5$. Beyond such condition, the aerodynamic effects become considerable and the in-vacuum condition of the numerical tests cannot be considered still valid. In fact, the experimental normal modes evaluated using the operational modal analyses are an estimate of

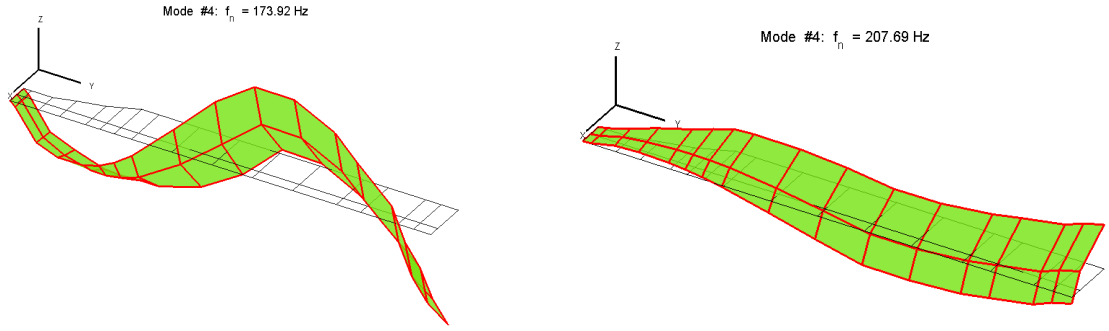

(a) Non rotating condition $\Omega = 0$ (b) Rotating condition $\Omega = \Omega_0$

Figure 11.19: Third Flapping mode.

the actual aeroelastic modes in the hover condition of the tests.

The first mode of the blade is a pure out-of-plane bending and it is characterized by a very high numerical-experimental correlation, as shown in Fig.11.20. In the fan plot both the numerical and the experimental solutions increases with analogous trend next to the $1/\text{rev}$. The normal mode experimentally estimated by the flapping strain gage sensors shows maximum value at the root and decreases spanwise. None contribution comes from the torsional sensors at this frequency. Also, the numerical solution do not show any torsional contribution and the flapping displacement is clearly related to the first out-of-plane bending mode shape.

On the contrary, the second flapping mode is coupled with the first torsional mode and in Fig.11.21 this behaviour is also observed by the numerical mode shape, in terms of displacements (with an easy understanding of the motion) and also by the experimental mode shape, in terms of strain gauges. In fact, in this case the torsional contribution is as high as the bending and both show the maximum value next to the root. Not as easy to recognize is the typical shape of a second flapping mode, but it has to be taken into account that the nodal point of the strain could be moved to the tip of the blade. The fan plot, in this case, has a fork shape, since the numerical and the experimental solutions start together when the blade is at rest and then diverge for $\Omega > 600\ RPM$. The reason for this behaviour has to be sought in the absence of the aerodynamics in the numerical simulations, which becomes more important as the rotating

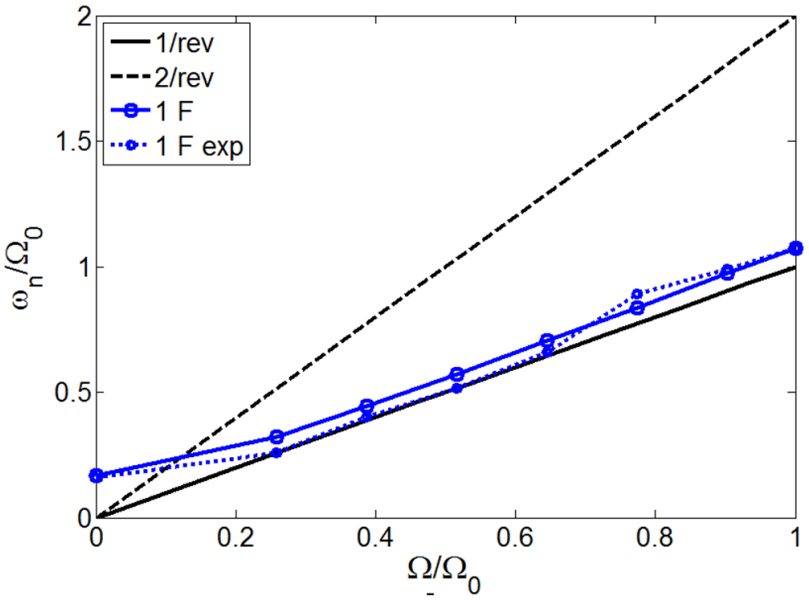

(a) fan plot

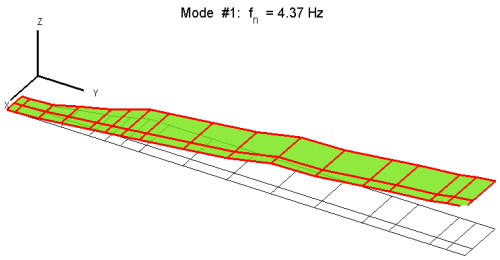

(b) numerical displacement

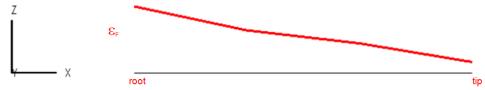

(c) experimental flapping strain

Figure 11.20: Experimental - Numerical comparison: Evolution of the natural frequency with the rotating speed and mode shape of the 1st out-of-plane bending (flapping) mode.

speed increases.

Similar considerations comes from the third flapping mode, as shown in Fig.11.22. It is worth to note that also in this case the experimental and numerical poles diverge with the increase of the rotating speed and the mode shape is characterized by high coupling between the torsion and bending displacement as well as strain.

Finally, Figure 11.23 shows the comparison for the first torsional mode. In this case only the torsional displacement and strain participate to the mode shape, so there is no coupling as in the case of the first flapping mode. Again in this case the fan plot shows good agreement between the experimental and the

numerical situations with the exception of the maximum speed at which it can be experimentally estimated, $\Omega/\Omega_0 = 0.9$, because the width of the frequency band is not wide enough to include this last value of the experimental fan plot. Both numerical and experimental analyses evaluate a very high natural frequency for this mode. This finding implies that a weakening of the blade could be made in a future prototype such as a changing of the stacking sequence of the composite material using layers at 25° instead of 45°, for example.

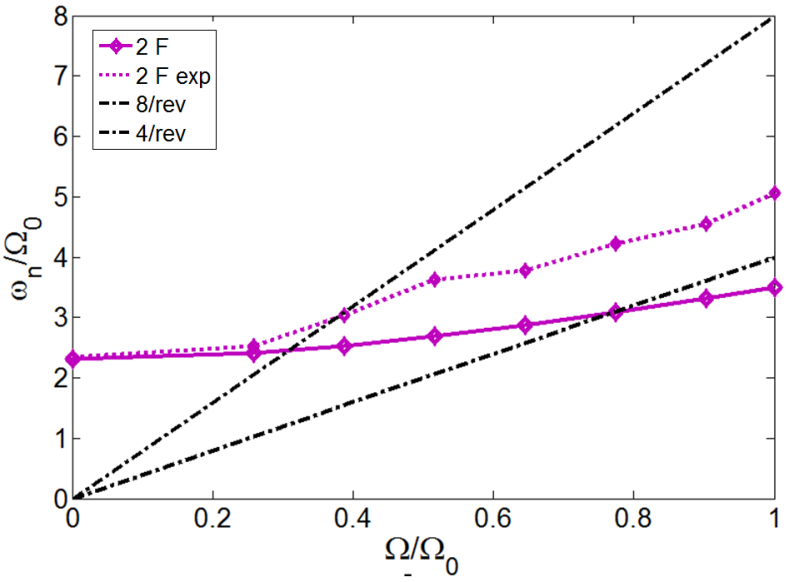

(a) fan plot

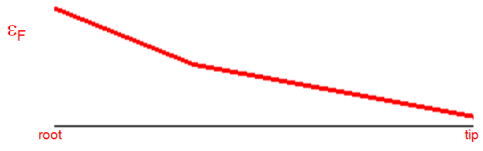

(b) experimental flapping strain

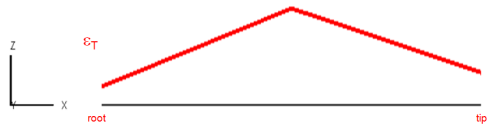

(c) experimental torsion strain

(d) numerical displacement

Figure 11.21: Experimental - Numerical comparison: Evolution of the natural frequency with the rotating speed and mode shape of the 2nd out-of-plane bending (flapping) mode.

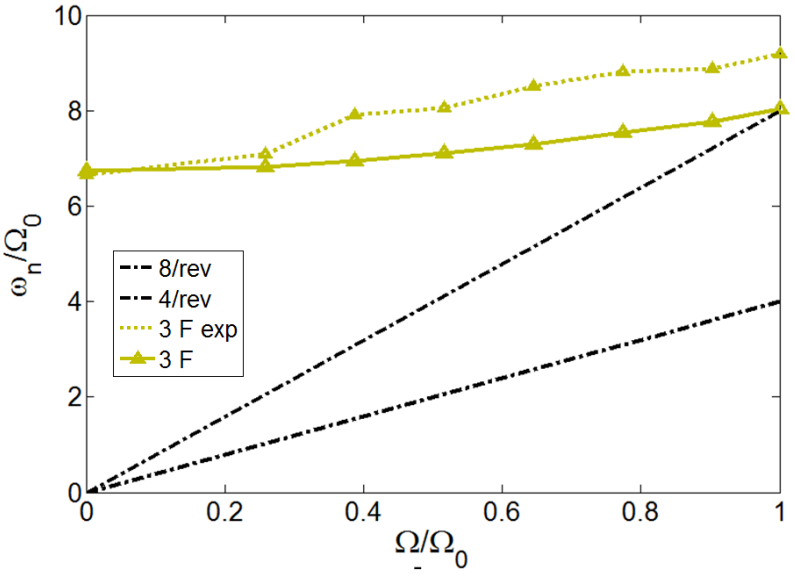

(a) fan plot

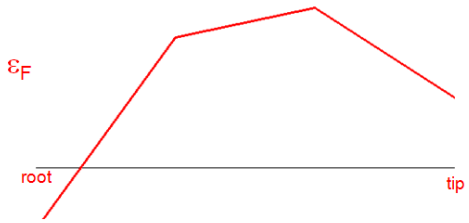

(b) experimental flapping strain

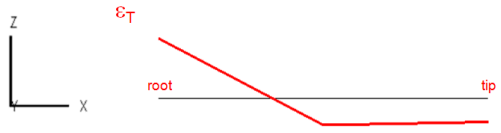

(c) experimental torsion strain

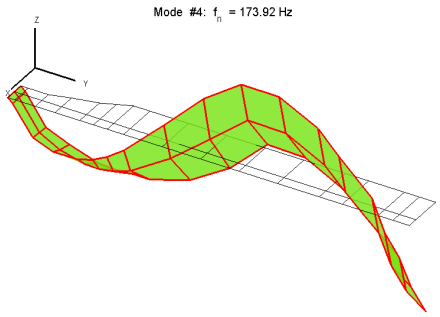

(d) numerical displacement

Figure 11.22: Experimental - Numerical comparison: Evolution of the natural frequency with the rotating speed and mode shape of the 3rd out-of-plane bending (flapping) mode.

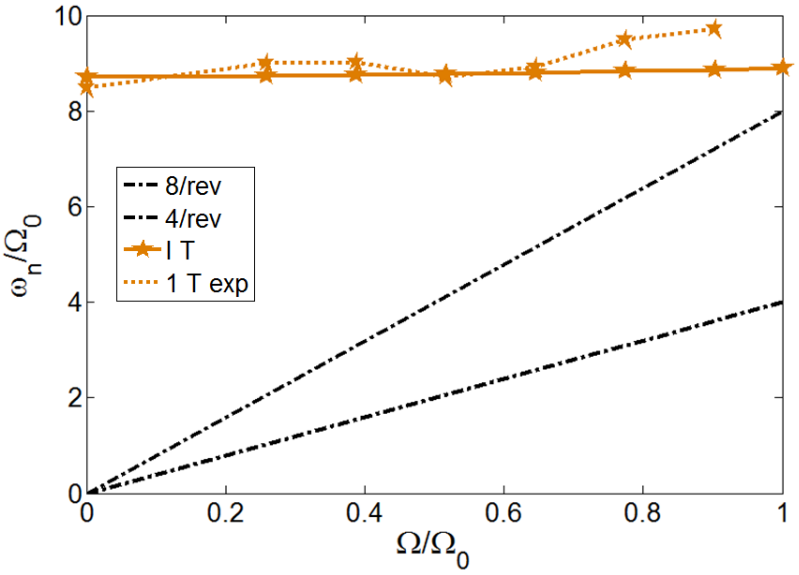

(a) fan plot

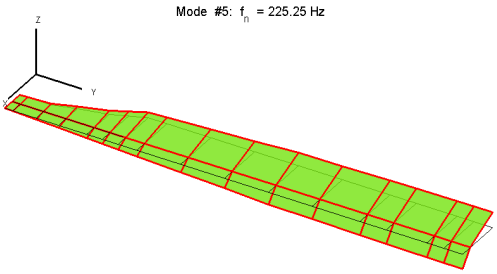

(b) numerical displacement

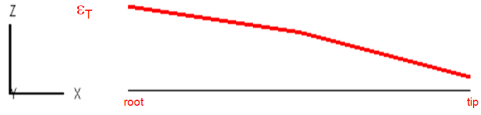

(c) experimental flapping strain

Figure 11.23: Experimental - Numerical comparison: Evolution of the natural frequency with the rotating speed and mode shape of the 1st torsional mode.

Chapter 12

Active Pitch Link Validation

In this chapter, the activities carried out to prove the effectiveness of the Active Pitch Link (APL) developed within the SHARCS project are summarized. The APL is an actively controlled Smart Spring used instead of the pitch link with the aim of modify the torsional characteristics of the blade to reduce vibration. Therefore, it is stressed that the thorough identification of the system is the important task to accomplish to evaluate a control law able to use the variable pitch link in order to reduce the vibrations. Hence, the influence of the APL to the normal modes of the rotating blade is investigated. At first, the solid pitch link is substituted by different elastic pitch links in order to evaluate the capability in changing the dynamical behaviour of the system. Tests in the non-rotating and rotating conditions are carried out and the results are shown in Sec.12.1. Moreover, from the characteristics of the blade described in Sec.11.1 and used to validate the fan plot, the simplified 1D model described in Chapter10 is implemented with the individual blade control strategy acting on the pitch link with variable stiffness. In the last section, the preliminary tests oriented to the vibration reduction are performed. An open-loop control law is presented. The obtained preliminary results on the vibration reduction are presented and compared with the numerical counterparts.

12.1 The Elastic Pitch Link

An assessment of the effect induced by the APL is performed by first introducing an elastic pitch link with three springs of different stiffness instead of the solid rigid pitch link. In this case, it is not actively controlled, so the identification of the modal properties of the system can be performed for each spring as reference configurations. Fig.12.1 shows the elastic pitch link connected to the blade in the experimental configuration on the whirl tower.

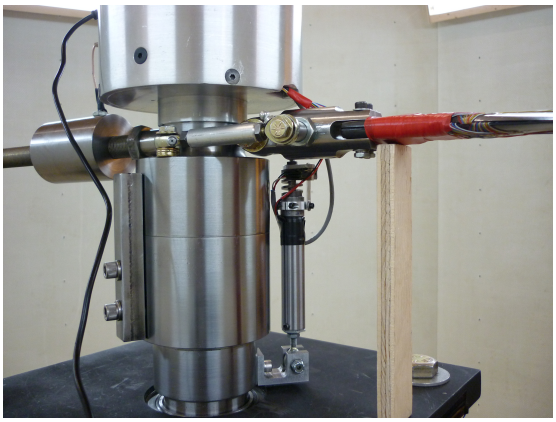

Figure 12.1: Adaptive Pitch Link connected to the blade during whirl tower tests.

The influence of the pitch link stiffness on the dynamic behavior of the system is evaluated by estimating the modal parameters of the system first in the non-rotating condition and then at each rotating speed. The stiffness values of the different springs used instead of the solid pitch link are the following: $k_{APL_1} = 254\,\mathrm{kN/m}$, $k_{APL_2} = 163\,\mathrm{kN/m}$, $k_{APL_3} = 88\,\mathrm{kN/m}$.

12.1.1 Non-rotating experimental investigations

A preliminary evaluation of the effect of softening the pitch link stiffness with respect to the rigid one has been performed in the non rotating configuration. A modal survey (based on the traditional input-output analysis) is performed in order to evaluate the effects on the dynamics of the blade of including the APL. The prototype of the Smart Spring is used in order to actuate the APL. The "OFF" and "ON" APL conditions, achieved by electrically controlling the piezoceramic device inside the pitch link through

the slip rings, allow to engage the rigid or the elastic link, respectively. The dynamic identification is performed in the non-rotating configuration because a known and measurable input has to be considered. The input-output experimental modal analysis is performed using the LMS SCADAS III and the LMS Testlab spectral acquisition software. The excitation is provided by a Bruel & Kiaer amplifier driven shaker (Type 2712/4808) connected to the trailing edge of the blade and 20 output positions are recorded with ICP PCB Piezotronics accelerometers through 5 runs, see Fig.12.2. It has to be noted that the sensors are placed on the blade along the leading and the trailing edge, on the upper and lower side of the APL and on the main shaft in the vertical direction. The sampling frequency is $2048\,\mathrm{Hz}$ and the frequency resolution is

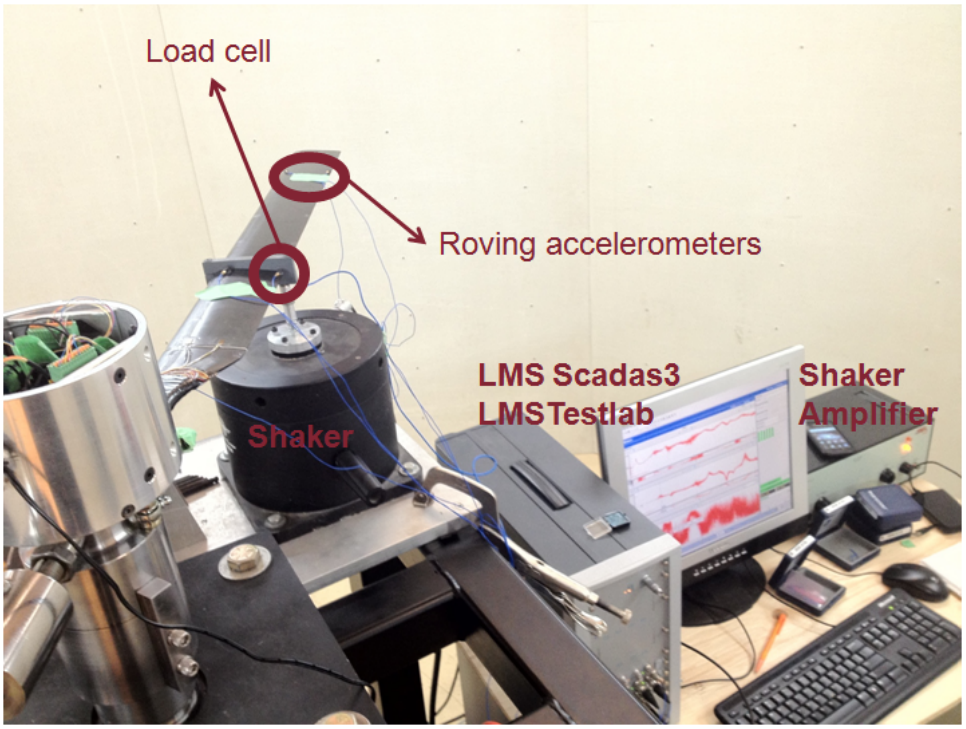

Figure 12.2: Experimental setup of the non rotating tests.

$0.0625\,\mathrm{Hz}$; the input loading is a random signal and is measured using an ICP PCB Piezotronics load cell. Either the force or the acceleration time signals are windowed by the hanning function and the Frequency Response Functions are evaluated using the Hv estimator by averaging 20 times in order to optimize the signal to noise ratio.

The effect of softening the pitch link stiffness is investigated taking the advantages of the non rotating

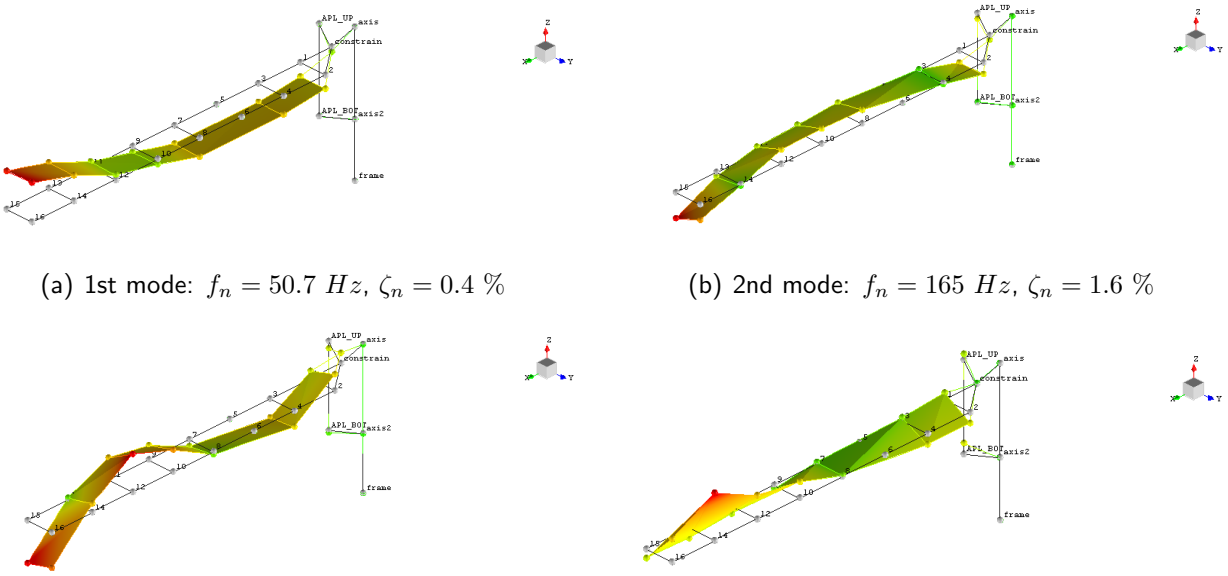

(a) 1st mode: $f_n = 50.7\ Hz$, $\zeta_n = 0.4\ \%$

(b) 2nd mode: $f_n = 165\ Hz$, $\zeta_n = 1.6\ \%$

(c) 3rd mode: $f_n = 284\ Hz$, $\zeta_n = 2.4\ \%$

(d) 4th mode: $f_n = 425\ Hz$, $\zeta_n = 1.8\ \%$

Figure 12.3: Normal modes of the non-rotating beam with the APL.

configuration, as a larger amount of sensors can be considered and a better resolution can be achieved because of the wider frequency band of the accelerometer responses with respect to the strain gauges. The modal analysis, performed on the FRF, highlights the coupling between the flap and torsion dynamics. Figure 12.3 shows the normal modes, in which the bending displacement is coupled with the torsional one and also a relative displacement between the top and the bottom part of the APL is involved. Moreover, from the analyses of the frequency response functions, the differences between the configuration with the rigid and the elastic pitch link are investigated. Although, almost all elastic modes of the blades seem to be not affected by the rigid and elastic pitch link, one mode shows a variation. The different mode shapes corresponding to the different APL configurations (solid/elastic pitch link) are shown in Fig.12.4. It is worth remarking that to this mode shape variation does not correspond a remarkable change of the natural frequency, whose value remains about $194\,\mathrm{Hz}$ regardless the value of the stiffness of the pitch link. In particular, the pitch mode of the blade becomes a complex mode shape involving bending and torsion strains, as noted by comparing the picture on the left with the one on the right, corresponding to the solid and the elastic pitch link respectively. It can be noted that the pitch link shows an elastic displacement

when the torsion of the blade is involved, whereas it is subjected to a rigid movement in the other cases. This is also the case of the rigid pitch link mode shown in Fig.12.4(a) The related damping ratio, as evaluated using the Polymax LMS estimator, is very high, about $6\,\%$, implying that an energy transfer from the blade to the mechanism inside the Smart Spring is occurring. Actually, the behaviour of the APL

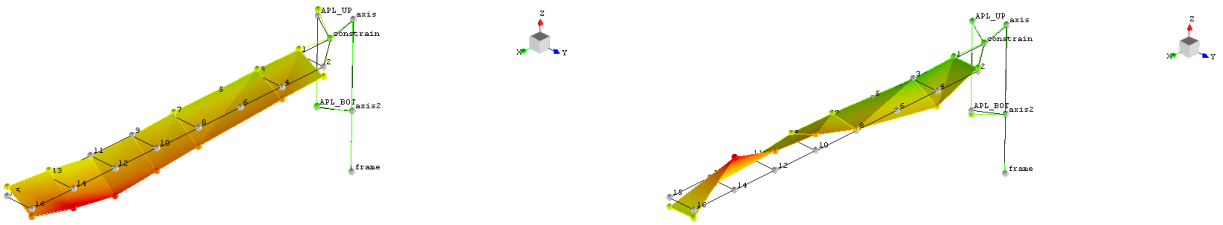

(a) Solid Pitch Link (b) Elastic Pitch Link

Figure 12.4: Effect of the pitch link on the mode shape from the input/output non rotating test.

seems to be more similar to a variable damping system than to a variable stiffness system because of the high values of the stiffness considered.

12.1.2 Rotating experimental investigations

Analogous results come from the analyses of the experimental tests in the rotating conditions. Data corresponding to several rotating velocities with different pitch links are collected and analyzed taking advantages of the developed modified OMA method capable to deal with harmonic excitation. The results are obtained for the rigid and elastic pitch link as in the previous Sec.11.5. Here they show that the flapwise and the lagwise dynamics are not influenced by the stiffness of the pitch link, as expected. On the contrary, the first torsional mode shows a weak dependence on the pitch link stiffness as represented in Fig.12.5, where the fan plot is depicted for each stiffness of the elastic pitch link. The first torsional natural frequency of the blade in both rotating and fix configuration varies because of different pitch links correspond to different boundary conditions of the blade and different pitch stiffness distribution along the blade. According to Fig.12.5, these variations are estimated but their values are too small with respect the reference rotating speed Ω_0. In order to increase these effects, a more flexible blade in torsion should be

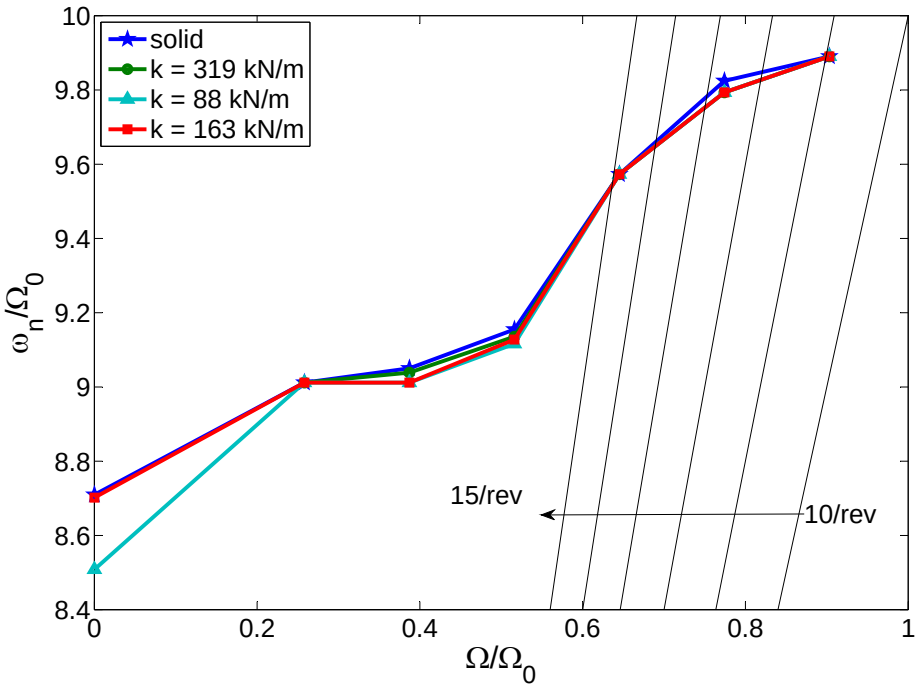

Figure 12.5: Effect of the pitch link on the fan plot of the rotating blade.

considered, or else a softer spring. Nevertheless, the mode shapes corresponding to the elastic pitch links look different with respect the ones obtained with the rigid pitch link. As it could be noted in Fig.12.6a (for $\Omega/\Omega_0 = 0.77$ but valid also for the other conditions), when the solid pitch link is considered, only the torsional strain gauges show significant signals. On the contrary, in presence of an elastic pitch link, all the flapping and the torsional strain gauges measure consistent values, resulting in the complex coupled mode shape represented in Fig.12.6b.

12.2 APL with open-loop control strategy

In this section, the experimental investigations carried out to simulate the IBC though the APL are presented. Inside the whirl tower test room a fan is activated with the aim of simulating the perturbations due to the forward-flight, see Fig.12.7, by inducing a discontinuity of the vertical flow of about $14\,\mathrm{m/s}$. This vertical disturbance is acting for about $16\,\mathrm{deg}$ along the azimuth coordinate and increases the vibration level of the whole system, especially at the 1/rev and 2/rev frequencies.

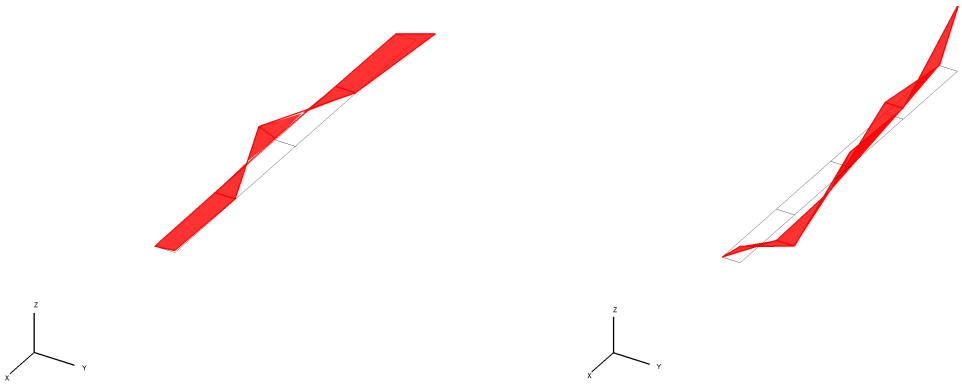

(a) Rigid Pitch Link (b) Elastic Pitch Link

Figure 12.6: Effect of the pitch link on the mode shape from the rotating test at $\Omega/\Omega_0 = 0.77$.

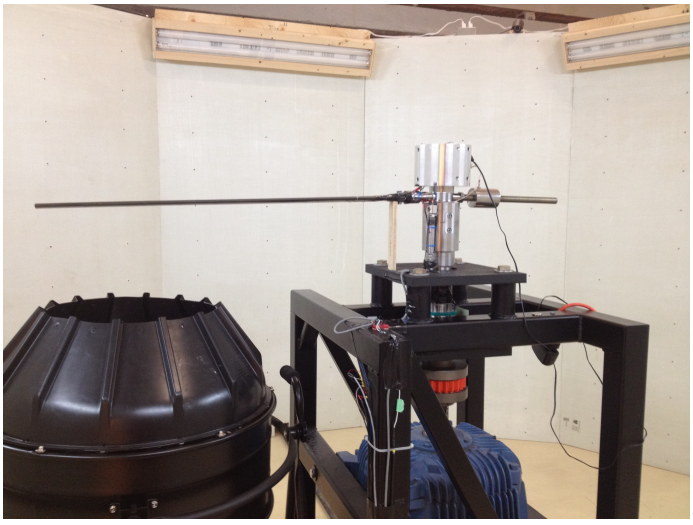

Figure 12.7: Fan simulating the forward flight inside the whirl tower test room.

During the tests the APL is connected to the main rotor through a rigid bracket, as shown in Fig.12.1. A full bridge strain gauge is put on the APL bracket in order to measure the transmitted vibration as means of a bending strain, as shown in Fig.12.8 from the top and the bottom. The behavior of the APL is also monitored through a Hall sensor measuring the axial displacement of the smart spring, to guarantee that the driving system correctly fed power through the slip rings.

When the fan is activated the evaluation of the system's modal parameters through the OMA is not possible anymore because, as expected, the multi-harmonic excitation is too high with respect the random. Moreover, the hall sensor on the APL shows that the device is not capable to work properly at high speed

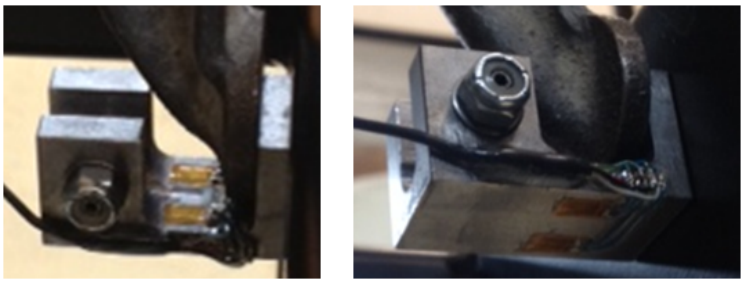

(a) Top view (b) Bottom view

Figure 12.8: Instrumentation of the APL bracket to measure the vibration coming to the rotor hub.

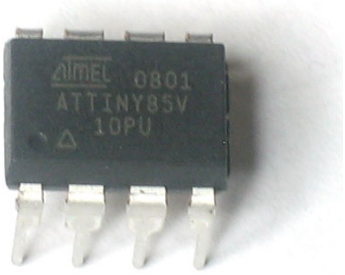

Figure 12.9: The ATtiny85/V micro-controller used inside the whirl tower test room to control the APL.

due to the centrifugal force acting on the internal mechanism preventing the quick variation of the smart spring from the rigid to the elastic condition of the APL. For these reasons the effects of the control action are investigated only at the n/rev frequencies, and for rotating speeds in the range from 600 RPM to 800 RPM. Figure 12.5 showed that in this range a weak variation in the fan plot is induced by the elastic pitch link: the green and the red lines, representing the $163\,\mathrm{kN/m}$ and $254\,kN/m$ springs only, depart from the blu line (the reference condition with the rigid pitch link) in the range $0.3 < \Omega/\Omega_0 < 0.5$.

An open-loop control law is implemented in order to activate the pitch link with the same frequency of the 2/rev in-phase with respect to the fan azimuth angle. This azimuthal control action is obtained by adding a programmable AVR 8-bit micro-controller (the ATtiny85/V in Fig.12.9) on the hub that according to the blade position drives the APL. The input is the signal coming from a hall sensor placed on the supporting structure of the whirl tower. It measures a spike every time the magnet under the APL bracket approaches a certain reference azimuth position. The spike is triggered with the blade approaching the fan and at every cycle this time instant is collected and averaged with the previous one in order to

predict the next. Then the output is sent from the micro-controller to the APL though the Amplifier and the slip rings. The easy and fast control action calculate also the A/D conversion of the signals, therefore, a RC filter is added to ensure the aliasing effects to do not occur. The time required to the system to elaborate the control action is taken into account, to avoid the overlapping of information. Once the program is compiled on the micro-controller and the executable file is stored in its internal memory, it can be placed on its board on the hub and it is ready to work. Since the adopted strategy is open-loop, the other available input channels are used to switch the control strategy among the OFF, ON and activate the 2/rev control from the control room.

All Figures 12.10-12.13 show bar plots, in which the amplitude of the strain average auto spectral density (evaluated by performing 35 averages) at the 2/rev is depicted for each condition (rigid, elastic and active pitch link) using the available sensors inside the blade. Moreover, the auto power spectral density of the bending strain evaluated on the bracket is shown as a measure of the vibration variation induced by the APL at the 2/rev. In all the conditions the strain distribution measured by the sensors inside the blade shows a maximum at the root, so this value, achieved with the rigid pitch link, is used to normalize the results, except for those coming from the test at 600 RPM with k_{APL_1}, in which the first torsional strain gauge did not work.

Figures 12.11 and 12.10 show the results achieved at 600 RPM using k_{APL_1} and k_{APL_2}, respectively. In particular, the softer spring gives better results. It can be noted that the elastic pitch link changes the distribution of the strain inside the blade, as expected, since it changes its boundary conditions. Then, the control action drives this variation in a beneficial way aiding the dissipation of the vibrational energy. This action is fundamental when the static variation of the boundary condition alone is not sufficient, as in the case with k_{APL_1}. Here, in fact, the spring is too stiff to let the flap strain increase, see Fig.12.11(b). Nevertheless, also in this case, the active control is capable to reduce the strain inside the blade and, as a consequence, to reduce the vibration measured at the pitch link bracket. It is important to note that when

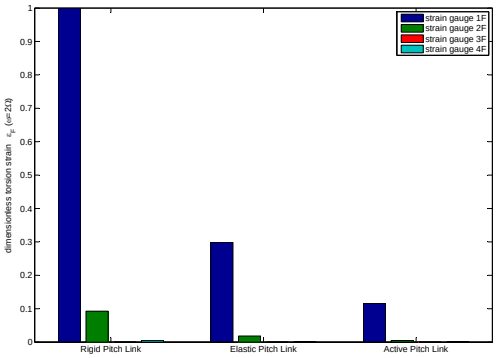

(a) blade bending

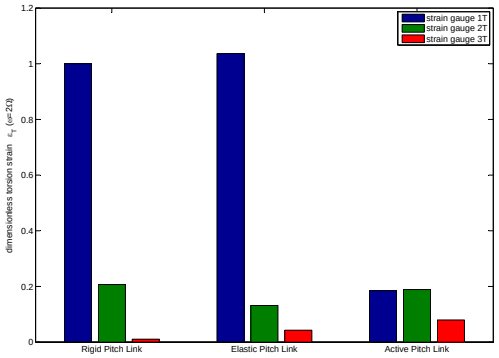

(b) blade torsion

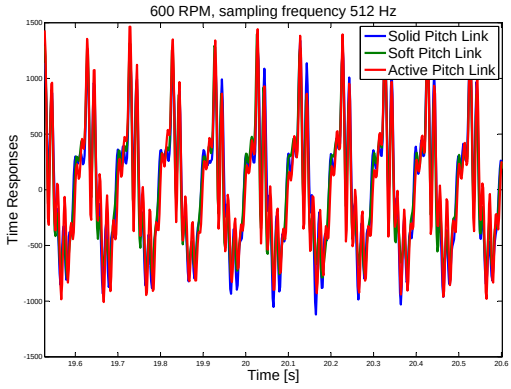

(c) bracket bending

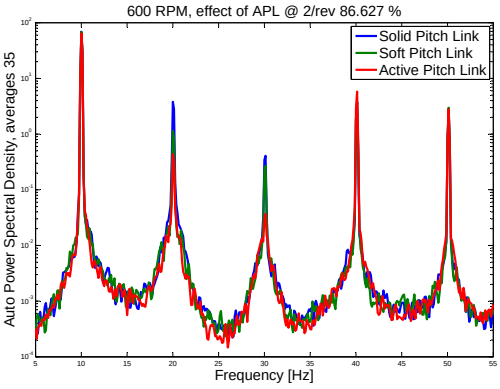

(d) bracket bending

Figure 12.10: Average strain variation at the 2/rev for $\Omega_0 = 600\ RPM$ and $k_2 = 163\ kN/m$ due to the pitch link.

a reduction of the vibration occurs as a consequence of the APL action, also a variation of the distribution of the strain inside the blade is generally achieved. This effect can be seen by comparing the spanwise trend of the bending or torsion strain in the reference condition with the trend in the controlled condition. If the Fig.12.10(b) is considered, the sharp peak of the strain measured at the root when the solid pitch link is engaged becomes of the same intensity of the strain measure in the mid section when the control is acting. This lead to a flat profile of the strain, to which also the strain measured next to the tip concurs.

For higher or lower rotating speeds, Fig.12.12 and 12.13, the vibration reduction at the bracket is very low (almost null at 800 RPM) and, in fact, it is the result of an inconsistent variation of the bending and torsion trend. At $\Omega = 800\ RPM$ the flap strain does not change and the torsion seems to increase a little. At $\Omega = 500\,\mathrm{RPM}$ the situation is less critical, and the bending strain for both rigid and active pitch link is almost the same, but the torsion strain decreases. This leads to a global small variation of the vibration transmitted to the bracket.

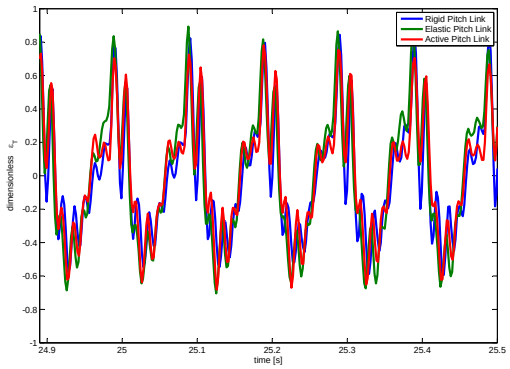

(a) blade bending

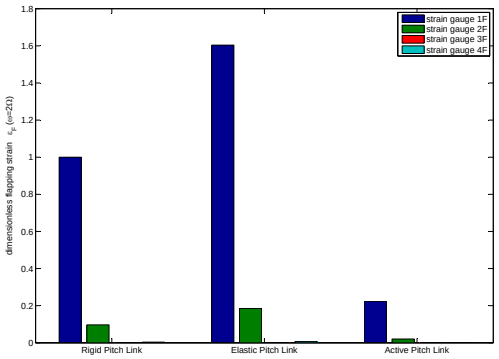

(b) blade bending

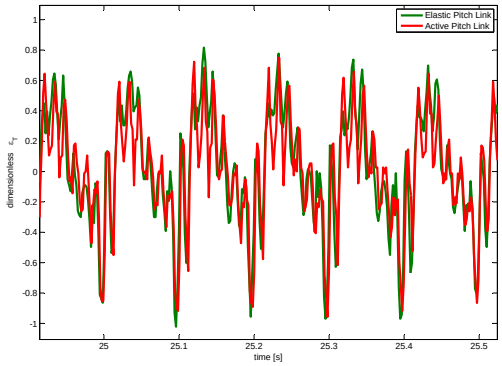

(c) blade torsion

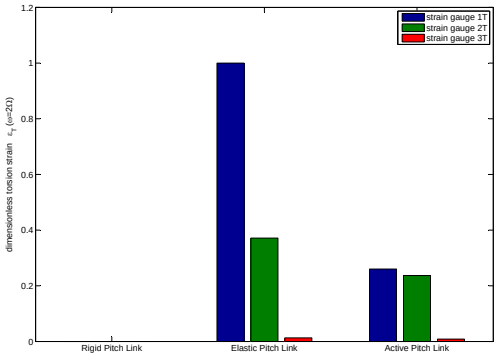

(d) blade torsion

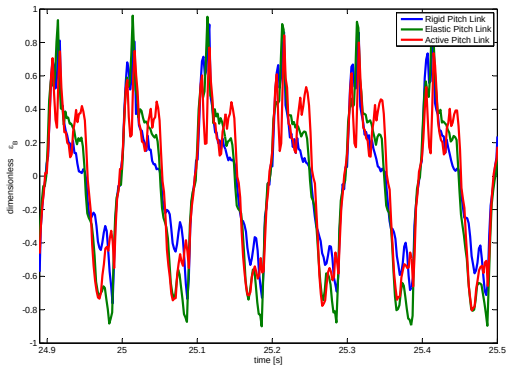

(e) bracket bending

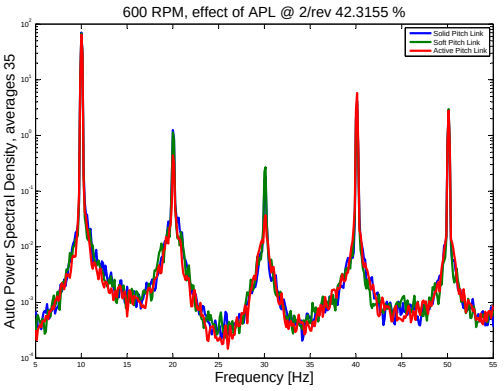

(f) bracket bending

Figure 12.11: Average strain variation at the 2/rev for $\Omega_0 = 600\ RPM$ and with $k_{APL_1} = 254\,\mathrm{kN/m}$ due to the pitch link.

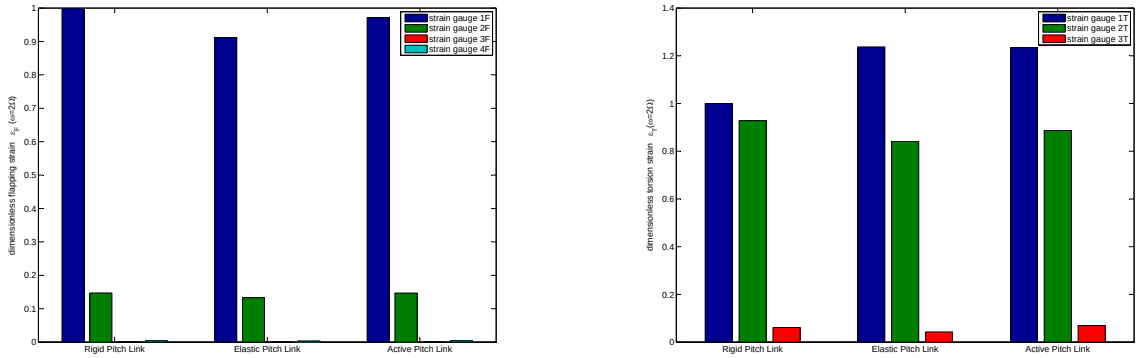

(a) blade bending

(b) blade torsion

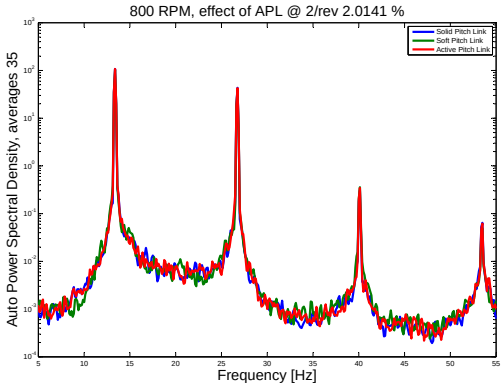

(c) bracket bending

Figure 12.12: Average strain variation at the 2/rev for $\Omega_0 = 800\ RPM$ and $k_{APL_1} = 254\,\mathrm{kN/m}$ due to the pitch link.

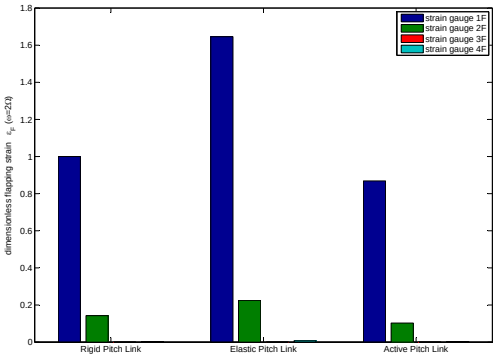

(a) blade bending

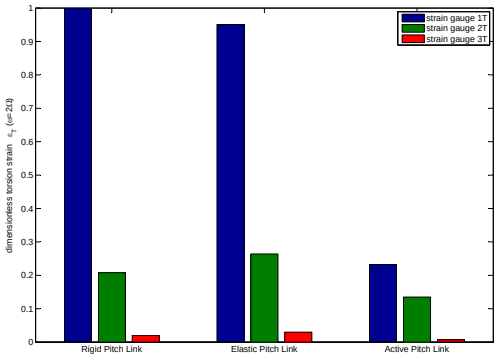

(b) blade torsion

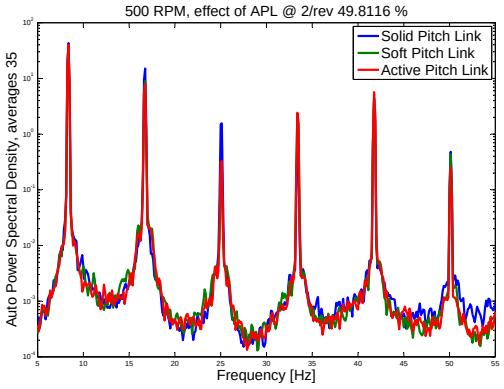

(c) bracket bending

Figure 12.13: Average strain variation at the 2/rev for $\Omega_0 = 500\ RPM$ and $k_{APL_2} = 166\,\mathrm{kN/m}$ due to the pitch link.

12.3 Aeroelastic numerical simulations of the IBC

A numerical procedure is implemented to solve the simplified aeroelastic problem described in Chapter 10. The blade's two degrees of freedom model is implemented with equivalent inertial and stiffness properties of the one used for the numerical evaluation of the fan-plot in Sec.11.6.1. This model is considered representative of the blade, that has been used for the experimental activities described in the Sec.11.5 and these numerical investigations are presented to explain how the Individual Blade Control, described in Chapter 10, acting on the boundary conditions affects the rotor vibration. In particular the spanwise variation of the dimensionless bending and torsional stiffness used for the simulations is depicted in Fig.12.14, together with the dimensionless mass distribution. These properties are given considering the blade discretized with 50 elements of the same length. The aerodynamic variables are set by considering the properties of the

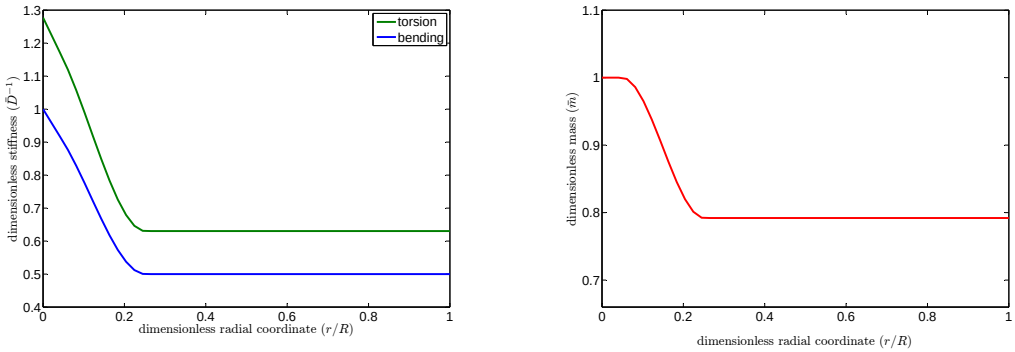

(a) stiffness (b) mass

Figure 12.14: Dimensionless stiffness and inertial distributions of the beam model.

NACA 0015 profile, the air density as $\rho = 1.225\,\mathrm{kg/m^3}$ and the advance ratio as $\mu = 0.14$. The Lock number is $\gamma = 5$ as for the true blade. Several simulations are carried out by varying the rotating speed from $600\,\mathrm{RPM}$ to $800\,\mathrm{RPM}$ and the stiffness of the pitch link to the values of $k_{APL_1} = 254\,\mathrm{kN/m}$ and $k_{APL_2} = 163\,\mathrm{kN/m}$, as in the experimental test cases. For each configuration three conditions are considered: the rigid, the elastic and the active pitch link. The first one corresponds to the cantilever condition, with infinity stiffness of the boundary conditions; this means that $C_{\theta 0} = 0$ and $\Delta C_\theta = 0$ in Eq.(10.6). The

second one consider a torsional spring with stiffness $C_{\theta 0} = k_{APL_1}$ or $C_{\theta 0} = k_{APL_2}$ as pitch link. In the last case an open-loop control is applied by means of a harmonic signal acting at the 2/rev.

Figures 12.15 and 12.16 show the results for $\Omega = 600\,\mathrm{RPM}$. It can be noted that the effect of changing the rigid pitch link with an elastic one, as expected, is detectable from the non-null value of the torsion angle in $r = 0$. On the contrary, the bending angle and displacement are still null. Although larger effects are obtained with the softer spring, in both cases the elastic boundary condition let the bending responses increase, otherwise the control acting at the 2/rev reduces them. This reduction is small, but still appreciable and shows that a softer spring has to be preferred. The variation of the torsion angle can be interpreted just as a variation of the equilibrium condition, given by the stiffness of the boundary conditions. In fact, the spanwise distribution does not change. This is due to the high values of the blade torsional stiffness distribution with respect to the bending ones. Therefore, with these blade properties, due to the coupling between torsion and bending, the vibration reduction can be achieved more from the flapping motion than from the torsion.

If higher rotating speeds are considered, the operating deflection shapes change because they depend by the frequency at which the system is excited, as can be noted from the distribution of the bending along the radial coordinate in Figs.12.17 and 12.18, for both the considered boundary conditions. Nevertheless, the torsion angle does not behave in this way, because of the high values of the torsional stiffness. In fact, it has to be considered that the first bending mode of this blade in the non-rotating condition is about $225\,\mathrm{Hz}$, much lower the considered 2/rev, that is about $27\,\mathrm{Hz}$. In these cases, the effect of the elastic pitch link on the vibration is almost the same that the one achieved for lower speed. The better performances are observed in the case of the active controlled boundary condition.

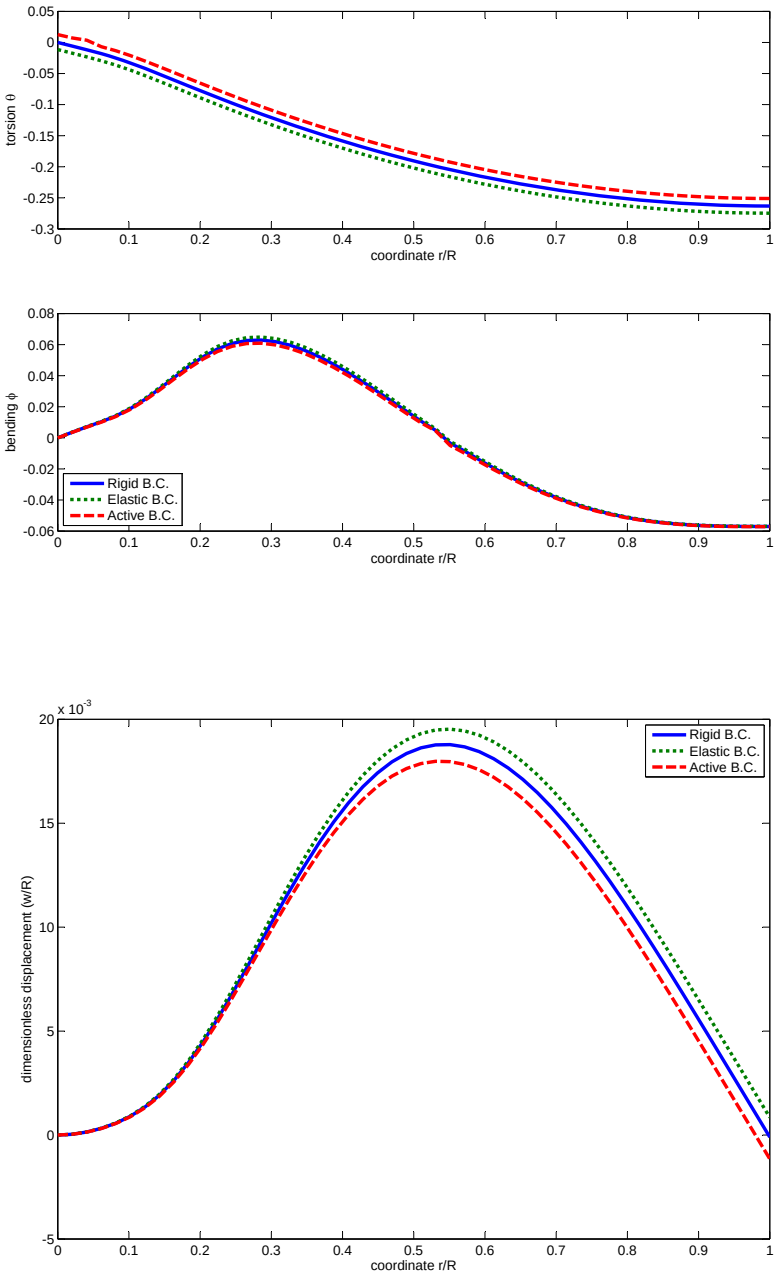

Figure 12.15: Influence of the IBC on the spanwise distribution of the torsion and bending slope and displacement for $k = k_{APL_1}$ and $\Omega = 600\,\mathrm{RPM}$.

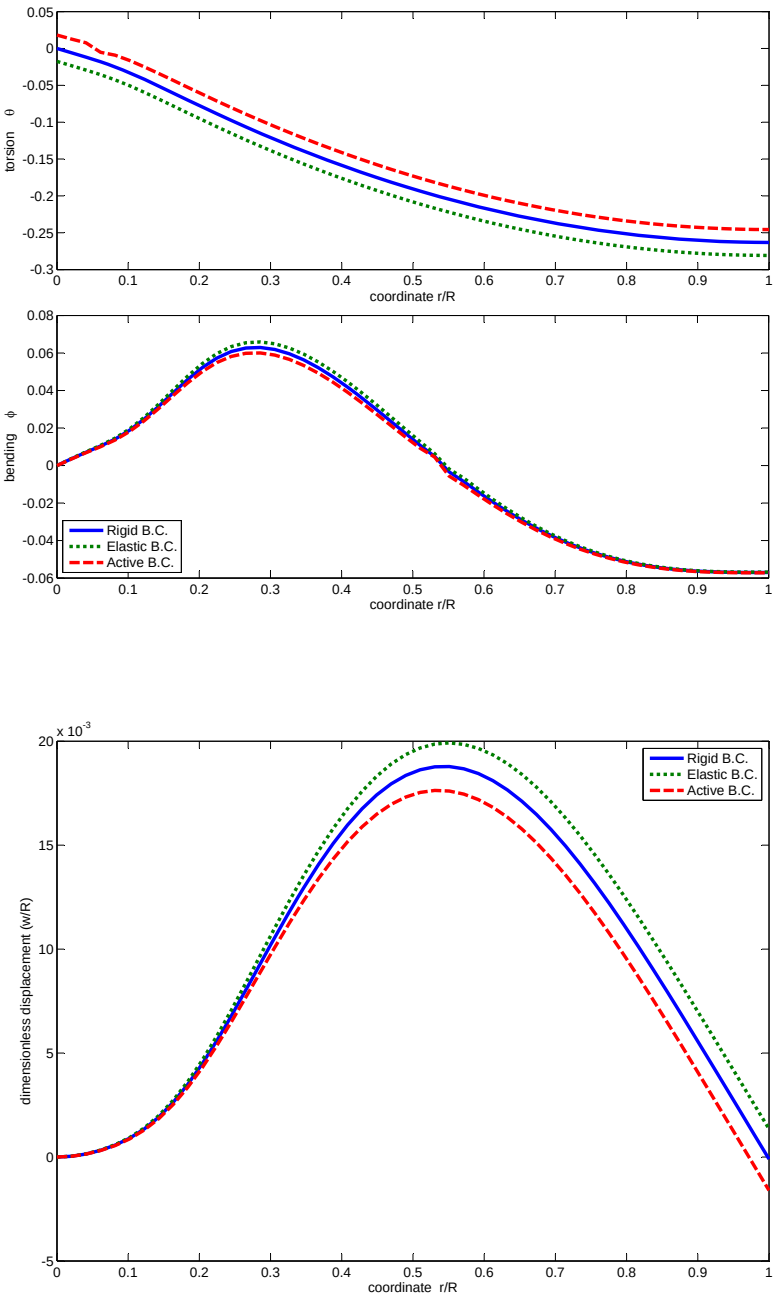

Figure 12.16: Influence of the IBC on the spanwise distribution of the torsion and bending slope and displacement for $k = k_{APL_2}$ and $\Omega = 600\,\mathrm{RPM}$.

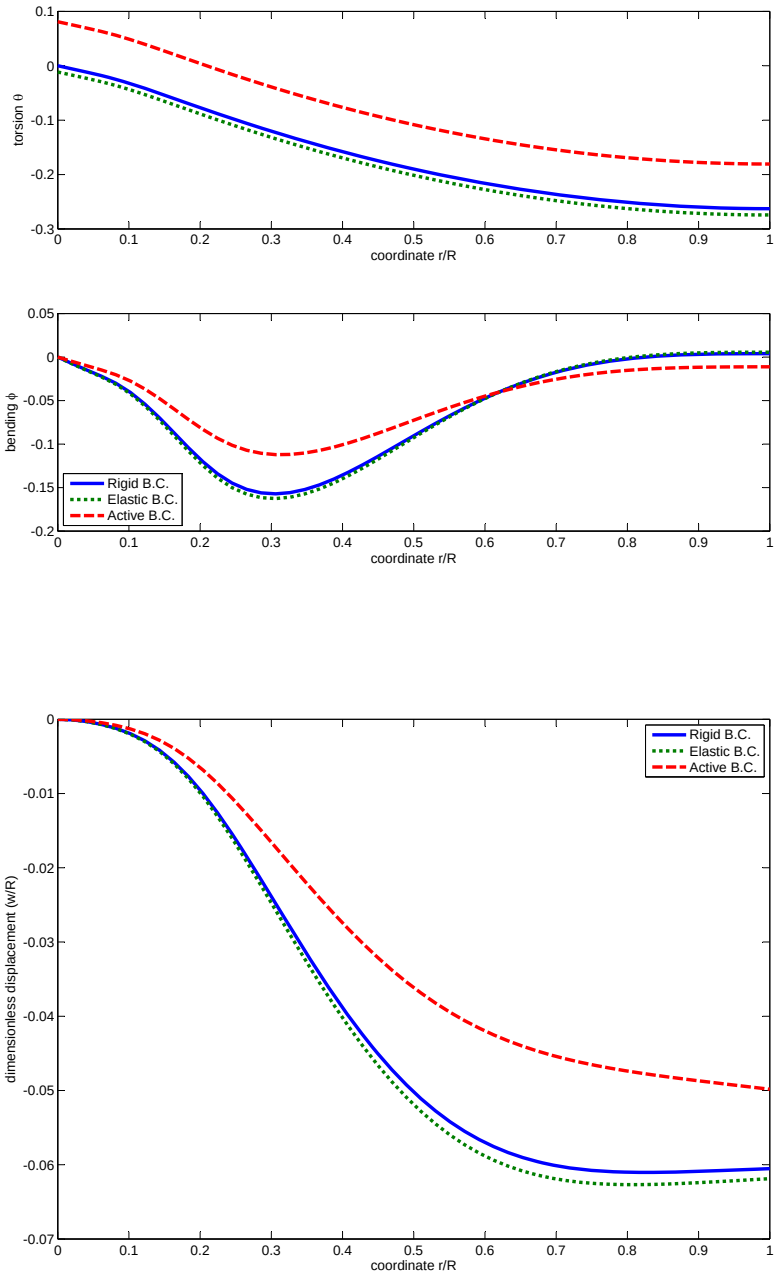

Figure 12.17: Influence of the IBC on the spanwise distribution of the torsion and bending slope and displacement for $k = k_{APL_1}$ and $\Omega = 800\,\mathrm{RPM}$.

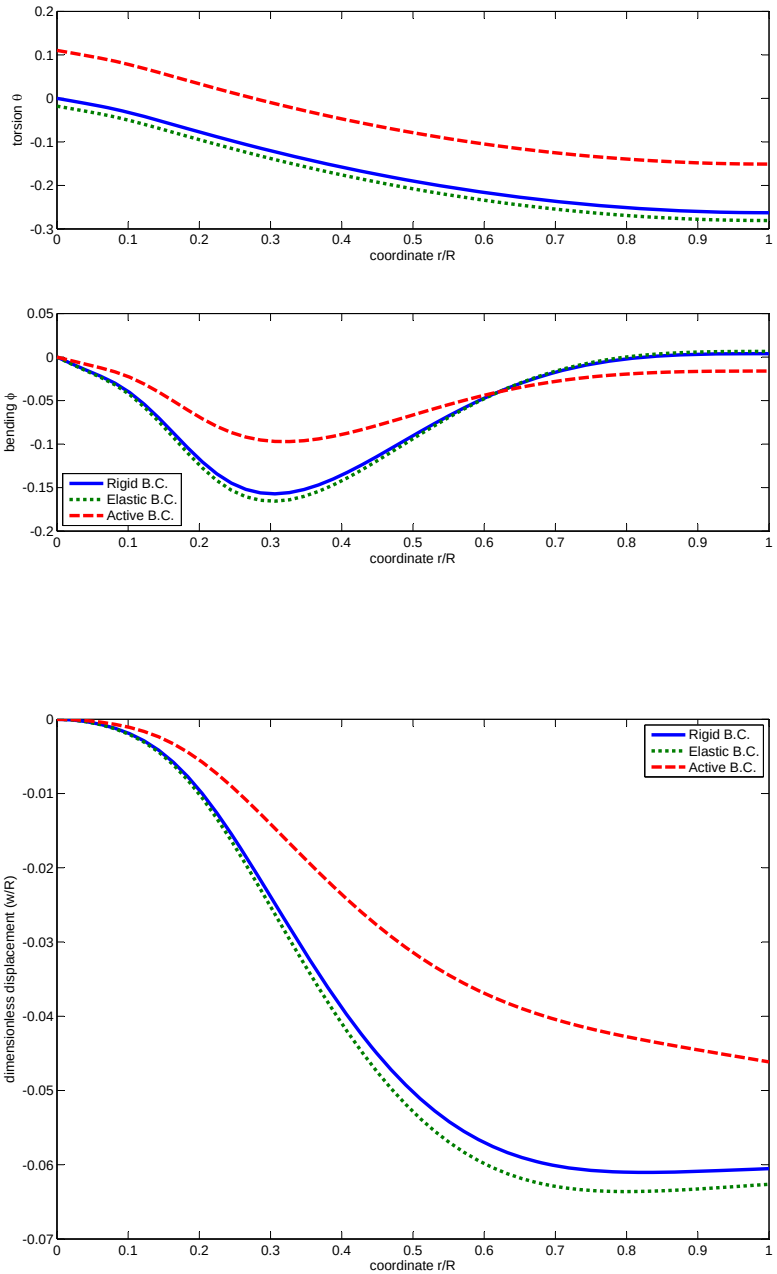

Figure 12.18: Influence of the IBC on the spanwise distribution of the torsion and bending slope and displacement for $k = k_{APL_2}$ and $\Omega = 800\,\mathrm{RPM}$.

12.3.1 Numerical - Experimental Comparison

As a final assessment a comparison with the numerical investigations described in Sec.12.3 can be performed by considering the Fig.12.19, in which the results coming from the theoretical model are shown together with the experimental results, in the reference condition, which is with the rigid pitch link. A first remark should be make about the numerical distribution of the strain, that is evaluated as a derivative of the rotation with respect to the radial coordinate. This corresponds to consider that plane sections remain plane and perpendicular to the neutral axis during bending, so for the bending bar the radial displacement $u(r, z)$ can be expressed as

$$u(r, z) = u_0(r) + z\varphi(r) \tag{12.1}$$

where φ is the bending rotation, according to the notation introduced in Chapter 10, and z is the distance from the neutral axis. The strain results:

$$\varepsilon = \frac{\partial u(r, z)}{\partial r} = \frac{\partial u_0(r)}{\partial r} + z\frac{\partial \varphi(r)}{\partial r} = \varepsilon_{0rr} + z\frac{\partial \varphi(r)}{\partial r} \tag{12.2}$$

The gauges measure the strain on the surface, so $z = \pm t/2$, being t the thickness of the profile, and the full bridge configuration cancels the pure axial strain ε_{0rr}. Therefore the bending strain experimentally evaluated is comparable with the radial derivative of the bending rotation φ numerically evaluated, unless considering the thickness as a scale factor to be included in the dimensionless factor. It should be noted that the numerical results in Fig.12.19 follow the same path of the experimental values, at least in correspondence of the measuring points. Indeed, the 1-D model of the blade, although very simple, is capable to describe the reference condition of the rotating blade, in which the rigid pitch link is used and the 2/rev is considered as target frequency.

In Fig.12.20 the numerical evaluations of the strain variations along the radial coordinate are represented by means of the bar plots, considering coordinates along the span next to the experimental sensor positions. These variations represent the effect of the elastic and active pitch link, evaluated with respect the rigid one,

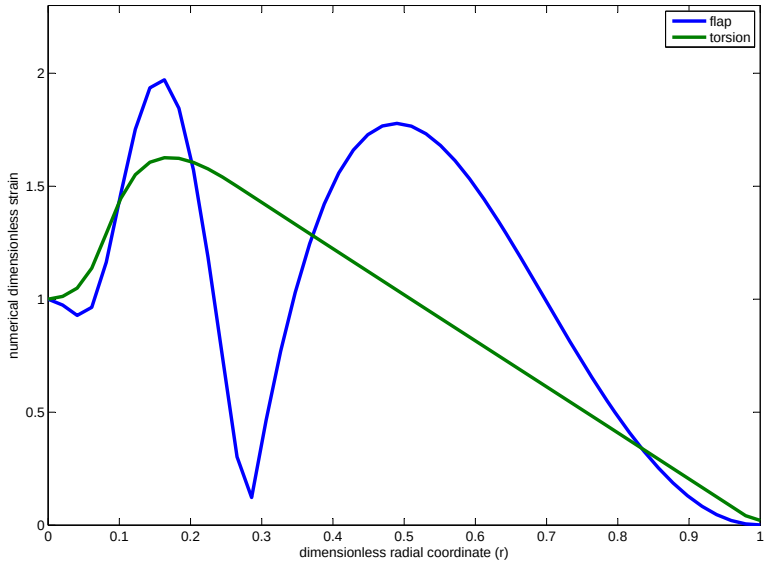

(a) numerical

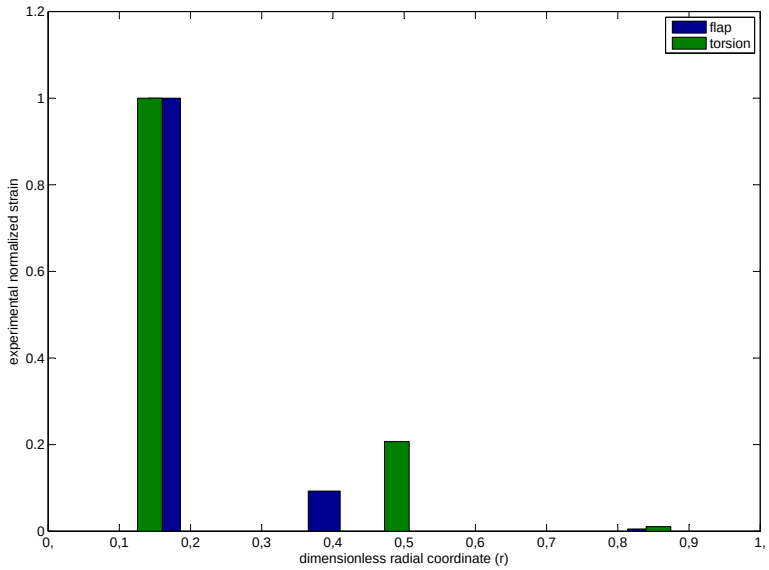

(b) experimental

Figure 12.19: Average vibration distribution of the dimensionless bending and torsion strain obtained from the numerical simulations and from the experimental analyses for $\Omega = 600\,\mathrm{RPM}$ with rigid pitch link.

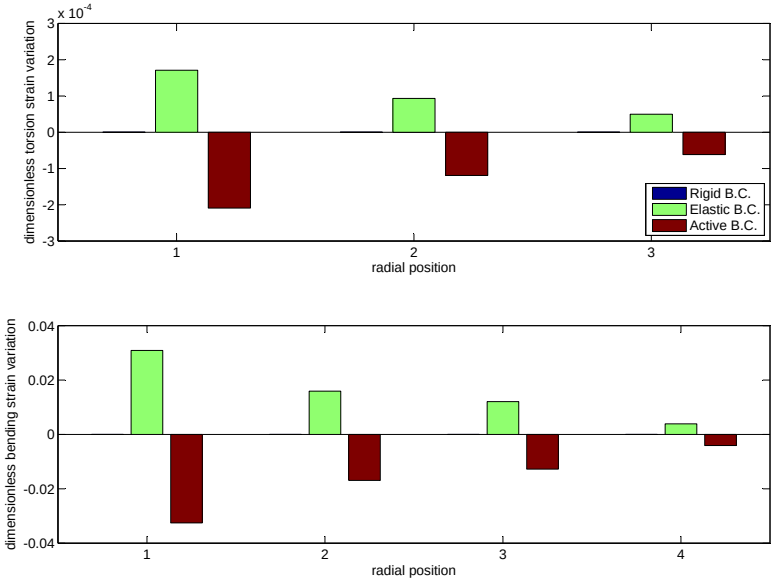

(a) k1

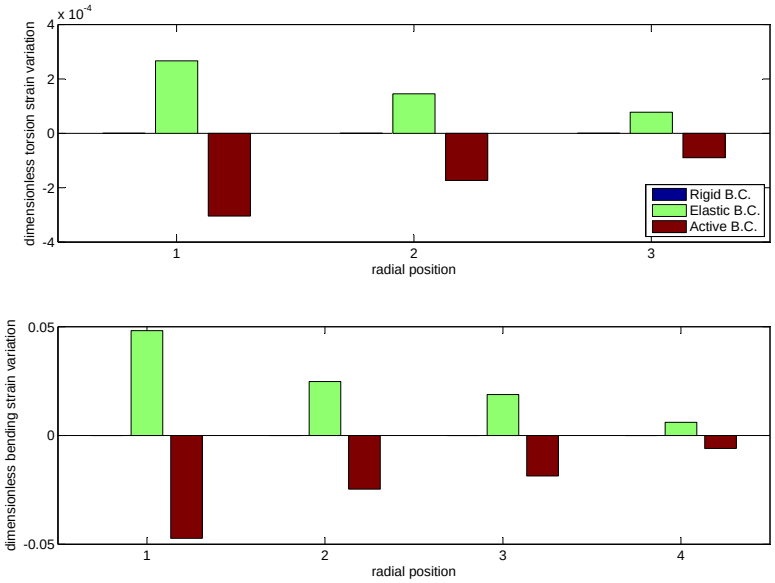

(b) k2

Figure 12.20: Average vibration variation on the dimensionless bending and torsion strain distribution due to the pitch link and obtained from the numerical simulations for $\Omega = 600\ RPM$ with $k_{APL_1} = 254\ kN/m$ and $k_{APL_2} = 166\ kN/m$.

when the rotating speed is 600RPM. In particular, positive values correspond to an increase of the strain and are achieved by using the uncontrolled elastic pitch link with both k_{APL_1} and k_{APL_2}. On the other hand, the negative values, obtained in the controlled condition, indicate that a reduction of the vibration is achieved. The same behavior has been described from the experimental results, in particular Figs.12.10 and 12.11 refer to the same operating conditions. It should be noted that there is not numerical-experimental correspondence between the absolute values of these strain variations, so only a quantitative comparison can not be made. Nevertheless as an overall evaluation it can be noted that the effects on the bending are about two order of magnitude higher than the effects on the torsion, although the variation in the boundary conditions affects the pitch link. As already highlighted previously, also in this case the coupling between torsion and bending plays the main role and allows the IBC to reach its purpose.

Concluding Remarks

The History of every major Galactic Civilization
tends to pass through three distinct and recognizable phases,
those of Survival, Inquiry and Sophistication,
otherwise known as the How, Why and Where phases.

[D.Adams, The Hitchhiker's Guide to the Galaxy]

The state-of-the-art in the field of vibration testing has been presented together with the developed methodologies. Within the Operational Modal Analysis the two major limitations regarding the application in presence of harmonic excitation and the scaling of the mode shapes have been addressed and the suggested solutions have been theoretically, numerically and experimentally validated. The mathematical formulations are described together with their implementation. Moreover, a numerical platform for the Operational Modal Analyses has been elaborated and it has been widely used.

In particular, it has been shown as the variation of the spatial properties of a structure (in terms of mass or stiffness) induces a modal variation that allows the evaluation of the modal masses. The numerical investigations showed how two different methods can be proficiently used and the experimental activities gave the proof that they can be applied in environmental testing for space structures to increase the amount of information on the test specimen necessary to validate a numerical finite element model of the structure.

A novel approach has been suggested and validated to identify the harmonic loadings acting on the structure by using the entropy statistical index. Moreover, a method on the application of the Operational Modal Analysis in case of colored noise (composed by these identified harmonic components and white noise) has been developed as a modified Hilbert Transform Method.

Several applications with different sensors (accelerometers, strain gauges, Fiber Bragg Grating), different

test articles (helicopters, blades, wind turbine) and several working conditions have been carried out with good results.

The complex rotorcraft applications have been deeply investigated starting from the mathematical formulation until the manufacturing aspects, passing through the design and validation of the entire experimental setup. The problem of vibration reduction has been considered and, starting from the formulation of the Individual Blade Control problem for the Active Pitch Link, numerical and experimental results showed the effectiveness of the suggested control strategy. It should be stressed that all these results have been possible thanks to the application of the Operational Modal Analysis during the whole developing process because it provided the experimental parameters necessary to tune the numerical simulations.

In conclusion, the importance of the Operational Modal Analysis for the aerospace applications has been proved and its capabilities to deal with different operating situations have been investigated.

Bibliography

[1] Bernal, D., "A receptance based formulation for modal scaling using mass perturbations," *Mechanical Systems and Signal Processing*, Vol. 25, No. 2, 2011, pp. 621 – 629.

[2] Coppotelli, G., "On the estimate of the FRFs from operational data," *Mechanical Systems and Signal Processing*, Vol. 23, No. 2, 2009, pp. 288 – 299.

[3] R.Brincker, L.Zhang, and P.Andersen, "Modal Identification from Ambient Responses Using Frequency Domain Decomposition," *XVIII IMAC Proceedings*, 2000.

[4] Agneni, A., Crema, L. B., and Coppotelli, G., "Time and Frequency Domain Modal Parameter Estimator by Output-Only Functions," *Proceedings*, 2001.

[5] Cauberghe, B., *Applied Frequency-Domain System Identification in the Field of Experimental and Operational Modal Analysis*, Ph.D thesis, 2004.

[6] Hermans, L. and Auweraer, H. V. D., "Modal testing and analysis of structures under operational conditions: industrial applications," *Mechanical Systems and Signal Processing*, Vol. 13, No. 2, 1999, pp. 193 – 216.

[7] Agneni, A., Coppotelli, G., and Grappasonni, C., "A method for the harmonic removal in operational modal analysis of rotating blades," *Mechanical Systems and Signal Processing*, Vol. 27, No. 0, 2012, pp. 604 – 618.

[8] Leishman, J., *Principles of Helicopter Aerodynamics*, Cambridge Aerospace Series, Cambridge University Press, 2002.

[9] Johnson, W., *Helicopter Theory*, Dover Books on Aeronautical Engineering Series, Dover Publications, 1994.

[10] Ulker, F., *A New Framework For Helicopter Vibration Suppression; Time-Periodic Identification and Controller Design*, PhD dissertation, 2011.

[11] Nitzsche, F., Feszty, D., Khomutov, K., Lynch, B., Mander, A., and Ulker, F., "Design and instrumentation of the SHARCS scaled rotor with three independent control systems," *64th Annual Forum of the American Helicopter Society Proceedings*, 2008.

[12] D.J.Inmann, *Engineering Vibration*, Prentice Hall, 1999.

[13] D.J.Ewins, *Modal Testing: Theory and Practice*, Research Studies Press Ltd., 1995.

[14] L.Meirovitch, *Analytical Methods in Vibrations*, Macmillan, 1967.

[15] L.Meirovitch, *Elements of vibration analysis*, McGraw-Hill, 1975.

[16] Morino, L. and Mastroddi, F., *Course notes in Structural Dynamics*, 2012.

[17] Géradin, M. and Rixen, D., *Mechanical vibrations : theory and application to structural dynamics*, Wiley, 1997.

[18] Robinson, E. and Silvia, M., *Digital signal processing and time series analysis*, Holden day series in time series analysis and digital processing, Holden-Day, 1978.

[19] Shin, K. and Hammond, P., *Fundamentals of Signal Processing for Sound and Vibration Engineers*, No. v. 10 in Fundamentals of Signal Processing for Sound and Vibration Engineers, John Wiley & Sons, 2008.

[20] Verboven, P., *Frequency-domain system identification for modal analysis*, PhD thesis, Vrije Universiteit Brussel, 2002.

[21] Ibrahim, S. and Mikulcik, E., "A method from the direct identification of vibration parameters from the free response," *The Shock and Vibration Bulletin*, Vol. 47, No. 4, 1977, pp. 183 – 198.

[22] Ibrahim, S., "Modal confidence factor in vibration testing," *The Shock and Vibration Bulletin*, Vol. 48, No. 1, 1977, pp. 65 – 75.

[23] Juang, J. and Pappa, R., "An eigensystem realization algorithm for modal parameter identification and model reduction," *Journal of guidance, control, and dynamics*, Vol. 8, No. 5, 1985, pp. 620 – 627.

[24] JUANG, J., "An eigensystem realization algorithm using data correlations(ERA/DC) for modal parameter identification," *Union College, International Modal Analysis Conference, 5 th, London, England*, 1987.

[25] Overschee, P., Moor, B., Hensher, D., Rose, J., Greene, W., Train, K., Greene, W., Krause, E., Gere, J., and Hibbeler, R., *Subspace Identification for the Linear Systems: Theory–Implementation*, Boston: Kluwer AcademicPublishers, 1996.

[26] Whittle, P., *Hypothesis testing in time series analysis*, Vol. 4, Almqvist & Wiksells boktr, 1951.

[27] Box, G., Jenkins, G., and Reinsel, G., *Time series analysis: forecasting and control*, Vol. 734, Wiley, 2011.

[28] Brown, D., Allemang, R., Zimmerman, R., and Mergeay, M., "Parameter estimation techniques for modal analysis," *SAE paper*, Vol. 790221, 1979.

[29] de Prony, B., "Essai éxperimental et analytique: sur les lois de la dilatabilité de fluides élastique et sur celles de la force expansive de la vapeur de l álkool,a différentes températures," *J. de l École Polytechnique*, Vol. 1, 1795, pp. 24–76.

[30] Vold, H., Kundrat, J., Rocklin, G., and Russel, R., *A multi-input modal estimation algorithm for mini-computers*, Vol. 820194, SAE, 1982.

[31] Juang, J. N. and Suzuki, H., "An eigensystem realization algorithm in frequency domain for modal analysis identification," *ASME Transactions on Vibrations, Acoustics, Stress*, Vol. 110, No. 24, 1988, pp. 24–29.

[32] Phillips, A. W., Allemang, R. J., and Fladung, W. A., "The complex mode indicator function (CMIF) as a parameter estimation method," *In Proceedings of the 16th International Modal Analysis Conference, Santa Barbara, CA, USA*, 1998, pp. 705–710.

[33] International, L., *The LMS Test.Lab Modal Analysis manual*, 2010.

[34] Heylen, W., Lammens, S., and Sas, P., *Modal Analysis Theory and Testing*, Katholieke Universiteit Leuven, Faculty of Engineering, Department of Mechanical Engineering, Division of Production Engineering, Machine Design and Automation, 1998.

[35] Pintelon, R., Guillaume, P., and Schoukens, J., "Measurement of noise (cross-) power spectra for frequency-domain system identification purposes: large-sample results," *IEEE Transactions on Instrumentation and Measurement*, Vol. 45, 1996, pp. 12–20.

[36] Basseville, M., Benveniste, A., Goursat, M., Hermans, L., Mevel, L., and der Auweraer, H. V., *Identification of linear systems. A practical guide to accurate modeling*, Transactions of the ASME: Journal of Dynamic Systems, Measurement, and Control, 2001.

[37] Guillaume, P., *Identification of multi-input multi-output systems using frequency-domain models*, Vrije Universiteit Brussel, 1992.

[38] El-Kafafy, M., Guillaume, P., Peeters, B., Marra, F., and Coppotelli, G., "Advanced Frequency-Domain Modal Analysis for Dealing with Measurement Noise and Parameter Uncertainty," *Topics in Modal Analysis I, Volume 5*, 2012, pp. 179–199.

[39] Agneni, A., Crema, L. B., and G.Coppotelli, "Output-Only Analysis of Structures with Closely Spaced Modes," *Mechanical System and Signal Processing. Special Issue: Operational Modal Analysis*, Vol. 24, No. 5, 2000, pp. 1240–1249.

[40] van Overschee, P. and de Moor, B., *Subspace identification for linear systems: theory, implementation, applications*, No. v. 1, Kluwer Academic Publishers, 1996.

[41] Bendat, J. and Piersol, A., *Random Data: Analysis and Measurement Procedures*, Wiley Series in Probability and Statistics, John Wiley & Sons, 2010.

[42] Brincker, R., Ventura, C. E., and Andersen, P., "Damping Estimation by Frequency Domain Decomposition," *XIX IMAC Proceedings*, 2001.

[43] Grappasonni, C., Coppotelli, G., and Agneni, A., "Operational Modal Analysis of a Helicopter UAV from Flight Tests," *International Operational Modal Analysis Conference Proceedings*, May 2011.

[44] Grappasonni, C., Coppotelli, G., and Nitzsche, F., "System identification of a reduced scale model blade with an Adaptive Pitch Link using whirl tower test data," *53rd AIAA/ASME/ASCE/AHS/ASC Structures, Structural Dynamics, and Materials Conference Proceedings*, 2012.

[45] Arsenault, T., Achuthany, A., Marzocca, P., Grappasonni, C., and Coppotelli, G., "Dynamic Identification of Wind Turbine System Under Operational Conditions Using FBG Transducers," *53rd AIAA/ASME/ASCE/AHS/ASC Structures, Structural Dynamics, and Materials Conference Proceedings*, 2012.

[46] Agneni, A., Coppotelli, G., and Grappasonni, C., "Operational Modal Analysis of a Rotating Helicopter Blade," *ISMA International Noise and Vibration Engineering Proceedings*, 2010.

[47] Shannon, C. E., "A mathematical theory of communication," *SIGMOBILE Mob. Comput. Commun. Rev.*, Vol. 5, No. 1, Jan. 2001, pp. 3–55.

[48] Jacobsen, N., "Separating Structural Modes and Harmonic Components in Operational Modal Analysis," *XXIV IMAC Proceedings*, 2006.

[49] N.J. Jacobsen, P.Andersen, R., "Eliminating the Influence of Harmonic Components in Operational Modal Analysis," *XXV IMAC Proceedings*, 2007.

[50] Snedecor, G. W. and Cochran, W., *Statistical Methods*, No. v. 276 in Statistical Methods, Iowa State University Press, 1989.

[51] Agneni, A. and Crema, L. B., "Damping ratio estimates from autocorrelation functions," *Proceedings of Damping*, Vol. 3, 1991.

[52] Hugin, C., Hatch, C., Ltd, Q., and Griffiths, T., "Active Vibration Control of the Lynx Helicopter Airframe," 2007.

[53] Hatch, C., Skingle, G., Greaves, C., Lieven, N., Coote, J., Friswell, M., Mottershead, J., Shaverdi, H., Mares, C., McLaughlin, A., et al., "Methods for Refinement of Structural Finite Element Models: Summary of the GARTEUR AG14 Collaborative Programme," 2006.

[54] Braun, S., "The Extraction of Periodic Waveforms by Time Domain Averaging," *Acoustica*, Vol. 23, No. 2, 1975, pp. 69 – 77.

[55] McFadden, P., "A revised model for the extraction of periodic waveforms by time domain averaging," *Mechanical Systems and Signal Processing*, Vol. 1, No. 1, 1987, pp. 83 – 95.

[56] Mohanty, P. and Rixen, D., "A modified Ibrahim time domain algorithm for operational modal analysis including harmonic excitation," *Journal of Sound and Vibration*, Vol. 275, No. 1, 2004, pp. 375–390.

[57] Bielawa, R., *Rotary wing structural dynamics and aeroelasticity*, AIAA education series, American Institute of Aeronautics and Astronautics, 2006.

[58] Coppotelli, G., Vetrano, F., Nitzsche, F., Feszty, D., Mander, A., P.Wierach, and J.Riemenschneider, "Identification of the Dynamic Properties of Active Twist Rotor Model Blade Using Output-Only Data," *International Operational Modal Analysis Conference Proceedings*, 2009.

[59] Schroeder, K., Ecke, W., Apitz, J., Lembke, E., and Lenschow, G., "A fiber Bragg grating sensor system monitors operational load in a wind turbine rotor blade," *Measurement Science and Technology*, 2006, pp. 1167 – 1172.

[60] Hameed, Z., Hong, Y. S., Cho, M. Y., Ahn, S. H., and Song, K. C., "Condition Monitoring and fault detection of wind turbines and related algorithms: a review," *Sustainable Energer Rev*, 2007.

[61] Schulz, M. J. and Sundaresan, M. J., "Smart sensor system for structural condition monitoring of wind turbines: Subcontract Report." *National Renewable Energy Laboratory, CO: NREL/SR-500 40089*, 2006.

[62] Sundaresan, M. J., Schultz, M. J., and Ghoshal, A., "Structural health monitoring static test of a wind turbine blade: Subcontract Report." *National Renewable Energy Laboratory, CO:NREL/SR-500-28719*, 2002.

[63] Wernicke, J., Shadden, J., Kuhnt, S., Byars, R., Rhead, P., and Damaschke., M., "Field Experience of fibre optical strains sensors for providing real time load information from wind turbine blades during operation," *European Wind Energy Conference Proceedings*, 2004.

[64] Takeda, N., "Characterization of microscopic damade in composite laminates and real-time monitoring by embedded optical fiber sensors." *International Journal of Fatigue*, Vol. 24, 2002, pp. 281 – 289.

[65] Fixter, L. and Williamson, C., "State of the art review - structural health monitoring," *QinetiQ ltd. and SMART.mat (The Smart Materials, strucutres and Surfaces Network)*, 2006.

[66] Ciang, C., Lee, J., and Bang, H., "Structural health monitoring for a wind turbine system: a review of damage detection methods," *Measurement Science and Technology*, 2008.

[67] Doyle, C., "Fibre Bragg Grating Sensors An Introduction to Bragg Gratings and Interrogation Techniques," *Smart Fibres Literature*, 2003.

[68] Kang, L.-H., Kim, D.-K., and Han, J.-H., "Estimation of dynamic structural displacements using fiber Bragg grating strain sensors," *Journal of Sound and Vibration*, Vol. 305, No. 3, 2007, pp. 534 – 542.

[69] Casola, A., Castelmani, F., and di Serio, M., "New Objectives of Vibration Testing During Intensive Rate Satellite Productions," *Fourth International Symposium Environmental Testing for Space Programmes*, 2001.

[70] Brinker, R. and Andersen, P., "A way of getting scaled mode shapes in output only modal analysis," *XXI IMAC Proceedings*, 2003.

[71] Parloo, E., Cauberghe, B., Benedettini, F., Alaggio, R., and Guillaume, P., "Sensitivity-based operational mode shape normalisation: Application to a bridge," *Mechanical Systems and Signal Processing*, Vol. 19, No. 1, 2005, pp. 43 – 55.

[72] Palmerini, G., Gasbarri, P., and Toglia, C., "Determination of kinematic state of an orbiting multi-body using GNSS signals," *Acta Astronautica*, Vol. 64, No. 11-12, 2009, pp. 1109–1122.

[73] Nitzsche, F., "Aeroelastic Analysis of a Rotor Blade with Active Impedance Control at the Root," *Canadian Aeronautics and Space Journal*, Vol. 47, No. 1, 2001.

[74] Nitzsche, F., Harold, T., Wickramasinghe, V. K., Young, C., and Zimcik, D. G., "Development of a Maximum Energy Extraction Control for the Smart Spring," *Journal of Intelligent Material Systems and Structures*, 2005.

[75] Voutsinas, S. G., "Vortex methods in aeronautics: how to make things work," *International Journal of Computational Fluid Dynamics*, Vol. 20, No. 1, 2006, pp. 3–18.

[76] Ulker, F., Voutsinas, S., Riziotis, V., and Nitzsche, F., "On the Necessity of High-Fidelity Aeroelastic Modeling of On-blade Control Surface for Helicopter Vibration Suppression," *AHS 68th Annual Forum and Technology Display*, May 2012.

[77] Hodges, D., Dowell, E., Center, A. R., Research, U. A. A. M., and Laboratory, D., *Nonlinear equations of motion for the elastic bending and torsion of twisted nonuniform rotor blades*, NASA technical note, National Aeronautics and Space Administration, 1974.

[78] F.Nitzsche, "A new Individual Blade Control Approach to Attenuate Rotor Vibration," *22nd European Rotorcraft Forum Proceedings*, 1996.

[79] Nitzsche, F. and E.J.Breitbach, "Using Adaptive Structures to Attenuate Rotary Wing Aeroelastic Response," *Journal of Aircraft*, Vol. 31, No. 5, 1994, pp. 1178 – 1188.

[80] Lehman, L., *Hybrid State Vector Methods for Structural Dynamic and Aeroelastic Boundary Value Problems*, NASA Rept. No. CR-3591, 1992.

[81] Theodorsen, T., *General Theory of Aerodynamic Instablility and the Mechanism of Flutter*, NACA Rept. No. 496, 1935.

[82] Yuy, W., *VABS Manual for Users*.

[83] SRS, "http://www.smartrotorsystems.ca/," 2009.